Examining Solvent Effects in Theoretical and Ultrafast Spectroscopy

by

Matthew A. P. Turner

Thesis

Submitted to the University of Warwick

in partial fulfilment of the requirements

for admission to the degree of

Doctor of Philosophy

Department of Physics

February 2020

Contents

List of Tables

List of Figures

Acknowledgments

I would firstly like to thank both my PhD supervisors. Thanks to Nick Hine for constant help and support throughout. This PhD would not have been possible without his guidance and assistance. Likewise I would like to thank my other supervisor Vas Stavros for his patience, guidance and always being about to answer my questions, numerous as they were.

I would like to thank the members of team Stavros past and present for everything they have done to make my time at Warwick excellent. Thanks to Mitch Horbury for this support and for his key role in the papers in this thesis. Thanks to Emily Holt, Nat Rodrigues Lopes, and Konstantina Krokidi for their continued hard work on the homosalate paper and for all the useful conversations over the years. Thanks to Jack Woolley as well, the conversations weren't always as useful but they were always entertaining. Thanks to Sofia Goia, Adam Cowden, and Abbie Wittock, it has been a pleasure working with you all and hopefully, along with Emily and Konstantina, you can continue the Stavros calculations legacy for years to come. Thanks to Mick Staniforth, Tosin Abiola, and Daniel Coxon for the company and making the office a great place to be. Thanks to past members of the Stavros group Neil Cole-Filipiak, Lewis Baker, and Ed Greenough for their help and company during their times in the group. Finally thanks to all the masters students over the years: Phillip Pearcy, Casey Ho, Barney Lewis, Rob Turner, Georgia Thornton, and Jack Peters.

I would also like the thank the members of the Hine group past and present: Nelson Yeung, Siow Mean Loh, Daniel Corken, Edoardo Carnio, Temok Salazar. Thanks for lots of interesting conversations and putting up with my chemistry-filled presentations.

I would like to thank my fiancée Sophie Thomas for proof-reading every paper and this thesis, for supporting me on the hardest days, and for so many other little things that made this thesis possible. Thanks to all my family for their encouragement, my friends for supporting me, and my fellow MASCDT students. Finally thanks to the MASCDT staff for helping me, especially Naomi Grew and Christina Forbes for their massive amounts of help in organising things.

Declarations

This thesis is submitted to the University of Warwick in support of my application for the degree of Doctor of Philosophy. It takes the form of a thesis by publication where chapters 2 [Turner *et al.*, *J. Phys. Chem. A*, **123**,873-880, 2019] and 3 [Turner *et al.*, *J. Chem. Phys.*, **151**, 084305, 2019] are papers which have been previously published and chapter 4 is a paper currently in preparation to be published.

The work in this thesis was carried out by the author except in the cases outlined below:

1. Transient electronic absorption spectroscopy data in the second presented paper (Turner *et al.*, *J. Chem. Phys.* 2019) was acquired by the author with help from R. J. Turner.

2. Time-resolved spectroscopy data in the third presented paper (Turner *et al.*, in prep.) was acquired by K. M. Krokidi and N. d. N. Rodrigues in the gas-phase, and E. L. Holt in the solution-phase.

3. Frequency-resolved spectroscopy data in the third presented paper (Turner *et al.*, in prep.) was acquired by P. Mishra under the supervision of T. S. Zwier.

4. The text for the fourth presented paper (Turner *et al.*, in prep.) was written by the author, E. L. Holt, K. M. Krokidi and N. d. N. Rodrigues

Abstract

The work in this thesis considers the effect of solvation on both electronic and vibrational spectroscopy. It examines the accurate modelling of solvation effects in the prediction of chemical properties and the influence of solvation when conducting ultrafast spectroscopy. In the first presented paper, the molecule alizarin is observed to have a secondary species in solution when dissolved in methanol. We identify this species first by conducting pump-dependent/pH-dependent transient electronic absorption spectroscopy (TEAS) and then by predicting the UV-Vis of different candidate species with explicit-solvent time-dependent density functional theory (TDDFT). This paper showed the three main considerations for UV-Vis prediction in solution are electrostatic effects, non-electrostatic effects (eg. hydrogen bonding), and possible photoactive equilibrium species in solution.

In the second presented paper catechol was examined in acetonitrile. Catechol is a key building block of the natural photoprotecting molecule eumelanin and hence is often used in a bottom-up approach to understand its photochemical properties. In this paper, we find that, contrary to previous work, catechol does not exist in two different conformers in polar and non-polar solvents. Rather, the differences in excited state lifetime in acetonitrile *versus* cyclohexane is due to hydrogen bonding to the solvent coupled with a higher propensity to aggregate in the former. This was studied using concentration-dependent TEAS and frequency prediction with explicitly modelled solvent.

The third presented paper considers the sunscreen component homosalate. Homosalate undergoes ultrafast intramolecular proton transfer to form a "*keto*" form when photoexcited. Following this, the *keto*-S_1 form decays non-radiatively, similarly to catechol, to the ground-state *via* a conical intersection. A small population of the *keto*-S_1 state decays radiatively *via* fluorescence. In the solution phase, alongside these two processes, there is evidence that inter-system crossing also takes place to form a triplet state, this decays via phosphorescence. While this molecule behaves favourably as a sunscreen, the formation of a potentially reactive triplet state warrants further investigation. These conclusions were the result of gas and solution phase ultrafast spectroscopy as well as implicit-solvent TDDFT.

Sponsorships and Grants

The author thanks EPSRC for a doctoral studentship through the EPSRC Centre for Doctoral Training in Molecular Analytical Science, Grant Number EP/L015307/1.

Acronyms

4-TBC 4-*tert*-butylcatechol.

BBO β-Barium Borate.

DCM Dichloromethane.

DHI Dihydroxyindole.

DHICA Dihydroxyindole-2-carboxylic Acid.

FTIR Fourier Transform Infrared.

GAFF Generalised Amber Forcefield.

GGA Generalised Gradient Approximation.

HEG Homogenous Electron Gas.

HF Hartree-Fock.

HK Hohenberg Kohn.

IC Internal Conversion.

IET Intermolecular Energy Transfer.

IR Infrared.

IVR Intramolecular Vibrational Redistribution.

KS Kohn Sham.

LDA Local Density Approximation.

LID Laser-Induced Dissociation.

LR-TDDFT Linear Response Time Dependent Density Functional Theory.

NAO Numeric Atomic Orbital.

NGWFs Non-orthogonal Generalised Wannier Functions.

NMR Nuclear Magnetic Resonance.

OD Optical Density.

PTFE polytetrafluoroethylene.

RG Runge-Gross.

SFG Sum Frequency Generation.

SIE Self Interaction Error.

STO Slater-Type Orbital.

TAS Transient Absorption Spectrum.

TDDFT Time Dependent Density Functional Theory.

TEAS Transient Electronic Absorption Spectroscopy.

TLC Thin Layer Chromatography.

UV Ultraviolet.

UV-Vis Ultraviolet-Visible.

V.O.I. Vibrational Overlap Integral.

VET Vibrational Energy Transfer.

XC Exchange Correlation.

Chapter 1

Introduction

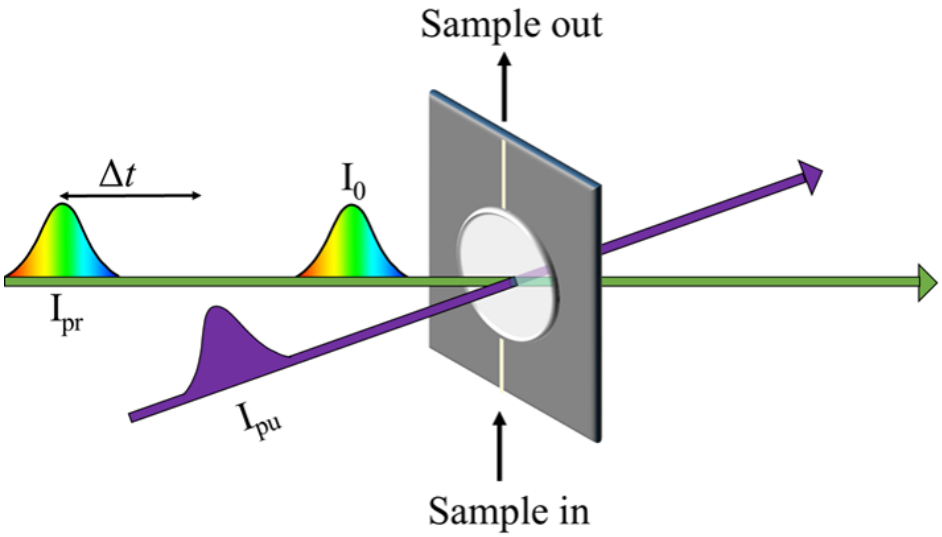

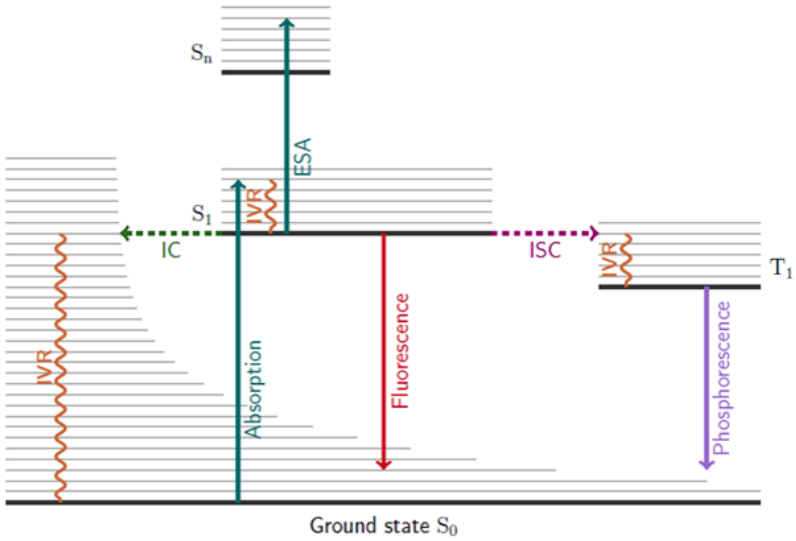

Legend

IC — Internal Conversion, $S_i \longrightarrow S_j$ non radiative transition.

ISC — Intersystem Crossing, $S_i, \longrightarrow T_j$ non radiative transition.

IVR — Intermolecular Vibrational Relaxation.

ESA — Excited State Absorption, $S_1 \longrightarrow S_n$, caused by second (probe) photon absorption.

1.1 Background

1.1.1 Motivations

In this thesis I will be using state-of-the-art ultrafast spectroscopy techniques alongside cutting-edge theoretical techniques to solve problems of photochemical interest. Theoretical spectroscopy is invaluable to photochemistry as it allows for the investigation of species that cannot be experimentally isolated. For example, molecules in dynamic equilibrium which cannot be deconvolved experimentally can be individually studied with theoretical techniques. Furthermore, a molecule that has a short lifetime before decaying experimentally, something very common in photochemistry, can be extensively probed theoretically. Owing to this, it is important to make sure theoretical models of species of interest are accurate whilst still being feasible to run in terms of computational expenditure.

The primary motivation within this work is to accurately quantify the effect of solvent on chromophores. For this, one must consider the multiple ways in which solvent can affect a solute. Firstly, solvents can exert electrostatic effects. The dielectric constant of a given solvent will directly affect the energy of a molecule's orbitals. This can be accounted for accurately with implicit-solvent modelling. Secondly, charge can delocalise between the solvent and the solute. This will influence photochemical properties and requires the explicit presence of solvent in the model to account for. Furthermore, solvent and solutes can explicitly interact, for example hydrogen bonding and π-stacking. Finally, a solvent influences the position of equilibriums of multiple species in solution, for example tautomerisation or deprotonation. This is challenging to predict theoretically and requires knowledge of the system to properly account for it.

In order to utilize explicit-solvent calculations in this fashion, one must employ molecular dynamics simulations to set up accurate solvent environments, followed by time-dependent density functional theory. These techniques are discussed further in sections 1.7, 1.8, and 1.9. One of the key challenges regarding this style of calculation was the computational cost of using large explicit-solvent models. Methods for addressing this problem are discussed in coming sections.

1.1.2 Overview of Sun-Protection

In the first presented paper (Turner *et al.*, *J. Phys. Chem A.* 2019) I utilize the exemplar dye alizarin in order to benchmark explicit-solvent TDDFT. I also show the value of pump-selective transient electronic absorption spectroscopy for identifying multiple species in solution. Alizarin was selected for this study as it had been well-studied theoretically and experimentally. This allowed us to showcase the capabilities of combining multiple techniques, and indeed the discoveries regarding the molecule itself were not the focus. In the two subsequent papers, as well as my further research not documented in this thesis, I studied molecules with more relevant applications, namely UV-filters for sun protection. Owing to this, in this section I will briefly discuss some relevant background to the development of UV-filters, with a focus on catechol and the

salicylic acid family, discussed in the second and third presented papers respectively. For a full rundown of the field of UV-filters, an extensive review was produced by Holt *et. al.*.[1]

The role of a successful UV-filter is to absorb potentially harmful UV-A (320-400 nm)and UV-B (290 - 320 nm) radiation and dissipate this safely. Two possible methods of conducting this are through scattering with inorganic nanoparticles [2, 3] and through absorption with organic chromophores[4, 5, 6, 7, 8], the latter will be our focus in this thesis. Organic chromophores act as UV-filters by absorbing UV radiation through promotion to the excited electronic state and then undergoing fast, usually non-radiative, decay back to the ground electronic state. These processes is discussed further in section 1.5.

An effective UV-filter usually has certain properties. Firstly, the filter must absorb strongly in the UV-A and/or UV-B regions. It is not essential that the filter absorbs in both as it is possible to create a mixture of multiple UV-filters which, together, cover both regions. Secondly, it is important that a UV-filter is photostable, as photodegradation over time will reduce the efficacy of the filter and potentially form harmful photoproducts. Finally, it is helpful that the excited-state formed by the photoexcitation of the UV-filter is short-lived as this results in a higher yield of photon absorption and less chance of a reactive excited-state species further reacting with surrounding molecules. Also worthy of note is that a realistic sun-cream will contain other ingredients such as emollients, other UV-filters, fragrances, moisturisers, and other compounds. Therefore, another favourable trait for UV-filters is to not be heavily affected by solvent environment.

One example of a set of effective UV-filters is the salicylate family. Salicylic acid derivatives are appealing UV-filters as they have low solvatochromic shift, indicating that their properties are not overly affected by environment.[9, 10] Furthermore, they can act as solubilizers for other UV-filters such as avobenzone.[11, 12, 13] There has, however, been some debate about the safety and stability of salicylates.[13, 14, 15, 16, 17, 18] In the third presented paper (Turner *et al.*, in prep.) we discuss the role of homosalate, a member of this family, as a UV-filter.

While artificial UV-filters are a fascinating area of research, arguably just as important is the understanding of biological UV-filters. Studies have been conducted extensively on UV-filters extracted from plants[19, 1], and in this thesis we investigate a class of natural UV-filters produced by humans, namely melanins. Melanin is a complex structure that is difficult to probe experimentally. One approach to the study of melanin is to take a bottom up approach and study smaller sections of the overall structure. A key building block of melanin is the molecule catechol. The photochemical properties of catechol, or the analogous 4-*tert*-butyl catechol (4-TBC), have been widely studied.[1, 20] It has been observed that 4-TBC acts in a drastically different way in different solvents and at different concentrations. It is therefore key to understand what structural changes take place in catechol in different solvents. In this thesis we compare Fourier-Transform Infrared (FTIR) spectroscopy results to predicted frequencies for

possible structures of catechol to accurately assess which structures are present in solution. It is key to note that these results will not necessarily be the same as those for 4-TBC, the otherwise analogous structure previously studied. One of the observations is that an aggregate can form, however the identity of this aggregate is not known and is likely to be very complex. This could be an interesting area of further research which can be conducted through the use of mass spectrometry.

1.2 An Introduction to Spectroscopy

Within this project I aimed to study the photochemistry of small organic molecules through a combination of experimental and computational techniques. I primarily achieved this through the use of, and modelling of, spectroscopy. Given this, I start my thesis by giving an overview of spectroscopy.

Spectroscopy is the study of the interactions between electromagnetic radiation and matter. Whilst some will credit the observation that white light from the sun could be dispersed into a continuous series of colours to Isaac Newton, it is possible to trace its origins as far back as Roman times, where it was already known that one could use a prism to generate an array of colours. It is apparent that Latin writer Lucius Anneus Seneca was fascinated by prisms.[21, 22] In his "Natural Questions", he discussed glass rods which displayed a rainbow of colours. Further to this, Pliny the elder wrote in his "Natural History" of a small precious stone: "for, when struck by the rays of the sun in a covered spot, it projects upon the nearest walls the form and diversified colours of the rainbow" [23]

As for the birth of modern spectroscopy, the first spectroscope was indeed designed by Newton. This consisted of a small aperture through which a beam of white light could be projected; a collimating lens; a glass prism to disperse it and a screen to display the resulting spectra. It was later discovered by W. Herschel (1800)[24] and J. W. Ritter (1801)[25] that the light of the sun extended into the infrared and ultraviolet regions of the electromagnetic spectrum respectively. In this work, I will consider the central region of the electromagnetic spectrum, including the UV region (10 nm - 380 nm; 124 eV - 3.25 eV), the visible region (380 nm - 700 nm; 3.25 eV - 1.8 eV), and the infrared region (700 nm - 1 mm; 1.7 eV - 1.24 meV).

For the purposes of spectroscopy it must be noted that electromagnetic radiation can exhibit both wave-like and particle-like characteristics. For a given wavelength of light, one can imagine a particle-like "light-quanta" which is referred to as a photon.[26, 27] When a given photon interacts with a molecule it can impart energy. By monitoring what energy photons are absorbed and the affect of the absorption of photons, we can gain key information about the structure and behaviour of the molecule. In this work, I specifically consider how the energy of photons can be dissipated safely for the purpose of sun protection, as well as the way in which the effect of solvent environments influences absorption of electromagnetic radiation in exemplar dyes.

1.3 The Principles Governing Electronic Spectroscopy

In this thesis, the majority of spectroscopy used will be in the UV/Visible region. This is known as electronic or optical spectroscopy. In this, a photon (typically of energy 1.8 - 4.1 eV or 300 to 700 nm) causes a quantized increase in energy to a higher electronic state. In this section I will discuss the key principles that govern electronic absorption.

1.3.1 The Beer-Lambert Law

In 1729, Pierre Bouguer discovered, whilst enjoying a glass of red wine on holiday in Alentejo (Portugal), that absorbance of a material sample was directly proportional to the thickness of said material (pathlength). This discovery is often attributed to Johann Heinrich Lambert, although Lambert himself directly cited Bouguer's "Essai d'optique sur la gradation de la lumière" (Claude Jombert, Paris, 1729) in his Photometria in 1760.[28, 29, 30] Regardless, this is referred to as Lamberts law to this day. In 1852, August Beer built on this work and found that absorbance is also directly proportional to concentration. From this, the Beer-Lambert law was born. The Beer-Lambert law can be expressed as:

$$A = log_{10}\left(\frac{I_0}{I}\right) = \epsilon(\lambda)bC, \tag{1.1}$$

where A represents absorbance. This can be seen as a function of the amount of photons projected into the sample (I_0) and those that are transmitted (I). As previously stated, the Beer-Lambert law dictates that absorption is proportional to pathlength (b) and concentration (C). This means that for a given sample a relationship can be derived that directly relates absorption to pathlength and concentration. This constant is known as the molar extinction coefficient and is represented by $\epsilon(\lambda)$. It is, however, only constant given fixed pressure, temperature, and wavelength.

1.3.2 A Quantum Mechanical Approach

The energy of a given molecule in a given state can be calculated using the Schrödinger equation:

$$i\hbar\frac{d}{dt}\psi(\mathbf{r},\mathbf{R},t) = \hat{H}\psi(\mathbf{r},\mathbf{R},t), \tag{1.2}$$

in which i is the imaginary unit, $\hbar = \dfrac{h}{2\pi}$ is the reduced Planck constant, and $\psi(t)$ is the wavefunction of the molecule at electronic configuration $\mathbf{r}$, nuclear configuration $\mathbf{R}$, and time t. The Hamiltonian, in this case $\hat{H}$, is an operator that derives from the sum of all kinetic energies plus potential energies of all the particles in the system. For a single particle the Hamiltonian can be described in the following fashion:

$$\hat{H} = \hat{T} + \hat{V} \tag{1.3}$$

where $\hat{T}$ is the kinetic energy operator and can be described as

$$\hat{T} = -\frac{\hbar^2}{2m}\nabla^2 \tag{1.4}$$

where m is the mass of the particle and ∇^2 is the Laplacian operator which in three dimensions is

$$\nabla^2 = \frac{\partial^2}{\partial x^2} + \frac{\partial^2}{\partial y^2} + \frac{\partial^2}{\partial z^2} \tag{1.5}$$

where $\hat{V}$ is the potential energy operator and can be described as

$$\hat{V} = V(\mathbf{r}, t) \tag{1.6}$$

where $V(\mathbf{r}, t)$ is potential energy at a given time t and position vector $\mathbf{r}$. In the many-particle system this can be built upon and the Hamiltonian can instead be expressed as

$$\hat{H} = \sum_{n=1}^{N} \hat{T}_n + V(\mathbf{r}_1, \mathbf{r}_2, ...r_n, t) \tag{1.7}$$

where N is the number of particles. Furthermore, the kinetic energy operator for particle n, now referred to as $\hat{T}_n$ can be evaluated as:

$$\sum_{n=1}^{N} \hat{T}_n = -\frac{\hbar^2}{2} \sum_{n=1}^{N} \frac{1}{m_n} \nabla_n^2 \tag{1.8}$$

therefore yielding the following Hamiltonian:

$$\hat{H} = -\frac{\hbar^2}{2} \sum_{n=1}^{N} \frac{1}{m_n} \nabla_n^2 + V(\mathbf{r}_1, \mathbf{r}_2, ...\mathbf{r}_n, t). \tag{1.9}$$

This is discussed further in regards to density functional theory later in the chapter. For the purposes of this work, a simple form of the interacting-particle Hamiltonian can be expressed as:

$$\hat{H} = T_e + T_n + V_{ee} + V_{nn} + V_{en} \tag{1.10}$$

Where T_e and T_n are the kinetic energies of the electrons and nuclei respectively, and V_{ee}, V_{en}, and V_{nn} are the potential energy deriving from coulombic attraction/repulsion from electron-electron interactions, electron-nuclei interactions, and nuclei-nuclei interactions respectively. In order to further simplify this system the Born-Oppenheimer approximation must be considered.

The Born-Oppenheimer Approximation

The Born-Oppenheimer approximation states that, as the mass difference between nuclei and electrons is large ($m_{\text{proton}}/m_{\text{electron}} \approx 1836$), nuclear and electronic motion can be separated. Furthermore, as electrons are significantly lighter they can be seen as moving

instantaneously on the timescale of nuclear motion. This has the advantage of creating separate Hamiltonians for nuclear and electronic motion, H_e and H_n respectively.

$$H_e = T_e + V_{en} + V_{ee} \tag{1.11}$$

$$H_n = T_n + V_{nn} + V_e \tag{1.12}$$

This allows us to define an electronic and nuclear Hamiltonian separately. In photochemistry we are mainly interested in the study of the wavefunction as calculated from the electronic Hamiltonian as described by

$$H_e\psi(\mathbf{r}) = E_e\psi(\mathbf{r}). \tag{1.13}$$

There are cases where the Born-Oppenheimer principle does not hold. A prominent example is where there is strong vibronic coupling between two electronic states. This can lead to non-radiative decay mechanisms such as internal conversion and inter system crossing, which will be discussed later.

The Franck-Condon Principle

The Franck-Condon principle describes the intensity of vibronic transitions. Building upon the Born-Oppenheimer approximation, it states that during an electronic transition, the nuclear configuration experiences no significant change. This is known as the classical Condon approximation. In this picture, after an electronic transition, the molecule is unlikely to be in the vibrational energy minimum of the excited state. This can be visualised by considering a potential energy cut along a given atomic coordinate, as shown in figure 1.1. This results in molecules having excess vibrational energy post-electronic excitation, which they can shed to reach the vibrational ground state. This is often referred to as being "vibrationally hot", and leads to a range of interesting photochemical effects which are discussed in section 1.4. The Franck-Condon principle explains the relative intensities of vibronic transitions by considering the probability of a vibronic transition in relation to the overlap of the vibrational wavefunctions. We can therefore state that the probability of a vibrational transition occurring is weighted by the Franck-Condon overlap integral:

The Franck Condon principle explains the relative intensities of vibronic transitions by considering the probability of a vibronic transition in relation to the overlap of the vibrational wavefunctions. We can therefore state that the probability of a vibrational transition occurring is weighted by the Franck-Condon overlap integral:

$$P_{i\to f} = |\int \psi_{\mathrm{f}}^{*}\hat{\mu}\psi_{\mathrm{i}}d\tau|^2 \tag{1.14}$$

Where ψ_{f}^{*} is the complex conjugate of the resulting wavefunction after the transition, ψ_{i} is the initial wavefunction, $\hat{\mu}$ is the electronic dipole oscillator, and $d\tau$ denotes an integral across all space.

The Franck-Condon principle has both classical and quantum applications. Clas-

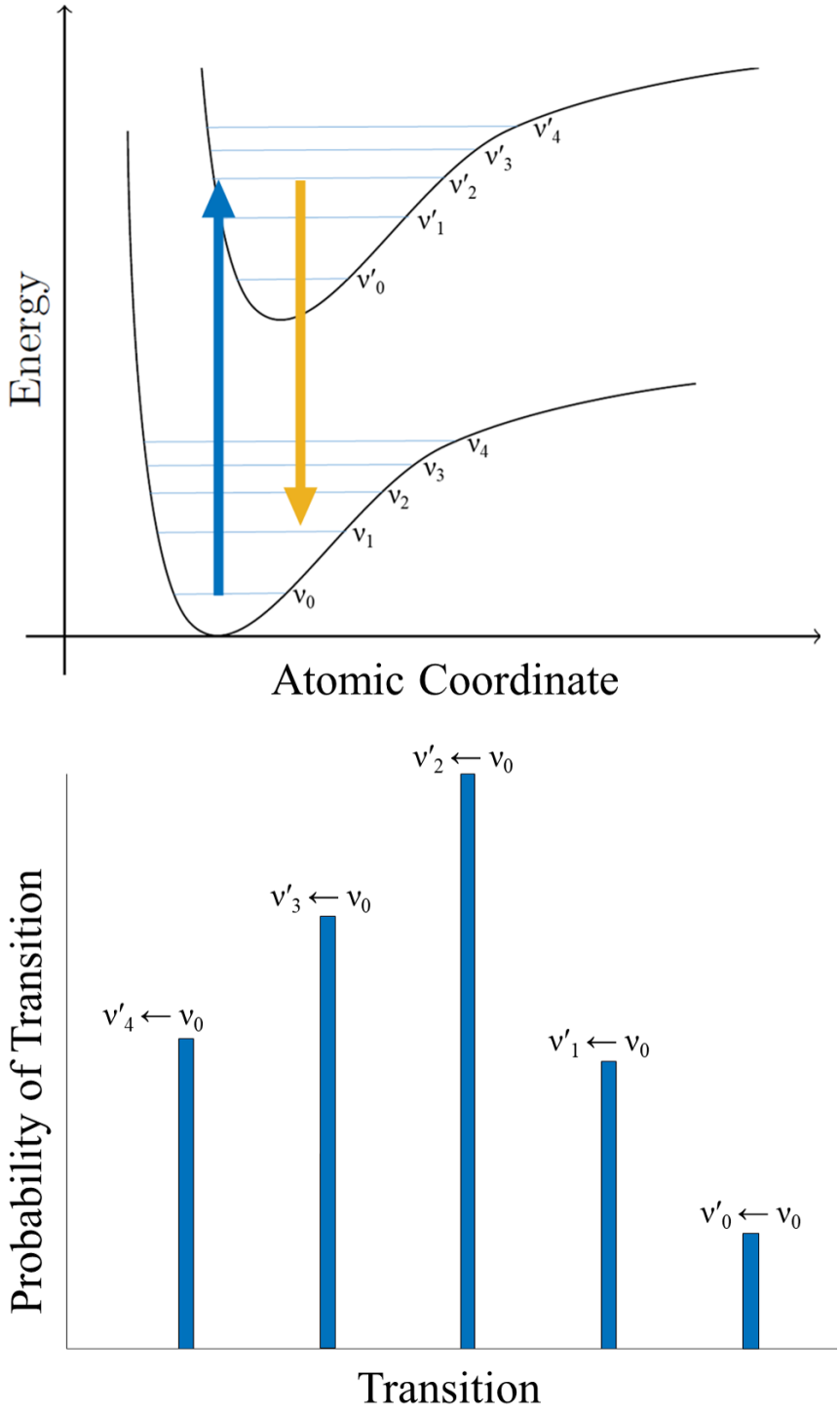

Figure 1.1: A schematic to show the Franck-Condon principle. This shows likelihood of electronic absorption to the given vibronic states in the electronic excited state. The vibronic energy levels in the electronic ground state (S_0) are denoted as ν_n, vibronic energy levels in the excited electronic state (S_1) are denoted ν'_n. The blue arrow represents a given electronic absorption and the orange arrow represents a given electronic emission.

sically, the Franck-Condon principle is the approximation that an electronic transition will occur without nuclear motion. The state generated by this is called the Franck-Condon geometry and the transition is known as a vertical transition. The quantum formulation of the Franck-Condon principle states that the intensity of the vibronic transition is proportional to the square of the overlap integral, as shown in equation 1.14. As in the bottom section of figure 1.1, this gives rise to what is known as a "vibronic progression" in optical spectroscopy.[4, 31] Since the electronic dipole oscillator only depends on the electronic component of the wavefunction, and given the Born-Oppenheimer approximation, we can split the Franck-Condon overlap integral into electronic and nuclear components:

$$P_{i\to f} = \int \psi_f^* \hat{\mu} \psi_i d\tau \underbrace{\int \chi_f \chi_i^* dR}_{V.O.I.} \tag{1.15}$$

here, χ represents nuclear components and ψ represents electronic components. The nuclear part of this equation is often known as the vibrational overlap integral or "Franck-Condon factor". If this factor is zero then a transition will not occur, regardless of the magnitude of the electronic component. It should be noted that the nuclear component of the wavefunction can be further split into vibrational and rotational parts. However, this is neglected in this explanation as it is beyond the scope of what is used in this thesis.

1.3.3 Selection Rules

When considering the magnitude of the electronic component of the transition, it is important to discuss selection rules. A selection rule is a formal constraint on the possible transitions from one state to another. These are key when considering the probability of different electronic transitions. First, we discuss the relevant electronic selection rules. The first is that the total spin of a system cannot change ($\Delta S = 0$). One can separate the electronic spin wavefunction from the spatial electronic wavefunctions. As electronic spin is a magnetic effect, dipole transitions should not alter electron spin. Spin-orbit coupling can, however, break this selection rule. This is discussed further in section 1.4.4.

The second electronic selection rule states that the total orbital angular momentum change should either be 0 or ± 1. This means that whilst one is likely to see transitions involving σ orbitals and π orbitals to themselves or between the two, one is less likely to see transitions to higher angular momentum states.

Finally, we discuss two vibrational selection rules. Firstly, where $V = 1, 2, 3, ...$ are vibrational energy levels, transitions of $\Delta\nu = \pm 1, \pm 2, ...$ are allowed but the probability of the transition decreases as $\Delta\nu$ increases. Secondly, transitions of $\Delta\nu = 0$ are allowed when transitioning between two electronic states, but they are unlikely to be the most likely probable transition owing to the difference in energy surface between the ground and excited electronic states, see figure 1.1.

Table 1.1: This table shows the approximate lifetimes of different excited state processes.

Decay process	Typical lifetime / s
Vibrational Energy Transfer	$10^{-12} - 10^{-8}$
Fluorescence	$10^{-7} - 10^{-1}$
Phosphorescence	$10^{-6} - 1$
Internal Conversion	$10^{-11} - 10^{-9}$
Inter system Crossing	$10^{-14} - 10^{-8}$

1.4 Excited State Decay Processes

The previous section discussed optical spectroscopy where the molecules are excited from the S_0 ground state to the excited S_n states. In this notation "S" denotes states with an overall spin quantum number of 0 (referred to as singlet states). It is important to understand what happens to the molecule in these excited states. The study of excited state decay is important in the fields of sun protection[7, 8], photodegradation[32, 33], medical applications [34, 35], and solar energy harvesting[36, 37, 38]. In later sections, I will discuss how these processes are measured and characterised. As an overview, table 1.1 shows these processes and their approximate range of lifetimes.[39] Alongside this, figure 1.2 shows these processes in a Jablonski diagram.[40]

1.4.1 Vibrational Energy Transfer

As discussed previously, when photoexcitation occurs it is unlikely to occur from ν_0 to ν_0'. Owing to this, after vertical excitation in the Franck-Condon region an excited state is usually vibrationally hot. Whilst this section will mainly deal with relaxation between electronic states, here I briefly discuss the two mechanisms for vibrational energy transfer (VET).

The first of these is intramolecular vibrational redistribution (IVR).[41] This is when the energy in the molecule redistributes amongst its vibrational modes. This will not lower the overall energy of the molecule, but will instead redistribute the energy across a series of orthogonal modes. IVR does not require vibrational coupling to a molecular bath and therefore can occur in the gas-phase. This does, however, require a multiatomic system. IVR proceeds via anharmonic coupling to various vibrational modes.[42] For larger systems, there is a much higher density of acceptor states than donor states. This causes the net flow out of the initially populated state to be irreversible. The rate, and by extension the probability, of the transition between initial state, i, and the set of states, j, is given by the following expression

$$k_{ij} = \frac{2\pi}{\hbar}|\nu_{ij}|^2\rho_j \tag{1.16}$$

where ν_{ij} is the strength of coupling between states i and j and ρ_{j} is the density of the j states. This relationship is known as Fermi's golden rule.[43]

The second process is intermolecular energy transfer (IET).[44] This process can

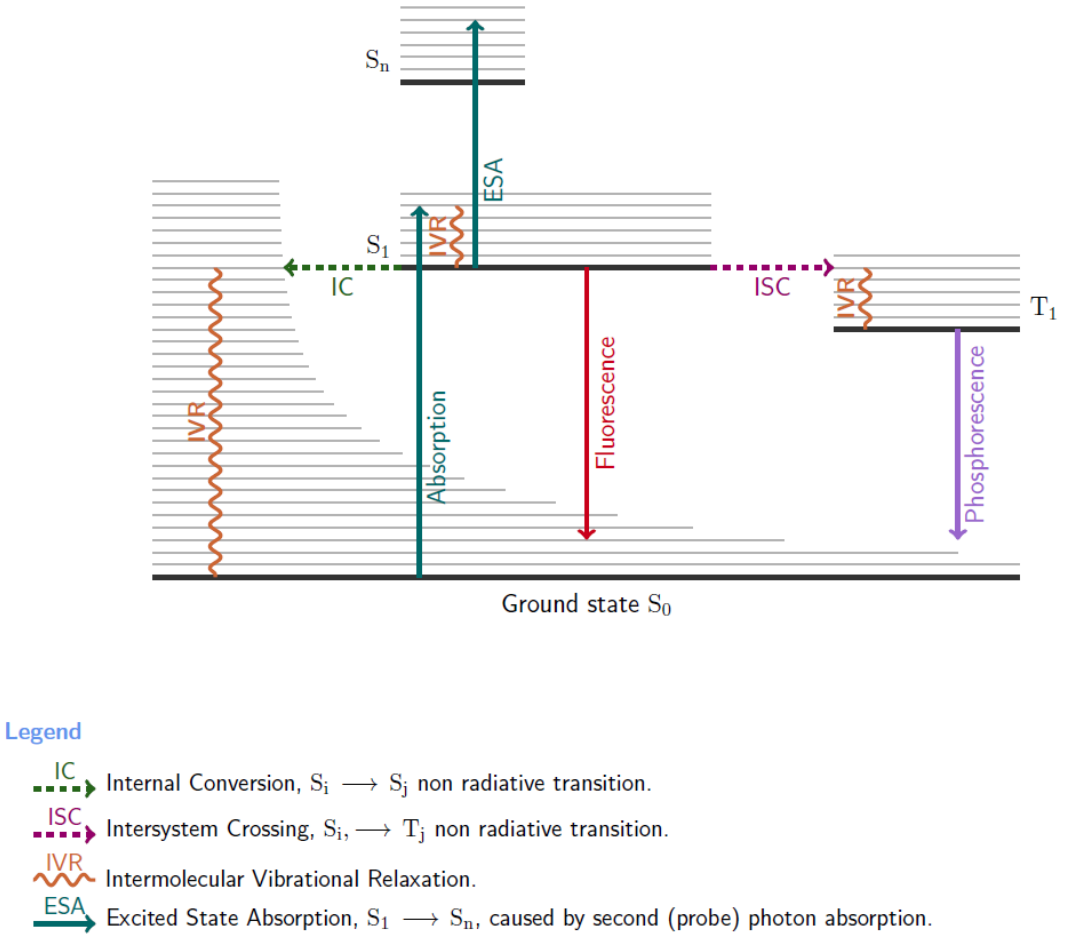

Figure 1.2: This figure shows a Jablonski diagram of different excited state processes. In this case "T" represents a triplet state, which is a state with spin quantum number (S) = 1. Therefore, quantum number m_s can take the values -1, 0 and 1. This state is thus threefold degenerate, hence the name triplet.

only take place when the molecule is in a bath to which it can transfer energy. This means it is not applicable in the gas-phase. In this case, the molecule imparts energy to its surroundings, thus lowering the vibrational energy level from ν'_n to ν'_0. IET is typically a slower effect than IVR. For example, in benzene $\tau_{\mathrm{IVR}} = 2$ ps and $\tau_{\mathrm{IET}} = 70$ ps [45]. The rate of IET was described by Hochstrasser *et al.* using the Landau-Teller approach. [44] The relationship is given by the following expression

$$k_{\mathrm{IET}} = \frac{2\tanh(\hbar\omega/2k_BT)}{\mu\hbar\omega/k_BT}\zeta(\omega) \tag{1.17}$$

where $\zeta(\omega)$ is the frequency dependent friction at oscillator frequency ω. IET in this case is clearly also heavily dependent on temperature. Both of these effects can occur in conjuncture with solvent rearrangement as part of an ensemble VET process.

1.4.2 Fluorescence and Stimulated Emission

Arguably the simplest form of excited state decay, fluorescence is the process of radiative decay from the excited state to the ground state. Whilst fluorescence can occur from any excited state, Kasha's rule dictates that it only happens in appreciable yield from the lowest available excited state, S_1.[46] In its simplest form, the molecule will absorb a photon to be electronically excited. Following this, the excited state of the molecule will evolve over time. When the excited state has settled in a minimum, it will then emit a photon and drop to a vibrationally hot form of the ground state. This usually happens on a timescale of the order of nanoseconds.

The difference between the energies of the absorbed photon and the emitted photon is referred to as the Stokes shift.[47] This shift can be due to large molecular change in the excited state, such as isomerisation, or merely just due to the difference in energy between the $\nu'_n \leftarrow \nu_0$ and $\nu'_0 \rightarrow \nu_n$ where $n > 0$. This shift is generally larger if the electronic properties (and often geometry) of the vibrationally relaxed electronic excited state is significantly different to that of the electronic ground state. The energy of the emitted photon, as well as the structure of the relaxed ground state, can be predicted theoretically.

Stimulated emission is a similar effect to fluorescence in that it involves the radiative decay of an electronic excited state to the ground state. It differs, however, as the emission is induced through interaction with a further photon. More specifically, one photon excites a given electron, following this a given time later, a second photon interacts with this excited electron. This causes it to drop to a lower energy level and emit a photon. The photon being emitted is coherent and propagates along the same vector as the stimulating photon. Stimulated emission happens on a significantly faster timescale and therefore can happen as the excited state is relaxing. In cases such as this, the stimulated emission signal will evolve along the time window.[19]

1.4.3 Internal Conversion

Unlike fluorescence, internal conversion (IC) is a nonradiative process. In IC, instead of losing energy through emission of a photon, the molecule transitions along some atomic reaction coordinate into another electronic state.[48, 49] IC is mediated through the coupling of vibrational modes from each electronic state. This interaction between vibrational and electronic behaviour is known as "non-adiabatic" due to it requiring the breakdown of the Born-Oppenheimer approximation.[31] The rate, and therefore its likelihood, of IC (k_{IC}) between states f and l is given by the following expression

$$k_{\mathrm{IC}} \propto \exp\left[\frac{-\Delta E_{fl}}{h\nu}\right] \tag{1.18}$$

where ΔE_{fl} is the energy gap between states f and l and ν is the vibrational frequency. IC tends to occur more in higher lying states as they are, in general, closer in energy due to anharmonicity, as shown in figure 1.1.

Practically, these transitions can occur through two mechanisms: via an avoided

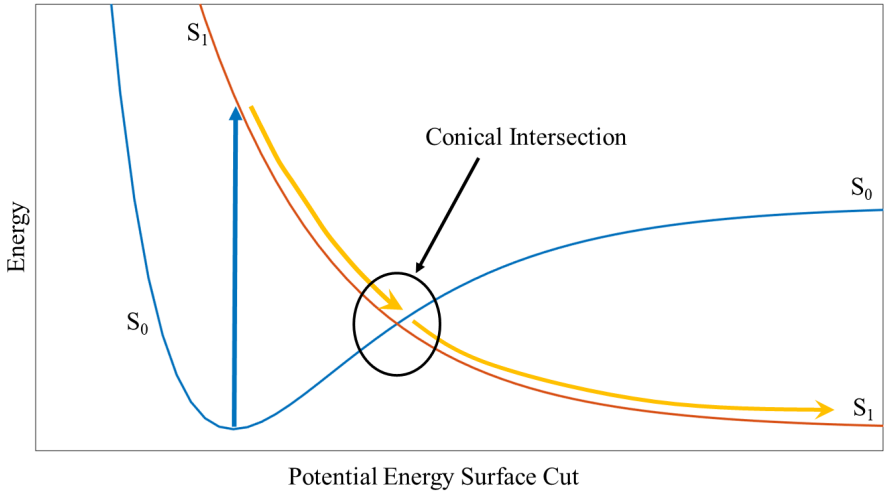

Figure 1.3: A schematic of the potential energy surface cut of a system at a conical intersection between the S_0 and S_1 states of a molecule. Here the blue arrow represents the absorption and the yellow arrows represent the vibrational relaxation towards the conical intersection. In this schematic, the internal conversion is a barrierless process but this is not always the case.

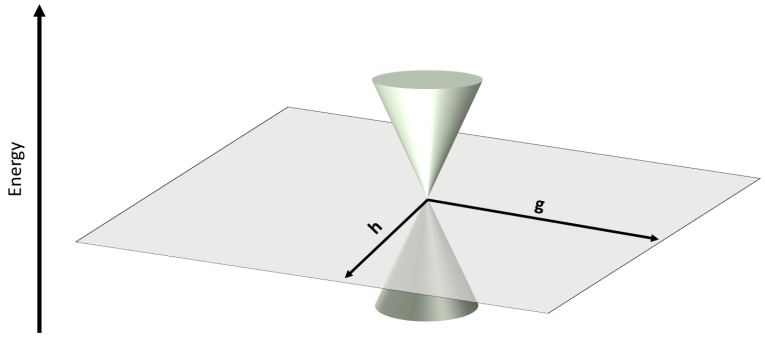

Figure 1.4: A schematic of a conical intersection in two-dimensional space where **h** is derivative coupling and **g** is gradient difference.

crossing or a conical intersection. A conical intersection occurs when two electronic states are degenerate within a $3N-8$ dimensional subspace of the $3N-6$ nuclear coordinate space. It is impossible for two states with the same spin multiplicity and symmetry to cross along a one-dimensional coordinate due to Pauli's exclusion principle.[43] If this condition of degeneracy is not possible an avoided crossing occurs. When at a conical intersection, non-adiabatic transfer occurs rapidly as E_{fl} is reduced to zero, this results in conical intersections often being the dominant factor in a molecules photodynamics. A graphical representation of a conical intersection is shown in figure 1.3.

This diagram is something of a simplification in that it allows us to consider the conical intersection with a two dimensional analogy. In reality, as stated previously, the intersection between the two states occurs within a subspace of the nuclear space. A further two dimensional representation of a conical intersection is shown in figure 1.4, which is, again, a simplification of the real picture.

In this subspace, we picture the intersecting states as two cones meeting at their tips, which is where the term conical intersection comes from. The two dimensional subspace consists of two coordinates, the derivative coupling and the gradient difference between the two states. In this, the gradient difference represents the steepness of the two cones leading to the intersection, a steeper gradient leads to a more likely transition. At the tips of the cones the Born-Oppenheimer approximation breaks down and coupling between electronic and nuclear motions can take place, this is called non-adiabatic coupling. The derivative coupling refers to the strength of non-adiabatic coupling between the two states.[50]

1.4.4 Inter System Crossing

Inter system crossing is similar to internal conversion but it also includes a change in spin quantum number. In practice, this means that the molecule will transition between a singlet and triplet state. This process is formally forbidden through the selection rule

$$\Delta S = 0$$

, where S is the spin quantum number although it can be made possible through spin orbit coupling. This is a slow effect and rarely competitive with other photodynamic processes as spin orbit coupling is unlikely, although is more likely to occur in systems with high nuclear mass. However, as we mainly deal with organic compounds in this thesis this does not have much bearing on this work.

Finally, a triplet state will often decay radiatively through phosphorescence. Phosphorescence is also a very slow effect as it involves the radiative transition from T_n to S_0 which is also formally forbidden by the spin selection rule discussed above.

1.5 Transient Electronic Absorption Spectroscopy

1.5.1 Introduction to Pump-Probe Spectroscopy

Transient absorption spectroscopy is a time-resolved pump-probe technique widely used in the study of dyes[51, 52], sun protection[5, 6], and fluorescent detection[53, 54]. Whilst transient absorption spectroscopy can be conducted with many parts of the electromagnetic spectrum, this thesis will focus on transient electronic absorption spectroscopy (TEAS) which uses light in the region of 330 nm to 675 nm. A schematic of the TEAS method is shown in figure 1.5.

In practice, TEAS works by photoexciting the molecule with a pump laser I_{pu}, this results in a population of the sample being in an electronically excited state (see figure 1.2). Following this, after a given time delay (Δt) a probe pulse interacts with the sample. By detecting the absorption of the probe, the decay of the electronic excited state can be monitored with respect to time. As TEAS is only interested in electronic excited state dynamics, an unpumped I_0 pulse is also taken, this is used to baseline the pumped TEAS signal using the following equation

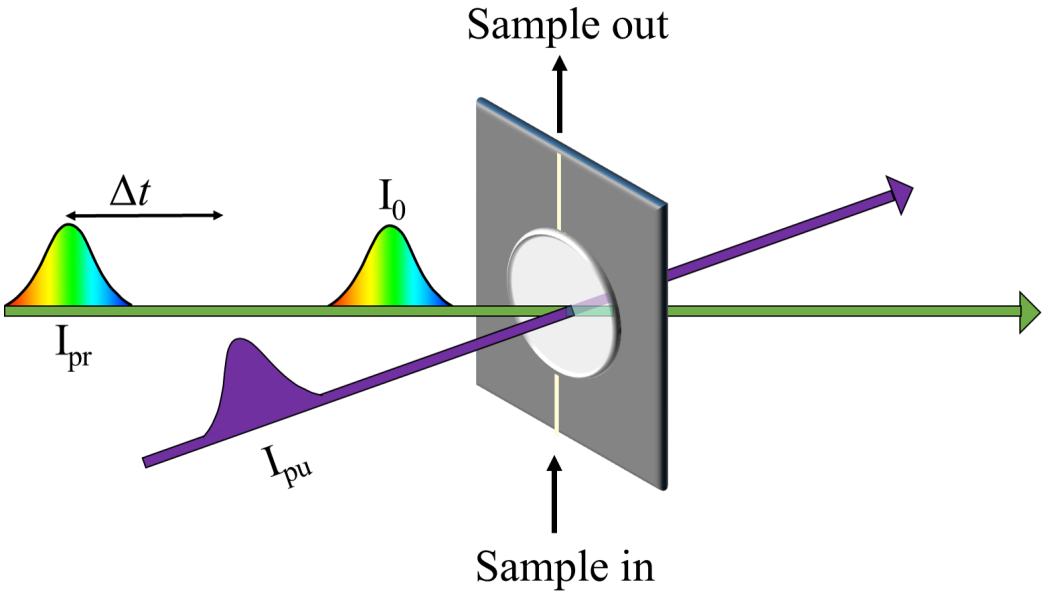

Figure 1.5: This figure shows a schematic of the transient electronic absorption spectroscopy set-up. In this, I_{pu} is the pump pulse, I_{pr} is the probe pulse, and I_0 is the unpumped reference pulse.

$$\Delta OD(\lambda, t) = \log(I_0(\lambda)) - \log(I_{pr}(\lambda, t)). \tag{1.19}$$

Here I_0 is the intensity of the probe pulse after passing through the sample pre-photoexcitation, and I_{pr} is the intensity of the I_{pr} post-photoexcitation. Figure 1.6 shows a typical slice from a transient absorption spectra and how certain effects contribute to it. Results from TEAS will be presented in this thesis in the form of false colour heatmaps where the x-axis will be the pump-probe delay time, the y-axis will be the wavelength of the probe-pulse, and the colour of the pixel will represent ΔOD with red colours representing strong positive signal and blue colours representing strong negative signal. This section will discuss these effects and how they can be used to monitor the electronic excited state decay mechanisms discussed in the previous section.

1.5.2 Excited State Absorption

Following photoexcitation from the S_0 state to the S_n state, it is possible for the molecule to undergo a further transition form the S_n state to an S_m state where $m > n$ if it receives further photoexcitation. This is known as excited state absorption and is observed frequently in TEAS results. The feature associated with an excited state absorption will decay as the S_n is depopulated. Therefore the lifetime of the S_n state can be studied by observing the lifetime of the excited state absorption. Theoretically, excited state absorption is challenging to predict owing to the evolution of the S_1 energy surface. Work is, however, being conducted in the field of predicting excited state absorption wherein linear-response TDDFT is coupled to real-time TDDFT.[55] This is an interesting future avenue and the explicit-solvent methodology discussed later in this

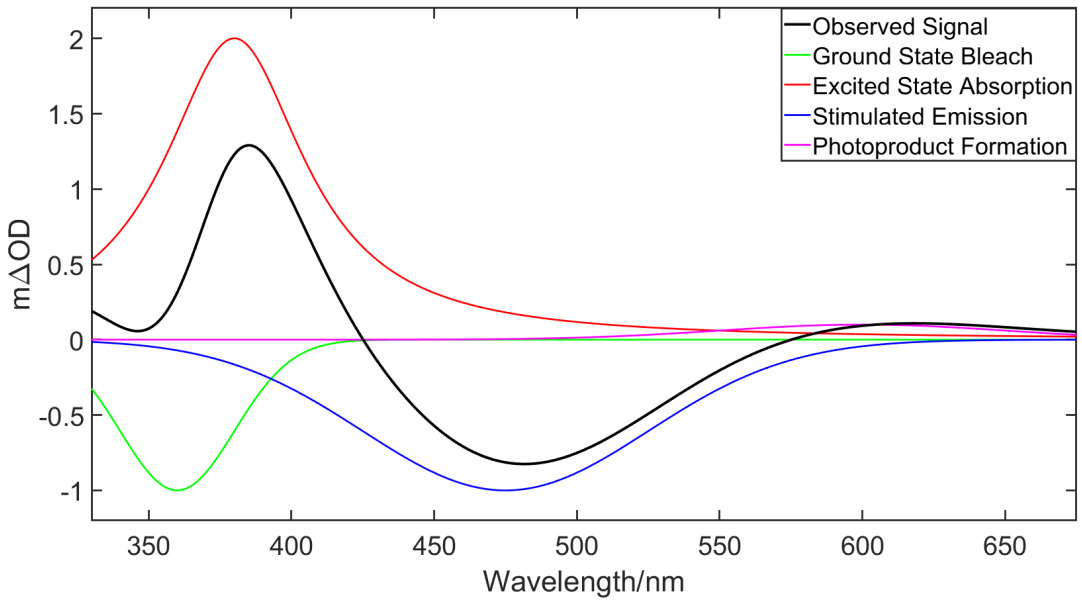

Figure 1.6: Schematic of a standard TAS slice at a given time delay, showing how the observed signal can be made up of different effects, this is further discussed in the main text.

thesis may in future be coupled with this to accurately predict electronic excited states.

1.5.3 Emission and Ground State Bleach

Both emission and ground state bleach give rise to features associated with negative ΔOD in the TEAS data. In the case of emission, the pumped pulse actually increases in intensity at the wavelength of the emitted photon. Emission from a triplet state, phosphorescence, happens on a significantly slower timescale than emission from a singlet state, fluorescence.

With ground state bleach, when the initial pump pulse is absorbed by the sample, the population of the ground state will be correspondingly depleted. When comparing pumped to unpumped samples, this will appear as a negative signal in ΔOD, as the unpumped sample will absorb the probe pulse to a greater extent in that region than the pumped sample. As the electronic excited states decay back to the ground state, this signal will be slowly reduced. This ground state recovery can be observed over time in order to judge the lifetime of all electronic excited state species. If there is a long-lived photoproduct formed then the ground state bleach may not fully recover within the time window of the experiment.

1.5.4 Fragmentation and Photoproducts

Fragmentation can occur due to photoexcitation and this will result in photoproduct formation. There are two primary ways in which fragmentation can occur. Firstly, the energy of the laser can impart heat upon the molecule. It is possible that this heat can provide sufficient activation enthalpy to break bonds. This is a similar process

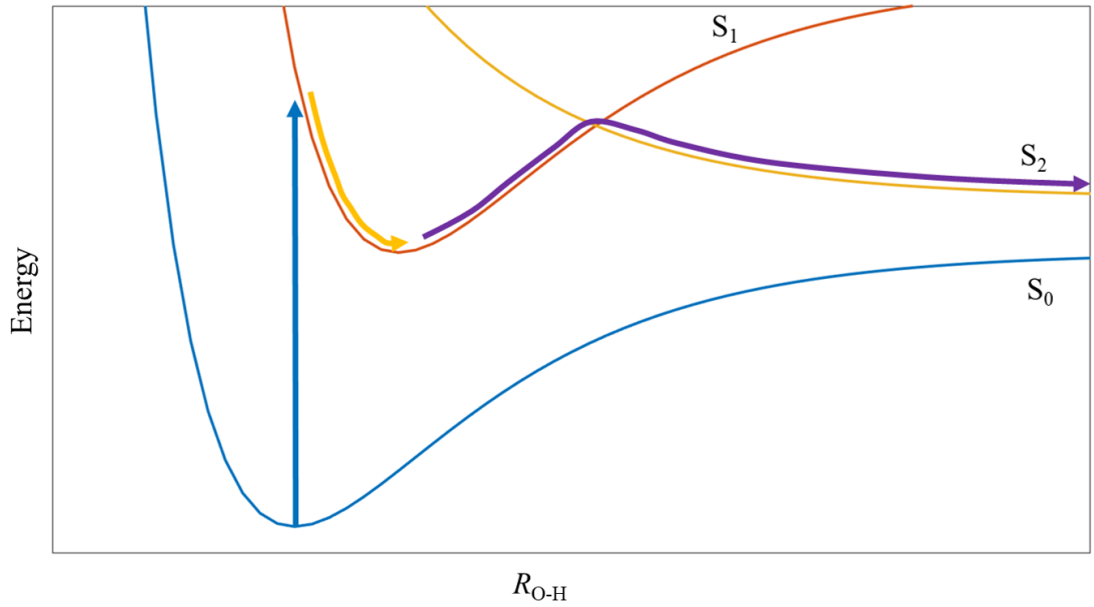

Figure 1.7: This figure shows a schematic of a dissociative O-H coordinate achieved through internal conversion. This is based on part of the electronic excited state mechanism for catechol, discussed further in the second presented paper.

to that which occurs in laser-induced dissociation (LID) mass spectrometry.[56] This form of dissociation will yield photoproducts proportional to pump power and is more prevalent in larger and more entropically unstable systems. The other way in which photoproducts can form is via coupling to a dissociative electronic excited state. In the case of catechol, discussed extensively in the second presented paper (Turner *et al.*, *J. Chem. Phys.* 2019), internal conversion can occur in the electronic excited state to a dissociative S_2 ($^1\pi\sigma^*$) state. As this state relaxes vibrationally, the O–H bond is broken, resulting in the formation of a semiquinonic catechoxyl radical. A schematic of this process is shown in figure 1.7. In this process, there is a barrier to the S_1/S_2 conical intersection, the height of this barrier is one of the key mediating factors in the dynamics of catechol in different environments.

Practically, photoproducts are unlikely to decay within the standard time window of a TEAS experiment, therefore the presence of a photoproduct is often marked by the lack of return to a baseline by the end of the time-stage. This is, however, not always due to the formation of a photoproduct and can instead be the result of a long-lived electronic excited state.

1.6 Introduction to Experimental Photochemistry

In this thesis, transient electronic absorption spectroscopy is used to analyse the excited state dynamics of a molecule. This section will discuss the experimental background behind performing these measurements. This will include the generation of the pump pulses used to excited the molecule, the white-light probe pulse used to examine the molecule in both the ground and excited state (as well as any photoproducts generated),

and the equipment used to manipulate these pulses.

1.6.1 Generation of the Fundamental Beam

We start our description of the laser setup, naturally, with an overview of the production of the fundamental beam. In our experiments, we utilise a commercial Newport Spectra Physics laser system to generate the fundamental 800 nm beam.[57] This system comprises of Ti:sapphire lasers (Tsunami oscillator and XP Regenerative amplifier) which exhibit strong lasing transitions around 800 nm. A seed laser optically pumps the (Tsunami) Ti:sapphire oscillator. This oscillator is mode-locked around 800 nm and releases pulses at a repetition rate of $\approx$ 80 MHz via an optical switch. Typically, one in 80,000 of these pulses is selected as an 800 nm seed for amplification (i.e. a repetition rate of 1 kHz). Inside the XP Regenerative amplifier (a Ti:sapphire chirp regenerative amplifier, optically pumped by another green seed laser) this 800 nm seed pulse is amplified by a factor of $\approx 10^6$ and recompressed to $\approx$ 40 fs in duration. The final output of this commercial system are pulses centred at 800 nm, with a pulsed duration of $\approx$ 40 fs and 1 kHz repetition rate. The spectral bandwidth of these pulses is approximately 30 nm; further details can be found in reference [4].

The 3 W fundamental beam (i.e. 3 mJ per pulse at 1 kHz) is split equally into three parts. 1 W is used to conduct gas-phase experiments (not discussed in this thesis) whilst the remaining 2 $\times$ 1 W are used for the present experiments. The first beam is directed onto a second optical table (the first houses the Newport-Spectra Physics system, *supra*, and TOPAS-*infra*) and is split further into two beams in a 19:1 (0.95 W and 0.05 W) power ratio. The lower powered 0.05 W beam is used for white light generation, discussed later. The 0.95 W beam can be used to provide pump pulses (800 nm, 400 nm, 267 nm) through frequency doubling (400 nm) and frequency tripling (267 nm) of the fundamental 800 nm. In a lot of cases, the three pump wavelengths provided by this methodology are not appropriate for the experiments we wish to conduct. Fortunately, we have another option when producing pump pulses. In this, the second 1 W beam discussed previously can by diverted into a TOPAS-C optical parametric amplifier which can be used to produce variable wavelength pump pulses, this is discussed later.

1.6.2 The Generation of White Light

The probe pulses used for our experiment comprise of a supercontinuum of white light. This allows us to probe multiple absorption and emission features from the excited state at multiple wavelengths. These pulses are generated by focusing the previously described 800 nm (0.05 W) beam on a 1 mm thick CaF_2 window. The advantage of using CaF_2 as our means of generating this continuum, instead of other media like air or sapphire, is that it has a large anti-Stokes shift.[58, 59, 4] This allows for the generation of wavelengths in the near-UV region. The generated supercontinuum is then collimated and focused on the sample. In order for stable white light generation to occur, a certain photon density must be reached. This is an issue as, at this density, the

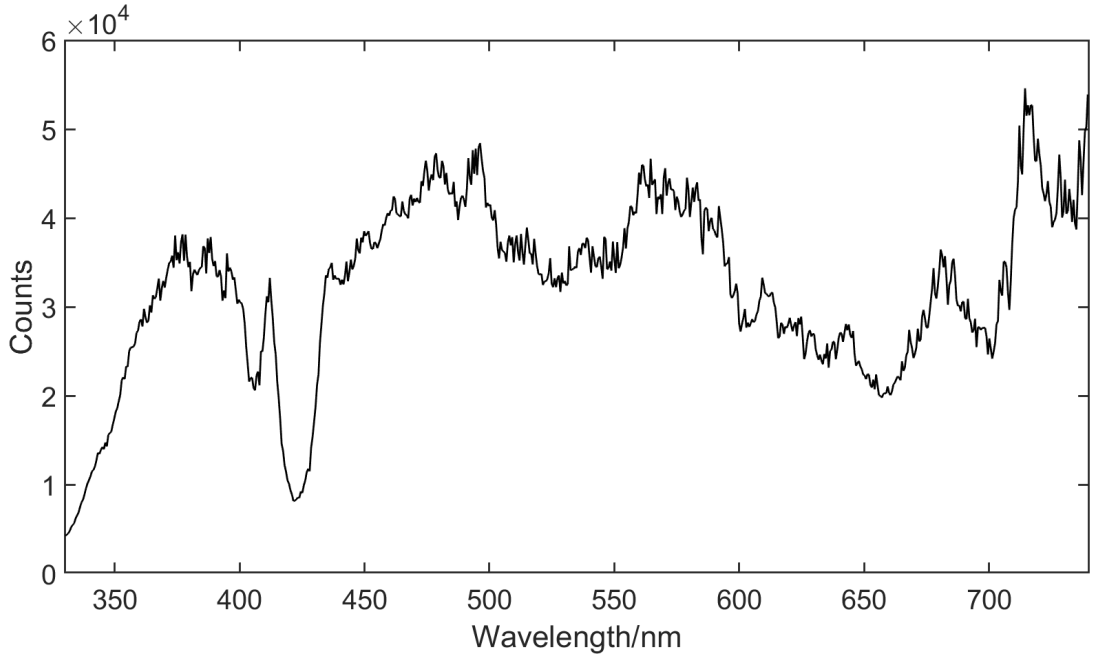

Figure 1.8: A typical spectral profile of the white-light continuum generated in our experiments.

beam will damage the CaF_2 window. This issue is circumvented in a number of ways. Firstly, the photon density used is carefully controlled. The 800 nm beam is focused through a focusing lens onto the CaF_2 window, which is mounted on a moving stage in order to carefully control the focal length (and therefore power). The 800 nm beam power is further moderated using a neutral density filter. Secondly, the CaF_2 window is mounted on a piezo motor (Newport Corp.) which translates it vertically. This ensures that the beam is not focused on the same point on the CaF_2 window for too long and minimizes damage. It is important that the window is translated vertically as the rotation of it is shown to cause intrinsic intensity and polarization modulations.[60] Figure 1.8 depicts a typical spectrum of this white light supercontinuum. Areas of this spectrum with more signal will have a greater signal-to-noise ratio and therefore give clearer results. One point that has lower signal is the dip at 425 nm, this is caused by a harmonic of the 800 nm beam. It is worth noting that, prior to white light generation, the seed beam is passed through a half-wave plate to set the polarization of the white light to 54.7° (magic angle). This process ensures anisotropy is not measured.

1.6.3 Pump-Pulse Generation

Harmonic Generation

As discussed above, there are two methods for generating pump pulses. The first of which is harmonic generation using the 0.95 W 800 nm beam. This is achieved through frequency doubling with up to two β-Barium Borate (BBO) crystals, see figure 1.9. This frequency doubling occurs via sum frequency generation (SFG). SFG happens when two photons interact in a non-linear medium. When this happens, one of these

photons will induce oscillation in the electron cloud of the medium with a frequency in line with that of the photon. Following this, the second photon will also induce oscillation. In this case however, the second photon will induce an oscillation equal to the sum of the frequencies of both the photons. After which, a photon is emitted with a frequency equal to that of the oscillation. This functionally combines the energy of two photons and is behind the "frequency doubling" discussed previously. When the two photons have the same energy, this is referred to as second harmonic generation; this is the case when generating 400 nm pulses for which one uses a single BBO crystal. When generating the 267 nm pump pulses, the wavelength used in the second presented paper (Turner *et al.*, *J. Chem. Phys.* 2019), BBO crystals are required. One of these is a "type I" BBO used to induce second harmonic generation of 400 nm light, and the second a "type II" BBO used to combine a photon of energy 400 nm with a photon of energy 800 nm to generate a photon of energy 267 nm. It is important to note that dielectric optics are used to filter out residual 800 nm when using 400 nm pump pulses, or residual 800 nm and 400 nm when using 267 nm pump pulses.

TOPAS-C

Harmonic generation is useful for generating 400 or 267 nm pulses as was the case in the second presented paper (Turner *et al.*, *J. Chem. Phys.* 2019), but often one may want to pump at a different wavelength. In the first presented paper (Turner *et al.*, *J. Phys. Chem A.* 2019), alizarin is pumped selectively at 425 nm and 550 nm in order to selectively probe what were believed to be two different species in equilibrium. In order to select these wavelengths, the TOPAS-C was used. The TOPAS-C is an optical parametric amplifier that allows a range of pump wavelengths from 230-2100 nm, which it achieves through a combination of different non-linear processes and supercontinuum generation, with the exact processes involved being wavelength specific.[4]

1.6.4 The Solution Phase layout

Having covered the important processes behind the generation of pump and probe pulses, it is now useful to consider the other experimental equipment used to conduct TEAS. In order to do this, we first consider a schematic of the laser table shown in figure 1.9.

The delay stage is designed to extend the length of the white light path in order to create a delay between the pump and probe pulses. In our case the maximum delay is 2 ns although this can be increased by manually extending this path.

The Delay stage

In order to create a pump-probe time delay, the 0.05 W beam (which will eventually become the white light probe beam) is passed through a variable optical delay stage allowing for the varying of its path length with respect to the pump beam. This delay stage consists of a motorised translation stage (Physik Instrumente, M-531.DD High

Precision Linear Translation Stage) driven by a motor controller (Physik Instrumente, C-863 Mercury Servo Controller) with a hollow gold retroreflector (RR) mounted atop the stage. It is key to accurately align the seed beam such that it is exactly parallel to the direction of motion of the variable delay stage. If this is not the case then as the delay stage moves the seed beam will move spatially and this will affect the overlap with the pump beam.

The delay stage allows for a minimum step of 7 fs, which is significantly smaller than the instrument response (around 80 fs) and is therefore comfortably small enough for our purposes. The maximum time delay possible with the translation stage is 2 ns. To obtain longer time delays, the path can be manually lengthened by moving mirrors; this was not necessary for any of the results in this thesis however.

The Chopper and the Shutters

For the recording of 'pump-on' and 'pump off' readings, it is necessary to block sequential pump pulses. This is achieved with an optical chopper (Thorlabs, MC1000A), which is a fan-like instrument that spins at a frequency of 500 Hz. As the laser has a 1 kHz repetition rate, this ensures that every second pulse is blocked and therefore leaves the detector with half the pulses blocked and half the pulses unblocked.

We use two optical shutters to block the white light line and the pump line respectively. These are, in practice, modified hard disk drives with moving arms which have a sheet of heat resistant plastic attached. This design is a modified version of that used by Maguire and co-workers.[61] The purpose of these shutters is to reduce irradiation of the sample when not acquiring data. Furthermore, the shutters are also used to conduct an automatic background subtraction to remove the dark noise of the detector and any scatter. Further removing of pump scatter can be achieved through use of a polarising filter after the sample, this was utilized in the first presented paper (Turner *et al.*, *J. Phys. Chem A.* 2019).

Sample Delivery

When conducting TEAS, we wish to ensure that each scan is of a population that has not been scanned before to avoid surveying longer-lived photoproducts instead of the ground state molecule. As stated previously, our laser scans the sample with a repetition rate of 1 kHz and therefore it must be quickly replenished. To achieve this, our sample is circulated through a flow-through cell (Demountable Liquid Cell by Harrick Scientific Products, Inc.). This cell consists of a steel housing for a pair of CaF_2 windows. The front window is 1 mm thick and the back window is 2 mm thick, the front window is thinner to avoid issues relating to group velocity dispersion. These windows are separated with a pair of polytetrafluoroethylene (PTFE) spacers, the size of these spacers can be varied to achieve an appropriate path-length. In the second presented paper (Turner *et al.*, *J. Chem. Phys.* 2019) these spacers were varied in order to study both 5 mM and 75 mM samples without over-saturating the detector. Another issue in this work was with aggregate forming on the windows of the flow cell. This is

was resolved by varying the position on which the pump and probe beams intersected with translation stages. We aim for a flow speed of $6.25 \times 10^{-6} Ls^{-1}$. If the flow-speed is significantly lower than this we observe an increase in probe noise, if it is significantly higher than this we observe turbulence beginning to affect the flow.

Detection and System Control

The white light continuum, after passing through the sample, is introduced into the fibre and transmitted into the spectrometer (Avantes Ltd, dual channel Avaspec-Fast, ULS1650F-2-USB2). The ΔOD of the light passing through the sample was calculated using equation 1.19 and displayed. The various components of this system are controlled through a computer, a custom made LabVIEW virtual instrument (VI) is used and fully automates the data acquisition, this was designed by M. D. Horbury.

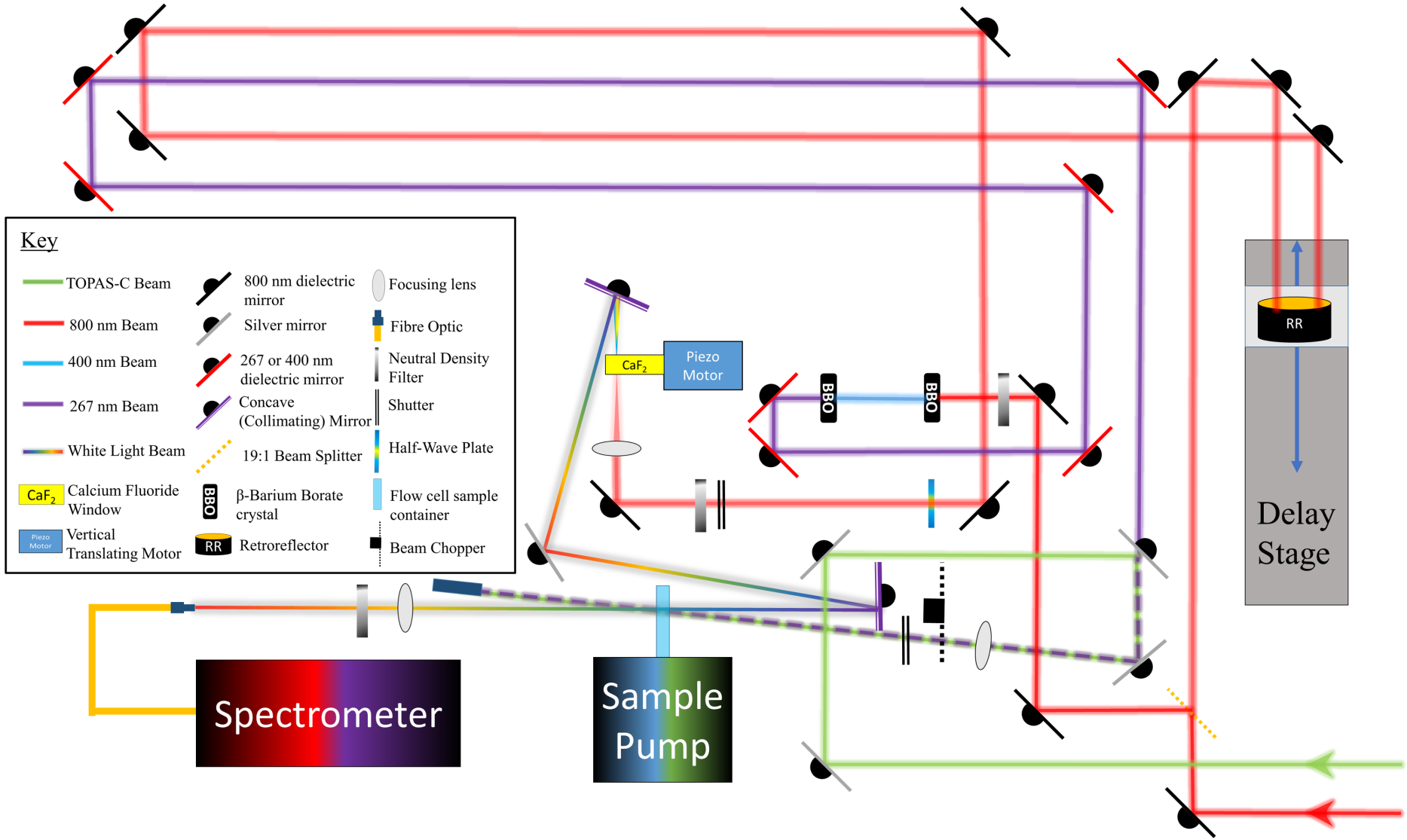

Figure 1.9: A schematic of the TEAS table set up.

1.7 An Introduction to Density Functional Theory

1.7.1 The Hohenberg-Kohn Approach

Density functional theory (DFT) is the most widely used technique in the field of computational chemistry and physics for studying small molecules[62, 63, 64], crystalline systems[65, 66, 67], metals[68, 69, 70], and even astrochemistry[71, 72]. It is valued for having relatively low computational cost compared to other techniques as well as high accuracy. The basic purpose of DFT is use the Schrödinger equation to provide a description of many interacting electrons in a system.

However, the defining feature of DFT is that is neglects the many-electron wavefunction, ψ, and to instead harnesses the fact that all properties of the quantum mechanical ground state of a system can be obtained through knowledge of electron density. This was shown by Hohenberg and Kohn in 1964 and is the theoretical underpinning of density functional theory.[73] Here, we define $n(\mathbf{r})$ as electron number density, and $n(\mathbf{r})d\mathbf{r}$ as the probability of finding an electron in $d\mathbf{r}$. Given that all properties of the ground state of a system are available from the electron density, it can be proven that there exists a universal functional[1] which calculates ground state total energy from the electron density. This is referred to as $E_{\mathrm{HK}}[n(\mathbf{r})]$ In this, HK stands for Hohenberg Kohn, the creators of this functional. To solve this equation, we need to minimize $E_{\mathrm{HK}}[n(\mathbf{r})]$ subject to the requirement that the density represents a certain number of electrons, N_e. In analogy to equation 1.11, we can divide up the terms of this functional into the sum of multiple functionals corresponding to the terms of the Hamiltonian

$$E_{\mathrm{HK}}[n(\mathbf{r})] = T[n] + E_{\mathrm{int}}[n] + E_{\mathrm{ext}}[n] + E_{\mathrm{II}}. \tag{1.20}$$

$T[n]$ represents the internal kinetic energy of the system; E_{int} represents coulombic forces between electrons, E_{ext} represents electron-nuclear coulombic interactions, and E_{II} represents nuclear-nuclear interactions. Note this is not a functional, rather, this is a constant under the Born-Oppenheimer approximation and can be calculated as

$$E_{\mathrm{II}} = \sum_{\alpha>\beta} \frac{Z_\alpha Z_\beta e^2}{4\pi\epsilon_0 |\mathbf{R}_\alpha - \mathbf{R}_\beta|}. \tag{1.21}$$

$E_{\mathrm{ext}}[n]$ can also be simply evaluated as

$$E_{\mathrm{ext}}[n] = \int V_{\mathrm{ext}}(\mathbf{r}) n(\mathbf{r}) d\mathbf{r} \tag{1.22}$$

where V_{ext} is the external potential arising from the nuclei. Unfortunately, $T[n]$ and $E_{\mathrm{int}}[n]$, both require knowledge of electron-electron interactions. Whilst calculating energies for non-interacting systems is simple, as discussed in section 1.3.2, calculating energies when there is meaningful interaction between particles is very challenging.

[1] A functional is similar to a function although it requires as an input argument a function across all space and outputs a scaler argument

1.7.2 The Kohn-Sham Approach

In 1965, Kohn and Sham proposed proposed the ansatz[2] that the ground state density of the original interacting system in the Hohenberg-Kohn equation is equal to that of some chosen non-interacting system. Therefore

$$E_{\mathrm{KS}} = E_{\mathrm{HK}}. \tag{1.23}$$

As this is a non-interacting system, the Hamiltonian operator can be split up into a sum of terms, each of which only containing one coordinate as can be seen in equations 1.9 and 1.10. Owing to this, the Schrödinger equation has separable solutions of the form

$$\psi(\mathbf{r}_1, \mathbf{r}_2, ..., \mathbf{r}_n) = \phi_1(\mathbf{r}_1)\phi_2(\mathbf{r}_1)...\phi_n(\mathbf{r}_n) \tag{1.24}$$

However, as the electrons are fermions and the overall wavefunction for a system of fermions must be antisymmetric[3] under exchange of any two particles. A Slater determinant can be seen as the minimum form of the many-body wavefunction that fits this requirement.[75, 76] This Slater determinant is associated with an electron density for a system with N_e electrons given by

$$n(\mathbf{r}) = \sum_{n=1}^{N_e} |\psi_n(\mathbf{r})|^2. \tag{1.25}$$

The Kohn-Sham total energy can be written as

$$E_{\mathrm{KS}} = T_{\mathrm{s}}[n] + E_{\mathrm{H}}[n] + E_{\mathrm{ext}}[n] + E_{\mathrm{II}} + E_{\mathrm{XC}}[n] \tag{1.26}$$

Here we have introduced three new terms, $T_{\mathrm{s}}[n]$, $E_{\mathrm{H}}[n]$, and $E_{\mathrm{XC}}[n]$. The first term, $T_{\mathrm{s}}[n]$, is the non-interacting kinetic energy and can be calculated as

$$T_{\mathrm{s}} = \sum_{n=1}^{N} \int \psi_n^*(\mathbf{r}) \Big(-\frac{\hbar^2}{2m}\nabla^2 \Big) \psi_n(\mathbf{r}) dr. \tag{1.27}$$

The second term, $E_{\mathrm{H}}[n]$, is the Hartree energy. This represents the coulombic interaction of the density with itself and is given by

$$E_{\mathrm{H}} = \frac{1}{2} \int \frac{n(\mathbf{r})n(\mathbf{r}')}{|\mathbf{r} - \mathbf{r}'|} d\mathbf{r} d\mathbf{r}' \tag{1.28}$$

The final term, $E_{\mathrm{XC}}[n]$ is the exchange correlation term and is at the heart of the Kohn-Sham method. This term encompasses all the effects of electron-electron interaction and, by definition, is the term that ensures E_{KS} is equal to E_{HK}, therefore

[2] Ansatz: attempt, approach. A mathematical assumption, especially about the form of an unknown function, which is made in order to facilitate solution of an equation or other problem [Oxford English Dictionary].

[3] Consider exchange operator p_{ij} such that $p_{ij}\psi(X_1, X_2) = \psi(X_2, X_1)$, an antisymmetric wavefunction fulfils the condition that $\psi(X_1, X_2) = -p_{ij}\psi(X_1, X_2)$, for further details on why the wavefunction of fermions is asymmetric under exchange of two particles see ref [74]

$$E_{\mathrm{XC}}[n] = T[n] - T_{\mathrm{s}}[n] + E_{\mathrm{int}}[n] - E_{\mathrm{H}}[n] \tag{1.29}$$

The relative ease of implementing this form of density functional theory is the reason it has become so widely used across so many fields.

1.7.3 Minimizing Energy with Kohn-Sham DFT

In order to minimize E_{KS}, and thereby find the ground state, we must differentiate the Kohn-Sham equation with respect to the single orbitals, $\psi_n(\mathbf{r})$. In this, we select constraints that ensure that the orbitals we are minimizing with respect to represent densities that integrate to the correct number of electrons. This allows us to minimize with respect to the single orbitals as opposed to the density. By using the chain rule to differentiate E_{KS} with respect to $\psi_n^*(\mathbf{r})$ we get

$$\frac{\delta E_{\mathrm{KS}}}{\delta \psi_n^*(\mathbf{r})} = \frac{\delta T_{\mathrm{s}}}{\delta \psi_n^*(\mathbf{r})} + \left[\frac{\delta E_{\mathrm{ext}}}{\delta n(\mathbf{r})} + \frac{\delta E_{\mathrm{H}}}{\delta n(\mathbf{r})} + \frac{\delta E_{\mathrm{XC}}}{\delta n(\mathbf{r})}\right] \frac{\delta n(\mathbf{r})}{\delta \psi_n^*(\mathbf{r})} \tag{1.30}$$

We then substitute in differentials calculated from equations 1.24, 1.22, 1.19, 1.18, and define $\dfrac{\delta E_{\mathrm{XC}}}{\delta n(\mathbf{r})} = V_{\mathrm{XC}}(\mathbf{r})$. We can now minimize E_{KS} subject to the constraint that the single particle orbitals are normalised. This is subject to the constraint that the wavefunctions are all mutually orthonormal,[4] which is achieved by adding a set of Lagrange multipliers. This results in the Kohn-Sham equation

$$\overbrace{\left[-\frac{\hbar^2}{2m}\nabla^2 + V_{\mathrm{ext}}(\mathbf{r}) + V_{\mathrm{H}}(\mathbf{r}) + V_{\mathrm{XC}}(\mathbf{r})\right]}^{Kohn-Sham\ Hamiltonian} \psi_n(\mathbf{r}) = \epsilon_n \psi_n(\mathbf{r}) \tag{1.31}$$

In practice, the Kohn-Sham equation is solved iteratively by generating a guess electron density and solving the Kohn-Sham equation for this to generate a set of orbitals. These orbitals are used to generate a set of better approximation of the electron density, which in turn results in a different value for n($\mathbf{r}$) than was previously found in equation 1.25, and the process is repeated. When the total energy of the system has stopped changing by more than some chosen tolerance, the calculation is said to have converged. In order to solve the Kohn-Sham equation, $V_{\mathrm{XC}}(\mathbf{r})$ must be approximated. Methods for approximating this are discussed in the following section.

1.7.4 An Overview of Functionals

There is an intrinsic trade-off with the approximation of the exchange-correlation functional between accuracy and computational cost. Perdew wrote of a "Jacobs ladder"[5] of functional classes in 2001 to describe the increasing rungs of functional

[4] Two functions $\psi_i(\mathbf{r})$ and $\psi_j(\mathbf{r})$ are said to be orthonormal if $\int \psi_i(\mathbf{r})\psi_j(\mathbf{r})dr = 0$; and $\int \psi_i(\mathbf{r})^2 dr = 1$. For further details as to why fermions occupying different normalised states must be orthonormal see reference [75]

[5] This is a biblical reference to a dream Jacob had of a ladder on earth with the top reaching to heaven.

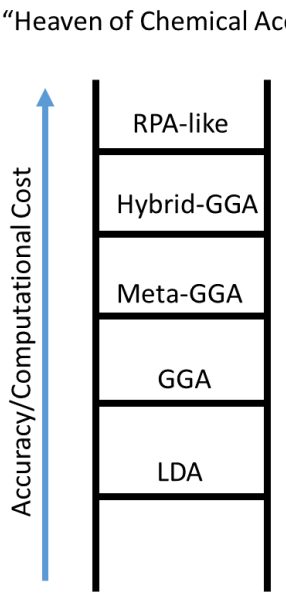

Figure 1.10: A "Jacobs ladder" of density functional approximations to the exchange correllation energy.

accuracy, see figure 1.10.[77] This was expanded upon by Casida *et al.* who in 2002 described a similar Jacobs ladder for time-dependent density functional theory, as is discussed later in this section.[78, 79]

The Local Density Approximation

In order to generate an accurate functional, one must accurately approximate $V_{\mathrm{XC}}(\mathbf{r})$. One common starting point for doing this is the local density approximation. In the local density approximation, it is proposed that E_{XC} depends only upon electron density and not on other factors such as the Kohn-Sham orbitals. Beyond this, the local density approximation uses a homogenous electron gas (HEG) model. The exchange-energy density of HEG is known analytically using the local-electron-gas formula.[80] We can use this formula point-wise for each particle of a uniform electron gas with density n to generate

$$E_{\mathrm{XC}}^{\mathrm{LDA}}[n(\mathbf{r})] = \int n(\mathbf{r})\epsilon_{\mathrm{XC}}(n(\mathbf{r}))d\mathbf{r} \tag{1.32}$$

where $\epsilon_{\mathrm{XC}}(n(\mathbf{r}))$ indicates the exchange and correlation energy per particle of a uniform electron gas of density $n(\mathbf{r})$. The function ϵ_{XC} can be split into two parts, the exchange contribution ($\epsilon_{\mathrm{X}}(n(\mathbf{r}))$) and the correlation-contribution ($\epsilon_{\mathrm{C}}(n(\mathbf{r}))$). The former is already known by the Dirac exchange energy function[80, 81]

$$\epsilon_{\mathrm{X}}(n(\mathbf{r})) = -\frac{3}{4}\left(\frac{3}{\pi}\right)^{\frac{1}{3}} n(\mathbf{r})^{\frac{1}{3}}. \tag{1.33}$$

The $\epsilon_{\mathrm{C}}(n)$ was obtained accurately in 1980 by Ceperley and Alder using diffusion quantum Monte Carlo calculations.[82] These values have been interpolated to find an analytic form of $\epsilon_{\mathrm{C}}(n)$. The LDA approximation is remarkably accurate and has

been used widely for many years. One major weakness is that it is inaccurate in highly inhomogeneous systems.

The Generalized Gradient Approximation

One downfall of the local density approximation is that it assumes the density of the electron gas to be homogenous with respect to distance from the point. As E_{X} is the significantly larger part of E_{XC} it followed that this would be the part that was first addressed.[84] It was suggested that the effect of non-homogeneity of the true electron system on E_{X} could be accounted for by expanding in terms of gradient of the density at each considered point.[85, 86] This yielded the following equation:

$$E_{\mathrm{X}}(n) = \int \epsilon_{\mathrm{X}}^{\mathrm{LDA}}(n) f_{\mathrm{X}}(s) dn \tag{1.34}$$

Where "s" is a dimensionless or "reduced" density gradient, and $f_{\mathrm{X}}(s)$ is called the "exchange enhancement factor". This equation is known as the "generalized gradient approximation". Later, functionals were developed for calculating correlation energy, for instance LYP, which also used the generalised gradient approximation manifold.[87] These exchange functionals, such as B88[85], and correlation functionals, such as LYP[88], were combined to generate $\mathrm{GGA_{XC}}$ functionals like BLYP. This technique is the basis of the PBE functional [89] that is widely used in this work, and also forms the starting point for hybrid [90, 91] and ranged separated functionals [92, 93] that will be discussed in the following section.

Hybrid Functionals

GGA functionals can be improved by calculating a fraction of the exchange energy portion of E_{XC} using the exact expression calculated from Hartree-Fock theory. In this, instead of using the Hartree-Fock orbitals, the Kohn-Sham orbitals are used for this calculation.[87] The remainder of the E_{XC} derives from the GGA or LDA functional.[94] In practice this is achieved through the linear combination of the Hartree-Fock exchange functional

$$E_{\mathrm{X}}^{\mathrm{HF}} = -\frac{1}{2} \sum_{i,j} \int \int \psi_i^*(\mathbf{r}_1) \psi_j^*(\mathbf{r}_2) \frac{1}{r_{12}} \psi_i(\mathbf{r}_1) \psi_j(\mathbf{r}_2) d\mathbf{r}_1 d\mathbf{r}_2 \tag{1.35}$$

with any number of exchange and correlation functionals. The weightings of these functionals are set *a priori* and will often be based on experimental data or previously conducted high level calculations.[94, 90, 91]

Two examples of hybrid functionals used in this work are PBE0[90] and B3LYP[91]. B3LYP takes the form:

$$E_{\mathrm{XC}}^{\mathrm{B3LYP}} = E_{\mathrm{X}}^{\mathrm{LDA}} + a_0(E_{\mathrm{X}}^{\mathrm{HF}} - E_{\mathrm{X}}^{\mathrm{LDA}}) + a_{\mathrm{X}}(E_{\mathrm{X}}^{\mathrm{GGA}} - E_{\mathrm{X}}^{\mathrm{LDA}}) + E_{\mathrm{C}}^{\mathrm{LDA}} + a_{\mathrm{C}}(E_{\mathrm{C}}^{\mathrm{GGA}} - E_{\mathrm{C}}^{\mathrm{LDA}}). \tag{1.36}$$

Where $a_0 = 0.20$; $a_X = 0.72$; and $a_C = 0.81$. These figures were calculated by Becke by fitting the analogous B3PW91 parameters to a set of atomization energies, ionization potentials, proton affinities, and total atomic energies.[91, 95] This functional was an attempt to balance the qualities of the LDA, GGA, and HF approaches to build the optimal functional. The PBE0 functional takes the form:

$$E_{XC}^{PBE0} = E_{XC}^{PBE} + \frac{1}{4}(E_X^{HF} - E_X^{PBE}). \tag{1.37}$$

This method is significantly simpler and uses the PBE functional to generate E_X^{PBE} and E_{XC}^{PBE}. The name PBE0 is used as this is, unlike B3LYP, a zero empirical parameter functional.

Range-Separated Functionals

Whilst hybrid functionals are very effective at calculating the energies of the vast majority of systems, issues can arise with some select cases. These include, but are not limited to, polarizability of long chains[96] and Rydberg states.[97] These issues are noticed primarily in excited state calculations (discussed later) and are not usually an issue with ground state calculations. A cause of this "inexactness" can be traced back to the one electron self-interaction error (1e-SIE).[98, 99] An important source of 1e-SIE is the incorrect treatment of E_X at long ranges. The V_{XC} of semi-local functionals decays exponentially along with the density, while the asymptotic form of the exact potential is $-1/r$. [100, 101, 99]

It has been suggested that it is possible to recover the $-1/r$ asymptote exactly by introducing range separation.[97, 102] Practically, this is implemented by splitting the coulomb operator in E_{XC} into two terms, a short range term and a long range term. This results in the following expression for E_{XC} for a range separated system based on the PBE functional

$$E_{XC}(n) = aE_X^{SR,HF}(n) + (1-a)E_X^{SR,PBE}(n) + bE_X^{LR,HF}(n) + (1-b)E_X^{LR,PBE}(n) + E_C^{PBE}(n) \tag{1.38}$$

By varying the weighting of these terms one can accurately represent long range interactions. The methodology behind this is beyond the scope of this work but can be found in references [97, 102, 103, 104, 105]. This type of functional is especially good for studying charge-transfer excitations. Some examples of range-separated functionals are CAM-B3LYP and LC-PBE0, both of which are utilized in the first presented paper (Turner *et al.*, *J. Phys. Chem A.* 2019).

1.7.5 Basis Sets

The previous section discussed at length the process of setting up the Schrödinger equation with Kohn-Sham theory and various functionals to approximate E_{XC}. This section looks further into how to actually solve the Schödinger equation in practice.

First, recall equation 1.31:

$$-\frac{\hbar^2}{2m}\nabla^2\psi_n(\mathbf{r}) + V_{\text{eff}}(\mathbf{r})\psi_n(\mathbf{r}) = \epsilon_n\psi_n(\mathbf{r}), \tag{1.39}$$

where V_{eff} encompasses all the potential energy terms for some effective potential. This effective potential would be computationally expensive to calculate in real-space on a grid. Instead, we represent $\psi_n(\mathbf{r})$ in terms of a sufficiently large set of "basis functions" such that

$$\psi_n(\mathbf{r}) = \sum_m c_{n,m}\chi_m(\mathbf{r}) \tag{1.40}$$

for a set of basis functions $\chi_m(\mathbf{r})$ and coefficients c_m. We can reduce the complexity of equation 1.40 by selecting a good set of basis functions. There are two main classes of basis functions, the unbiased grid or plane-wave based methods and local orbital methods. The grid-based methods reduce the complexity of solving the problem by using a large number of simple functions in terms of which the Hamiltonian has a very simple form. This class of basis functions is better for periodic extended systems as well as being very simple and having tunable accuracy. The local orbital based method simplifies the problem by limiting the number of basis functions that need to be used, choosing them to best represent the orbitals. The method is often a lot cheaper as it already contains a lot of information about the system as a starting point. In this section we will discuss both methods.

Local Orbital Basis Sets

A local orbital basis set uses functions of the form $\chi_\alpha(\mathbf{r} - R_I)$ for orbitals based on atom position R_I. The "minimal" basis set uses one function per occupied orbital, but this is however not normally sufficient to accurately describe the system. Even in this simple system, there is normally more than one function per location, therefore the index "m" is used here to denote the specific combination of index α and position I. The matrix elements of the Hamiltonian are defined by

$$H_{m,m'} = \int \chi^*(\mathbf{r} - \mathbf{R}_m)\hat{H}\chi(\mathbf{r} - \mathbf{R}_{m'}) \tag{1.41}$$

As these orbitals will not be mutually orthogonal we must also define an overlap matrix as

$$S_{m,m'} = \int \chi^*(\mathbf{r} - \mathbf{R}_m)\chi(\mathbf{r} - \mathbf{R}_{m'}) \tag{1.42}$$

Therefore, we can solve the secular equation[6]

[6] A characteristic polynomial of a square matrix is a polynomial which has eigenvalues as its roots and is invariant under matrix similarity. It has the determinant and the trace of the matrix as coefficients. A characteristic or "secular" equation is where a characteristic polynomial is set to 0.

$$\sum_{m'}[H_{m,m'} - \epsilon_i S_{m,m'}]c_{i,m'} = 0 \tag{1.43}$$

These local basis functions in practice often take the form of Gaussian orbitals, Slater-type orbitals (STO), or numeric atomic orbitals (NAO).

In this thesis an array of basis sets are used, all of which are considered "split-valence basis sets". In this approach a different number of basis functions is used on the valence orbitals to the ground orbitals. This comes from the belief that the valence orbitals are more important to the behaviour of the atom and therefore need to be treated more accurately. An example of one such basis set is 6-31G. In this Pople-style basis set, six primitive Gaussians make up the function used to represent the core orbitals. The valence orbitals are represented by two functions in this case, one made up of three primitive Gaussians and one made up of one primitive Gaussian, this is referred to as a "double ζ" basis set. Another example of a double ζ basis set is cc-pVDZ where DZ stands for double ζ. Triple ζ basis sets include 6-311G and cc-pVTZ. For more details on Pople basis sets and how they are formed from these primitive Gaussians, see reference [106]. In this reference two other additional modifications are discussed, polarization and diffuse functions, which will now be explored in further detail.

First, we will discuss polarization functions. An atomic orbital may shift as a response to the presence of other nearby atomic orbitals. This is referred to as polarization. For example, an s orbital can polarize in a specific way when mixed with a p orbital, this is how carbon-carbon double bonds are formed. In general, to polarize a basis function with angular momentum l one must mix it with basis functions with angular momentum $l + 1$. This form of modification is important when studying highly polarized and conjugated systems. In Pople basis sets the addition of polarization functions is often denoted with a star (*). Normally, one star is used to denotes the adding of one set d-type polarization functions to all non-hydrogen atoms and two stars denotes the adding one set of d-type polarization functions on all non-hydrogen atoms and one set of p-type functions to all hydrogen atoms. Another notation for this is to list the added functions in parenthesis after the basis set. Correlation-consistent basis sets (cc-p) include a full set of polarization functions for each atom.

Diffuse functions deal with situations where the electron is held far away from the nucleus. They are necessary for anions, Rydberg states, and highly electronegative atoms with high electron density, such as fluorine. In Pople basis sets, diffuse functions are indicated with a plus symbol (+). Analogously to polarization functions, a single plus indicates the addition of one set of sp-type diffuse functions on all non-hydrogen atoms and two pluses indicate the addition of one set of sp-type diffuse functions to all non-hydrogen atoms and one set of s-type functions to all hydrogen atoms. In correlation-consistent basis sets the addition of diffuse functions is indicated by the presence of the prefix "aug". In the first presented paper (Turner *et al.*, *J. Phys. Chem A.* 2019) the vertical excitations of different tautomers of alizarin were calculated. As two of these tautomers were anions, this set of calculations was conducted using

the basis set aug-cc-pVTZ. These correlation-consistent basis sets were optimized for use in MP2 calculations. However they are still accurate when used with high accuracy DFT functionals owing to the reasonable degree of similarity of the results of advanced functionals to post-HF methods. In this thesis we have in several cases used correlation-consistent basis sets as these were used in several previous papers we wished to benchmark our results against, even though in all cases Pople basis sets would likely be just as appropriate.

Grid Based/Plane-Wave Basis Sets

Plane-wave basis sets are very useful for periodic systems. This is due to the fact that the plane-wave approach utilizes a periodic boundary condition over some volume V. It is still possible to use plane-wave codes in a non-periodic system as long as there is sufficient empty space between the molecule and the edge of the defined "box". Any periodic function can be written as a set of Fourier components

$$\psi_{\mathbf{r}} = \sum_{\mathbf{q}} c_{i,\mathbf{q}} e^{i\mathbf{q}.\mathbf{r}}, \tag{1.44}$$

for wavevector $\mathbf{q}$. We note that wavevectors are orthonormal, in that

$$\int_V e^{i\mathbf{q}'.\mathbf{r}} e^{i\mathbf{q}.\mathbf{r}} = \delta_{\mathbf{q}',\mathbf{q}}. \tag{1.45}$$

We can, therefore, calculate the matrix elements by inserting equation 1.44 into equation 1.39. This, after applying the kinetic energy operator and using the previously discussed orthonormality condition gives us

$$\sum_{\mathbf{q}} \left(\frac{1}{2} q^2 \delta_{\mathbf{q}',\mathbf{q}} + \int_V V_{\text{eff}}(\mathbf{r}) e^{i(\mathbf{q}-\mathbf{q}').\mathbf{r}} d\mathbf{r} \right) c_{i,\mathbf{q}} = \epsilon_i c_{i,\mathbf{q}'}. \tag{1.46}$$

If we write all our wavevectors $\mathbf{q}$ in terms of one wavevector $\mathbf{k}$ inside the first Brillouin zone we can write the following equation where $\mathbf{G}$ are reciprocal lattice vectors of the periodic lattice.

$$H_{\mathbf{G},\mathbf{G}'}(\mathbf{k}) = \left(\frac{1}{2}(k^2 + G^2)\delta_{\mathbf{G},\mathbf{G}\text{'}} + V_{\text{eff}}(\mathbf{G} - \mathbf{G}\text{'}) \right) \tag{1.47}$$

We have a separate Hamiltonian matrix for each $\mathbf{k}$-point therefore we can solve a matrix of the form

$$\sum_{\mathbf{G}\text{'}} H_{\mathbf{G},\mathbf{G}'}(\mathbf{k}) c_{i,\mathbf{k}+\mathbf{G}'} = \epsilon_i c_{i,\mathbf{k}+\mathbf{G}} \tag{1.48}$$

for the coefficients $c_{i,\mathbf{k}+\mathbf{G}}$ giving solutions $\psi_{\mathbf{i},\mathbf{k}}(\mathbf{r})$ for each $\mathbf{k}$-point. It is, however, not possible to treat our G-vectors as an infinite set so we must discretize them to form a useful finite basis. We know that larger —$\mathbf{G}$— terms correspond to basis functions that vary rapidly in space. If we are confident we have reasonably smooth wavefunctions we can discard larger —$\mathbf{G}$— terms. We do this by implementing a cutoff energy term

(E_{cut}) term where only G-Vectors that obey

$$\frac{1}{2}|k+G|^2 < E_{\text{cut}}$$

are included in the basis. As the cutoff energy increases, total energy of the system with decrease to a convergence point. Due to this, we can describe total energy as variational to E_{cut}. This style of basis set works more effectively for systems with periodic boundary conditions, which does not apply within our system. Owing to this, they have not been used in this thesis.

Pseudopotentials

In this work, we will often use pseudopotentials as a method of lowering computational complexity. A pseudopotential is a substitution of the Coulombic potential for a bare atomic nucleus with a pre-calculated potential representing the nucleus and tightly bound electrons. This varies less rapidly and therefore reduces the size of basis set needed to represent these orbitals. Also, this lowers the number of electrons in the system dramatically. These pseudopotentials will be generated *a priori* with a stand alone *ab initio* calculation.

1.7.6 Time-Dependent Density Functional Theory

Time-dependent density functional theory (TDDFT) is a method which attempts to model the response of the system to time dependent potentials. This allows us to investigate the dynamics of the electron system and is key to predicting UV-Vis and fluorescence results. It does this by predicting the excited states of a system. TDDFT works through the principle that one can directly model a time-dependent potential, $\nu_{\text{ext}}(\mathbf{r},t)$, with a time dependent density, $n(\mathbf{r},t)$. This is known as the Runge-Gross (RG) theorem and is directly analogous to the Hohenberg-Kohn theorem, which holds the same for time-independent potentials, as discussed previously.[107] Also like HK theorem, it therefore proves that for the time-dependent many-body wavefunction there exists a uniquely defined time-dependent density.

Whilst there are a number of ways to approach TDDFT in this thesis we use the Casida approach to linear response TDDFT (LR-TDDFT).[108, 109] LR-TDDFT, unlike real-time TDDFT, does not propagate time explicitly. Rather, it uses a Fourier Transform with respect to time to give the response to excitations at a given frequency, ω. The underlying Casida methodology relies on the ability to form a Dyson-like equation[7] within Kohn-Sham theory. This relates the exact response of the density to an external perturbation to the Kohn-Sham response and to the Kohn-Sham effective potential. The poles of this exact response function are the excitation energies of the system.

Stepping back briefly, with any approach, we start by considering an external

[7] A Dyson equation summarizes the Feynman-Dyson perturbation theory. Further information can be found at reference [110]

potential, $v_{\text{ext}}(\mathbf{r})$, of the system, in this case we perturb it with a external time dependent potential:

$$v_{\text{ext}}(\mathbf{r},t) = v_{\text{ext}}(\mathbf{r},t=0) + \delta v_{\text{ext}}(\mathbf{r},t). \tag{1.49}$$

For this, the system will respond, giving a time-dependent density $n(\mathbf{r},t)$. This can be expanded as a Taylor series wherein the first term ($n_1(\mathbf{r},t)$) represents the direct response to $\delta v_{\text{ext}}(\mathbf{r},t)$, the second ($n_2(\mathbf{r},t)$) represents the response to that response and so on. We truncate after the first term and define

$$n_1(\mathbf{r},t) = \int_0^\infty dt' \int d\mathbf{r}' \chi(\mathbf{r},t;\mathbf{r}',t')\delta v_{\text{ext}}(\mathbf{r}',t'), \tag{1.50}$$

where $\chi(\mathbf{r},t;\mathbf{r}',t')$ is the response function which expresses the change in the density at $(\mathbf{r},t)$ due to a change in the potential at $(\mathbf{r}',t')$. We can therefore simply define this as

$$\chi(\mathbf{r},t;\mathbf{r}',t') = \left.\frac{\partial n_1(\mathbf{r},t)}{\partial \delta v_{\text{ext}}(\mathbf{r}',t')}\right|_{v_{\text{ext}}(\mathbf{r},t=0)}. \tag{1.51}$$

In the appendix we show how knowledge of the KS system can be used to find the poles of the response function of the full interacting system. Once this has been achieved Casida [108, 109] showed how the challenge of finding these poles can be set as an eigenvalue problem:

$$\begin{pmatrix} A & B \\ B* & A* \end{pmatrix} \begin{pmatrix} X \\ Y \end{pmatrix} = \omega \begin{pmatrix} -1 & 0 \\ 0 & 1 \end{pmatrix} \begin{pmatrix} X \\ Y \end{pmatrix} \tag{1.52}$$

Where

$$A_{ia,jb} = \delta_{ij}\delta_{ab}(\epsilon_a - \epsilon_i) + 2\int d\mathbf{r} \int d\mathbf{r}' \Phi_q^*(\mathbf{r}) f_{\text{Hxc}}(\mathbf{r},\mathbf{r}')\Phi_{q'}(\mathbf{r}') \tag{1.53}$$

and

$$B_{\text{ia,jb}} = 2\int d\mathbf{r} \int d\mathbf{r}' \Phi_q^*(\mathbf{r}) f_{\text{Hxc}}(\mathbf{r},\mathbf{r}')\Phi_{-q'}(\mathbf{r}') \tag{1.54}$$

Which has the same structure as the eigenvalue problem arising from the time-dependent Hartree-Fock theory and can be solved in the same fashion.[111]

It is worth noting that the accuracy of TDDFT is significantly more dependent on the choice of exchange-correlation functional than is ground state DFT. While one can obtain good geometries and relative energetics using a semilocal functional like PBE, within TDDFT a hybrid functional is often necessary, see section 1.7.4. Another limitation is that charge-transfer style excitations are often underestimated in TDDFT compared to local excitations. The Casida approach allows us to predict excited state forces as well. This is useful as it allows for excited state relaxation calculations like those present in the third presented paper (Turner *et al.*, in prep.).

1.7.7 Improved Scaling in Density Functional Theory

The computational effort in solving the Kohn-Sham equations scales cubically with system size ($O(N^3)$). Traditional Kohn-Sham methods seek eigenstates $\psi_n(\mathbf{r})$ with eigenvalues ϵ_n. To fill a number of occupied orbitals $\propto O(N)$, one must calculate a number of eigenstates which itself $\propto O(N)$. Further to this, each eigenstate is described by basis functions, the number of which scales $\propto O(N)$. Finally, each eigenstate must be kept proportional to all the others during the process of finding the solution, where the number of others is $\propto O(N)$. In recent years, an effort has been made to improve the scaling of TDDFT culminating a linear scaling methodology.[112, 113] In this thesis, I conduct linear-scaling calculations using the ONETEP code.[114]

The linear scaling methodology is born out of a simple premise - it is not necessary to know every eigenstate individually and instead an averaged description of all the eigenstates together can suffice. We can consider the single electron density matrix

$$n(\mathbf{r},\mathbf{r}') = \sum_n \psi_n^*(\mathbf{r}) f_n \psi_n(\mathbf{r}') \tag{1.55}$$

Where f_n is the occupancy of state n and can be either 1 or 0. The single electron density matrix contains all the information about the ground state of the system. If we want the band structure energy, for example, we can calculate it using this matrix. This is done by taking the trace of the Hamiltonian acting on the density operator:

$$\begin{aligned} E_{\mathrm{bs}} &= \sum_m \int d\mathbf{r} \int d\mathbf{r}' \psi_m(\mathbf{r}) \hat{H}_{\mathrm{KS}} n(\mathbf{r},\mathbf{r}') \psi_m^*(\mathbf{r}') \\ &= \sum_{n,m} f_n \int \psi_n^*(\mathbf{r}) \psi_m(\mathbf{r}) d\mathbf{r} \int \psi_m^*(\mathbf{r}') \hat{H}_{\mathrm{KS}} \psi_m(\mathbf{r}') d\mathbf{r}' \\ &= \sum_n \epsilon_n f_n \end{aligned} \tag{1.56}$$

Charge density is given by the diagonal elements of the density matrix:

$$n(\mathbf{r}) = 2n(\mathbf{r},\mathbf{r}') \tag{1.57}$$

In this the factor of 2 is to account for electron spin as we assume a closed shell system. Provided there is a band gap, the density matrix has been shown to decay exponentially as a function of the distance between $\mathbf{r}$ and $\mathbf{r}'$.[115, 116, 117, 114] This property can be exploited to truncate the density matrix such that the amount of information it holds will increase only linearly with size.[118] In practice this is achieved through expressing the matrix as:

$$n(\mathbf{r},\mathbf{r}') = \sum_{\alpha\beta} \phi_\alpha(\mathbf{r}) K^{\alpha\beta} \phi_\beta^*(\mathbf{r}'), \tag{1.58}$$

where the ϕ_α is a set of spatially, localised non-orthogonal basis functions and K is a matrix referred to as the density kernel.[119] The density matrix can be simplified through truncation of the density kernel:

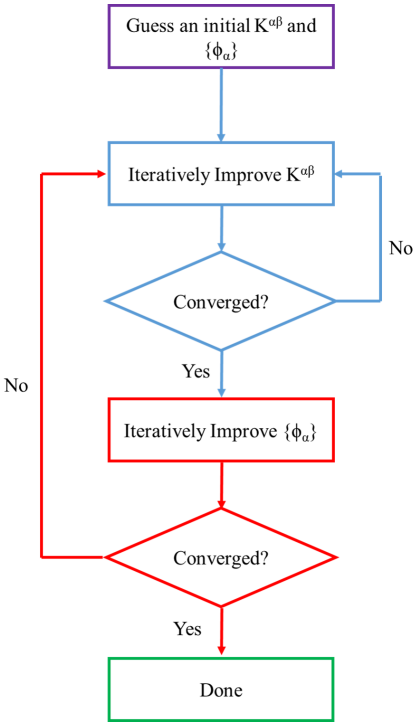

Figure 1.11: A flow chart to show the methodology by which ONETEP conducts linear-scaling TDDFT. Typical convergence criteria involve RMS values of $\frac{\partial E}{\partial K^{\alpha\beta}}$

$$K^{\alpha\beta} = 0 \text{ when } |\mathbf{R}_\alpha - \mathbf{R}_\beta| > r_{\text{cut}} \tag{1.59}$$

in this, $\mathbf{R}_\alpha$ and $\mathbf{R}_\beta$ are the centres of the localisation regions of functions ϕ_α and ϕ_β respectively. In ONETEP we use a minimal number of localised functions per atom and optimize these functions during the calculation. Therefore, we no longer consider ϕ_α as our atomic basis set *a priori*, rather, they are quantities set to be determined during the calculation alongside the density kernel. Figure 1.11 shows a flow chart of how this takes place. This is a two loop process, with the density kernel being optimized for every given set of optimized ϕ_α.

We call the ϕ_α non-orthogonal generalised Wannier functions (NGWFs) and centre them on the atoms in the system.[120] We enforce strict localisation on them by truncating any contributions from outside localised spheres of radius r_{loc}^{α}. This is achieved by expanding ϕ_α in the basis of periodic sinc or "psinc" functions[121] $D_k(\mathbf{r})$:

$$\phi_\alpha(\mathbf{r}) = \sum_k D_k(\mathbf{r}) C_{k,\alpha}. \tag{1.60}$$

Each psinc function is a delta-function expressed in a plane wave basis with limited bandwidth. These occur at a given grid point k for function $D_k(\mathbf{r})$, figure 1.12 shows a plot of a psinc function, reproduced from reference [122]. Psinc functions are only non-zero on a single grid point. The set of psinc functions forms a regular grid as shown in figure 1.13. Each $\phi_\alpha(\mathbf{r})$ is confined to a local sphere on this grid of radius r_{loc}^{α}

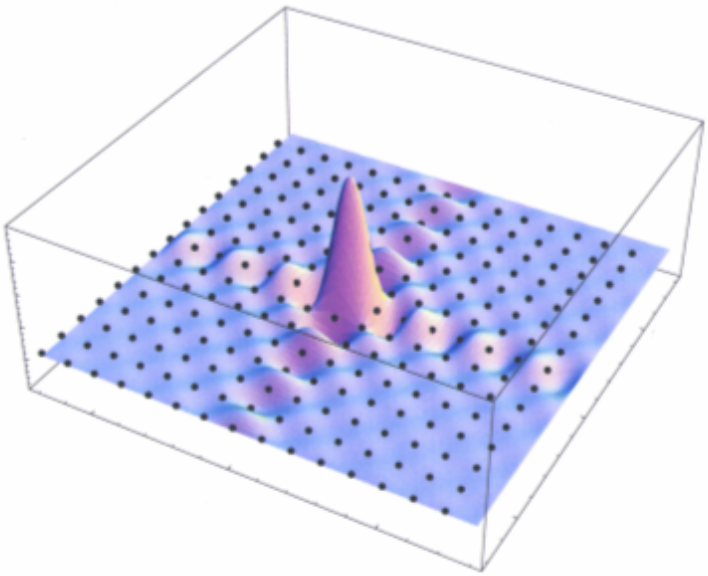

Figure 1.12: A psinc basis function, reproduced from reference[122]

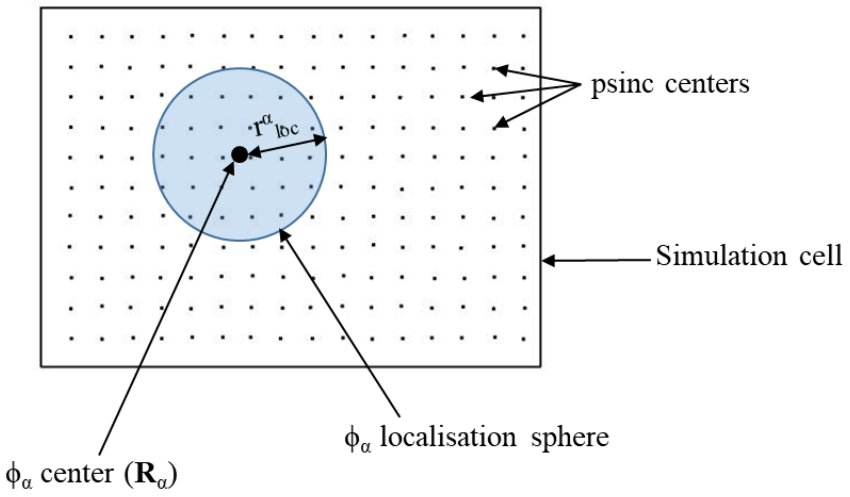

Figure 1.13: Adapted from a schematic of the ONETEP simulation cell.[114]

centred on an atom by truncating its expansion. The psinc functions are connected to plane-waves by Fourier transform. Due to this, it can be said that ONETEP is a linear scaling formalism of the plane-wave pseudopotential DFT approach (see section 1.7.5). Analogously to E_{cut} in the plane wave method, the grid spacing of the psinc basis set can be reduced, causing a variational increase in calculation accuracy.

Whilst this method is in precise agreement with plane-wave methods when studying occupied states, unoccupied states may have significant error. One way of solving this, proposed by Ratcliff *et al.* (2011), was to optimise a second set of localised functions for the unoccupied states.[123] This method uses a second density matrix

($n^{\{c\}}(\mathbf{r},\mathbf{r}')$ and set of NGWFs (χ_β) such that:

$$n^{\{c\}}(\mathbf{r},\mathbf{r}') = \sum_{c}^{N_c} \psi_c^*(\mathbf{r})\psi_c(\mathbf{r}') = \sum_{\alpha\beta} \chi_\alpha(\mathbf{r}) K^{\{c\}\alpha\beta} \chi_\beta^*(\mathbf{r}'), \tag{1.61}$$

where $\{c\}$ denotes conduction states. The single particle density matrix for the occupied orbitals will now be referred to as $K^{\{v\}}$. These conduction states are treated in the same fashion as the occupied states and therefore computational complexity scales linearly with system size. The main limitation of this NGWF representation is that the localised functions often do not form an accurate representation of high energy delocalised and unbound conduction states.[124]

In order to perform linear scaling TDDFT, analogously to in section 1.7.6, we must first define a first order response density $n^{\{1\}}(\mathbf{r})$ associated with eigenvector $\mathbf{X}$ such that:

$$\begin{aligned} n^{\{1\}}(\mathbf{r}) &= \sum_{c,v} \psi_c(\mathbf{r}) X_{c,v} \psi_v(\mathbf{r}) \\ &= \sum_{c,v} \chi_\alpha(\mathbf{r}) K^{\{1\}\alpha\beta} \phi_\beta(\mathbf{r}). \end{aligned} \tag{1.62}$$

For this, we employ the Tamm-Dancoff approximation. We note that $K^{\{1\}}$ is a representation of X in mixed occupied/unoccupied space. The matrix-vector product $\mathbf{f} = \mathbf{AX}$ can the be constructed in the NGWF space as:

$$\mathbf{f}^{\chi\phi} = K^{\{c\}} H^{\chi} K^{\{1\}} - K^{\{1\}} H^{\phi} K^{\{v\}} + K^{\{c\}} (V^{\{1\}\chi\phi}[K^{\{1\}}]) K^{\{v\}}. \tag{1.63}$$

Here, H^χ and H^ϕ denote the ground-state Kohn-Sham Hamiltonian in the χ_α and ϕ_β representations respectively. $V^{\{I\}\chi\phi}[K^{\{1\}}]$ is the self consistent field response of the system to perturbation $n^{\{1\}}(\mathbf{r})$ in the ground state density. The lowest excited state energy can be written as:

$$\omega_{\min} = \frac{\mathrm{Tr}[K^{\{1\}} S^\chi f^{\chi\phi} S^\phi]}{\mathrm{Tr}[K^{\{1\}} S^\chi K^{\{1\}} S^\phi]}, \tag{1.64}$$

where S^χ and S^ϕ denote the overlap matrices of χ_α and ϕ_β respectively. Higher excited states can be obtained using the same variational principle by enforcing an orthogonality constraint between all excited states.[125] Similarly to in ground-state linear scaling DFT, as $K^{\{c\}}$, $K^{\{v\}}$, and $K^{\{1\}}$ can be made to be sparse for sufficiently large system size [123], the calculation of $\omega_{\min}$ scales as $O(N)$ with respect to system size.

1.7.8 Calculation of Vibronic Properties

In the second presented paper (Turner *et al.*, *J. Chem. Phys.* 2019), we calculate the vibrational modes associated with catechol in solution and compare them to results from infrared spectroscopy. The method we followed was similar to that used by a related paper on the subject by Grieco *et al.*[20] and involved carrying out a well-converged

geometry optimization followed by a frequency calculation using density functional theory. It is therefore important at this stage to briefly discuss how density functional theory calculates vibrational frequencies. A longer exploration of the field of frequency calculations can be found at references [126, 127]. First we define a set of N atoms and write there coordinates as a a single vector $\mathbf{r}$ with $3N$ components. If we consider $\mathbf{r}_0$ as a local minimum we can define the distance from that as $\mathbf{x} = \mathbf{r}_0 - \mathbf{r}$. The Taylor expansion of the energy is (to second order):

$$E = E_0 + \frac{1}{2}\sum_{i=1}^{3N}\sum_{j=1}^{3N}\left[\frac{\partial^2 E}{\partial x_i \partial x_j}\right]_{x=0} x_i x_j. \tag{1.65}$$

Because this is evaluated at an energy minimum, all terms with first order differentials go to zero, and we can define a $3N \times 3N$ Hessian matrix[127]:

$$H_{i,j} = \left[\frac{\partial^2 E}{\partial x_i \partial x_j}\right]_{\mathbf{x}=0} \tag{1.66}$$

From this, we can now derive an equation of motion for the classical dynamics of atoms. This is done by writing down the force associated with the ith coordinate, F_i:

$$F_i = m_i\left(\frac{d^2 x_i}{dt^2}\right) = \frac{-\partial E}{\partial x_i} \tag{1.67}$$

In matrix form the equations that we obtain from this are:

$$\frac{d^2\mathbf{x}}{dt^2} = -\mathbf{A}\mathbf{x}, \tag{1.68}$$

where the elements of matrix $\mathbf{A}$ are $A_{ij} = H_{ij}/m_i$. This is known as the mass weighted-Hessian matrix. These equations of motion have a set of solutions associated with the eigenvectors of $\mathbf{A}$. The given eigenvectors of this matrix are the vectors $\mathbf{e}$ that satisfy the equation:

$$\mathbf{A}\mathbf{e} = \lambda\mathbf{e} \tag{1.69}$$

Given the initial conditions $\mathbf{x}(t = 0) = a\mathbf{e}$ for a given arbitrary constant a and $d\mathbf{x}(t = 0)/dt = 0$, we can define

$$\mathbf{x}(t) = a\cos(\omega t)\mathbf{e} \text{ where } \omega = \sqrt{\lambda} \tag{1.70}$$

These solutions are known as "normal modes". The general solution of these equations of motion can be written in terms of a linear combination of these normal modes. One way to determine a full set of normal modes in DFT is to use the finite differences to calculate the force constant matrix. This method is computationally expensive and inefficient on a larger scale. Instead, one can use a linear response methodology based on the calculated forces within density functional theory. Full details on this method were expressed by Wong *et al.* (1996).[126]

Either way, the mass weighted Hessian matrix can be calculated, $\mathbf{A}$, and this is used to calculate the eigenvalues and eigenvectors of the forces using equation 1.69 and

the normal modes using equation 1.70. It is worth noting that for frequency calculations it is imperative to use the same level of theory on the geometry optimization as the frequency calculation as the normal mode calculation will not give meaningful results if not initiated from a well-converged local minimum.

1.8 Introduction to Molecular Dynamics Techniques Used In This Thesis

In both the first presented paper (Turner *et al.*, *J. Phys. Chem A.* 2019) and the second presented paper (Turner *et al.*, *J. Chem. Phys.* 2019) molecular dynamics is used to set up explicit-solvent environments. These environments are later examined with TDDFT to predict UV-Vis and FTIR spectra. This section will briefly address the molecular dynamics techniques used in order to provide sufficient background for the calculations conducted. A more thorough discussion of molecular dynamics can be found within references [128, 129, 130].

Molecular dynamics is a method for simulating the movement of atoms. The interactions of these atoms are determined numerically by solving Newton's equations of motion for a system of interacting particles. The forces between these particles and their potential energies are calculated using molecular dynamics forcefields. In this work, we perform molecular dynamics calculations with the AMBER package with the generalized Amber forcefield (GAFF).[131, 132] Force field parameters for molecular species were generated using the antechamber tool.[133] Temperature is a key consideration when aiming to mimic a realistic system. Where appropriate, temperature is controlled with a Langevin thermostat.[134] A Langevin thermostat attempts to model the effect of moving solvent molecules, thus accounting for friction and the occasional high velocity collision. Langevin dynamics mimic the viscous aspect of a solvent, whilst not accounting for electrostatic or hydrophobic effects. This is key when generating snapshots of explicit-solvent for accurately equilibrating systems.

The standard process is to take an optimized solute geometry and to place it in a bath of solvent molecules. This system then undergoes heating and equilibration to create a realistic starting system. Finally, this system is observed at constant temperature for a set period of time to obtain "trajectories". Further information on the parameters used for each calculation are discussed in the individual papers. One will often conduct two different types of molecular dynamics run. The first is a thermal equilibration with an NVT ensemble, this equilibrates the system while keeping number of molecules (N), volume (V), and temperature (T) constant. The second type of equilibration is a density equilibration, which uses an NPT ensemble. This ensures the density of the system is treated correctly by fixing number of molecules, pressure, and temperature and letting volume vary.[129] In the first presented paper (Turner *et al.*, *J. Phys. Chem A.* 2019) a pre-equilibrated box of methanol is utilized as the solvent, therefore the density equilibration step was not necessary. A density equilibration was conducted for the second presented paper (Turner *et al.*, *J. Chem. Phys.* 2019),

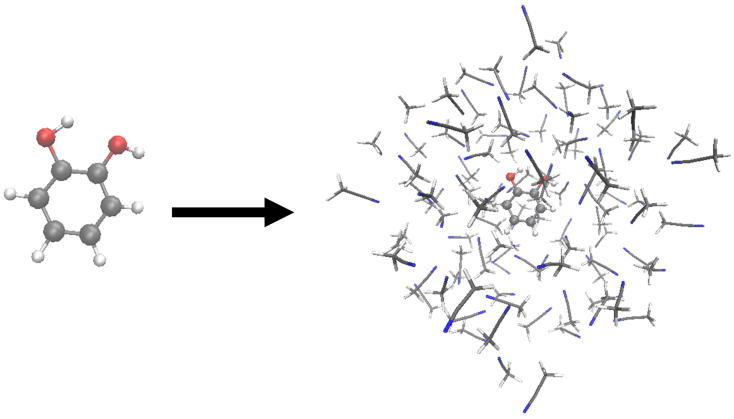

Figure 1.14: This figure shows the act of explicit solvation. In this case, a catechol molecule is solvated in acetonitrile.

however. It is key to generate a set of statically uncorrelated snapshots to create a "fair" sample of the different configurations possible in the system. A statistically correlated trajectory can lead to biased sampling and an unrealistic distribution of structures.

1.9 Explicit-Solvent Calculations

In this thesis solvation is often modelled *explicitly*, see figure 1.14. This is to say that, solvent molecules are explicitly present in the calculation, rather than just being represented by a polarizable continuum with a given dielectric constant. This allows for the modelling of non-electrostatic interactions such as hydrogen bonding and π-stacking. The downside to this is that it greatly increases computational expense. In this section we discuss the methodology by which one can combine molecular dynamics simulations and linear-scaling TDDFT in order to conduct explicit-solvent calculations.

In the past, a highly popular approach to conducting explicit-solvent calculations was to use a mixed quantum mechanics/classical mechanics method (QM/MM). This gave a good compromise between computational cost and accuracy. In this method, chromophores are treated on a quantum mechanical level with long range electronic screening provided at a classical level.[135, 136, 137] While this approach has been widely used in the literature[138, 139, 140] more recent studies have shown that, in some circumstances, this technique is insufficient.[141, 142] Specifically, it appeared that the explicit inclusion of large parts of the solvent in the QM description was necessary when calculating long-range electrostatic effects. It was shown in 2016, in a paper that was a key influence to the first presented paper (Turner *et al.*, *J. Phys. Chem A.* 2019), that to converge the solvatochromic shift of alizarin in water one must treat a significantly larger solvated system quantum mechanically.[143] These calculations were facilitated using the linearly-scaling TDDFT methodology discussed in section 1.7.7.

To further reduce the computational expenditure of these methods one can use a technique known as spectral warping. This technique, pioneered by Ge *et al.* [144], involves utilizing the fact that it is not necessary to employ as expensive a level of

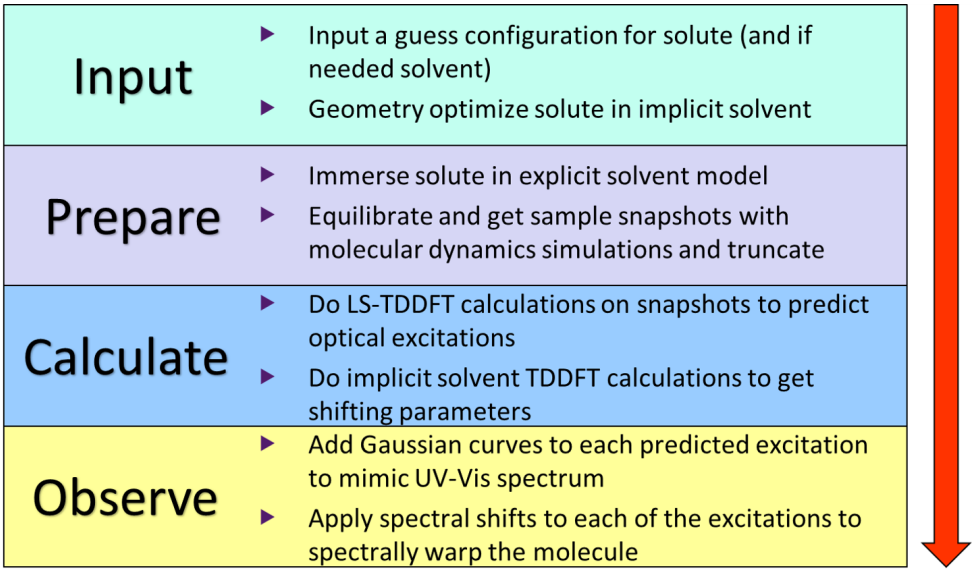

Figure 1.15: A flow chart showing the methodology behind generating a predicted UV-Vis spectrum using explicit-solvent linear-scaling TDDFT

theory on the solvent as the solute. First, one conducts a calculation using a high level of theory on the molecule in implicit-solvent, normally using an expensive basis set and functional. Next, one conducts a calculation on the same system using a computationally less-expensive methodology, but still one which one believes produces a result whose relationship with that of the expensive methodology is predictable (eg a constant energy offset). Following this, warping parameters are established which map the cheap calculation onto the more expensive one. Next, calculations using the cheaper level of theory are conducted on an explicit solvent cluster model, with an implicit solvent model beyond the cluster, to screen surface charge on the edge of the explicit cluster. Finally, the previously-calculated warping factor is applied to the cheaper explicit-solvent calculation to mimic the effect of using a more expensive level of theory on the explicit-solvent model. Zuehlsdorff *et al.* used this method to produce accurate UV-Vis spectra for the dye molecule nile red.[137] For this, they generated spectra for 50 different snapshots, convolved each excitation with a Gaussian curve of broadness 0.1 eV, and averaged them together. This methodology is used in the first presented paper (Turner *et al.*, *J. Phys. Chem A.* 2019) and is expressed by the flow chart in figure 1.15.

The final aspect of these calculations to discuss are the empirical scaling factors used in the first and second presented papers. In the first presented paper a constant energy offset is used to correct electronic excitations. This is utilized because the common issue experienced with calculating electronic excitations in TDDFT is an incorrect treatment of the band gap, see section 1.7.4 and reference [84]. Ideally, an accurate calculation would not require this offset, as the expensive functional would be sufficiently accurate without further correction. In the first presented paper PBE0 and B3LYP only require relatively small offsets of 0.15 and 0.03 eV respectively to reproduce experimental spectra. The range-separated hybrids required significantly larger offsets which, whilst surprising, was in line with previous literature indicating

specific weaknesses in these functionals for similar systems.[2, 3, 4, 145]

In the second presented paper, infrared spectra are predicted. In this case the primary error arising from the approximations of DFT is the incorrect curvature of the energy surface. It has been shown previously that multiplicative scaling factors can account for and correct this.[20, 146] However, if these scaling factors were significantly different from 1.0, less confidence would be inspired in the quality of the result. In these previous papers, scaling factors between 0.95 and 1.05 are utilised, by calibrating the scaling factor for a given level of theory using known results for similar systems to those being studied. In the second presented paper, scaling factors were within this range for the explicit-solvent results, but by contrast were significantly out of this range for the implicit solvent results, further adding evidence for the necessity of explicit solvent.

With these calculation methods now mapped out, in the coming chapters I will be using these methods along with the experimental methods discussed previously, to solve problems relevant to photochemical systems.

Bibliography

1. Holt, E. L. & Stavros, V. G. Applications of ultrafast spectroscopy to sunscreen development, from first principles to complex mixtures. *International Reviews in Physical Chemistry* **38,** 243–285 (2019).
2. Serpone, N., Dondi, D. & Albini, A. Inorganic and organic UV filters: Their role and efficacy in sunscreens and suncare products. *Inorganica chimica acta* **360,** 794–802 (2007).
3. Antoniou, C., Kosmadaki, M. G., Stratigos, A. J. & Katsambas, A. D. Sunscreens–what's important to know. *Journal of the European academy of dermatology and venereology* **22,** 1110–1119 (2008).
4. Horbury, M. D. *Probing the Photodynamics of Photoprotective Molecules and Two-photon Activated Metal Complexes* PhD thesis (2016).
5. Rodrigues, N. D. & Stavros, V. G. From fundamental science to product: a bottom-up approach to sunscreen development. *Science progress* **101,** 8–31 (2018).
6. Horbury, M., Flourat, A., Greenough, S., Allais, F & Stavros, V. Investigating isomer specific photoprotection in a model plant sunscreen. *Chemical communications* **54,** 936–939 (2018).
7. Stavros, V. G. Photochemistry: A bright future for sunscreens. *Nature chemistry* **6,** 955 (2014).
8. Baker, L. A., Horbury, M. D., Greenough, S. E., Coulter, P. M., Karsili, T. N., Roberts, G. M., Orr-Ewing, A. J., Ashfold, M. N. & Stavros, V. G. Probing the ultrafast energy dissipation mechanism of the sunscreen oxybenzone after UVA irradiation. *The journal of physical chemistry letters* **6,** 1363–1368 (2015).
9. Agrapidis-Paloympis, L. E., Nash, R. A. & Shaath, N. The effect of solvents on the ultraviolet absorbance of sunscreens. *J Soc Cosmet Chem* **38,** 209–221 (1987).
10. Beyere, L, Yarasi, S & Loppnow, G. Solvent effects on sunscreen active ingredients using Raman spectroscopy. *Journal of Raman Spectroscopy* **34,** 743–750 (2003).
11. Beyere, L, Yarasi, S & Loppnow, G. Solvent effects on sunscreen active ingredients using Raman spectroscopy. *Journal of Raman Spectroscopy* **34,** 743–750 (2003).

12. Benazzouz, A., Moity, L., Pierlot, C., Molinier, V. & Aubry, J.-M. Hansen approach versus COSMO-RS for predicting the solubility of an organic UV filter in cosmetic solvents. *Colloids and Surfaces A: Physicochemical and Engineering Aspects* **458,** 101–109 (2014).

13. Palm, M. D. & O'Donoghue, M. N. Update on photoprotection. *Dermatologic Therapy* **20,** 360–376 (2007).

14. Hexsel, C. L. & Lim, H. W. in *Preventive Dermatology* 81–91 (Springer, 2011).

15. Lowe, N. An overview of ultraviolet radiation, sunscreens, and photo-induced dermatoses. *Dermatologic clinics* **24,** 9–17 (2006).

16. Sambandan, D. R. & Ratner, D. Sunscreens: an overview and update. *Journal of the American Academy of Dermatology* **64,** 748–758 (2011).

17. Couteau, C., Faure, A., Fortin, J., Paparis, E. & Coiffard, L. J. Study of the photostability of 18 sunscreens in creams by measuring the SPF in vitro. *Journal of pharmaceutical and biomedical analysis* **44,** 270–273 (2007).

18. Wang, S. Q., Lim, H. W. *et al. Principles and practice of photoprotection* (2016).

19. Woolley, J. M., Staniforth, M., Horbury, M. D., Richings, G. W., Wills, M. & Stavros, V. G. Unravelling the Photoprotection Properties of Mycosporine Amino Acid Motifs. *The journal of physical chemistry letters* **9,** 3043–3048 (2018).

20. Grieco, C., Kohl, F. R., Zhang, Y., Natarajan, S., Blancafort, L. & Kohler, B. Intermolecular Hydrogen Bonding Modulates O-H Photodissociation in Molecular Aggregates of a Catechol Derivative. *Photochemistry and photobiology* (2018).

21. Sparavigna, A. C. The play of colours of prisms. arXiv: 1207.3504 (2012).

22. Hine, H. Rome, the Cosmos, and the Emperor in Seneca's Natural Questions*. *cambridge.org.* https://www.cambridge.org/core/journals/journal-of-roman-studies/article/rome-the-cosmos-and-the-emperor-in-senecas-natural-questions/5C05B974D491F2663B8B12E551162917.

23. Sparavigna, A. C. Materials Science in Ancient Rome. arXiv: 1107.3831. http://arxiv.org/abs/1107.3831 (2011).

24. Ring, E. The discovery of infrared radiation in 1800. *The Imaging Science Journal* **48,** 1–8 (2000).

25. Ritter, J. W. Kurze Mitteilung uber die Endeckung der Uv-Strahlen. *Ann. Phys* **7,** 527 (1801).

26. Slavnov, D. A. The wave-particle duality. *Physics of Particles and Nuclei* **46,** 665–677. ISSN: 1531-8559. https://doi.org/10.1134/S106377961504005X (2015).

27. Einstein, A., Podolsky, B. & Rosen, N. Can Quantum-Mechanical Description of Physical Reality Be Considered Complete? *Phys. Rev.* **47,** 777–780. https://link.aps.org/doi/10.1103/PhysRev.47.777 (10 1935).

28. Bouguer, P. *Essai d'optique sur la gradation de la lumière* (chez Claude Jombert ruë S. Jacques au coin de la ruë des Mathurins à l ..., 1729).

29. Lambert, J.-H. *Photometria, sive de Mensura et gradibus luminis, colorum et umbrae* (sumptibus viduae E. Klett, 1760).

30. Beer, A. Bestimmung der absorption des rothen lichts in farbigen flussigkeiten. *Ann. Physik* **162,** 78–88 (1852).

31. Förster, T. Diabatic and adiabatic processes in photochemistry. *Pure and Applied Chemistry* **24,** 443–450 (1970).

32. Young, J. D., Staniforth, M., Dean, J. C., Roberts, G. M., Mazzoni, F., Karsili, T. N., Ashfold, M. N., Zwier, T. S. & Stavros, V. G. Towards understanding photodegradation pathways in lignins: The role of intramolecular hydrogen bonding in excited states. *The journal of physical chemistry letters* **5,** 2138–2143 (2014).

33. Sengupta, A, Mandal, K. & Zhang, J. Ultrafast electronic relaxation dynamics in layered iodide semiconductors: a comparative study of colloidal BiI3 and PbI2 nanoparticles. *The Journal of Physical Chemistry B* **104,** 9396–9403 (2000).

34. Alfano, R., Demos, S., Galland, P, Gayen, S., Guo, Y., Ho, P., Liang, X, Liu, F, Wang, L, Wang, Q. *et al.* Time-Resolved and Nonlinear Optical Imaging for Medical Applications a. *Annals of the New York Academy of Sciences* **838,** 14–28 (1998).

35. Lubatschowski, H., Heisterkamp, A., Will, F., Serbin, J., Bauer, T., Fallnich, C., Welling, H., Mueller, W., Schwab, B., Singh, A. I. *et al. Ultrafast laser pulses for medical applications* in *Commercial and Biomedical Applications of Ultrafast and Free-Electron Lasers* **4633** (2002), 38–49.

36. Paracchino, A., Brauer, J. C., Moser, J.-E., Thimsen, E. & Graetzel, M. Synthesis and characterization of high-photoactivity electrodeposited Cu2O solar absorber by photoelectrochemistry and ultrafast spectroscopy. *The Journal of Physical Chemistry C* **116,** 7341–7350 (2012).

37. Ponseca Jr, C. S., Savenije, T. J., Abdellah, M., Zheng, K., Yartsev, A., Pascher, T., Harlang, T., Chabera, P., Pullerits, T., Stepanov, A. *et al.* Organometal halide perovskite solar cell materials rationalized: ultrafast charge generation, high and microsecond-long balanced mobilities, and slow recombination. *Journal of the American Chemical Society* **136,** 5189–5192 (2014).

38. Baxter, J. B., Richter, C. & Schmuttenmaer, C. A. Ultrafast carrier dynamics in nanostructures for solar fuels. *Annual review of physical chemistry* **65,** 423–447 (2014).

39. Valeur, B. *Molecular Fluorescence Wiley* (VCH Weinheim, 2002).

40. Jablonski, A. Efficiency of anti-Stokes fluorescence in dyes. *Nature* **131,** 839 (1933).

41. Reid, K. L. Picosecond time-resolved photoelectron spectroscopy as a means of gaining insight into mechanisms of intramolecular vibrational energy redistribution in excited states. *International Reviews in Physical Chemistry* **27,** 607–628 (2008).

42. Boyall, D. & Reid, K. L. Modern studies of intramolecular vibrational energy redistribution. *Chemical society reviews* **26,** 223–232 (1997).

43. Atkins, P. W. & Friedman, R. S. *Molecular quantum mechanics* (Oxford university press, 2011).

44. Owrutsky, J., Raftery, D & Hochstrasser, R. Vibrational relaxation dynamics in solutions. *Annual review of physical chemistry* **45,** 519–555 (1994).

45. Aßmann, J., Kling, M. & Abel, B. Watching photoinduced chemistry and molecular energy flow in solution in real time. *Angewandte Chemie International Edition* **42,** 2226–2246 (2003).

46. Kasha, M. Characterization of electronic transitions in complex molecules. *Discussions of the Faraday society* **9,** 14–19 (1950).

47. Ren, T.-B., Xu, W., Zhang, W., Zhang, X.-X., Wang, Z.-Y., Xiang, Z., Yuan, L. & Zhang, X.-B. A General Method To Increase Stokes Shift by Introducing Alternating Vibronic Structures. *Journal of the American Chemical Society* **140.** PMID: 29792690, 7716–7722 (2018).

48. Bixon, M. & Jortner, J. Intramolecular radiationless transitions. *The Journal of Chemical Physics* **48,** 715–726 (1968).

49. Turro, N. J. *Modern molecular photochemistry* (University science books, 1991).

50. Domcke, W., Yarkony, D. R. & Köppel, H. *Conical intersections: theory, computation and experiment* (World Scientific, 2011).

51. Anderson, A. Y., Barnes, P. R., Durrant, J. R. & O'Regan, B. C. Simultaneous transient absorption and transient electrical measurements on operating dye-sensitized solar cells: elucidating the intermediates in iodide oxidation. *The Journal of Physical Chemistry C* **114,** 1953–1958 (2010).

52. Van Kuiken, B. E., Huse, N., Cho, H., Strader, M. L., Lynch, M. S., Schoenlein, R. W. & Khalil, M. Probing the electronic structure of a photoexcited solar cell dye with transient x-ray absorption spectroscopy. *The journal of physical chemistry letters* **3,** 1695–1700 (2012).

53. Staniforth, M., Quan, W.-D., Karsili, T. N., Baker, L. A., O'Reilly, R. K. & Stavros, V. G. First Step toward a Universal Fluorescent Probe: Unravelling the Photodynamics of an Amino–Maleimide Fluorophore. *The Journal of Physical Chemistry A* **121,** 6357–6365 (2017).

54. Ehli, C., Oelsner, C., Guldi, D. M., Mateo-Alonso, A., Prato, M., Schmidt, C., Backes, C., Hauke, F. & Hirsch, A. Manipulating single-wall carbon nanotubes by chemical doping and charge transfer with perylene dyes. *Nature Chemistry* **1,** 243 (2009).

55. Fischer, S. A., Cramer, C. J. & Govind, N. Excited state absorption from real-time time-dependent density functional theory. *Journal of chemical theory and computation* **11,** 4294–4303 (2015).

56. Shenar, N., Sommerer, N., Martinez, J. & Enjalbal, C. Comparison of LID versus CID activation modes in tandem mass spectrometry of peptides. *Journal of mass spectrometry: JMS* **44,** 621–632 (2009).

57. Moulton, P. F. Spectroscopic and laser characteristics of Ti: Al 2 O 3. *JOSA B* **3,** 125–133 (1986).

58. Brodeur, A & Chin, S. Ultrafast white-light continuum generation and self-focusing in transparent condensed media. *JOSA B* **16,** 637–650 (1999).

59. Nagura, C., Suda, A., Kawano, H., Obara, M. & Midorikawa, K. Generation and characterization of ultrafast white-light continuum in condensed media. *Applied optics* **41,** 3735–3742 (2002).

60. Johnson, P. J., Prokhorenko, V. I. & Miller, R. D. Stable UV to IR supercontinuum generation in calcium fluoride with conserved circular polarization states. *Optics express* **17,** 21488–21496 (2009).

61. Maguire, L., Szilagyi, S & Scholten, R. High performance laser shutter using a hard disk drive voice-coil actuator. *Review of Scientific Instruments* **75,** 3077–3079 (2004).

62. Runge, E. & Gross, E. K. Density-functional theory for time-dependent systems. *Physical Review Letters* **52,** 997 (1984).

63. Car, R. & Parrinello, M. Unified approach for molecular dynamics and density-functional theory. *Physical review letters* **55,** 2471 (1985).

64. Petersilka, M., Gossmann, U. & Gross, E. Excitation energies from time-dependent density-functional theory. *Physical review letters* **76,** 1212 (1996).

65. Ravindran, P, Fast, L., Korzhavyi, P. A., Johansson, B, Wills, J & Eriksson, O. Density functional theory for calculation of elastic properties of orthorhombic crystals: Application to TiSi 2. *Journal of Applied Physics* **84,** 4891–4904 (1998).

66. Kootstra, F, De Boeij, P. & Snijders, J. Application of time-dependent density-functional theory to the dielectric function of various nonmetallic crystals. *Physical Review B* **62,** 7071 (2000).

67. Lejaeghere, K., Van Speybroeck, V., Van Oost, G. & Cottenier, S. Error estimates for solid-state density-functional theory predictions: an overview by means of the ground-state elemental crystals. *Critical Reviews in Solid State and Materials Sciences* **39,** 1–24 (2014).

68. Cramer, C. J. & Truhlar, D. G. Density functional theory for transition metals and transition metal chemistry. *Physical Chemistry Chemical Physics* **11,** 10757–10816 (2009).

69. Meng, S., Wang, E.-G. & Gao, S. Water adsorption on metal surfaces: A general picture from density functional theory studies. *Physical Review B* **69,** 195404 (2004).

70. Siegbahn, P. E. & Blomberg, M. R. Density functional theory of biologically relevant metal centers. *Annual review of physical chemistry* **50,** 221–249 (1999).

71. Stahl, F., von Ragué Schleyer, P., Bettinger, H., Kaiser, R., Lee, Y. & Schaefer III, H. Reaction of the ethynyl radical, C 2 H, with methylacetylene, CH 3 CCH, under single collision conditions: Implications for astrochemistry. *The Journal of Chemical Physics* **114,** 3476–3487 (2001).

72. Barone, V., Biczysko, M. & Puzzarini, C. Quantum chemistry meets spectroscopy for astrochemistry: Increasing complexity toward prebiotic molecules. *Accounts of chemical research* **48,** 1413–1422 (2015).

73. Hohenberg, P & Kohn, W. *Phys. Rev. B* **136,** 864–871 (1964).

74. Peskin, M. & Schroeder, D. *An Introduction to Quantum Field Theory* 52–58. ISBN: 9780201503975. `https://books.google.co.uk/books?id=i35LALN0GosC` (Avalon Publishing, 1995).

75. McQuarrie, D., Simon, J., Cox, H. & Choi, J. *Physical Chemistry: A Molecular Approach* ISBN: 9780935702996. `https://books.google.co.uk/books?id=f-bje0-DEYUC` (University Science Books, 1997).

76. Löwdin, P.-O. Expansion theorems for the total wave function and extended Hartree-Fock schemes. *Reviews of Modern Physics* **32,** 328 (1960).

77. Perdew, J. P. & Schmidt, K. *Jacob's ladder of density functional approximations for the exchange-correlation energy* in *AIP Conference Proceedings* **577** (2001), 1–20.

78. Casida, M. E. in (ACS Publications, 2002).

79. Casida, M. E. & Huix-Rotllant, M. Progress in time-dependent density-functional theory. *Annual review of physical chemistry* **63,** 287–323 (2012).

80. Parr, R. G. & Yang, W. *Density-functional theory of atoms and molecules* 152–156 (Oxford University Press, 1994).

81. Parr, R. G. & Yang, W. *Density-functional theory of atoms and molecules* 108–109 (Oxford University Press, 1994).

82. Ceperley, D. M. & Alder, B. Ground state of the electron gas by a stochastic method. *Physical Review Letters* **45,** 566 (1980).

83. Langreth, D. C. & Mehl, M. Beyond the local-density approximation in calculations of ground-state electronic properties. *Physical Review B* **28,** 1809 (1983).

84. Becke, A. D. Perspective: Fifty years of density-functional theory in chemical physics. *The Journal of chemical physics* **140,** 18A301 (2014).

85. Becke, A. D. Density-functional exchange-energy approximation with correct asymptotic behavior. *Physical review A* **38,** 3098 (1988).

86. Perdew, J. P., Chevary, J. A., Vosko, S. H., Jackson, K. A., Pederson, M. R., Singh, D. J. & Fiolhais, C. Atoms, molecules, solids, and surfaces: Applications of the generalized gradient approximation for exchange and correlation. *Physical review B* **46,** 6671 (1992).

87. Jambrina, P. & Aldegunde, J. in *Tools For Chemical Product Design* (eds Martín, M., Eden, M. R. & Chemmangattuvalappil, N. G.) 583 –648 (Elsevier, 2016). `http://www.sciencedirect.com/science/article/pii/B9780444636836000204`.

88. Lee, C., Yang, W. & Parr, R. G. Development of the Colle-Salvetti correlation-energy formula into a functional of the electron density. *Physical review B* **37,** 785 (1988).

89. Perdew, J. P., Burke, K. & Ernzerhof, M. Generalized gradient approximation made simple. *Phys. Rev. Lett.* **77,** 3865 (1996).

90. Adamo, C. & Barone, V. Toward reliable density functional methods without adjustable parameters: The PBE0 model. *J. Chem. Phys.* **110,** 6158–6170 (1999).

91. Becke, A. D. Density-functional thermochemistry. III. The role of exact exchange. *jcp* **98,** 5648–5652 (Apr. 1993).

92. Yanai, T., Tew, D. P. & Handy, N. C. A new hybrid exchange–correlation functional using the Coulomb-attenuating method (CAM-B3LYP). *Chem. Phys. Lett.* **393,** 51–57 (2004).

93. Rohrdanz, M. A. & Herbert, J. M. Simultaneous benchmarking of ground-and excited-state properties with long-range-corrected density functional theory. *The Journal of chemical physics* **129,** 034107 (2008).

94. Perdew, J. P., Ernzerhof, M. & Burke, K. Rationale for mixing exact exchange with density functional approximations. *The Journal of chemical physics* **105,** 9982–9985 (1996).

95. Stephens, P. J., Devlin, F., Chabalowski, C. & Frisch, M. J. Ab initio calculation of vibrational absorption and circular dichroism spectra using density functional force fields. *The Journal of physical chemistry* **98,** 11623–11627 (1994).

96. Perpète, E. A., Jacquemin, D., Adamo, C. & Scuseria, G. E. Revisiting the nonlinear optical properties of polybutatriene and polydiacetylene with density functional theory. *Chemical Physics Letters* **456,** 101–104 (2008).

97. Tawada, Y., Tsuneda, T., Yanagisawa, S., Yanai, T. & Hirao, K. A long-range-corrected time-dependent density functional theory. *The Journal of chemical physics* **120,** 8425–8433 (2004).

98. Perdew, J. P. & Zunger, A. Self-interaction correction to density-functional approximations for many-electron systems. *Physical Review B* **23,** 5048 (1981).

99. Jiménez-Hoyos, C. A., Janesko, B. G. & Scuseria, G. E. Evaluation of range-separated hybrid density functionals for the prediction of vibrational frequencies, infrared intensities, and Raman activities. *Physical Chemistry Chemical Physics* **10,** 6621–6629 (2008).

100. Della Sala, F. & Görling, A. Asymptotic behavior of the Kohn-Sham exchange potential. *Physical review letters* **89,** 033003 (2002).

101. Almbladh, C.-O. & von Barth, U. Exact results for the charge and spin densities, exchange-correlation potentials, and density-functional eigenvalues. *Physical Review B* **31,** 3231 (1985).

102. Savin, A. Recent Developments and Applications of Modern Density Functional Theory edited by JM Seminario Elsevier. *New York,* 327 (1996).

103. Leininger, T., Stoll, H., Werner, H.-J. & Savin, A. Combining long-range configuration interaction with short-range density functionals. *Chemical physics letters* **275,** 151–160 (1997).

104. Iikura, H., Tsuneda, T., Yanai, T. & Hirao, K. A long-range correction scheme for generalized-gradient-approximation exchange functionals. *The Journal of Chemical Physics* **115,** 3540–3544 (2001).

105. Gerber, I. C. & Angyán, J. G. Hybrid functional with separated range. *Chemical physics letters* **415,** 100–105 (2005).

106. Parrill, A. L. & Lipkowitz, K. B. *Reviews in computational chemistry, Volume 30* 93–145 (NJ).

107. Gross, E. & Kohn, W. in *Advances in quantum chemistry* 255–291 (Elsevier, 1990).

108. Casida, M. E. in *Recent Advances In Density Functional Methods: (Part I)* 155–192 (World Scientific, 1995).

109. Casida, M. E., Jamorski, C., Casida, K. C. & Salahub, D. R. Molecular excitation energies to high-lying bound states from time-dependent density-functional response theory: Characterization and correction of the time-dependent local density approximation ionization threshold. *The Journal of chemical physics* **108,** 4439–4449 (1998).

110. Cvitanovic, P. & Kinoshita, T. Feynman-Dyson rules in parametric space. *Physical Review D* **10,** 3978 (1974).

111. Bauernschmitt, R. & Ahlrichs, R. Treatment of electronic excitations within the adiabatic approximation of time dependent density functional theory. *Chemical Physics Letters* **256,** 454–464 (1996).

112. Galli, G. Linear scaling methods for electronic structure calculations and quantum molecular dynamics simulations. *Current Opinion in Solid State and Materials Science* **1,** 864–874 (1996).

113. Goedecker, S. Linear scaling electronic structure methods. *Reviews of Modern Physics* **71,** 1085 (1999).

114. Skylaris, C.-K., Haynes, P. D., Mostofi, A. A. & Payne, M. C. Introducing ONETEP: Linear-scaling density functional simulations on parallel computers. *The Journal of chemical physics* **122,** 084119 (2005).

115. Baer, R. & Head-Gordon, M. Sparsity of the density matrix in Kohn-Sham density functional theory and an assessment of linear system-size scaling methods. *Physical review letters* **79,** 3962 (1997).

116. Ismail-Beigi, S. & Arias, T. A. Locality of the density matrix in metals, semiconductors, and insulators. *Physical review letters* **82,** 2127 (1999).

117. He, L. & Vanderbilt, D. Exponential decay properties of Wannier functions and related quantities. *Physical Review Letters* **86,** 5341 (2001).

118. Li, X.-P., Nunes, R. & Vanderbilt, D. Density-matrix electronic-structure method with linear system-size scaling. *Physical Review B* **47,** 10891 (1993).

119. McWeeny, R. Some recent advances in density matrix theory. *Reviews of Modern Physics* **32,** 335 (1960).

120. Skylaris, C.-K., Mostofi, A. A., Haynes, P. D., Pickard, C. J. & Payne, M. C. Accurate kinetic energy evaluation in electronic structure calculations with localized functions on real space grids. *Computer physics communications* **140,** 315–322 (2001).

121. Mostofi, A. A., Haynes, P. D., Skylaris, C.-K. & Payne, M. C. Preconditioned iterative minimization for linear-scaling electronic structure calculations. *The Journal of chemical physics* **119,** 8842–8848 (2003).

122. Mostofi, A. A., Haynes, P. D., Skylaris, C.-K. & Payne, M. C. ONETEP: linear-scaling density-functional theory with plane-waves. *Molecular Simulation* **33,** 551–555 (2007).

123. Ratcliff, L. E., Hine, N. D. & Haynes, P. D. Calculating optical absorption spectra for large systems using linear-scaling density functional theory. *Physical Review B* **84,** 165131 (2011).

124. Zuehlsdorff, T. J., Hine, N. D., Spencer, J. S., Harrison, N. M., Riley, D. J. & Haynes, P. D. Linear-scaling time-dependent density-functional theory in the linear response formalism. *The Journal of chemical physics* **139,** 064104 (2013).

125. Zuehlsdorff, T. J., Hine, N., Payne, M. C. & Haynes, P. Linear-scaling time-dependent density-functional theory beyond the Tamm-Dancoff approximation: obtaining efficiency and accuracy with in situ optimised local orbitals. *The Journal of chemical physics* **143,** 204107 (2015).

126. Wong, M. W. Vibrational frequency prediction using density functional theory. *Chemical Physics Letters* **256,** 391–399 (1996).

127. Sholl, D. S. & Steckel, J. A. *Density functional theory: a practical introduction* (John Wiley & Sons, 2009).

128. Paquet, E. & Viktor, H. L. Molecular dynamics, monte carlo simulations, and langevin dynamics: a computational review. *BioMed research international* **2015** (2015).

129. Rapaport, D. C. *The art of molecular dynamics simulation* (Cambridge University Press, 2010).

130. Satoh, A. *Introduction to practice of molecular simulation* (Elsevier, 2011).

131. Case, D. A., Berryman, J. T., Betz, R. M., Cerutti, D. S., Cheatham III, T. E., Darden, T. A., Duke, R. E., Giese, T. J., Gohlke, H, Goetz, A. W., Homeyer, N, Izadi, S, Janowski, P, Kaus, J, Kovalenko, A, Lee, T. S., LeGrand, S, Li, P, Luchko, T, Luo, R, Madej, B, Merz, K. M., Monard, G, Needham, P, Nguyen, H, Nguyen, H. T., Omelyan, I, Onufriev, A, Roe, D. R., Roitberg, A, Salomon-Ferrer, R, Simmerling, C. L., Smith, W, Swails, J, Walker, R. C., Wang, J, Wolf, R. M., Wu, X, York, D. M. & Kollman, P. A. AMBER 2015, University of California, San Francisco (2015).

132. Wang, J., Wolf, R. M., Caldwell, J. W., Kollman, P. A. & Case, D. A. Development and testing of a general amber force field. *J. Comput. Chem.* **25,** 1157–1174 (2004).

133. Wang, J., Wang, W., Kollman, P. A. & Case, D. A. Automatic atom type and bond type perception in molecular mechanical calculations. *J. Mol. Graph.* **25,** 247–260 (2006).

134. Kremer, K. & Grest, G. S. Dynamics of entangled linear polymer melts: A molecular-dynamics simulation. *The Journal of Chemical Physics* **92,** 5057–5086 (1990).

135. Lin, H. & Truhlar, D. G. QM/MM: what have we learned, where are we, and where do we go from here? *Theoretical Chemistry Accounts* **117,** 185 (2007).

136. Warshel, A. & Levitt, M. Theoretical studies of enzymic reactions: dielectric, electrostatic and steric stabilization of the carbonium ion in the reaction of lysozyme. *Journal of molecular biology* **103,** 227–249 (1976).

137. Zuehlsdorff, T., Haynes, P., Payne, M. & Hine, N. Predicting solvatochromic shifts and colours of a solvated organic dye: The example of nile red. *The Journal of Chemical Physics* **146,** 124504 (2017).

138. Houjou, H., Inoue, Y. & Sakurai, M. Study of the opsin shift of bacteriorhodopsin: Insight from QM/MM calculations with electronic polarization effects of the protein environment. *The Journal of Physical Chemistry B* **105,** 867–879 (2001).

139. Altun, A., Yokoyama, S. & Morokuma, K. Spectral tuning in visual pigments: an ONIOM (QM: MM) study on bovine rhodopsin and its mutants. *The Journal of Physical Chemistry B* **112,** 6814–6827 (2008).

140. Gao, J., Shi, W.-J., Ye, J., Wang, X., Hirao, H. & Zhao, Y. QM/MM modeling of environmental effects on electronic transitions of the FMO complex. *The Journal of Physical Chemistry B* **117,** 3488–3495 (2013).

141. Murugan, N. A., Jha, P. C., Rinkevicius, Z, Ruud, K. & Ågren, H. Solvatochromic shift of phenol blue in water from a combined Car–Parrinello molecular dynamics hybrid quantum mechanics-molecular mechanics and ZINDO approach. *The Journal of chemical physics* **132,** 234508 (2010).

142. Isborn, C. M., Mar, B. D., Curchod, B. F., Tavernelli, I. & Martinez, T. J. The charge transfer problem in density functional theory calculations of aqueously solvated molecules. *The Journal of Physical Chemistry B* **117,** 12189–12201 (2013).

143. Zuehlsdorff, T., Haynes, P. D., Hanke, F., Payne, M. & Hine, N. D. Solvent effects on electronic excitations of an organic chromophore. *Journal of Chemical Theory and Computation* **12,** 1853–1861 (2016).

144. Ge, X., Timrov, I., Binnie, S., Biancardi, A., Calzolari, A. & Baroni, S. Accurate and inexpensive prediction of the color optical properties of anthocyanins in solution. *The Journal of Physical Chemistry A* **119,** 3816–3822 (2015).

145. Douma, D. H., M'Passi-Mabiala, B. & Gebauer, R. Optical properties of an organic dye from time-dependent density functional theory with explicit solvent: The case of alizarin. *J. Chem. Phys.* **137,** 154314 (2012).

146. Halls, M. D. & Schlegel, H. B. Comparison of the performance of local, gradient-corrected, and hybrid density functional models in predicting infrared intensities. *The Journal of chemical physics* **109,** 10587–10593 (1998).

Chapter 2

Determination of Secondary Species in Solution through Pump-Selective Transient Absorption Spectroscopy and Explicit-Solvent TDDFT

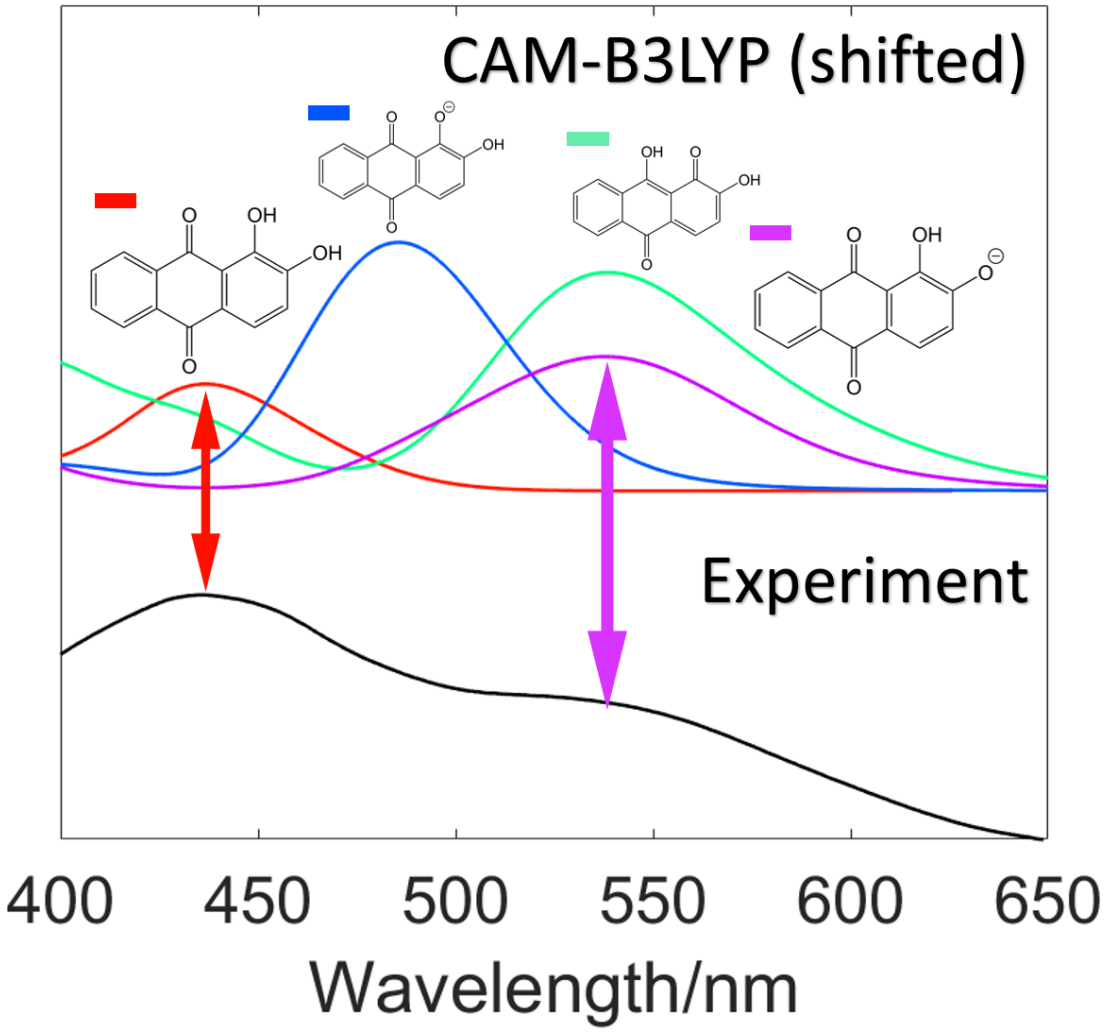

THE JOURNAL OF PHYSICAL CHEMISTRY A

Article

Cite This: J. Phys. Chem. A 2019, 123, 873−880

pubs.acs.org/JPCA

Determination of Secondary Species in Solution through Pump-Selective Transient Absorption Spectroscopy and Explicit-Solvent TDDFT

M. A. P. Turner,*[,†,‡,¶] M. D. Horbury,[†] V. G. Stavros,[†] and N. D. M. Hine*[,‡]

[†]Department of Chemistry, University of Warwick, Coventry, CV4 7AL, U.K.

[‡]Department of Physics, University of Warwick, Coventry, CV4 7AL, U.K.

Supporting Information

ABSTRACT: The measured electronic excitations of a given species in solution are often a composite of the electronic excitations of various equilibrium species of that molecule. It is common for a proportion of a species to deprotonate in solution, or form a tautomeric equilibrium, producing new peaks corresponding to the electronic excitations of the new species. One prominent example is alizarin in methanol, which at different temperatures, and in solutions with differing pH, has an isosbestic point between the two dominant excitations at 435 and 540 nm. The peak at 435 nm has been attributed to alizarin; the peak at 540 nm, however, more likely results from a species in equilibrium with alizarin. In this work, we were able to use both experimental and computational techniques to selectively examine electronic properties of both alizarin and its secondary species in equilibrium. This was achieved through use of transient electronic absorption spectroscopy, following selective photoexcitation of a specific species in equilibrium. The resulting transient electronic absorption spectra were compared to the known transient absorption spectra of potential secondary equilibrium species. The ground state absorption spectra associated with each species in equilibrium were predicted using linear-scaling time-dependent density functional theory with an explicitly modeled solvent and compared to the experimental result. This evidence from both techniques combines to suggest that the excitation at 540 nm arises from a specific monoanionic form of alizarin.

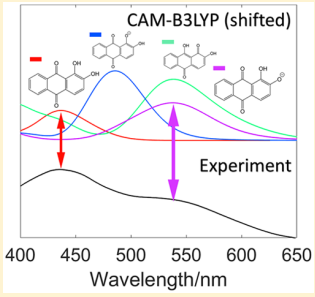

INTRODUCTION

The optical absorption spectrum of a molecule in solution often comprises a superposition of spectra originating from several different species, each arising from the equilibrium process associated with a given parent molecule.[1,2] For example, tautomeric equilibria and equilibrium between possible charge states will produce a wide range of species each providing different contributions to the total spectrum. These equilibrium species may result in unwanted effects, for instance in medicine where potentially dangerous side products may be formed,[3] or in dyes or paints whose color may be affected by properties which influence the equilibrium, such as solvent, pH, or temperature.[4] Determining the identity of the various species present is the first step to controlling them, but is currently challenging both for experimental and theoretical methods. In this paper we apply a combination of state-of-the-art experimental and theoretical techniques to deconvolve the spectrum of a widely studied exemplar dye, namely alizarin. Alizarin is a common dye used frequently for biological staining of cells, bones, and cartilage[5,6] as well as for studying inorganic processes like the growth of TiO_2 nanotubes.[7] It has been subjected to experimental[8,9] and computational[10−19] studies with a wide range of techniques, but as we show here, the identity of the main secondary absorption peak in protic solvents has not previously been unambiguously determined. Here we use a combination of methods that enables definitive identification of peaks, pointing the way to increased feasibility of ultraviolet−visible (UV−vis) based tools for analysis of organic compounds in a range of solvents.

Figure 1 shows the UV−vis spectrum of alizarin in a selection of common solvents. When alizarin is dissolved in

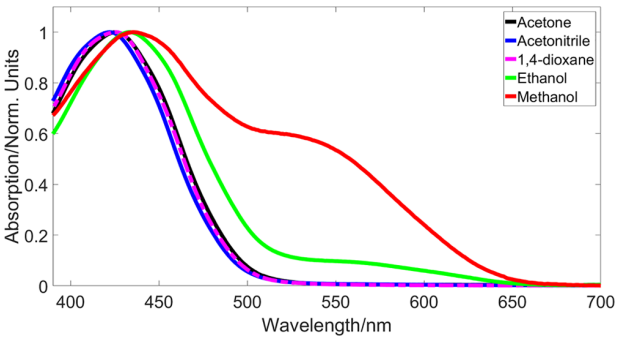

Figure 1. UV−vis spectra of alizarin in different solvents. A prominent shoulder is observed in methanol, and to a lesser extent in ethanol, at around 540 nm.

Received: November 13, 2018
Revised: December 19, 2018
Published: January 8, 2019

DOI: 10.1021/acs.jpca.8b11013
J. Phys. Chem. A 2019, 123, 873−880

nonprotic solvents, the resulting spectrum displays only one major peak, at approximately 435 nm, which we call excitation α. However, in protic solvents such as methanol, and to a lesser extent ethanol, a clear secondary peak is present at approximately 540 nm, which we call excitation β. As it represents the clearest example of this secondary excitation, we elect to study alizarin in methanol as an exemplar system for secondary species determination. UV−vis spectra of alizarin in methanol taken at varying temperatures show a clear decrease in absorption for excitation α and increase in absorption for excitation β as temperature increased (see Supporting Information, Figure S1). A clear isosbestic point is present between the two excitations, implying that the secondary excitation is not the result of a lower-energy electronic excitation of the highest-concentration species of alizarin, but rather is likely due to the presence of a secondary species of alizarin whose concentration varies with temperature. This peak has been observed previously, and has prompted debate as to whether it corresponds to a monoanionic form of alizarin or a tautomer.[12,14,20] Parts A−D of Figure 2 enumerate the candidate species we consider in this work.

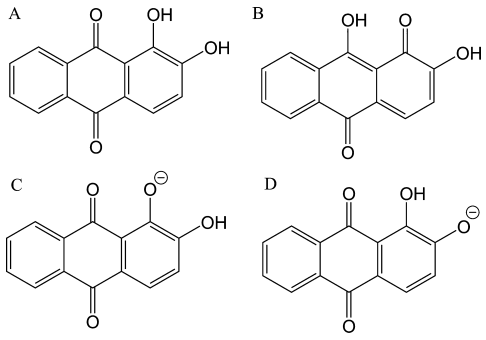

Figure 2. Primary (A) and secondary (B−D) structures considered within this work: (A) alizarin-a tautomer; (B) alizarin-b tautomer; (C) alizarin monoanion-a; (D) alizarin monoanion-b.

Le Person et al. concluded that this excitation was due to both monoanionic alizarin and the alizarin-b tautomer.[20] Others in the literature however question the presence of the alizarin-b tautomer in methanol, instead suggesting that the β excitation is entirely caused by different tautomeric and rotameric monoanionic species.[11,14,21] In some cases where there is a need to distinguish secondary species, nuclear magnetic resonance can be a good option. However, in this system the rate in which the equilibria species interconverted is too fast for them to be distinguishable. In other situations, infrared-based techniques are ideal. However, for this combination of solvent and solute, the vibrational frequencies of interest, specifically those arising from the hydroxyl groups, are also present in the methanol solvent, causing the signal to be eclipsed. The use of deuterated solvent can be ruled out owing to the fast exchange of hydrogen/deuterium between solute and solvent. The unclear overall situation thus suggests alizarin as an ideal testing ground for novel approaches to determining the identity of secondary species.

Two complementary techniques are required for an unambiguous species determination: high-accuracy theoretical spectroscopy on each candidate species, and species-selective "fingerprinting" via time-resolved spectroscopy. We achieve the necessary accuracy in theoretical spectroscopy by using a newly emerging combination of methodologies: linear-scaling time-dependent DFT[22,23] and spectral warping.[24] The reduced scaling of the computational effort associated with linear-scaling forms of linear-response time-dependent density functional theory (TDDFT)[25] enables calculations on an ensemble of model systems each incorporating a large solvent cluster, as has been shown to be necessary to fully converge the solvatochromic shift.[23] Meanwhile spectral warping[24] enables excitation energies calculated with a computationally "cheap" density functional, allowing high-throughput calculations but relatively limited overall accuracy, to be transformed by a simple predetermined warping function to produce results equivalent to calculations using a much higher-accuracy, but correspondingly expensive, state-of-the-art functional. The combination of these techniques has been shown to enable accurate color prediction of dyes exhibiting strong solvatochromism resulting from various competing effects.[13] In the current work it can be used to predict the excitation energies from each species in a given solvent, which can be compared to experimental spectra to determine the likely concentration of each of the candidate molecules. However, it has also been observed that with the available accuracy of even state-of-the-art exchange-correlation (xc) functionals, confidence in theoretical color prediction can be difficult to obtain, due to the spread of results obtained for different functionals. Therefore, in this work, we use alignment with the known experimental spectra for the majority species to eliminate the main part of the functional-dependent error, resulting in close alignment of the predicted secondary peaks.

To enable even greater confidence in the identity of equilibrium species giving rise to specific absorption peaks, we also examine their excited state properties. Experimentally, these are assessed via transient electronic absorption spectroscopy (TEAS), commonly used to probe excited state decay in molecules.[26−28] In this work, the pump wavelength was specifically selected to excite the α and β excitations separately. The resulting excited state dynamics were then compared to excited state dynamics of a buffered solution certain to contain the monoanionic form of alizarin.

METHODOLOGY

Experimental Methodology. All steady state UV−vis measurements were taken on the a Cary 60 spectrophotometer. Alizarin (SIGMA-Aldrich, 97%) was dissolved in spectroscopy grade methanol (3 μM). This solution was used for all studies aside from the UV−vis spectra taken in other solvents in Figure 1, for which the concentration used was also 3 μM. Buffer solutions were made for the pH 3 buffer with trichloroacetic acid (ACS Reagent, SIGMA-Aldrich, 99.5%) and sodium trichloroacetate (SIGMA-Aldrich, 97%). The pH 7 buffer was made using acetic acid (SIGMA-Aldrich, 97%) and sodium acetate (SIGMA-Aldrich, 99%). Buffers were made by dissolving reagents in methanol, the concentrations of each component is shown in Table 1. The components were mixed

Table 1. Starting Concentrations for Making pH Buffers

buffer component	concentration/mM
trichloroacetic acid (pH = 3 buffer)	2.27
sodium trichloroacetate (pH = 3 buffer)	27.0
acetic acid (pH = 7 buffer)	24.1
sodium acetate (pH = 7 buffer)	1.4

DOI: 10.1021/acs.jpca.8b11013
J. Phys. Chem. A 2019, 123, 873−880

in a 4:1 acid to salt ratio, although these were calculated using approximate pK_a values so the pH was corrected by adding components dropwise until at the right pH, monitored using pH paper. This was due to difficulty with using electrochemical probes in organic solution. The basic alizarin was made by adding aqueous sodium hydroxide. This was not a buffer owing to the safety issues surrounding making basic buffers in methanol. The pH was regularly monitored and did not deviate from approximately 9 therefore we believe this method to be reliable.

The transient electronic absorption spectroscopy set up is the same as used in several previous works, including Greenough et al. and Horbury et al.[29−31] The concentration of alizarin in each solution was increased to 0.1 mM. The broadband probe pulse was generated through focusing 800 nm incident light on a 2 mm CaF_2 window, this was translated vertically and spanned a spectral region of 345 to 675 nm. The femtosecond (fs, 10^{-15} s) pump pulses were produced using an optical parametric amplifier (TOPAS-C, spectra-physics). The path length used for each scan was 100 μm and the fluence was ≈1−2 mJ cm^{-2}, while the appropriate pump wavelengths are stated in the text. The absorption at 100 μm path length was 0.045 OD. The instrument response of the TEAS measurements was retrieved by fitting Gaussians to the time-zero artifacts present in the solvent scans in the acidic and neutral solutions (MeOH and buffer only solutions, see figure S5) and taking the full width half-maximum; this gave a value of ≈80 fs.

Computational Methodology. For LR-TDDFT calculations in vacuum and in implicit solvent, we use the NWChem package.[32] We have employed the cc-pVTZ basis set and performed a full geometry optimization for each combination of functional and environment unless otherwise stated.[33] For implicit solvent calculations, we use the COSMO model[34−36] as implemented in NWChem, with dielectric parameters set to represent the methanol environment.

For explicit solvent calculations, to generate an ensemble of realistic configurations of the molecule immersed in methanol solvent, we first perform molecular dynamics calculations with the AMBER package.[37] Force field parameters for each molecular species were generated using the antechamber tool, in their DFT-optimized geometry.[38] The molecules were then placed in a box of methanol of side length 20 Å. The generalized Amber force field (GAFF)[39] was used to first conduct an energy minimization of the box and then to equilibrate the box by raising the temperature up to 300 K over the course of 3 ps. Following this, the box was maintained via a Langevin thermostat at a constant temperature of 300 K over the course of 2 ns, during which 60 snapshots were extracted at regular time intervals. This procedure is thus imagined to generate statistically independent set of snapshot representa-tions of the box.

A spherical region of the periodic box is then extracted, of a fixed radius centered on the center-of-mass of the target molecule. The required radius of this region is chosen to balance a desired degree of convergence of the solvatochromic shift against increasing computational cost as the sphere radius is increased. The principal hydrogen bonding interactions would occur for solvent molecules within 2.5 Å of the solute, while electrostatic interactions originating from the solvent dipoles will fall off rapidly with increasing distance. On the basis of previously reported studies,[40] we determined that the solvent sphere can, in this case, be truncated to a radius of 10 Å. The usage of implicit solvent model[41] surrounding the explicit solvent shell was necessary in order to correctly screen the surface dipoles and prevent a net dipole across the solvent cluster. This is in agreement with previous work[42] which showed that an appropriate treatment of the electrostatics of solvent clusters is necessary to retain physically reasonable behavior of the HOMO−LUMO gap. Truncation of radius 10 Å produced models of typical size 500−600 atoms (the exact number is dependent on the specific configuration of the snapshot), which is beyond the capabilities of traditional approaches to LR-TDDFT calculations.

For LR-TDDFT calculations on the solvent and solute clusters, we therefore utilize the ONETEP linear-scaling density functional theory package.[43] ONETEP uses a representation of valence, conduction and transition density matrices in terms of localized support functions referred to as nonorthogonal generalized Wannier functions (NGWFs). A minimal number of NGWFs per atom (here four per C and O atom, and 1 per H atom), strictly localized to a sphere of a given radius (here 10 Å), are expressed in terms of an underlying basis of psinc functions (equivalent to plane-waves, with a cutoff energy of 800 eV in this case) and are optimized in situ during the calculation. Density kernel and NGWF optimization is applied separately to valence and conduction NGWF sets,[44] then the combined "joint" set is used for LR-TDDFT calculations within a modified version of the Casida formalism[25] adapted for the linear-scaling framework.[22,23] The first five LR-TDDFT excited states are found for 60 snapshots for each candidate species, utilizing the PBE[33] exchange-correlation functional.

While PBE calculations are not expected to provide quantitatively accurate spectra, it is expected that they will provide an accurate representation of the solvent-induced broadening and solvent−solute specific interactions. In order to then obtain more accurate results for the ensemble of solvent−solute clusters within feasible computational effort, spectral warping was applied. This is a technique devised by Ge et al. which aims to reproduce the accuracy associated with hybrid functionals by correcting results obtained for an ensemble of large models treated using a less expensive semilocal functional.[24] For each of the candidate species, otherwise identical LR-TDDFT calculations were performed with several functionals: PBE (semilocal), B3LYP and PBE0 (global hybrids) and CAM-B3LYP and LC-PBE (range-separated hybrids) in their relaxed gas phase geometry. A linear transformation of the energies associated with each excitation is then constructed, which maps the PBE results onto the (range-separated) hybrid functional result. This same linear transformation can then be applied to each of excitations from the explicit solvent snapshots, to approximately reproduce the effect of using the hybrid functional on the full cluster.

RESULTS AND DISCUSSION

Acid/Base UV−Vis Studies. Alizarin in methanol was buffered at pH 3 and pH 7 using methanol-based buffers as described in the methodology section. Alizarin in methanol was also studied at pH 9 through addition of sodium hydroxide in water. UV−vis spectra were taken at each pH value, and are shown in Figure 3. When buffered to pH 3 the β excitation is no longer present. We suggest that, as there is likely no monoanion at pH = 3, the β excitation was a result of a monoanionic species. However, one could argue that alizarin-b is stabilized in methanol through hydrogen bonding and this is

DOI: 10.1021/acs.jpca.8b11013
J. Phys. Chem. A 2019, 123, 873−880

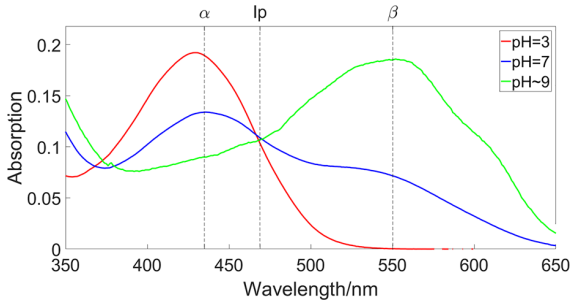

Figure 3. Alizarin in methanol at various pH values: (red line) buffered to pH 7 using an acetate buffer; (blue line) buffered at pH 3 using a trichloroacetate buffer; (green line) pushed to pH 9 through addition of NaOH(aq). The dotted line (Ip) shows the position of the isosbestic point.

perturbed by addition of acid. Alternatively, the buffer could be reacting in order to remove alizarin-b, although this is less likely as no signs of a reaction are evidenced by decoloration or the appearance of new features not present in the original spectrum. Under basic conditions, the α excitation decreases as the alizarin-a is largely deprotonated. At around 469 nm there is an isosbestic point, which lends further credence to the theory that an equilibrium between two species is observed. This occurs close to where Miliani et al. observed an isosbestic point, 463 nm when alizarin was dissolved in water. This further supports that the same equilibrium is forming.[12] From this evidence, it is highly likely that monoanionic alizarin is present in neutral methanol and is responsible for a peak at 540 nm.

Transient Electronic Absorption Spectroscopy Results. Transient electronic absorption spectroscopy is a useful technique for verifying that the features present in the transient absorption spectra for samples with different solvent environments (pH in this case) share a common photoactive species. We can use a combination of two indicators within the transient absorption spectra as a two-tier identification process for the photoactive species. Firstly, one can observe whether the same spectral features appear, such as stimulated emission and excited state absorption occur at the same pump wavelength λ_{ex}. Secondly, one can observe whether the different samples have similar temporal evolution of these excited state features as well as decay pathways. This can be especially useful to confirm that there is not a mix of species being probed, as this would lead to the superposition of multiple decay pathways in the time-resolved responses of the different samples. Using this two-tier identification, if different samples have the same features that evolve in the same temporal manner in their transient absorption spectra, it is very likely the same photoactive species is present.

Transient electronic absorption spectra of alizarin in methanol were taken with the photoexcitation (or pump) pulse at 425 nm, near excitation α, and 550 nm, near excitation β. These wavelengths were chosen to excite the individual species as much as possible without exciting the tail of the other form. These were conducted under acidic, neutral, and basic conditions, see Figure 4. When exciting at 425 nm under acidic and neutral conditions, parts a and b of Figure 4, we see very similar features, with an excited state absorption at 500 nm and a stimulated emission at 675 nm. This is due to the fact that in both cases alizarin a is excited by the pump pulse. There are similarities in the transient electronic absorption data when exciting at 550 nm under basic and neutral conditions, as seen in parts c and d of Figure 4, as well. This is interesting as the species excited under basic conditions is very likely a monoanionic form. This is due to the fact both alizarin-a and alizarin-b will deprotonate in a basic environment, as evidenced by earlier UV−vis studies. As the results for parts c and d of Figure 4 show such similar features, with two excited state absorption features at 390 and 450 nm and a stimulated emission at 550 nm, it is likely that in both cases a monoanionic form of alizarin is excited.

The excited state absorption features observed were fitted with a biexponential decays, these were convolved with Gaussian curves to account for instrument response. While each appeared to have a monoexponential character, a second exponential is necessary to account for the different, smaller scale, early-time effects, such as vibrational cooling. These features were normalized by pump power. Plots of each of

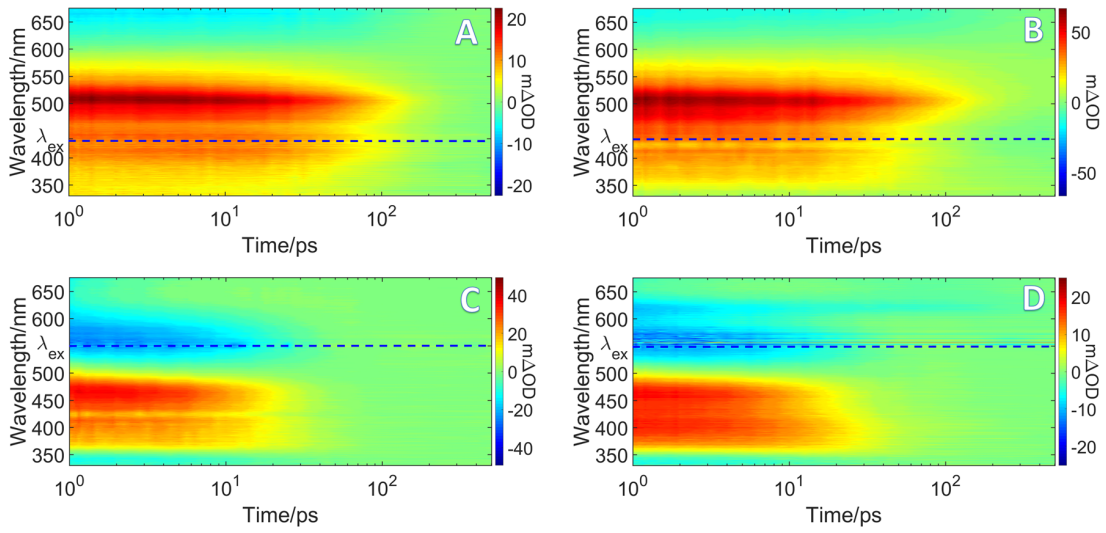

Figure 4. TEAS of alizarin in methanol (0.1 mM). The blue dashed line on each plot represents the excitation wavelength: (a) pH = 3, λ_{ex} = 425 nm; (b) pH = 7, λ_{ex} = 425 nm; (c) pH = 7, λ_{ex} = 550 nm; (d) pH = 9, λ_{ex} = 550 nm.

DOI: 10.1021/acs.jpca.8b11013
J. Phys. Chem. A 2019, 123, 873−880

these fitted features are in Figures S2 and S3 with the lifetimes of features shown in Table 2.

Table 2. Lifetimes Extracted from Fitted Curves for the Excited State Features of Alizarin Observed

pH	λ_{ex}/nm	λ_{pr}/nm	lifetime (τ_1)/ps	lifetime (τ_2)/ps
3	425	500	<0.04	120 ± 21
7	425	500	<0.04	94 ± 4
7	550	460	0.41 ± 0.05	15.8 ± 0.5
9	550	460	0.4 ± 0.1	17 ± 1

Each of the scans at 425 nm had a long lifetime decay on the order of approximately 100 ps as well as a decay of <40 fs, which is within our instrument response. This result is similar to what was observed by Lee et al. when observing the ultrafast dynamics of alizarin with an excitation wavelength of 403 nm in ethanol.[45] Lee et al. observed two lifetimes for alizarin, one at 84 ps and one at 3 ps. We did not pick up on the 3 ps lifetime, likely due to its low intensity, but it is likely that we are observing the same long-lived decay of alizarin-a. Lee et al. suggested that the process responsible for this lifetime was proton-transfer and the formation of alizarin-b in the excited state. The amplitude of the long-lived process was significantly higher than that of the short-lived by a factor of approximately 30 in each case.

The scans at 550 nm show two decays, one of approximate lifetime 16 ps and one of approximate lifetime 400 fs. Again, the long-lived process had a much higher amplitude in both cases, this time by a factor of approximately 20. The smaller 400 fs lifetime is likely due to vibrational cooling. The longer lifetime is harder to assign but is also likely due to hydrogen transfer. The species formed lives for a significantly shorter time than in alizarin-a, this could be due to instability of the hydrogen transfer state or proximity to a triplet state, resulting in intersystem crossing. The difference in lifetimes between the neutral and basic solutions is sufficiently small that it is, again, likely these are the same species. This further confirms that the species that is present in the acidic system is also present in the neutral system and is what is giving rise to the α excitation. Furthermore, the β excitation in the neutral system is likely the result of exciting the species found in the basic system. It also shows that it is unlikely that both alizarin-b and the monoanion are present as this would likely give rise to a higher number of exponentials required to fit the neutral species than the basic species, which is not the case.

Explicit Solvent TDDFT Calculations. While the experimental results already appear to rule out the tautomeric alizarin-b form, they are not able to provide a positive identification of which species is responsible for the secondary peak. To provide a clear differentiation between the two proposed tautomeric forms of the monoanion, we turn to theoretical spectroscopy.

To address this question, we use TDDFT to predict the excitation energies arising from all of the proposed structures within a realistic model of the alizarin/methanol solution. As discussed, we find that the combination of explicitly modeled solvent and a high-accuracy, though computationally costly, exchange-correlation functional such as a hybrid or range-separated hybrid is required for sufficient accuracy. We therefore use a simple spectral warping technique: we first use the semilocal PBE[33] functional to predict (at feasible computational cost) the excitations of a large ensemble of large snapshot models for each species, including explicit solvent. This is then followed by a warp of the resulting spectra to what would have been predicted had one of the more expensive functionals been used (in this case PBE0, LC-PBE0, B3LYP, and CAM-B3LYP).[46−49] Since the spectra are dominated in each case by a single peak, the spectral warp required here is relatively simple: just a constant energy shift equal to the difference between the equivalent excitation energies for a given species calculated in the two functionals, within an implicit representation of the solvent. Applying this shift to all the excitation energies calculated for the snapshots in the less expensive functional in explicit solvent then results in a set of excitations mimicking a hypothetical set of calculations on the explicit solvent snapshots using the more expensive functional.

Figure 5 shows the results of implicit solvent calculations used to determine the shift parameter for each species, using

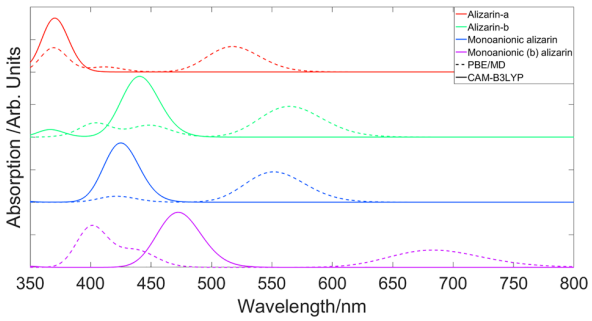

Figure 5. PBE and CAM-B3LYP calculations of forms of alizarin in implicit methanol solvent with 0.1 eV Gaussian broadening, used for calculation of spectral warping parameters. These parameters are acquired through computing the difference between the PBE S_1 peak and the CAM-B3LYP S_1 peak.

the CAM-B3LYP shift as an example. It was observed that the predicted S_1 excitation energy for alizarin-a was 0.05 eV different from the observed experimental value when calculated using B3LYP. Furthermore, there was an observed error of 0.55 eV in this predicted excitation from CAM-B3LYP. These errors are consistent with those observed by Anouar et al., who, when utilizing an implicit PCM solvent model, also observed a large error associated with CAM-B3LYP; they found an error of 0.75 eV in this case as opposed to an error of just 0.15 eV when using B3LYP.[19]

As alizarin-a has already been confirmed as the source of the α excitation, a further small energy shift was applied to all the spectra for a given functional in order to align the theoretical and experimental peaks of the alpha excitation. The assumption underlying this is that the error associated with the xc functional will have a similar value in each of these closely related alizarin-derived species, allowing us to apply the same functional-dependent shift to all species. All the predicted explicit-solvent spectra were given a rigid shift of 0.05 (B3LYP), 0.15 (PBE0), 0.55 (CAM-B3LYP), and 0.95 eV (LC-PBE0) to produce the final comparison with experiment. The results are shown in Figure 6. After these shifts have been applied, the results between different functionals show a very high degree of consistency. It appears highly likely that the monoanion-b produces the β excitation and is thus the dominant second species, since in all four cases this species is closest to the observed position of the β excitation. The predicted position of alizarin-b is also close in several

DOI: 10.1021/acs.jpca.8b11013
J. Phys. Chem. A 2019, 123, 873−880

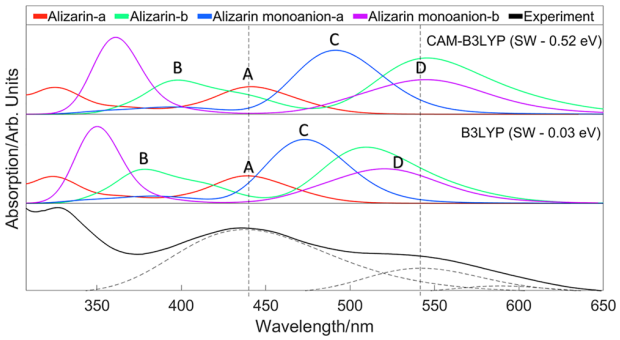

Figure 6. Predicted spectra for different forms of alizarin in explicit methanol solvent: (A) red is alizarin-a, (B) green is alizarin-b, (C) blue is alizarin monoanion-a, and (D) pink is alizarin monoanion-b. The top panel shows the results of CAM-B3LYP spectral warp corrections. The middle panel shows the results of B3LYP spectral warp corrections. The bottom panel (black lines) shows the experimental spectra for comparison, with the main peaks deconvolved by fitting to gaussians.

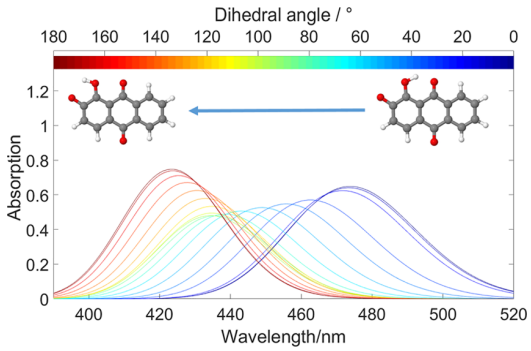

Figure 7. Range of predicted UV−vis spectra for different rotamers of monoanionic alizarin-b, CAM-B3LYP/6-311G* implicit methanol PCM solvent.

functionals, but it is unlikely this as evidenced by the previous experimental findings. Monoanion-a was a viable candidate following the experimental work, however it is significantly less likely given that the predicted peak is at least 75 nm away from the β excitation.

This process was repeated with PBE0 and LC-PBE0 as the more expensive functionals, the results for this are shown in Figure S4. Table 3 shows shifting parameter required to match the predicted S_1 excitation result for alizarin-a to the experimental value of α as well as the S_1 excitation of alizarin-b, monoanion-a, and monoanion-b postshift.

As previously discussed, Le Person et al. showed that the β excitation can be deconvolved into two Gaussian peaks, and suggested that this was due to the presence of both a monoanionic species and the alizarin-b tautomer.[20] It can, however, be shown that the rotation of the dihedral angle associated with the OH bond in monoanion-b can shift the energy of the S_1 excitation. Figure 7 shows the range of UV−vis absorption peaks associated with this rotation, as predicted by fixed-angle rotation calculations of alizarin in implicit methanol solvent; these were conducted using the cam-B3LYP functional. The range of absorption maxima caused by rotamers suggests that the broadness of the β excitation could be due to the rotation of this bond. The explicit solvent calculation for monoanion-b shows a broadened peak as well: this is due to the wide range of motion associated with this bond in the molecular dynamics snapshots.

We note also that in the explicit solvent spectra for monoanion-b, a higher-energy excitation at around 350−360 nm is predicted. In the experimental spectra which show the β-excitation we are now ascribing to monoanion-b, there is no clear evidence for that peak. However, the peak is in very close proximity to the higher-energy excitation of alizarin-a, which the explicit solvent results seem to be predicting accurately. We thus presume these peaks are to some extent merging, resulting in the monoanion-b peak not being seen experimentally.

CONCLUSIONS

The present work has provided a combination of methodologies appropriate to identifying secondary species in solvent. We apply this methodology to alizarin in methanol, and show that the most likely source of the secondary β excitation, at 540 nm, is monoanion-b form of alizarin. The broadness of this peak is likely due to the rotation of the alcohol group. In contrast to previous studies, we do not believe that alizarin-b is present, as evidenced by a number of observations: firstly, when acid is added to the system the peak completely disappears. It is unlikely the addition of acid would completely remove the alizarin-b tautomer. Secondly, in the transient absorption spectroscopy results we see a high degree of similarity between the TEAS spectrum for monoanionic alizarin and the TEAS spectrum for the β excitation. Both seem to have two excited state absorption peaks at 380 and 460 nm, and stimulated emission at 550 nm. This implies that in both cases, a monoanionic form of alizarin is being observed. The lack of any features unique to the TEAS data taken at neutral conditions with an excitation wavelength at 550 nm imply that alizarin-b is not being accessed.

We then proceed to show using theoretical calculations that the monoanion present is most likely to be monoanion-b. Using spectral-warping on explicit solvent calculations, we have demonstrated that monoanion-b has an excitation much closer in energy to the β peak than monoanion-a in all four considered functionals.

Table 3. Energy Shifts Required for each Functional, To Ensure the Predicted S_1 Excitation Result for Alizarin-a Matches the Experimental Value of Excitation α (435 nm)[a]

functional	shift/eV	alizarin b/nm	monoanion-a/nm	monoanion-b/nm
B3LYP	0.03	513	476	525
CAM-B3LYP	0.52	526	491	548
PBE0	0.15	508	471	523
LC-PBE0	0.95	575	502	536

[a]Also shown are the S_1 excitation wavelengths of alizarin-b, monoanion-a, and monoanion-b after the shift for each functional has been applied. For reference, the experimental value of the unknown β peak is 540 nm.

DOI: 10.1021/acs.jpca.8b11013
J. Phys. Chem. A 2019, 123, 873−880

Desirable further work could include computational prediction of the excited state absorption and stimulated emission properties of monoanion-b, as well as monoanion-a and alizarin-b to further confirm the β excitation entirely arises from the former.

We propose that approaches to the identification of secondary species which are based solely on UV/vis-based methods and theoretical modeling would have strengths in addressing systems in dynamic equilibrium, specifically where the rate of conversion is sufficiently fast to preclude the use of NMR spectroscopy. It would also be advantageous in situations where there is no clear way to differentiate between candidate species using vibrational spectroscopy. Such a situation occurs whenever there are overlapping absorption features between the solvent and solute, or between different functional groups on the solute.

The ability to identify photoactive equilibria samples in solution is of utmost importance in fields as wide ranging as dyes, sun protection, biological staining, and general organic synthesis. We feel this combination of methodologies offers a pathway to routinely identifying secondary species with considerably increased confidence.

■ ASSOCIATED CONTENT

Supporting Information

The Supporting Information contains the following plots: The Supporting Information is available free of charge on the ACS Publications website at DOI: 10.1021/acs.jpca.8b11013.

UV−vis scans of alizarin in methanol at different temperatures, fitted plots of TEAS slices of alizarin in methanol, predicted spectra for different forms of alizarin in methanol in PBE-based functionals, and solvent scans (PDF)

■ AUTHOR INFORMATION

Corresponding Authors

*(M.A.P.T.) E-mail: m.turner.1@warwick.ac.uk.
*(N.D.M.H.) E-mail: n.d.m.hine@warwick.ac.uk.

ORCID

M. A. P. Turner: 0000-0003-4213-1036
V. G. Stavros: 0000-0002-6828-958X
N. D. M. Hine: 0000-0001-5613-3679

Present Address

¶Top Floor Senate House, University of Warwick, Coventry, CV4 7AL, U.K.

Notes

The authors declare no competing financial interest.
The underlying data of this publication can be accessed via the Zenodo Archive at DOI: 10.5281/zenodo.1483226

■ ACKNOWLEDGMENTS

M.A.P.T. thanks EPSRC for a doctoral studentship through the EPSRC Centre for Doctoral Training in Molecular Analytical Science, Grant Number EP/L015307/1. We thank G. W. Richings for useful discussions. M.D.H. thanks the Leverhulme Trust for postdoctoral funding. Computing facilities were provided by the Scientific Computing Research Technology Platform of the University of Warwick. We acknowledge the use of Athena at HPC Midlands+, which was funded by the EPSRC by Grant EP/P020232/1, in this research, as part of the HPC Midlands+ consortium. V.G.S. is grateful to the EPSRC for an equipment grant (EP/N010825) and the Royal Society and the Leverhulme Trust for a Royal Society Leverhulme Trust Senior Research Fellowship. N.D.M.H. acknowledges the support of EPSRC Grant EP/P02209X/1 and Royal Society Research Grant RG150013.

■ REFERENCES

(1) Antonov, L.; Nedeltcheva, D. Resolution of overlapping UV−Vis absorption bands and quantitative analysis. *Chem. Soc. Rev.* **2000**, *29*, 217−227.
(2) Antonov, L.; Gergov, G.; Petrov, V.; Kubista, M.; Nygren, J. UV−Vis spectroscopic and chemometric study on the aggregation of ionic dyes in water. *Talanta* **1999**, *49*, 99−106.
(3) Günther, M.; Wagner, E.; Ogris, M. Acrolein: unwanted side product or contribution to antiangiogenic properties of metronomic cyclophosphamide therapy? *J. Cell. Mol. Med.* **2008**, *12*, 2704−2716.
(4) Magde, D.; Rojas, G. E.; Seybold, P. G. Solvent dependence of the fluorescence lifetimes of xanthene dyes. *Photochem. Photobiol.* **1999**, *70*, 737−744.
(5) Springer, V. G.; David Johnson, G. Use and advantages of ethanol solution of alizarin red S dye for staining bone in fishes. *Copeia* **2000**, *2000*, 300−301.
(6) Ovchinnikov, D. Alcian blue/alizarin red staining of cartilage and bone in mouse. *Cold Spring Harb Protoc* **2009**, *2009*, pdb.prot5170.
(7) Park, J.; Bauer, S.; Schlegel, K. A.; Neukam, F. W.; von der Mark, K.; Schmuki, P. TiO2 nanotube surfaces: 15 nm - an optimal length scale of surface topography for cell adhesion and differentiation. *Small* **2009**, *5*, 666−671.
(8) Szostek, B.; Orska-Gawrys, J.; Surowiec, I.; Trojanowicz, M. Investigation of natural dyes occurring in historical Coptic textiles by high-performance liquid chromatography with UV−Vis and mass spectrometric detection. *J. Chromatogr. A* **2003**, *1012*, 179−192.
(9) Moriguchi, T.; Yano, K.; Nakagawa, S.; Kaji, F. Elucidation of adsorption mechanism of bone-staining agent alizarin red S on hydroxyapatite by FT-IR microspectroscopy. *J. Colloid Interface Sci.* **2003**, *260*, 19−25.
(10) Douma, D. H.; M'Passi-Mabiala, B.; Gebauer, R. Optical properties of an organic dye from time-dependent density functional theory with explicit solvent: The case of alizarin. *J. Chem. Phys.* **2012**, *137*, 154314.
(11) Cysewski, P.; Jeliński, T.; Przybyłek, M.; Shyichuk, A. Color prediction from first principle quantum chemistry computations: a case of alizarin dissolved in methanol. *New J. Chem.* **2012**, *36*, 1836−1843.
(12) Miliani, C.; Romani, A.; Favaro, G. Acidichromic effects in 1, 2-di-and 1, 2, 4-trihydroxyanthraquinones. A spectrophotometric and fluorimetric study. *J. Phys. Org. Chem.* **2000**, *13*, 141−150.
(13) Zuehlsdorff, T. J.; Haynes, P. D.; Payne, M. C.; Hine, N. D. M. Predicting solvatochromic shifts and colours of a solvated organic dye: The example of nile red. *J. Chem. Phys.* **2017**, *146*, 124504.
(14) Preat, J.; Laurent, A. D.; Michaux, C.; Perpète, E. A.; Jacquemin, D. Impact of tautomers on the absorption spectra of neutral and anionic alizarin and quinizarin dyes. *J. Mol. Struct.: THEOCHEM* **2009**, *901*, 24−30.
(15) Jacquemin, D.; Perpete, E. A.; Scuseria, G. E.; Ciofini, I.; Adamo, C. TD-DFT performance for the visible absorption spectra of organic dyes: conventional versus long-range hybrids. *J. Chem. Theory Comput.* **2008**, *4*, 123−135.
(16) Savko, M.; Kaščáková, S.; Gbur, P.; Miškovskỳ, P.; Uličnỳ, J. Performance of time dependent density functional theory on excitations of medium sized molecules−Test on ionic forms of anthraquinone dihydroxy derivatives. *J. Mol. Struct.: THEOCHEM* **2007**, *823*, 78−86.
(17) Mech, J.; Grela, M. A.; Szaciłowski, K. Ground and excited state properties of alizarin and its isomers. *Dyes Pigm.* **2014**, *103*, 202−213.
(18) Dev, P.; Agrawal, S.; English, N. J. Determining the appropriate exchange-correlation functional for time-dependent density functional

DOI: 10.1021/acs.jpca.8b11013
J. Phys. Chem. A 2019, 123, 873−880

theory studies of charge-transfer excitations in organic dyes. *J. Chem. Phys.* **2012**, *136*, 224301.
(19) Anouar, E. H.; Osman, C. P.; Weber, J.-F. F.; Ismail, N. H. UV/Visible spectra of a series of natural and synthesised anthraquinones: experimental and quantum chemical approaches. *SpringerPlus* **2014**, *3*, 233.
(20) Le Person, A.; Cornard, J.-P.; Say-Liang-Fat, S. Studies of the tautomeric forms of alizarin in the ground state by electronic spectroscopy combined with quantum chemical calculations. *Chem. Phys. Lett.* **2011**, *517*, 41−45.
(21) Carta, L.; Biczysko, M.; Bloino, J.; Licari, D.; Barone, V. Environmental and complexation effects on the structures and spectroscopic signatures of organic pigments relevant to cultural heritage: the case of alizarin and alizarin−Mg (II)/Al (III) complexes. *Phys. Chem. Chem. Phys.* **2014**, *16*, 2897−2911.
(22) Zuehlsdorff, T. J.; Hine, N. D. M.; Spencer, J. S.; Harrison, N. M.; Riley, D. J.; Haynes, P. D. Linear-scaling time-dependent density-functional theory in the linear response formalism. *J. Chem. Phys.* **2013**, *139*, 064104.
(23) Zuehlsdorff, T. J.; Hine, N. D. M.; Payne, M. C.; Haynes, P. D. Linear-scaling time-dependent density-functional theory beyond the Tamm-Dancoff approximation: obtaining efficiency and accuracy with in situ optimized local orbitals. *J. Chem. Phys.* **2015**, *143*, 204107.
(24) Ge, X.; Timrov, I.; Binnie, S.; Biancardi, A.; Calzolari, A.; Baroni, S. Accurate and inexpensive prediction of the color optical properties of anthocyanins in solution. *J. Phys. Chem. A* **2015**, *119*, 3816−3822.
(25) Casida, M. E.; Gutierrez, F.; Guan, J.; Gadea, F.-X.; Salahub, D.; Daudey, J.-P. Charge-transfer correction for improved time-dependent local density approximation excited-state potential energy curves: Analysis within the two-level model with illustration for H2 and LiH. *J. Chem. Phys.* **2000**, *113*, 7062−7071.
(26) Roberts, G. M.; Marroux, H. J.; Grubb, M. P.; Ashfold, M. N.; Orr-Ewing, A. J. On the participation of photoinduced N−H bond fission in aqueous adenine at 266 and 220 nm: a combined ultrafast transient electronic and vibrational absorption spectroscopy study. *J. Phys. Chem. A* **2014**, *118*, 11211−11225.
(27) Kimura, Y.; Alfano, J. C.; Walhout, P.; Barbara, P. F. Ultrafast transient absorption spectroscopy of the solvated electron in water. *J. Phys. Chem.* **1994**, *98*, 3450−3458.
(28) Greene, B.; Hochstrasser, R.; Weisman, R. Picosecond transient spectroscopy of molecules in solution. *J. Chem. Phys.* **1979**, *70*, 1247−1259.
(29) Greenough, S. E.; Horbury, M. D.; Thompson, J. O.; Roberts, G. M.; Karsili, T. N.; Marchetti, B.; Townsend, D.; Stavros, V. G. Solvent induced conformer specific photochemistry of guaiacol. *Phys. Chem. Chem. Phys.* **2014**, *16*, 16187−16195.
(30) Greenough, S. E.; Roberts, G. M.; Smith, N. A.; Horbury, M. D.; McKinlay, R. G.; Żurek, J. M.; Paterson, M. J.; Sadler, P. J.; Stavros, V. G. Ultrafast photo-induced ligand solvolysis of cis-[Ru (bipyridine) 2 (nicotinamide) 2] 2+: experimental and theoretical insight into its photoactivation mechanism. *Phys. Chem. Chem. Phys.* **2014**, *16*, 19141−19155.
(31) Horbury, M.; Quan, W.-D.; Flourat, A.; Allais, F.; Stavros, V. Elucidating nuclear motions in a plant sunscreen during photoisomerization through solvent viscosity effects. *Phys. Chem. Chem. Phys.* **2017**, *19*, 21127−21131.
(32) Valiev, M.; Bylaska, E. J.; Govind, N.; Kowalski, K.; Straatsma, T. P.; Van Dam, H. J.; Wang, D.; Nieplocha, J.; Apra, E.; Windus, T. L.; et al. NWChem: a comprehensive and scalable open-source solution for large scale molecular simulations. *Comput. Phys. Commun.* **2010**, *181*, 1477−1489.
(33) Perdew, J. P.; Burke, K.; Ernzerhof, M. Generalized gradient approximation made simple. *Phys. Rev. Lett.* **1996**, *77*, 3865.
(34) Klamt, A.; Schüürmann, G. COSMO: a new approach to dielectric screening in solvents with explicit expressions for the screening energy and its gradient. *J. Chem. Soc., Perkin Trans. 2* **1993**, 799−805.
(35) York, D. M.; Karplus, M. A smooth solvation potential based on the conductor-like screening model. *J. Phys. Chem. A* **1999**, *103*, 11060−11079.
(36) Winget, P.; Dolney, D. M.; Giesen, D. J.; Cramer, C. J.; Truhlar, D. G. *Minnesota solvent descriptor database*; Department of Chemistry and Supercomputer Institute, University of Minnesota: Minneapolis, MN, 1999, 55455.
(37) Case, D. A.; Berryman, J. T.; Betz, R. M.; Cerutti, D. S.; Cheatham, T. E., III; Darden, T. A.; Duke, R. E.; Giese, T. J.; Gohlke, H.; Goetz, A. W.; et al. *AMBER 2015*. 2015, University of California: San Francisco, CA.
(38) Wang, J.; Wang, W.; Kollman, P. A.; Case, D. A. Automatic atom type and bond type perception in molecular mechanical calculations. *J. Mol. Graphics Modell.* **2006**, *25*, 247−260.
(39) Wang, J.; Wolf, R. M.; Caldwell, J. W.; Kollman, P. A.; Case, D. A. Development and testing of a general amber force field. *J. Comput. Chem.* **2004**, *25*, 1157−1174.
(40) Zuehlsdorff, T. J.; Haynes, P. D.; Hanke, F.; Payne, M. C.; Hine, N. D. M. Solvent effects on electronic excitations of an organic chromophore. *J. Chem. Theory Comput.* **2016**, *12*, 1853−1861.
(41) Dziedzic, J.; Helal, H. H.; Skylaris, C.-K.; Mostofi, A. A.; Payne, M. C. Minimal parameter implicit solvent model for ab initio electronic-structure calculations. *EPL (Europhys. Lett)* **2011**, *95*, 43001.
(42) Lever, G.; Cole, D. J.; Hine, N. D. M.; Haynes, P. D.; Payne, M. C. Electrostatic considerations affecting the calculated HOMO−LUMO gap in protein molecules. *J. Phys.: Condens. Matter* **2013**, *25*, 152101.
(43) Skylaris, C.-K.; Haynes, P. D.; Mostofi, A. A.; Payne, M. C. Introducing ONETEP: Linear-scaling density functional simulations on parallel computers. *J. Chem. Phys.* **2005**, *122*, 084119.
(44) Ratcliff, L. E.; Hine, N. D. M.; Haynes, P. D. Calculating optical absorption spectra for large systems using linear-scaling density functional theory. *Phys. Rev. B: Condens. Matter Mater. Phys.* **2011**, *84*, 165131.
(45) Lee, S.; Lee, J.; Pang, Y. Excited state intramolecular proton transfer of 1, 2-dihydroxyanthraquinone by femtosecond transient absorption spectroscopy. *Curr. Appl. Phys.* **2015**, *15*, 1492−1499.
(46) Adamo, C.; Barone, V. Toward reliable density functional methods without adjustable parameters: The PBE0 model. *J. Chem. Phys.* **1999**, *110*, 6158−6170.
(47) Rohrdanz, M. A.; Herbert, J. M. Simultaneous benchmarking of ground-and excited-state properties with long-range-corrected density functional theory. *J. Chem. Phys.* **2008**, *129*, 034107.
(48) Becke, A. D. Density-functional thermochemistry. III. The role of exact exchange. *J. Chem. Phys.* **1993**, *98*, 5648−5652.
(49) Yanai, T.; Tew, D. P.; Handy, N. C. A new hybrid exchange−correlation functional using the Coulomb-attenuating method (CAM-B3LYP). *Chem. Phys. Lett.* **2004**, *393*, 51−57.

NOTE ADDED AFTER ASAP PUBLICATION

This paper was originally published ASAP on January 18, 2019. Edits were made to numbers in the Computational Methodology section, and the corrected version was reposted on January 18, 2019.

DOI: 10.1021/acs.jpca.8b11013
J. Phys. Chem. A 2019, 123, 873−880

Chapter 3

Examining solvent effects on the ultrafast dynamics of catechol

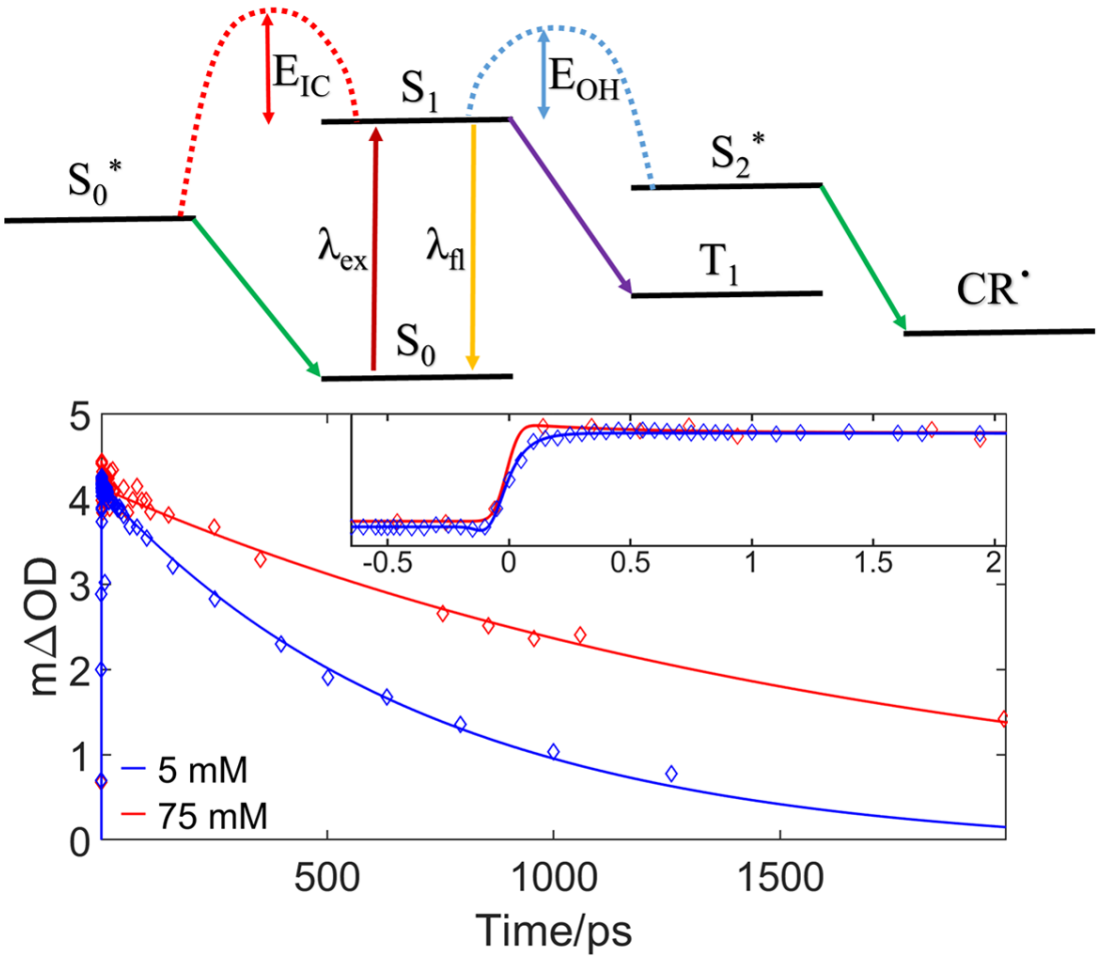

The Journal of Chemical Physics ARTICLE scitation.org/journal/jcp

Examining solvent effects on the ultrafast dynamics of catechol

Cite as: J. Chem. Phys. 151, 084305 (2019); doi: 10.1063/1.5116312
Submitted: 24 June 2019 • Accepted: 1 August 2019 •
Published Online: 27 August 2019

M. A. P. Turner,[1,2] R. J. Turner,[2] M. D. Horbury,[2] N. D. M. Hine,[1] and V. G. Stavros[2,a)]

AFFILIATIONS

[1] Department of Physics, University of Warwick, Coventry, CV47AL, United Kingdom
[2] Department of Chemistry, University of Warwick, Coventry, CV47AL, United Kingdom

Note: The paper is part of the JCP Special Topic on Ultrafast Molecular Sciences by Femtosecond Photons and Electrons.
[a)] v.stavros@warwick.ac.uk

ABSTRACT

We consider the effect of a polar, hydrogen bond accepting, solvent environment on the excited state decay of catechol following excitation to its first excited singlet state (S_1). A comparison of Fourier transform infrared spectroscopy and explicit-solvent *ab initio* frequency prediction suggests that 5 mM catechol in acetonitrile is both nonaggregated and in its "*closed*" conformation, contrary to what has been previously proposed. Using ultrafast transient absorption spectroscopy, we then demonstrate the effects of aggregation on the photoexcited S_1 lifetime: at 5 mM catechol (nonaggregated) in acetonitrile, the S_1 lifetime is 713 ps. In contrast at 75 mM catechol in acetonitrile, the S_1 lifetime increases to 1700 ps. We attribute this difference to aggregation effects on the excited-state landscape. This work has shown that explicit-solvent methodology is key when calculating the vibrational frequencies of molecules in a strongly interacting solvent. Combining this with highly complementary steady-state and transient absorption spectroscopy enables us to gain key dynamical insights into how a prominent eumelanin building block behaves when in polar, hydrogen bond accepting solvents both as a monomer and as an aggregated species.

I. INTRODUCTION

The Sun can be approximated as a classical black-body radiator, emitting a broad range of light centered in the visible region of the electromagnetic spectrum (400–800 nm). Although the bulk of the radiation reaching the Earth's surface is within this visible region, approximately 6% is in the form of ultraviolet (UV) radiation.[1]

Without photoprotection from UV radiation, many biomolecules essential for life, such as nucleobases in DNA, would be quickly degraded, leading to extensive mutagenesis and other unwanted effects.[2] Melanin is a class of pigment found in humans, providing a pertinent example of how nature seeks to mitigate these effects, with eumelanin being the most prominent.[3–6] Although the exact structure of eumelanin is not entirely clear, it is known to be a heterogeneous macromolecule comprising multiple subunits including dihydroxyindole (DHI) and dihydroxyindole-2-carboxylic acid (DHICA), shown in Fig. 1.[7–10] Eumelanin has many other functions attributed to it aside from photoprotection. Some of these include thermal-regulation, cation chelation, antibiotic properties, and acting as a free-radical sink.[2,11–13] Intermolecular hydrogen bonding has previously been shown to be an important factor in the photoprotection of eumelanin, both through stabilization of photoproducts and through direct interaction.[14,15]

It had previously been shown that catechol has a key role in the photoprotection provided by eumelanin.[16] To study the photoprotective properties of eumelanin, a bottom-up approach was employed by Horbury *et al.*, using 4-*tert*-butylcatechol (4-TBC), an analog of catechol with greater solubility in cyclohexane (a property that was useful for this work).[17] Transient Electronic (UV/visible) Absorption Spectroscopy (TEAS) was used in conjunction with time-resolved velocity ion map imaging to determine the lifetime of excited states of 4-TBC after excitation with UV radiation at 267 nm, in both the gas- and condensed-phase. Horbury *et al.* found that the first excited singlet state (S_1, $^1\pi\pi^*$) decayed via multiple pathways, depending on which solvent 4-TBC was present in, inferred through two features in the transient absorption spectrum (TAS). First, it appears that the 4-*tert*-butylcatechoxyl radical (4-TBC$^{\cdot}$) is forming. This is evidenced by an absorption feature at 390 nm, notably similar

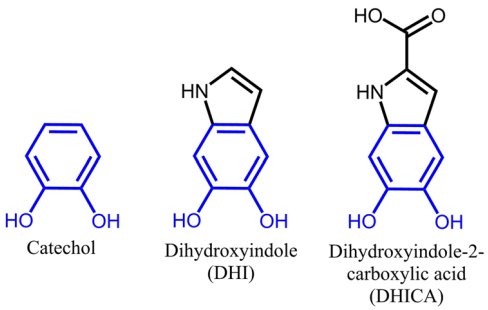

FIG. 1. Shown is (left) catechol, (center) dihydroxyindole (DHI), and (right) dihydroxyindole-2-carboxylic acid (DHICA). Catechol is a key component of different building blocks of eumelanin found in the human body. Blue highlighted catechol units show how it constitutes a key component of DHI and DHICA, important subunits of eumelanin.

to where the catechoxyl radical was observed in liquid paraffin previously (382 nm).[18,19] Second, intersystem crossing is taking place, evidenced through the broad TAS which sees a maximum at less than 350 nm and sloped across the entire probe window, a signifier of a triplet state.[20]

The lifetime of 4-TBC photoexcited to S_1 was observed to be significantly longer when dissolved in the polar solvent acetonitrile compared to when dissolved in nonpolar cyclohexane and measurements in the gas-phase. In acetonitrile, it was suggested that internal conversion (IC), fluorescence, and intersystem crossing were occurring, owing to evidence of similar processes happening in analogous systems, namely, phenol and guaiacol.[19,21,22] A kinetic isotope study involving the deuterated form of 4-TBC (4-TBC-d_2) found a fourfold increase in the lifetime of S_1 in cyclohexane. This suggests that the homolytic cleavage of the O–H bond is a barriered process.[23] The increase in the excited state lifetime in a polar solvent and the observation of a kinetic isotope effect led Horbury *et al.* to plausibly suggest that there are conformational differences in the OH groups within different solvent environments. These were defined as either *closed* or *open* conformation, and shown in Fig. 2, with the nonpolar solvent, cyclohexane, favoring the *closed* conformation. In contrast, in the polar solvent acetonitrile, 4-TBC favors the

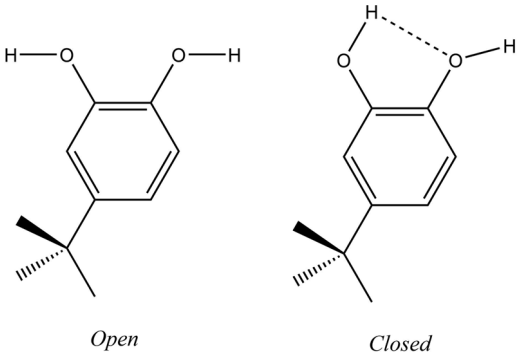

FIG. 2. *Open* and *closed* conformers of 4-*tert*-butylcatechol (4-TBC).

open conformation with two intermolecular hydrogen bonds to the solvent.

This assertion has previously been evidenced by Navarrete *et al.* who showed, through Raman spectroscopy, that catechol adopts the *open* conformer in water, acetone, and ethanol and the *closed* conformer in ether, chloroform, and benzene.[24] They went on to note that, as the previous three solvents were all highly polar and the latter three were significantly less polar, high solvent polarity leads to an *open* structure. Further to this, Varfolomeev *et al.* also proposed the breaking of the intramolecular hydrogen bond, this time in basic, hydrogen bond accepting solvents.[25] It was suggested that, ordinarily, the intramolecular hydrogen bond of catechol would have a cooperative effect on the vibrational modes of the intermolecularly bonded O–H. However, in basic, hydrogen-bond accepting solvents, this effect was no longer observed; therefore, the intramolecular hydrogen bond was likely being broken. The structure proposed by Varfolomeev *et al.* following this cleavage was not, however, an *open* structure.

Time-dependent density functional theory (TDDFT) calculations of the energy of each conformation of the S_1 state showed that while in the *open* conformation, 4-TBC remained planar, whereas the *closed* conformation buckled. Horbury *et al.* suggested that a reduction in the tunneling barrier to O–H dissociation for the buckled *closed* conformation relative to the planar *open* conformation significantly reduced the excited state lifetime.

In 2019, Grieco *et al.* built on these results, studying both the steady-state and ultrafast dynamics of varying concentrations of 4-TBC in cyclohexane.[26] In both UV-Vis and Fourier transform infrared spectroscopy (FTIR), increasing the concentration of 4-TBC in cyclohexane led to loss of fine structure and the increasing intensity of broad peaks in the steady-state spectra. This was attributed to the formation of aggregates within 75 mM 4-TBC in cyclohexane that were not present at 5 mM. This behavior is similar to that previously observed in phenol.[27–29]

The effect on the lifetime of the S_1 state of 4-TBC caused by aggregation was studied through TEAS. The results for 5 mM 4-TBC in cyclohexane were in broad agreement with that observed by Horbury *et al.* for 35 mM, with slight differences being attributed to the amount of aggregation that will have already taken place at 35 mM as opposed to 5 mM.[17] The lifetime of the S_1 state was determined to be 12 ps, predominantly decaying through the O–H dissociation pathway previously suggested. At 75 mM, however, the S_1 state decayed over a lifetime in the region of 150–200 ps. In this case, the O–H dissociation pathway having been significantly retarded was in competition with other relaxation pathways. Notably, the front-runner pathway was IC to the ground state (S_0), likely mediated through a conical intersection. Grieco *et al.* proposed that the lifetime of the O–H dissociation in this system is 190 ps and the lifetime of IC is 154 ps.[26] Owing to the similarity of these time scales, it is likely that both effects are in competition.

In the present work, we investigate the concentration dependent steady-state and time-resolved spectroscopy of catechol in acetonitrile. We use catechol (instead of 4-TBC) as no solubility issues are present in acetonitrile (which inspired the previous studies discussed *supra*), while concurrently it is a closer analog to DHI and DHICA. Furthermore, the smaller size of catechol, compared to 4-TBC, reduces the cost of computational modeling.

Our evidence strongly suggests that the primary controlling factor as to how quickly the S_1 of catechol decays is determined by the nature of the solvent environment, both through its affinity to hydrogen bond and polarity. We suggest that different hydrogen bonding environments hinder the loss of hydrogen (through O–H dissociation), both through solvent-solute interactions and through solute-solute aggregation. We also observe that polarity likely affects barrier height for both O–H dissociation and IC. Furthermore, through comparison with theoretical predictions of vibrational frequencies, we show that the monomer of catechol in acetonitrile must exist in the *closed* form, contrary to what has previously been proposed.[17,24]

II. METHODOLOGY

A. Experimental methodology

In order to carry out FTIR spectroscopy, catechol (Agros Organics, >99%) was dissolved in anhydrous acetonitrile (Sigma-Aldrich, 98%, 5 mM) under a nitrogen environment. The masking effect of water on the vibrational modes associated with the OH groups of catechol necessitated efforts to keep the solution dry. The solution was placed inside a sealed cell with pathlength 500 μm, itself located in a Bruker Vertex 70V IR spectrometer. FTIR spectroscopy was conducted with energy ranging from 500 cm^{-1} to 4000 cm^{-1} with a resolution of 1 cm^{-1}. The same methodology was followed for TEAS experiments using acetonitrile (FISCHER SCIENTIFIC, 99.8% HPLC grade); as anhydrous conditions were not essential, the nitrogen environment was also no longer necessary.

The TEAS setup was the same as used in previous studies.[22,30,31] In brief, the sample was circulated through a flow-through cell (Demountable Liquid Cell by Harrick Scientific Products, Inc.), the position of which was varied with translation stages to minimize surface aggregation. A 1 mJ/pulse 800 nm laser beam is split into two laser beams with a power ratio of 0.95:0.05. The more powerful beam was used to generate the 267 nm pump pulse through second and then third harmonic generation using two β-barium borate crystals. The remaining weaker beam was used to generate the broadband probe pulse by focusing the 800 nm incident light onto a CaF_2 window of 2 mm thickness. This window was translated vertically in order to minimize damage. The white-light probe spanned a spectral region 350–675 nm. The path lengths in the flow-through cell used for 5 mM and 75 mM solutions were, respectively, 500 μm and 56 μm. The fluence of the pump beam was ≈1–2 mJ cm^{-2}, and the absorption at both concentrations was ≈0.4 OD (where OD denotes optical density). The pump-probe time delay (Δt) was varied by altering the optical pathlength of the probe (prior to white-light generation). The instrument response function of the TEAS measurements was retrieved by fitting Gaussians to the time-zero artifacts present in pure acetonitrile and taking the full width half-maximum. These returned values of ≈80 fs; a representative data-set is shown in Fig. 1 in the supplementary material. When studying the 75 mM solution, an aggregate was observed to form on the window of the flow-through cell as the scan progressed; scans typically take 1–2 h to acquire TAS datasets (from which we obtain our transients discussed *infra*). This was evidenced by the drastically altered dynamics of the system, shortening the lifetimes extracted from our transients.

TAS in 75 mM were therefore obtained by randomly distributing all required pump-probe time-delays across six shorter scans (20 mins each), with the sample cell dismantled and cleaned whenever aggregate was observed through its excited state dynamics. The mΔOD signal from each of these data sets was normalized with pump power through matching of consecutive intensities, and the resulting TAS data were recorded as a combination of these, as depicted in Fig. 5. Confidence in this methodology is assured due to the similarity of the lifetime observed with previous literature.[17] While this was not necessary in the case of the 5 mM solution, we reduced the number of time points in order to completely remove any risk of surface aggregation. Owing to this, no data were acquired (in 5 mM samples) beyond 1.25 ns as the lifetime of this species seemed significantly shorter than this. In Fig. 5, we extrapolate these data to 2 ns for comparison with the 75 mM scan.

B. Computational methodology

We calculate predicted vibrational frequencies of catechol in the context of various implicitly and explicitly represented acetonitrile solvent environments. DFT calculations were used to optimize the proposed structures of isolated models of both the *open* and the *closed* conformers of catechol, using the NWChem package.[32] We employed the cc-pVTZ basis set and the PBE functional for initial geometry optimizations.[33,34] These calculations were performed in an implicit solvent using the COSMO solvent model for acetonitrile.[35–37] The *closed* conformer was confirmed to be the overall ground state. For the *open* form, the dihedral angles of both C–C–O–H linkages were locked in order to ensure that the *open* structure was maintained. Following this, the *open* structure was optimized without constraints to confirm that it had relaxed to a local minimum.

To map out the ground state energy surface between these minima, we then perform constrained geometry optimizations at a range of fixed dihedral angles. Results are shown in Fig. 2 of the supplementary material at the PBE/6-31G* level of theory and confirm that the two minima suggested by Horbury *et al.* previously are the only local minima with respect to the O–H dihedral bond angle.

Further to this, each of the minimum energy geometries underwent further optimization and frequency prediction with an implicit solvent model at the PBE0/cc-pVTZ level of theory; this result is shown in Fig. 3 of the supplementary material. Owing to the evident inaccuracy of this calculation, both in regard to absolute energy and energy differences between bands, it was determined that explicit solvent effects needed to be accounted for to construct an accurate model. Results for these more accurate models can be seen in Fig. 3 and in Fig. 4 in the supplementary material and are discussed *infra*.

Candidate structures for catechol in the *open* and *closed* conformers were optimized with two explicit acetonitrile molecules added. These structures are shown in Fig. 5 of the supplementary material. The lowest energy structure resulting from each of these candidates was further refined with geometry optimization and frequency prediction at the PBE0/cc-pVTZ level of theory. Common practice in comparing calculated vibrational frequencies to experiment involves rescaling all computational frequencies by a factor

close to 1 so that a calculated reference peak exactly matches the corresponding experimental result (an approach also applied for this system previously[26]). Scaling factors were determined for the *open* and *closed* conformers to be 0.966 and 0.975, respectively, for the PBE0/cc-pVTZ level of theory.

To verify that the optimized structures obtained are representative of realistic hydrogen-bonding interactions in this pairing of solvent and solute, we also generate several models containing explicit-solvent shells for the two structures. We apply a similar method to that previously used for explicit-solvent calculations for optical absorption spectra.[38,39] First, a classical molecular dynamics calculation is performed using the AMBER package.[40] For a given structure, the solute model was immersed in a 20 Å cube of explicit acetonitrile. For the *open* form, a dihedral angle restraint was applied to both C–C–O–H dihedral angles to ensure that the model could not flip between the *open* and *closed* conformers. The system was heated over 20 ps in the NVT ensemble wherein the temperature is raised from 0 to 300 K using the Langevin thermostat with a collision frequency of 2 ps^{-1}. This collision frequency is used for all further calculations. Following this, a 400 ps pressure equilibration is utilized in the PVT ensemble with the pressure fixed at 1 atm. Next, the system was equilibrated at a constant temperature of 300 K for 100 ps. Finally, snapshot generation proceeds via a further NVT ensemble run, this time with a fixed temperature of 300 K for 800 ps. 200 snapshots are taken by saving a configuration every 4 ps, with the intention being that the resulting snapshots are statistically uncorrelated in terms of the immediate solvent-solute environment. Three of these snapshots for each of the two systems were used for the following vibrational frequency calculations, with the full periodic box cut down to a cluster wherein any solvent molecule further away than 3 Å from the solute was removed. This results in models of size 56–74 atoms.

For each of these clusters, further geometry optimization and frequency calculations were performed, this time with the PBE/cc-pVDZ level of theory. This lower level of theory was used due to the increased computational effort associated with the larger models. A scaling factor was added to both the results for the *open* and *closed* form, 1.058 and 1.062, respectively; these results are shown in Fig. 4 of the supplementary material. For reference, the scaling factors associated with the models used above containing just two solvent molecules, were, at the same PBE/cc-pVDZ level of theory, 1.039 and 1.056 for the *open* and *closed* species, respectively, indicating a degree of consistency between the vibrational frequencies of the small and large models. It is worth noting that the calculations conducted with the PBE functional appear to underestimate the energy of the vibrational modes, whereas those conducted with the PBE0 functional appear to overestimate energy of the vibrational modes, in line with previous findings.[41]

III. RESULTS AND DISCUSSION

A. Examining the structure of monomeric catechol through theoretical frequency prediction

In previous work from our group, it was proposed that 4-TBC existed in two conformers in different solvent environments.[17] In nonpolar environments and the gas-phase, 4-TBC contains an intramolecular hydrogen bond. This structure is referred to, herein, as the *closed* conformer (Fig. 2). In polar solvents, the intramolecular hydrogen bond is broken, with the resulting structure referred to as an *open* conformer (Fig. 2). We investigated this dichotomy through a comparison of predicted vibrational frequencies in explicitly modeled solvent with experimental FTIR data; see Fig. 3.

In the O–H stretch region (3250–3600 cm^{-1}) of the experimental FTIR data of catechol in acetonitrile (5 mM), there are two bands with significant splitting, around 128 cm^{-1}. We attribute this splitting to the inhomogeneity between intramolecularly hydrogen bonded environments and the intermolecularly hydrogen bonded environments. As the *open* conformer does not have an intramolecular hydrogen bond, it is likely that the structure observed in acetonitrile is the *closed* conformer. This is further confirmed using of explicit-solvent frequency prediction with DFT. When predicting frequencies of the closed conformer, after applying the scaling factors discussed in Sec. II B, the results match the experimental data well. There are two bands predicted in the region of interest (red vertical lines) with an average splitting of 120 cm^{-1}, similar to the splitting observed experimentally (*cf.* 128 cm^{-1}). In this, the lower energy vibrational mode is associated with the intermolecularly bonded O–H stretch and the (weaker) higher energy vibrational mode is associated with the intramolecularly bonded O–H stretch; Table 1 in the supplementary material depicts these vibrational modes. This is in contrast to the predicted frequencies of the *open* form, which do not match the experimental result nearly as well. There are still two bands predicted in the region of interest although they are of a very similar energy with an average splitting of 7 cm^{-1} (blue vertical lines), with the predicted relative intensity of the secondary band being significantly weaker. The larger intensity band is associated with the asymmetric stretch of the O–H bonds with the weaker band being associated with the symmetric stretch; as before, Table 1 in the supplementary material depicts these vibrational modes. Given this, we re-evaluate previous findings and

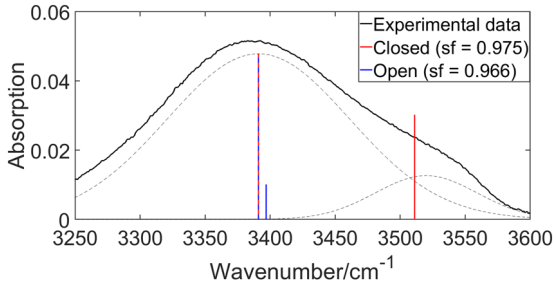

FIG. 3. A comparison between the experimental FTIR spectrum of catechol at 5 mM in acetonitrile (solid black line) and theoretical predictions of vibrational frequencies of catechol complexed with explicit acetonitrile solvent (vertical lines). The red lines are the predicted frequencies of the closed conformer, and the blue lines are the predicted frequencies of the open conformer. Where the red and blue lines lie on top of one another, the line is dashed red and blue. The experimental FTIR spectrum has been deconvolved into two Gaussian functions (shown through dashed black lines) after correcting for a small broad band associated with water absorption. This deconvolution serves to show the similarities between theoretical and experimental results. Calculated lines were shifted to align with the lower energy excitation (see text for details). Note: sf denotes scaling factor.

propose that the *closed* conformer of catechol (and 4-TBC) is the more likely candidate in acetonitrile.

When considering the effect of explicit solvent, it is important to use sufficient solvent molecules to accurately describe nonelectrostatic effects. Unfortunately, DFT is problematically expensive for hybrid functionals such as PBE0 with a large number of atoms. Because of this, more expensive calculations (PBE0/cc-pVTZ) were conducted on a system with just two solvent molecules. Calculations with a full shell of solvent molecules (3 Å radii) were conducted using a less expensive level of theory (PBE/cc-PVDZ) on three snapshots generated with molecular dynamics simulations. Further details can be found in Sec. II B and the supplementary material. As can be seen in Fig. 4 of the supplementary material, when using a full solvent shell, similar results are obtained to the more expensive calculations. In this case, this returns scaling factors of 1.062 and 1.058 for the *closed* and *open* conformers, respectively. This set of calculations predicted a splitting of 125 cm^{-1}. A caveat is warranted here: This result was obtained with only three snapshots and hence the variance in the calculated splittings was quite large, ≈35 cm^{-1}. This variation based on local environment is to be expected, however, and is reflected in the broadness of the corresponding experimental band. Vibrational O–H stretching bands are often broadened due to an array of local minima possible within different solvent configurations. Additionally, homogeneous broadening will also be influencing the peak widths. In order to properly sample the full array of potential configurations, one would need to run significantly more snapshots, at great computational cost. For our purposes, however, three snapshots seem to be sufficient to confirm that the methodology described previously using two solvent molecules gives a result in qualitative agreement to that with the full 3 Å solvent shell.

In recent work, Grieco *et al.* recorded a similar frequency spectrum when studying 3,5-di-*t*-butylcatechol and 3,5-di-*t*-butyl-*o*-quinone aggregates in cyclohexane.[42] They observed one broader band which they attributed to the intermolecularly hydrogen bonded O–H (referred to as bond "D") and one sharp band which they attributed to the intramolecularly hydrogen bonded O–H (referred to as bond "*b*"). The band we attribute to "D" (in the present work) was observed in acetonitrile at a similar frequency to that observed by Grieco *et al.*, albeit slightly shifted (at 3391 cm^{-1} as opposed to ≈3450 cm^{-1} observed previously), this is likely due to electrostatic effects. The band we attribute to "*b*" is broadened in acetonitrile (*cf.* sharp in cyclohexane); we plausibly suggest that this is due to a bifurcated hydrogen bond, similar to that shown in Fig. 6 in the supplementary material, which does not occur in cyclohexane.

We note that based on these results, it is unlikely that both the *open* and *closed* conformers are present. The splitting between the bands of the *open* form would not be visible even if it was present, given that they are only 7 cm^{-1} apart and have an intensity ratio of 1:15. However, we propose that there would be a significant difference in frequencies associated with the respective intermolecularly bonded O–H stretches of the *open* and *closed* forms. This is confirmed by the calculations, where the predicted energies for the lower energy band in *open* and *closed* conformers are 32 cm^{-1} apart. As we only see one primary band in the experimental spectrum, the *open* conformer is likely not present in a measurable quantity. This difference is not seen in Fig. 3 as both peaks were heterogeneously scaled and therefore are on top of one another. This difference can, however, be seen in Table 1 in the supplementary material.

Finally, Varfolomeev *et al.* noted that the presence of a basic species hydrogen bonded to catechol could weaken the internal hydrogen bond.[25] In our calculated geometries, when moving from catechol in implicit solvent to catechol with two explicit solvent molecules present, we observe an increase in bond-length from 2.10 Å to 2.25 Å. While 2.25 Å is still well within the expected bond length for hydrogen bonding, it is clear that the internal hydrogen bond is being weakened by the presence of the solvent. We do not measure the strength of the hydrogen bonding and to what degree it is weakened by collaborative effects from the basic acetonitrile as it is beyond the scope of this work, although it would definitely be an interesting avenue for future research.

We close this section noting that it has been suggested in the literature that guaiacol (2-methoxyphenol) exhibits the same *open* and *closed* behavior in solution as was previously suggested for catechol.[22] As guaiacol has no intermolecular hydrogen bond in the *closed* form, it is unlikely it behaves analogously with catechol. The lack of this intermolecular hydrogen bond will prevent aggregation and solvent-solute hydrogen bonding interactions. Furthermore, the *open* form of guaiacol is also likely to behave differently to that of catechol. As there is no internal hydrogen bond, the collaborative effects discussed by Varfolomeev *et al.* will not be present.[25] We therefore make no suggestion about the structure of guaiacol in polar solution based on the present work.

B. Transient electronic absorption spectroscopy results

The previous measurements by Horbury *et al.* in 4-TBC showed that the lifetime of the S_1 state in cyclohexane is significantly shorter than that in acetonitrile. Following our discussion *supra* regarding the absence of the previously predicted *open* conformer, we sought an alternative explanation for this difference in lifetime. For this, TEAS was conducted on catechol in acetonitrile at two different concentrations: 5 mM and 75 mM. Figure 4 shows representative TAS at 5 mM (top) and 75 mM (bottom) at four different pump-probe time-delays (Δt).

Two major points are worth acknowledging at this stage. First, the absorption feature at 390 nm associated with the formation of the catechoxyl radical is present in both cases; however, it is clearly much weaker compared to previous work in cyclohexane.[17–19] The size of this radical feature at 75 mM is consistent with previous observations in acetonitrile in a 35 mM solution. In 5 mM solution, however, it appears to be even further depleted, the reason for this will be discussed shortly. Second, it can clearly be seen that catechol in 5 mM solution decays (from the S_1 state) much faster than in 75 mM solution. Owing to this, a feature which resembles a triplet state can be more clearly evidenced at Δt = 2000 ps.[17,20] This feature has a maximum at below 350 nm and appears to slope across the entire spectral window of the probe. Interestingly, this agrees with Gauden *et al.* who find this same triplet state formation in their studies of dihydroxyindole (Fig. 1), further verifying the validity of this bottom-up approach.[17,43]

The decay of the excited state for each of these concentrations was studied in more detail by examining transient slices across the full set of time delays. These transients were obtained by integrating

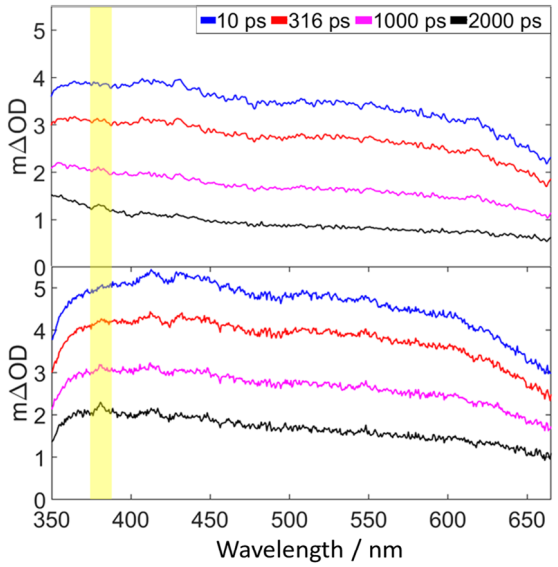

FIG. 4. Selected TAS at different Δt values of catechol in acetonitrile at (top) 5 mM and (bottom) 75 mM, following photoexcitation at 267 nm. The yellow bar serves to highlight the absorption of the catechoxyl radical species.

a 5 nm slice centered on the probe wavelength of 450 nm; these are shown in Fig. 5. This wavelength was selected as the radical photoproduct does not absorb in this region, an approach also followed by Horbury *et al.*[17] To extract the dynamical information, these transients were fit with a biexponential decay function which was convolved with a Gaussian function to model our instrument response function (≈80 fs). From these transients, two time-constants were extracted, τ_1 and τ_2.

The time-constant τ_1 was 70 ± 40 fs and 450 ± 50 fs for 5 mM and 75 mM concentration solutions, respectively. When studying 4-TBC in acetonitrile (35 mM), Horbury *et al.* observed similar time scales or τ_1 of 230 ± 20 fs, which they assigned to vibrational energy transfer as well as solvent rearrangement.[17,44] Based on this, we attribute the present τ_1 to a similar relaxation pathway.

Somewhat more interesting is the time-constant τ_2 extracted from the fit. The dynamics captured by this time-constant are

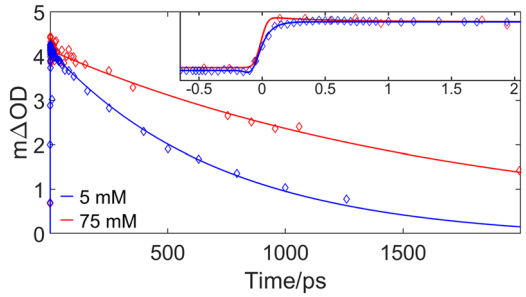

FIG. 5. TAS transients of catechol at a probe wavelength of 450 nm in acetonitrile at (blue) 5 mM and (red) 75 mM, following photoexcitation at 267 nm. Early time delays are shown in the inset.

TABLE I. Excited state lifetimes of catechol and 4-TBC in different solvents, cyclohexane (CHX) and acetonitrile (CH_3CN) at different concentrations. α and β denote, respectively, data taken from Horbury *et al.*[17] and Grieco *et al.*[26] in 4-TBC. Remaining data correspond to the present work on catechol.

Concentration (mM)	Lifetime in CH_3CN (ps)	Lifetime in CHX (ps)
5	730 ± 30	$12.15 \pm 0.3^{\beta}$
35	$1700 \pm 100^{\alpha}$	$18 \pm 1^{\alpha}$
75	1700 ± 200	$154 \pm 2^{\beta}$

assigned to depletion of the excited S_1 state. This will depend on the potential for O–H dissociation and access to the S_0/S_1 IC pathway. The lifetime observed for the S_1 state of catechol in acetonitrile at 5 mM was 0.73 ± 0.03 ns, increasing to 1.7 ± 0.2 ns for 75 mM. Table I collates the time-constants from the present work on catechol and that of Horbury *et al.* and Grieco *et al.* on 4-TBC, in cyclohexane and acetonitrile at different solvent concentrations.[17,26] The relative amplitudes of these exponential functions are displayed in Table 2 of the supplementary material.

When studying catechol in acetonitrile at 35 mM, Horbury *et al.* observed an S_1 lifetime of 1.7 ns. We observe this same lifetime at 75 mM concentration. This suggests that Horbury *et al.* were likely observing the properties of aggregated 4-TBC in their previous work;[17] we add here that Grieco *et al.* noted that 38 mM 4-TBC in cyclohexane is ≈50% aggregated. It was proposed that this accounts for shorter lifetime of τ_2 measured at 5 mM vs what Horbury *et al.* measured at 35 mM.[26]

Figure 6 shows a schematic of the different decay pathways available to the S_1 state of catechol. As stated in previous work, the primary route of S_1 decay for monomeric 4-TBC in cyclohexane, and likely catechol, is through homolytic fission of the nonintramolecularly bound O–H bond and the formation of the catechoxyl radical.[17,26] This is identified through the growth of an absorption feature at 390 nm.[18,19] In this case, the energy barrier along the reaction

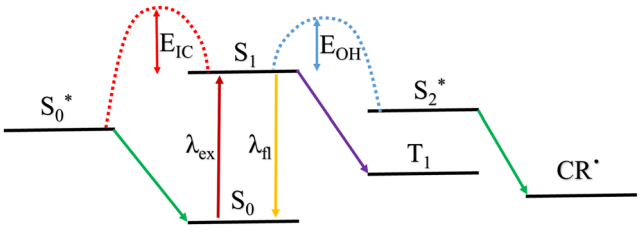

FIG. 6. A schematic to show different decay pathways for the S_1 state of catechol. The maroon arrow labeled λ_{ex} denotes the pump pulse, which excites the system into the S_1 state; this is, in this case, at 267 nm. This S_1 state can undergo either IC through transition to a vibrationally hot S_0 state (denoted S_0^*) or O–H dissociation transition to yield the catechoxyl radical ($CR^{\bullet}$), mediated through transition to the S_2 state ($^1\pi\sigma^*$). Both of these are barriered processes, both of which have suggested barriers (labeled E_{IC} and E_{OH}) which govern the excited state behavior of catechol. If barriers are sufficiently large, then two further paths become available: fluorescence and intersystem crossing; these are represented by the yellow (labeled λ_{fl}) and purple arrows, respectively.

coordinate associated with O–H dissociation, which we call E_{OH}, is small. This O–H dissociation pathway has previously been attributed to tunneling from the $S_1\ ^1\pi\pi^*$ state to the dissociative (along O–H) $^1\pi\sigma^*$ state (S_2).[45] Owing to the small energy barrier along this pathway (denoted E_{OH} in Fig. 6), the process is therefore ultrafast (≈12 ps), outcompeting other processes.

It has been shown previously that when aggregated in cyclohexane, the S_1 state of 4-TBC decayed through two competing mechanisms: (1) O–H dissociation (*vide supra*) and (2) IC mediated via an S_1/S_0 conical intersection.[26] This was seen through the apparent reduction in the signal intensity of the catechoxyl radical feature although this was somewhat challenging to observe due to a solvatochromic shift and broadening caused by hydrogen bonding. These studies revealed a lifetime for IC of 154 ps, meaning that O–H dissociation has sufficiently been hindered to enable this pathway to be competitive (with O–H dissociation). An increase in E_{OH} from 0.1 eV for free O–H dissociation to 0.51 eV for O–H dissociation when bonded via intermolecular hydrogen bond has been calculated previously.[26] This increased barrier height resulted in a lifetime for O–H dissociation of 190 ps. This was broadly in agreement with the previous literature in which the effect of intermolecular hydrogen bonding was observed in phenol clusters in the gas-phase.[46] It was shown that hydrogen bonding causes the dissociative S_2 ($^1\pi\sigma^*$) state to become bound at higher bond distances. This work was based on calculations previously conducted on dimeric water.[26,47]

Returning to present studies, when studying catechol in acetonitrile at 5 mM, a concentration that we consider catechol to be primarily monomeric, we observe a τ_2 of 730 ps. This lifetime is significantly longer than the lifetime of both IC and O–H dissociation seen in 4-TBC at 5 mM in cyclohexane (see above). There are multiple factors that could be influencing the increase in τ_2. The first of which are the barriers along the reaction coordinates toward IC and O–H bond dissociation (E_{IC} and E_{OH}, respectively), which must be increasing in order for a lifetime of 730 ps to be observed. This could be a consequence of energy level stabilization or destabilization by the solvent/aggregate. To garner a quantitative picture, one would need to theoretically determine the relative energy landscapes associated with each of these processes as well as conduct target analysis of the TAS data. The latter was previously conducted by Grieco *et al.* when studying these processes in 4-TBC when aggregated in cyclohexane.[26] This goes beyond the scope of the present study. Ultimately, the slowing of these two processes has allowed two other mechanisms to begin to compete. The first is an intersystem crossing pathway, which is evidenced in Fig. 4 by the growth of an absorption feature in the TAS around 350 nm which slopes across our entire spectral window of our probe.[20] This triplet state was also observed by Horbury *et al.*; however, as discussed previously, it is likely that they were observing an aggregated species. The second process is fluorescence, which is also likely occurring, as discussed in Sec. I. As can be seen in Fig. 4, the signal associated with the catechoxyl radical absorption is almost not visible in this case owing to the degree of competition from intersystem crossing, and fluorescence (in addition to IC).

When observing aggregated catechol in acetonitrile, at 75 mM, τ_2 increases further to 1.7 ns. This is the same lifetime that was previously observed by Horbury *et al.* in 35 mM 4-TBC in acetonitrile.[17] This is over double that of the monomeric species in acetonitrile. We speculate that E_{IC} is increasing, viewed through the aggregate taking up a rigid structure which hinders the geometric rearrangement necessary to approach the conical intersection geometry along the IC reaction pathway. Naturally, this may also likely lead to an increase in catechoxyl radical formation (which could explain the increased radical signature seen in Fig. 4), fluorescence, and intersystem crossing although we are unable to directly measure these quantum yields from the present experimental setup.

IV. CONCLUSIONS

In this paper, we have considered solvent effects on the lifetime of the S_1 state of catechol in solution drawing on (primarily) two previous studies, as well as our present findings. Horbury *et al.* previously suggested that 4-TBC, a catechol mimic, existed in an *open* conformer when in polar solvents and a *closed* conformer when in nonpolar solvents or the gas-phase.[17] We argue this is not the case by showing that in acetonitrile, a polar solvent, catechol is in the *closed* form. This was shown through a comparison of predicted vibrational frequencies in explicitly modeled solvent allied with experimental FTIR data. In the O–H stretch region (3200–3600 cm^{-1}) of the experimental FTIR spectrum of catechol in acetonitrile (5 mM), there are two peaks with significant splitting, around 128 cm^{-1}. This was compared to frequency prediction with DFT using an explicit solvent model. When considering the *closed* conformer, there were two peaks predicted in the region of interest with an average splitting of 120 cm^{-1}; this matches well with what was observed experimentally. The predicted frequencies of the *open* conformer still yield two peaks predicted in the region of interest. They are, however, of a very similar energy with an average splitting of 7 cm^{-1}; we suggest the *closed* conformer is the species present in acetonitrile. While it has been shown by Huijser *et al.* that O–H dissociation in the catechol moiety is not the primary decay pathway when considering DHICA, it is still valuable when considering a bottom-up approach to know the exact geometry of catechol in different solvents.[48] The existence of the *closed* form in DHICA in polar solvents will change the way we view the structure of this important eumelanin building block.

Given that the *open* vs *closed* dichotomy is not the cause of the observed differences in the S_1 lifetime of catechol in cyclohexane and acetonitrile, we aimed to find other explanations. Grieco *et al.* suggested that when aggregated, 4-TBC undergoes intermolecular hydrogen bonding, the barrier along the O–H dissociation (E_{OH}) coordinate is significantly increased.[26] This leads to an increase in the time taken to undergo O–H dissociation (from 12 ps up to 190 ps) which allows IC to the ground state to occur as a competing mechanism. In acetonitrile at 5 mM, which we assume catechol to be primarily monomeric, the lifetime observed for S_1 of catechol was 713 ps. From this, it is reasonable to suggest that both the IC path and the O–H dissociation are retarded significantly by the change in the solvent. When studying aggregated catechol (75 mM), the lifetime of the S_1 state increases further still to around 1700 ps. We suggest that aggregation disfavors IC, possibly due to a rigid structure decreasing the molecules ability to reach a geometric conical intersection. This work has shown that explicit-solvent methodology is key when calculating the vibrational frequencies of molecules in interacting solvent. Combining this with highly complementary steady-state and transient absorption spectroscopy enables us to gain

key dynamical insights into how a prominent eumelanin building block behaves when in polar, hydrogen bond accepting solvents both as a monomer and as an aggregated species.

While this work was under review, Grieco *et al.* published a further related work (Ref. 49), which addresses the effect of inter- and intramolecular hydrogen bonding on the ultrafast photochemistry of catechol. This was achieved through varying concentrations of Et_2O, resulting in three different hydrogen bonding arrangements.

SUPPLEMENTARY MATERIAL

The supplementary material for this paper includes a fitted time-zero artifact for the TEAS setup in acetonitrile solvent; a two-dimensional plot of S_0 energy of catechol with respect to the dihedral angles of the two OH groups; calculated frequencies for catechol in the *open* and *closed* conformer as calculated using both an implicit solvent model and an explicit solvent shell; the starting geometries for the two-solvent frequency calculations; the vibrational modes in the O–H stretch region associated with the two-solvent frequency calculations; and a representation of the three different types of hydrogen bonding possible in the *closed* conformer of catechol in acetonitrile; and a table of amplitudes for the fitted biexponential functions described in Sec. III B.

The underlying data of this publication can be accessed via the Zenodo Archive at DOI: 10.5281/zenodo.3241438.

ACKNOWLEDGMENTS

M.A.P.T. thanks the EPSRC for a doctoral studentship through the EPSRC Centre for Doctoral Training in Molecular Analytical Science, Grant No. EP/L015307/1. M.D.H. thanks the Leverhulme Trust for postdoctoral funding. Computing facilities were provided by the Scientific Computing Research Technology Platform of the University of Warwick. We acknowledge the use of Athena at HPC Midlands+, which was funded by the EPSRC by Grant NO. EP/P020232/1, in this research, as part of the HPC Midlands+ consortium. N.D.M.H. acknowledges the support of EPSRC Grant No. EP/P02209X/1 and Royal Society Research Grant No. RG150013. V.G.S. is grateful to the EPSRC for an equipment grant (No. EP/N010825) and the Royal Society and the Leverhulme Trust for a Royal Society Leverhulme Trust Senior Research Fellowship.

REFERENCES

[1] J. Moan, "Visible light and UV radiation," in *Radiation at Home, Outdoors and in the Workplace* (Scandinavian Publisher, Oslo, 2001), pp. 69–85.
[2] N. Agar and A. R. Young, "Melanogenesis: A photoprotective response to dna damage?," Mutat. Res., Fundam. Mol. Mech. Mutagen. **571**, 121–132 (2005).
[3] N. Kollias, R. M. Sayre, L. Zeise, and M. R. Chedekel, "New trends in photobiology: Photoprotection by melanin," J. Photochem. Photobiol., B **9**, 135–160 (1991).
[4] M. A. Weinstock, "Epidemiology of melanoma," *Current Research and Clinical Management of Melanoma* (Springer, 1993), pp. 29–56.
[5] H. Z. Hill, "The function of melanin or six blind people examine an elephant," Bioessays **14**, 49–56 (1992).
[6] A. Büngeler, B. Hämisch, and O. Strube, "The supramolecular buildup of eumelanin: Structures, mechanisms, controllability," Int. J. Mol. Sci. **18**, 1901 (2017).
[7] S. Ito, "Reexamination of the structure of eumelanin," Biochim. Biophys. Acta, Gen. Subj. **883**, 155–161 (1986).
[8] W. L. Cheun, "The chemical structure of melanin," Pigm. Cell Res. **17**, 422–423 (2004).
[9] J. Simon and S. Ito, "The chemical structure of melanin-reply," Pigm. Cell Res. **17**, 423–424 (2004).
[10] E. Kaxiras, A. Tsolakidis, G. Zonios, and S. Meng, "Structural model of eumelanin," Phys. Rev. Lett. **97**, 218102 (2006).
[11] W. L. Morison, "What is the function of melanin?," Arch. Dermatol. **121**, 1160–1163 (1985).
[12] P. U. Giacomoni, "Open questions in photobiology III. Melanin and photoprotection," J. Photochem. Photobiol., B **29**, 87–89 (1995).
[13] H. Z. Hill and G. J. Hill, "Uva, pheomelanin and the carcinogenesis of melanoma," Pigm. Cell Res. **13**, 140–144 (2000).
[14] L. Panzella, G. Gentile, G. D'Errico, N. F. Della Vecchia, M. E. Errico, A. Napolitano, C. Carfagna, and M. d'Ischia, "Atypical structural and π-electron features of a melanin polymer that lead to superior free-radical-scavenging properties," Angew. Chem., Int. Ed. **52**, 12684–12687 (2013).
[15] C. Frontana and I. González, "The role of intramolecular hydrogen bonding in the electrochemical behavior of hydroxy-quinones and in semiquinone stability," J. Braz. Chem. Soc. **16**(3A), 299–307 (2005).
[16] P. Meredith and T. Sarna, "The physical and chemical properties of eumelanin," Pigm. Cell Res. **19**, 572–594 (2006).
[17] M. D. Horbury, L. A. Baker, W.-D. Quan, J. D. Young, M. Staniforth, S. E. Greenough, and V. G. Stavros, "Bridging the gap between the gas phase and solution phase: Solvent specific photochemistry in 4-tert-butylcatechol," J. Phys. Chem. A **119**, 11989–11996 (2015).
[18] E. Land and G. Porter, "Primary photochemical processes in aromatic molecules. Part 7.—Spectra and kinetics of some phenoxyl derivatives," Trans. Faraday Soc. **59**, 2016–2026 (1963).
[19] O. Brede, S. Kapoor, T. Mukherjee, R. Hermann, and S. Naumov, "Diphenol radical cations and semiquinone radicals as direct products of the free electron transfer from catechol, resorcinol and hydroquinone to parent solvent radical cations," Phys. Chem. Chem. Phys. **4**, 5096–5104 (2002).
[20] D. Bent and E. Hayon, "Excited state chemistry of aromatic amino acids and related peptides. I. Tyrosine," J. Am. Chem. Soc. **97**, 2599–2606 (1975).
[21] Y. Zhang, T. A. Oliver, M. N. Ashfold, and S. E. Bradforth, "Contrasting the excited state reaction pathways of phenol and para-methylthiophenol in the gas and liquid phases," Faraday Discuss. **157**, 141–163 (2012).
[22] S. E. Greenough, M. D. Horbury, J. O. Thompson, G. M. Roberts, T. N. Karsili, B. Marchetti, D. Townsend, and V. G. Stavros, "Solvent induced conformer specific photochemistry of guaiacol," Phys. Chem. Chem. Phys. **16**, 16187–16195 (2014).
[23] A. Douhal, F. Lahmani, and A. H. Zewail, "Proton-transfer reaction dynamics," Chem. Phys. **207**, 477–498 (1996).
[24] J. L. Navarrete and F. Ramírez, "A study by Raman spectroscopy and the semiempirical am1 method on several 1, 2-dihydroxybenzene solutions," Spectrochim. Acta, Part A **49**, 1759–1767 (1993).
[25] M. A. Varfolomeev, D. I. Abaidullina, A. Z. Gainutdinova, and B. N. Solomonov, "FTIR study of h-bonds cooperativity in complexes of 1, 2-dihydroxybenzene with proton acceptors in aprotic solvents: Influence of the intramolecular hydrogen bond," Spectrochim. Acta, Part A **77**, 965–972 (2010).
[26] C. Grieco, F. R. Kohl, Y. Zhang, S. Natarajan, L. Blancafort, and B. Kohler, "Intermolecular hydrogen bonding modulates O-H photodissociation in molecular aggregates of a catechol derivative," Photochem. Photobiol. **95**, 163 (2018).
[27] J. Dearden, "Investigation of the self-association of phenols and anilines by ultraviolet spectroscopy," Can. J. Chem. **41**, 2683–2691 (1963).
[28] K. B. Whetsel and J. Lady, "Self-association of phenol in nonpolar solvents," in *Spectrometry of Fuels* (Springer, 1970), pp. 259–279.
[29] D. Gerrard and W. Maddams, "Solvent effects in uv absorption spectra. I. Phenol in cyclohexane ethanol mixtures," Spectrochim. Acta, Part A **34**, 1205–1211 (1978).
[30] S. E. Greenough, G. M. Roberts, N. A. Smith, M. D. Horbury, R. G. McKinlay, J. M. Żurek, M. J. Paterson, P. J. Sadler, and V. G. Stavros, "Ultrafast photoinduced ligand solvolysis of *cis*-[Ru (bipyridine)$_2$ (nicotinamide)$_2$]$^{2+}$: Experimental and theoretical insight into its photoactivation mechanism," Phys. Chem. Chem. Phys. **16**, 19141–19155 (2014).

[31] M. Horbury, W.-D. Quan, A. Flourat, F. Allais, and V. Stavros, "Elucidating nuclear motions in a plant sunscreen during photoisomerization through solvent viscosity effects," Phys. Chem. Chem. Phys. **19**, 21127–21131 (2017).
[32] M. Valiev, E. J. Bylaska, N. Govind, K. Kowalski, T. P. Straatsma, H. J. Van Dam, D. Wang, J. Nieplocha, E. Apra, T. L. Windus *et al.*, "NWChem: A comprehensive and scalable open-source solution for large scale molecular simulations," Comput. Phys. Commun. **181**, 1477–1489 (2010).
[33] J. P. Perdew, K. Burke, and M. Ernzerhof, "Generalized gradient approximation made simple," Phys. Rev. Lett. **77**, 3865 (1996).
[34] E. R. Davidson, "Comment on 'comment on Dunning's correlation-consistent basis sets'," Chem. Phys. Lett. **260**, 514–518 (1996).
[35] A. Klamt and G. Schüürmann, "COSMO: A new approach to dielectric screening in solvents with explicit expressions for the screening energy and its gradient," J. Chem. Soc., Perkin Trans. 2 **1993**, 799–805.
[36] D. M. York and M. Karplus, "A smooth solvation potential based on the conductor-like screening model," J. Phys. Chem. A **103**, 11060–11079 (1999).
[37] P. Winget, D. M. Dolney, D. J. Giesen, C. J. Cramer, and D. G. Truhlar, *Minnesota Solvent Descriptor Database* (Deptartment of Chemistry and Supercomputer Institute, University of Minnesota, Minneapolis, MN, 1999).
[38] M. A. Turner, M. D. Horbury, V. G. Stavros, and N. D. Hine, "Determination of secondary species in solution through pump-selective transient absorption spectroscopy and explicit-solvent TDDFT," J. Phys. Chem. A **123**, 873 (2019).
[39] T. J. Zuehlsdorff, P. D. Haynes, M. C. Payne, and N. D. M. Hine, "Predicting solvatochromic shifts and colours of a solvated organic dye: The example of nile red," J. Chem. Phys. **146**, 124504 (2017).
[40] D. A. Case, J. T. Berryman, R. M. Betz, D. S. Cerutti, T. E. Cheatham III, T. A. Darden, R. E. Duke, T. J. Giese, H. Gohlke, A. W. Goetz, N. Homeyer, S. Izadi, P. Janowski, J. Kaus, A. Kovalenko, T. S. Lee, S. LeGrand, P. Li, T. Luchko, R. Luo, B. Madej, K. M. Merz, G. Monard, P. Needham, H. Nguyen, H. T. Nguyen, I. Omelyan, A. Onufriev, D. R. Roe, A. Roitberg, R. Salomon-Ferrer, C. L. Simmerling, W. Smith, J. Swails, R. C. Walker, J. Wang, R. M. Wolf, X. Wu, D. M. York, and P. A. Kollman, *Amber 2015*, University of California, San Francisco, 2015.
[41] I. Alecu, J. Zheng, Y. Zhao, and D. G. Truhlar, "Computational thermochemistry: Scale factor databases and scale factors for vibrational frequencies obtained from electronic model chemistries," J. Chem. Theory Comput. **6**, 2872–2887 (2010).
[42] C. Grieco, J. M. Empey, F. R. Kohl, and B. Kohler, "Probing eumelanin photoprotection using a catechol: Quinone heterodimer model system," Faraday Discuss. **216**, 520 (2019).
[43] M. Gauden, A. Pezzella, L. Panzella, A. Napolitano, M. d'Ischia, and V. Sundström, "Ultrafast excited state dynamics of 5, 6-dihydroxyindole, a key eumelanin building block: Nonradiative decay mechanism," J. Phys. Chem. B **113**, 12575–12580 (2009).
[44] E. W. Castner, Jr., M. Maroncelli, and G. R. Fleming, "Subpicosecond resolution studies of solvation dynamics in polar aprotic and alcohol solvents," J. Chem. Phys. **86**, 1090–1097 (1987).
[45] A. S. Chatterley, J. D. Young, D. Townsend, J. M. Żurek, M. J. Paterson, G. M. Roberts, and V. G. Stavros, "Manipulating dynamics with chemical structure: Probing vibrationally-enhanced tunnelling in photoexcited catechol," Phys. Chem. Chem. Phys. **15**, 6879–6892 (2013).
[46] V. Poterya, L. Šištík, P. Slavíček, and M. Fárník, "Hydrogen bond dynamics in the excited states: Photodissociation of phenol in clusters," Phys. Chem. Chem. Phys. **14**, 8936–8944 (2012).
[47] G. Quinkert, "Photochemistry of linearly conjugated cyclohexadienones in solution," Pure Appl. Chem. **33**, 285–316 (1973).
[48] A. Huijser, A. Pezzella, J. K. Hannestad, L. Panzella, A. Napolitano, M. d'Ischia, and V. Sundström, "UV-dissipation mechanisms in the eumelanin building block DHICA," ChemPhysChem **11**, 2424–2431 (2010).
[49] C. Grieco, A. T. Hanes, L. Blancafort, and B. Kohler, "Effects of intra-and intermolecular hydrogen bonding on O–H bond photodissociation pathways of a catechol derivative," J. Phys. Chem. A **123**, 5356–5366 (2019).

Chapter 4

Insights into the photoprotection mechanism of the UV filter homosalate

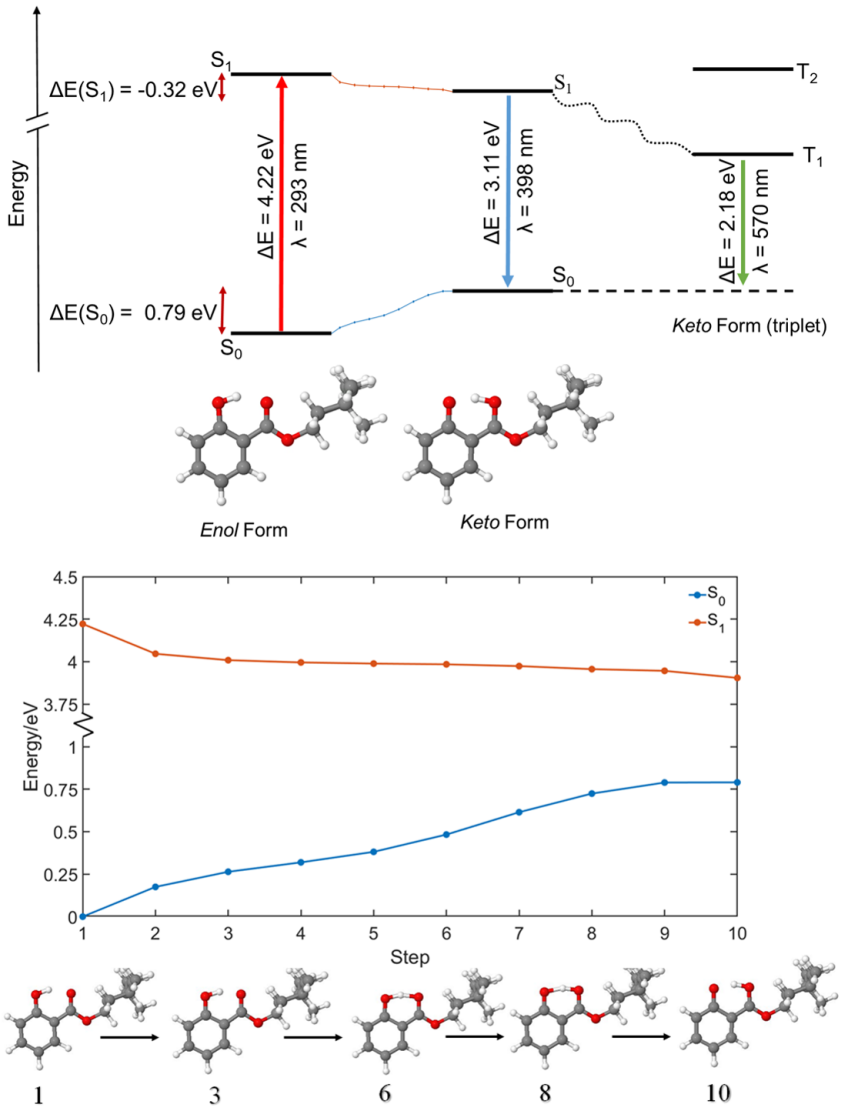

Journal Name

ARTICLE TYPE

Cite this: DOI: 10.1039/xxxxxxxxxx

Insights into the photoprotection mechanism of the UV filter homosalate†

Matthew A. P. Turner,‡[a,b] Emily L. Holt,‡[a,b] Konstantina M. Krokidi,‡[a] Piyush Mishra,[c] Timothy S. Zwier,[c] Natércia d. N. Rodrigues,*[a] Vasilios G. Stavros*[a]

Received Date
Accepted Date

DOI: 10.1039/xxxxxxxxxx

www.rsc.org/journalname

Homosalate (HMS) is a salicylate molecule that is commonly included within commercial sunscreen formulations to provide protection from the adverse effects of ultraviolet (UV) radiation exposure. In the present work, the mechanisms by which HMS provides UV photoprotection have been explored, using a combination of time-resolved ultrafast laser spectroscopy in the gas-phase and in solution, laser-induced fluorescence (LIF), steady-state absorption spectroscopy, and computational methods. These techniques combine to show that the *enol* tautomer of HMS undergoes ultrafast excited state intramolecular proton transfer (ESIPT) upon photoexcitation in the UVB (280 – 315 nm) region; once in the *keto* tautomer, the excess energy is predominantly dissipated non-radiatively. Sharp transitions are observed in the LIF spectrum at close-to-origin excitation energies, which points towards a second conformer that does not undergo ESIPT. While we propose that, overall, HMS exhibits mostly favourable photophysical characteristics of a UV filter for inclusion in sunscreen formulations, the potential reactivity and toxicity of long-lived states warrants further investigation.

Introduction

Salicylates are defined as salts or esters derived from salicylic acid, several of which have uses within the personal care and pharmaceutical industries.[1] In addition to being included in cosmetics for fragrance and antioxidant properties,[1,2] salicylates are used as chemical (organic) filters in sunscreen blends, for solar protection via absorbance of ultraviolet (UV) radiation, specifically UVB radiation (290 – 320 nm).[3,4] Despite regulated exposure to UV radiation having positive effects on human health, such as facilitating the synthesis of vitamin D, the use of UV filters in sunscreen formulations is necessary to prevent the adverse effects of overexposure, such as an increased risk of skin cancers.[5–12]

Despite having a low extinction coefficient compared to other available UV filters,[13] salicylates are an appealing choice for sunscreen formulators for several reasons. Firstly, the minimal solvatochromic shift that is observed in salicylates upon significant changes in solvent polarity has been demonstrated in at least 13 different solvents.[14,15] This negligible shift in peak absorption implies that a range of excipients may be used in a formulation without changing the protection range of wavelengths afforded by these molecules. Furthermore, salicylates contained within sunscreen formulations can serve as solubilizers for other UV filters such as avobenzone, which to date remains the most widely implemented UVA (320 – 400 nm) filter in the world.[16–18] In addition, salicylates have a favourable safety record, with few

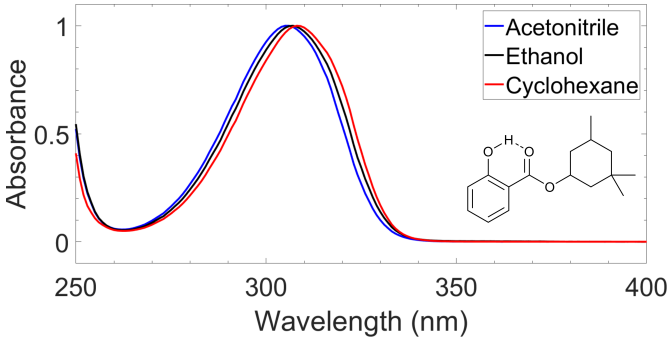

Fig. 1 (a) Normalised UV-visible spectra of homosalate (HMS) in acetonitrile (blue line), ethanol (black line) and cyclohexane (red line), with molecular structure of HMS inset. The dashed line indicates the presence of an intramolecular hydrogen bond.

[a] *Department of Chemistry, University of Warwick, Gibbet Hill Road, Coventry, CV4 7AL, United Kingdom; *E-mail: v.stavros@warwick.ac.uk or n.das-neves-rodrigues@warwick.ac.uk*

[b] *Molecular Analytical Science Centre for Doctoral Training, Senate House, University of Warwick, Coventry, CV4 7AL, United Kingdom*

[c] *Department of Chemistry, Purdue University, West Lafayette, Indiana 47907-2084, United States*

† Electronic Supplementary Information (ESI) available: [details of any supplementary information available should be included here]. See DOI: 10.1039/b000000x/

‡These authors contributed equally to this work.

reports of allergenic effects of these compounds.[19,20] However, a consensus is yet to be reached on whether salicylates used in sunscreens are photostable, that is, if they do not degrade upon prolonged UV exposure. Many publications report that they are indeed photostable,[18,21–23] while other reports also exist to the contrary.[24,25]

The molecule chosen as the focus of this study is homomenthyl salicylate (herein referred to as homosalate, HMS); its molecular structure and the range of UVB protection it provides is shown in Fig. 1. This molecule is approved for use in sunscreen formulations worldwide and can be employed in substantial quantities (*e.g* up to 15% w/w in the United States).[26] Recent studies in rat models have shown that HMS had low dermal permeability and did not cause any endocrine disruption, both of which are major concerns for many existing UV filters used in sunscreen formulations.[27,28] In addition, an earlier review by Nash[29] deemed HMS to have a favourable toxicological profile. However, in the MCF-7 cell line, HMS was shown to have cytotoxic and genotoxic characteristics, and extensive studies on the toxicological effects of HMS are recommended.[30]

In this study, femtosecond (fs, 10^{-15} s) pump-probe spectroscopy techniques in both the gas-phase and in solution have been used to elucidate the excited state photodynamics of HMS upon absorption of UVB radiation. By using ultrafast spectroscopy, a deeper insight into the specific relaxation mechanism(s) of salicylates upon exposure to solar radiation can be gained, which in turn can be beneficial to determine whether molecules of this type dissipate their incident UV radiation safely, *i.e.* quickly and without generating any harmful and/or reactive photoproducts.[31,32] Other UV filters with an intramolecular hydrogen bond have previously been investigated with these techniques.[33,34] For example, upon excitation at its UVA absorption maximum, oxybenzone was shown to exhibit excited state intramolecular proton transfer (ESIPT), followed by a molecular rotation which facilitated a fast decay to the ground electronic state on a picosecond timescale, an ideal behaviour for a UV filter.[33] Conversely, menthyl anthranilate (MenA) was shown to undergo hydrogen atom *dislocation*, rather than transfer, and a significant energetic barrier towards a nearby conical intersection (CI) was found to prevent fast and efficient excited state relaxation.[34] Due to its long-lived nature ($\gg$ nanoseconds), MenA is an unsuitable candidate for inclusion in sunscreen formulations as it is vulnerable to detrimental relaxation pathways.[34] Therefore, the effect of the intramolecular hydrogen bond in these salicylates is worthy of further investigation to determine its potential suitability as a UV filter. A review of sunscreen molecules that undergo *keto-enol* tautomerisation and ESIPT, studied by ultrafast spectroscopy techniques, has been published by Rodrigues and Stavros.[35]

In the present work, a *bottom-up* approach is employed to investigate the ultrafast molecular dynamics of HMS upon photoexcitation with UVB radiation. The starting point is taken to be HMS in the gas-phase, whereby the influence of external stimuli is eliminated, focusing on establishing the intramolecular photodynamic processes in operation. Complexity is then increased through the addition of a solvent, which serves as a mimic for the more realistic conditions UV filters are found in within a sunscreen formulation. The ultrafast pump-probe spectroscopy measurements conducted in this work are supported by laser-induced fluorescence measurements and computational calculations, which can assist with the assignment of spectral features to molecular photodynamics. The results of these complementary techniques combine not only to enrich our understanding of the photoprotection mechanisms within HMS, thus elucidating on its inclusion in sunscreens and other cosmetic formulations, but also to compile further information for future UV filter design and sunscreen formulation development.

Experimental

Ultrafast laser spectroscopy setup

A fundamental laser beam centred at 800 nm with $\sim$ 40 fs pulse width, $\sim$ 3 mJ per pulse and 1 kHz repetition rate was produced by a commercial femtosecond laser system comprised of a Ti:Sapphire oscillator (Spectra-Physics Tsunami) and a regenerative amplifier (Spectra-Physics Spitfire XP). This fundamental beam was subsequently split into three beams of $\sim$ 1 mJ per pulse each, two of which were used to pump two separate optical parametric amplifiers (Light Conversion, TOPAS-C), producing the pump beams for the experiments both in the gas-phase and in solution. Experiments in the gas-phase employed a single-wavelength probe, while in solution the probe beam consisted of a white light continuum, as detailed below.

Experiments in vacuum

a. Time-resolved ion yield (TR-IY)

The time-resolved ion yield (TR-IY) apparatus used for the present experiments has been previously described in detail;[36] specific details relevant to the present work are provided herein.

Homosalate (HMS, provided by Lipotec SAU) was studied as provided and without any further purification. HMS was vaporised via heating to approximately 130°C and subsequently seeded into helium buffer gas ($\sim$ 3 bar). The gaseous mixture was then expanded into vacuum ($\sim 10^{-7}$ mbar) via an Even-Lavie pulsed solenoid valve[37] to create the sample molecular beam. The pump and probe beams intersected the molecular beam, while the pump-probe time delay (at predefined time intervals Δt) was controlled by a gold retroreflector mounted on a motorised delay stage along the 800 nm fundamental beam path (used to generate the 200 nm probe, see below). The maximum temporal window provided by the delay stage was 1.3 nanoseconds (ns). At the laser-molecular beam intersection point, the pump photoexcited the sample and the probe ionised the excited species.

The pump wavelengths for TR-IY measurements ($\lambda_{\text{pump}} = 305$ – 335 nm) were chosen in order to sample the different absorption regions probed in our laser induced fluorescence measurements (see Fig. 4 and discussion below), starting from the $S_1(v = 0)$ origin of HMS (29833.4 cm^{-1}, $\sim$ 335 nm, see Fig. 4) and evaluating the effect of photoexcitation with higher energies. The 200 nm probe beam used to photoionize any excited species was generated by successive frequency conversion of the remaining $\sim$ 1 mJ part of the fundamental 800 nm beam using barium borate (BBO) crystals in the following sequence: type I, type II, type I.

The pump-probe ion signal was monitored with a time-of-flight (TOF) mass spectrometer apparatus, equipped with a detector consisting of two microchannel plates (MCPs) coupled to a metal anode. The output from the MCP was measured by a digital oscilloscope (LeCroy LT372 Waverunner) and gated in ion flight time over the mass channel of the parent (HMS^+) ion. The parent TOF signal was then monitored as a function of pump-probe time delay (Δt), resulting in the TR-IY transients. For all TR-IY measurements, the polarizations of the pump and probe beams were kept at magic angle (54.7°) with respect to each other in order to minimize any rotational effects.[38] Additionally, power dependence studies were conducted to ensure single-photon initiated dynamics under the current experimental conditions, as shown in section 1.1 (S1.1) of the Supplementary Information (SI).[39]

The quoted time constants were extracted from the TR-IY transients by a non-linear curve fitting algorithm (further discussed in the SI, S1.2), comprising a sum of exponential decays convoluted with a Gaussian instrument response function (IRF, typically $\sim$ 170 fs at relevant powers for this experiment, see S1.3).The kinetic model employed in these fits assumes parallel dynamics, *i.e.* it assumes that all processes start at $\Delta t = 0$. The standard errors provided by the kinetic fit have been herein reported as estimated errors associated with quoted time constants.

c. Laser induced fluorescence (LIF) and dispersed fluorescence (DFL)

To complement our gas-phase ultrafast laser spectroscopy studies, high frequency resolution laser induced fluorescence (LIF) measurements were carried out using a separate laser system to the one described above; a detailed description of this apparatus has been provided in previous publications[40–42] and therefore only specific details pertaining to the present studies are given here.

Helium was used as the seed gas at a pressure of 3 – 4 bar, flowing over a solid sample of HMS maintained at 110°C to produce sufficient vapour pressure. A pulsed valve (Parker General Valve Series 9) with an orifice of 500 μm operating at 20 Hz was used to supersonically cool the sample as it expanded into vacuum. The sample was interrogated with the doubled output of a Nd:YAG (Quantel Q-smart 450) pumped tunable dye laser (Radiant Dyes Narrowscan). LIF excitation scans were recorded by collecting the emission from the jet-cooled molecules with a set of collection/steering optics, and imaging the emission onto a UV-enhanced photomultiplier tube (PMT). The PMT was outfitted with long-pass filters to reduce the scattered light from the laser. A sampling gate was placed around the fluorescence decay profile, digitized by an oscilloscope (Tektronix, model 3052B), and integrated. The tunable dye laser (Exciton laser dye: DCM) was scanned in the 29800 – 32800 cm^{-1} (335.5 – 305.0 nm) range.

This setup was also employed to obtain gas-phase dispersed fluorescence (DFL) spectra of HMS. These spectra were obtained by fixing the laser wavelength resonant with selected transitions in the excitation spectrum, and imaging the fluorescence onto the entrance slit of a $^3/_4$ m monochromator. Since the fluorescence was spread over a large range, red-shifted from the excitation frequency, distinct peaks were not observed in the DFL spectrum. In order to obtain the shape of the broad DFL spectra, the slit width was set at 1 mm and an intensified CCD camera (Andor SOLIS iStar) collected the total dispersed emission signal impinging on the CCD at a fixed grating position. The grating position was tuned point-by-point and the entire spectrum for a given central grating position was integrated. Fluorescence lifetime traces were also recorded by exciting select transitions, and directly recording the time profile of the fluorescence signal from the PMT on the digital oscilloscope. The gas-phase fluorescence lifetimes of HMS were extracted from the resulting transients following the same method as for the TR-IY transients (see above and further details in the SI, S1.4), using in this case an instrument response full width at half maximum of 8 ns.

Experiments in solution

a. Transient electronic absorption spectroscopy (TEAS)

The ultrafast transient electronic (UV-visible) absorption spectroscopy (TEAS) setup used in these present studies, which uses the aforementioned ultrafast laser spectroscopy setup, has been described previously;[43] specific details regarding these experiments are provided below.

Three separate solutions of HMS dissolved in cyclohexane (CHX, Fisher Scientific, $>$ 99.9%), ethanol (EtOH, VWR Chemicals, $>$ 99.9%) and acetonitrile (ACN, Fisher Scientific, $>$ 99.8%) were prepared to a concentration of $\sim$ 10 mM. This concentration ensured a sample optical density (OD) of less than 0.5, thus avoiding pulse saturation. To prevent photodegradation of the sample between laser shots, a diaphragm pump (Simdos K2) was used to recirculate the solutions via a flow-through sample cell (Harrick Scientific) between two CaF_2 windows (thickness 1–2 mm, 25 mm diameter). PTFE spacers maintained a sample path length of 100 μm.

The wavelength of the pump pulses was chosen to be the peak absorption of HMS in each solvent, shown in Fig. 1: λ_{pump}(CHX) = 309 nm, λ_{pump}(EtOH) = 307 nm and λ_{pump}(ACN) = 306 nm. The fluence of the pump pulses at all wavelengths was $\sim$ 0.5 $\mu J\ cm^{-2}$. The probe pulses were broadband white light pulses (320 – 720 nm), generated by focusing a 5 mW portion of the fundamental 800 nm beam onto a CaF_2 crystal (2 mm thick). The pump-probe time delays in our TEAS setup were controlled by a gold retroreflector mounted on a motorised delay stage, similar to that described for the TR-IY setup. In this instance, the delay stage was situated along the portion of the 800 nm fundamental that generates the white light continuum, and facilitated a maximum Δt of 2 ns. The fluence of the probe pulse was changed post-sample by a neutral density filter as required to avoid saturating the detector. The transient absorption data collected with this setup was quantitatively analysed via global analysis fitting using Glotaran, a graphical user interface for the R package TIMP.[44–46] Once again, the fitting is carried out assuming a parallel kinetic model; more details regarding the fitting procedures and the IRF of our TEAS experiments are given in the SI, in sections 2.1 and 2.2, respectively. Moreover, similar to our experiments in the gas-phase, TEAS power dependence studies were carried out to ensure single-photon initiated dynamics for our experiments in solution (S2.3).

Steady-state spectroscopy

UV-visible spectroscopy measurements were conducted for solutions ($\sim$ 100 μM) of HMS in each solvent (CHX, EtOH and ACN) using a quartz cuvette of 10 mm path length in a Agilent Cary-60 spectrophotometer. All fluorescence measurements (emission spectra and lifetimes, see S2.4 of the SI) of HMS were acquired using a Horiba Fluorolog-3. Each solution of HMS was prepared in this instance to a concentration of around $\sim$ 10 μM to ensure that the absorbance of the solution was approximately 0.1. More detailed information pertaining to these fluorescence measurements, alongside the UV-visible spectra of all fluorescence samples, can be found in S2.4. The quantum yield of HMS was also determined; full experimental details can be found in the SI (S2.4.1).

Computational methods

All calculations were conducted in the NWChem software package.[47] Density functional theory (DFT) geometry relaxation was performed on three conformers of HMS, each of which is suspected to be close to a local geometric energy minima. This relaxation was conducted with the PBE functional and cc-pVTZ basis set.[48] Of the three previously mentioned structures of HMS, the one of lowest energy — herein referred to as the *enol* form (conformer 1), see Fig. 2a — was selected as the likely global minimum and carried forward for further testing. These calculations were conducted in vacuum as well as in implicitly modelled ethanol, cyclohexane, and acetonitrile using the COSMO solvent model inbuilt in NWChem to generate four structures.[49–51] The second lowest energy conformer, which will be referred to as conformer 2, was also retained for further testing. The structures of both conformers are presented in the SI, S3.1.

The *enol* structure was then relaxed in the first excited singlet state (S_1, $\pi\pi^*$) in order to predict the structure of the system after photoexcitation in vacuum. This was achieved by first relaxing at the PBE/cc-pVDZ level of theory and then further relaxing the resulting structure at the PBE0/cc-pVTZ level of theory. Following this, the species was further relaxed in each of the implicit solvents. These relaxations resulted in the *keto* form of HMS shown in Fig. 2a, which was again taken forward for further analysis employing the cc-pVTZ/PBE0 level of theory as is now described. Using each of the eight structures, *enol* and *keto* structures in all three implicit solvents and vacuum, time-dependent DFT was carried out in order to find singlet (S_n) and triplet (T_n) vertical excitations. The energy of the T_1 state was more accurately calculated using a ΔSCF methodology.[52] This was achieved by conducting single point energy calculations with state multiplicity set to 3 (triplet state) on each of the previously obtained *enol* and *keto* structures; the results were then compared to the S_0 energies for each form, once again in all three solvents as well as in vacuum. Conformer 2 also underwent excited state relaxation along the first excited singlet state (S_1, $\pi\pi^*$). This was conducted at the PBE0/cc-pVTZ level of theory. Single point energy calculations were conducted on both conformers 1 and 2 in vacuum at the PBE0/cc-pVTZ level of theory.

Finally, in order to estimate the excited state barrier between the *enol* and *keto* forms (conformer 1), a set of linear interpolations of internal coordinates (LIIC) were acquired. Vertical excitations, again at the PBE0/cc-pVTZ level of theory, were calculated in vacuum for each step, and the resulting ground state (S_0), S_1 and S_2 energies were plotted. The results of these calculations along a LIIC are shown in Fig. 2b (for S_0 and S_1; results for S_2 are shown in the SI, Fig. S12).

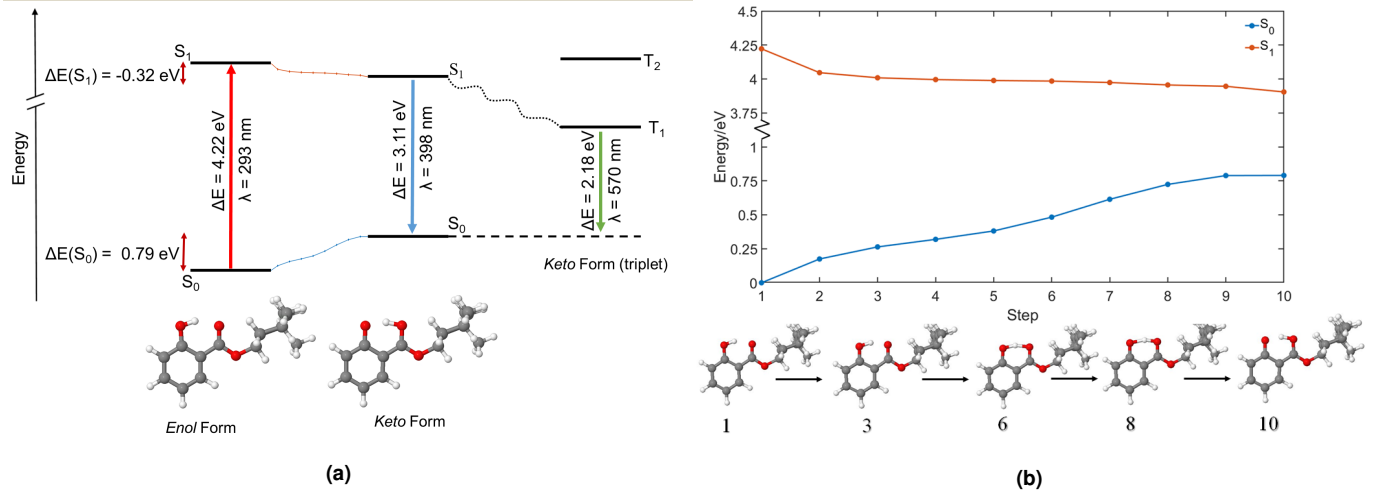

Fig. 2 (a) A representation of the different energy levels of HMS (conformer 1) in vacuum in the *enol* (left) and *keto* (right) form, as predicted using the PBE0/cc-pvtz level of theory. In (a), red arrows represent the absorption of a photon, blue arrows represent fluorescence, and green arrows represent phosphorescence. The dotted lines in blue and orange between the S_0 and S_1 states are indicative of the linear interpolation of internal coordinates calculated for HMS in vacuum at the PBE0/cc-pvtz level of theory, shown in further detail in (b) alongside the predicted structures of homosalate at selected steps. These calculations suggest that, when in the ground state, conformer 1 of HMS exists in the *enol* form, whereas in the first excited singlet state (S_1) HMS converts to the *keto* state in an energetically barrierless process.

Results and Discussion

Gas-phase experiments

TR-IY HMS parent ion (HMS^+) transients are presented in Fig. 3 along with the extracted time constants at $\lambda_{pump} = 305$ nm, 320 nm and 335 nm (the latter of which corresponds to photoexcitation centred at the S_1 origin of HMS, see below), with $\lambda_{probe} = 200$ nm. In all cases, the gas-phase photodynamics of HMS following UV photoexcitation are described by two time constants. In what follows, we will firstly focus on discussing the assignment of τ_1 and addressing apparent discrepancies between our time- and frequency-resolved studies, after which the discussion regarding the assignment of τ_2 will become straight-forward.

The first time constant, τ_1, is always defined within the limits of our IRF, typically ~ 170 fs as previously mentioned. It is common for such IRF-limited features to be due to multiphoton coherent artifacts,[53,54] and it is also likely that probe-initiated reverse dynamics contribute to the large amplitude of the feature associated with τ_1 (particularly in Fig. 3(c)). Nevertheless, gas-phase power studies (presented in S1.1, Fig. S1) reveal that the feature associated with τ_1 is linearly dependent on pump power, indicative of single-photon pump-initiated photodynamics via S_1. It has been reported that excited state intramolecular proton transfer (ESIPT), involving migration of the proton on the $-$OH group along the O$-$H$-$O coordinate towards the neighbouring carbonyl group (thus forming the *keto* tautomer), takes place in methyl salicylate (a smaller analogue of HMS) on sub-100 fs timescales.[55] It is therefore plausible that such an ESIPT process would also take place in photoexcited HMS. In fact, our computational studies, the results of which are presented in Fig. 2, predict a barrierless S_1-*enol* to S_1-*keto* tautomerisation for conformer 1 of HMS, with the *keto* tautomer lying 0.32 eV lower in energy than the *enol* tautomer (see Fig. 2b). In addition, the large Stokes shift observed in the DFL spectrum of HMS upon photoexcitation at its $S_1(v = 0)$ origin, as shown in Fig. S3a in the SI, suggests a significant geometry change upon excitation to the S_1 state. The experimentally observed Stokes shift in the gas-phase is approximately 0.71 eV, which compares with the theoretically calculated 1.1 eV difference between the S_1–S_0 transitions for the *enol* and *keto* tautomers (in vacuum, see Table S3 and Table S4 in the SI). While there is a discrepancy of approximately 0.4 eV between the experimental and theoretical value for this Stokes shift, DFT methods have generally been found to overestimate transition energies.[56,57] Nevertheless, the experimental observation of a large Stokes shift upon photoexcitation to the S_1 state of HMS, in accordance and in addition to the large computationally predicted Stokes shift, supports the hypothesis that ESIPT would take place in HMS within τ_1.

We note, however, that sharp features in the LIF spectrum of HMS, shown in Fig. 4, are retained even at energies > 1000 cm^{-1} above the $S_1(v = 0)$ origin. Excitation energies above 31000 cm^{-1} result in a loss of the fine structure, which could point towards vibronic congestion.[58] The instrument-limited linewidth of the LIF origin peak (see SI, S1.5) suggests a significantly longer S_1 origin lifetime than the IRF-limited τ_1 extracted from our TR-IY measurements. We reconcile these contradictory observations by considering previously published work in which the existence of different conformers is suggested for closely related salicylates. For example, Bisht *et al.* proposed two potential conformers in salicylic acid undergoing different excited state dynamics,[59] while Zhou *et al.* hypothesised that the slowest dynamics observed in their studies on methyl salicylate could be due to a conformer in which the ESIPT process is hindered.[60] Moreover, both Zhou *et al.* and Massaro *et al.*[61] report an energy difference between the two lowest energy conformers of methyl salicylate in the ground

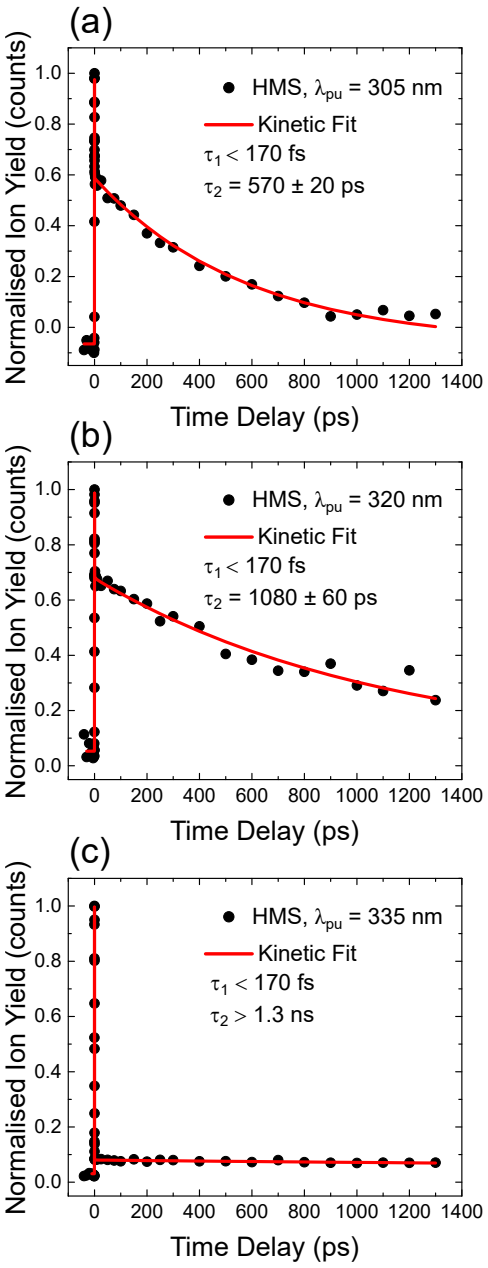

Fig. 3 TR-IY magic angle transients for HMS photoexcited at (a) 305 nm, (b) 320 nm and (c) 335 nm, the $S_1(v = 0)$ origin of HMS, with a 200 nm probe. Black circles are experimental points, while the red curves correspond to kinetic fits (discussed in the SI, S1.2), from which the time constants shown inset are extracted.

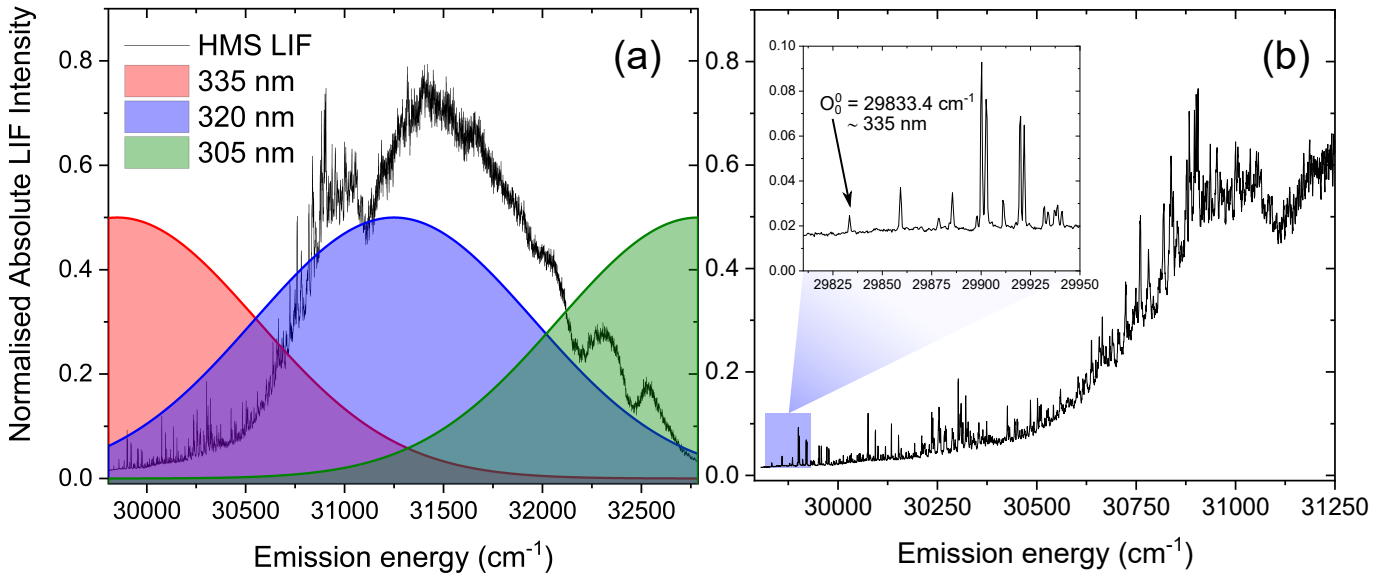

Fig. 4 (a) LIF spectrum of vaporised HMS upon photoexcitation in the 29806 – 32787 cm^{-1} energy region, with Gaussian curves (FWHM = 500 cm^{-1}) demonstrating the regions photoexcited in the TR-IY measurements with $\lambda_{pump} = 335$ nm (red), 320 nm (blue) and 305 nm (green). (b) The same LIF spectrum in more detail, with the inset showing the peak and energy corresponding to the $S_1(v = 0)$ origin of HMS.

state ($\sim 0.1 - 0.2$ eV) that is comparable to the energy difference predicted by our computational studies for conformers 1 and 2 of HMS (0.17 eV, see Fig. S11 in the SI). In addition, Zhou *et al.* have shown that interconversion of the two lowest energy conformers in the ground state has a significant barrier (0.63 eV), hindering interconversion between the two conformers; it is therefore not unreasonable to assume that a similar barrier to interconversion between conformer 1 and conformer 2 of HMS also exists. Taken together, and given that our calculations show that there is a stable excited state structure of the *enol* tautomer of conformer 2, we propose that conformer 2 is photoexcited and trapped in its *enol* structure (*i.e.* not undergoing ESIPT), which fluoresces, thus accounting for the sharp features observed in our LIF measurements. However, the (apparent) low abundance of this conformer makes it difficult to identify from our TR-IY measurements. We add that further experiments (such as spectral hole-burning) are warranted to confirm the existence of conformer 1 and 2.

The second time constant, τ_2, clearly decreases with increasing energy, *i.e.* energy dissipation becomes faster with increasing energy. This behaviour is typical of systems for which there is an energetic barrier to be surmounted in order for a key relaxation pathway to be accessed.[62,63] Presumably, when exciting HMS at the $S_1(v = 0)$ origin (within the 500 cm^{-1} bandwidth of our time-resolved measurements, see Fig. 4) excited state population is unable to access any nearby CIs and therefore fluorescence takes place to the ground state as excited state population samples the shallow S_1 energy potential. Indeed, the LIF measurements presented in Fig. 4 show that there is significant fluorescence from the vibrational levels accessed by $\lambda_{pump} = 335$ nm used in our TR-IY measurements (see Fig. 4), further supporting our assignment of $\tau_2 > 1.3$ ns (at this pump wavelength) to a long-lived, fluorescing S_1 surface. As the pump energy is increased, τ_2 decreases considerably, now being defined within the temporal window of our measurements. It is plausible that at these higher pump energies excited state population would be increasingly more likely to access a nearby CI within the S_1 state through which it would undergo internal conversion (IC) to the S_0 state. Nevertheless, while fluorescence may not be the predominant relaxation pathway at above-origin pump energies (for which IC becomes increasingly competitive), the strong LIF signal at these energies is evidence that it is still an active relaxation pathway.

Gas-phase fluorescence lifetime measurements taken upon photoexcitation at 305 – 335 nm, an example of which is presented in the SI (S1.4), yield fluorescence lifetimes of 12 – 20 ns, and our attempts to detect gas-phase phosphorescence from HMS were unsuccessful, suggesting that triplet states are unlikely to be involved in the gas-phase photodynamics of HMS on the timescales of the present measurements. Nevertheless, one could envisage that excited state population would migrate to nearby triplet states (the existence of which is confirmed by our computational work, see Fig. 2a and section 3 of the SI) and then undergo reverse intersystem crossing (ISC) back into a singlet state (namely S_0), thus justifying the absence of observable phosphorescence. Moreover, it is also possible that photoreactions would take place from the excited triplet state manifold. The absence of observable phosphorescence does not, therefore, conclusively rule out ISC as a potential relaxation pathway for HMS in the gas-phase.

In summary, our gas-phase and computational results suggest that conformer 1 of HMS (the lowest energy conformer) undergoes ultrafast *enol-keto* tautomerisation, followed by either fluorescence from the S_1 surface or, in the case of higher photoexcitation energies which allow for a higher lying CI to be accessed,

fast repopulation of the S_0 state via IC. Furthermore, we suggest that the sharp peaks in the LIF spectrum of HMS around $S_1(v=0)$ origin energies – which do not agree with a fast ESIPT process taking place – are due to the presence of a second conformer in the molecular beam. We found no evidence of phosphorescence within the timescales of our experiments and, therefore, propose that any contribution from triplet states to the gas-phase photodynamics of HMS, while possible, would be negligible.

Transient electronic absorption spectroscopy (TEAS)

To gain further insights into the behaviour of HMS in environments with different polarities and protic natures, ultrafast spectroscopy studies were conducted in solution, in line with a *bottom-up* approach.

Given the similarities of the UV-visible spectra of HMS in different solvents (as shown in Fig. 1), it could be expected that the excited state dynamics of HMS would not differ dramatically in the different solvent environments. Indeed, all transient absorption spectra (TAS) of HMS, displayed as false colour heat maps in Fig. 5, are very similar and reveal similar dynamics; as such, it seems appropriate that the results should be discussed together.

Each solute/solvent combination displays a strong excited state absorption (ESA) in the range 330 – 360 nm, with evidence of a positive feature, tailing off at ∼ 400 nm. A separate ESA feature appears between 500 – 590 nm. There is also a stimulated emission (SE) feature, the negative ΔOD feature between probe wavelengths of 430 – 500 nm. A quantitative insight into the assignment of these spectral features has been attained by following the global fitting procedure described in the SI (S2.1). As is the case for the model used to fit our time-resolved gas-phase data, this procedure implements a parallel model, which assumes all processes begin immediately after excitation. This is also the same style of model that is used to quantitatively analyse the time-resolved gas-phase data. The results of this fitting are shown in Table 1.

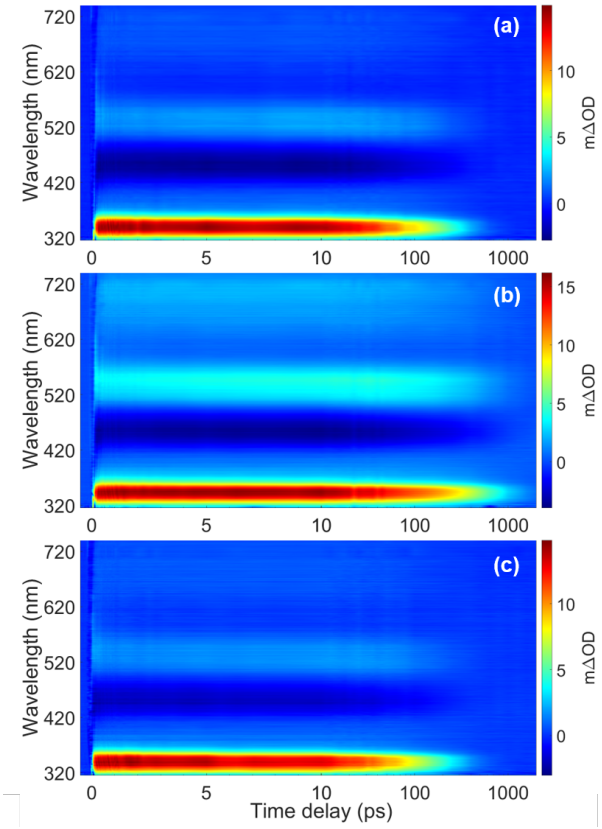

Fig. 5 False colour heat maps showing TAS of HMS in (a) EtOH (λ_{pump} = 307 nm), (b) CHX (λ_{pump} = 309 nm) and (c) ACN (λ_{pump} = 306 nm).

Table 1 Transient electronic absorption spectroscopy (TEAS) time constants for three homosalate solutions upon excitation at their respective absorption maxima, obtained via global fitting techniques using a parallel model.[44]

Time constant	Ethanol	Cyclohexane	Acetonitrile
τ_1 (fs)	50 ± 35	100 ± 30	80 ± 40
τ_2 (ps)	10.4 ± 0.4	14.2 ± 0.5	9.1 ± 0.4
τ_3 (ps)	199 ± 2	533 ± 6	176 ± 2
τ_4 (ns)	$> 2^*$	$> 2^*$	$> 2^*$

* Outside the temporal window of the instrument

For all sets of TEAS data (in all solvents and at all pump wavelengths), τ_1 is defined within instrument response (Fig. S5). Following consideration of our previous observations and discussion regarding our gas-phase results, and given that ESIPT has been observed experimentally on comparable timescales in similar systems in solution (*e.g.* methyl salicylate), we assign τ_1 in our studies in solution to *enol-keto* tautomerisation.[64–67] Further evidence for ESIPT in HMS is two-fold. Akin to the dispersed fluorescence observations in gas-phase, there is a large Stokes shift (∼ 120 nm, see Fig. S8 in the SI) upon photoexcitation of HMS at its respective absorption peak in each solvent, which is indicative of a significant structural change upon photoexcitation to the S_1 state. This observation is similar to that previously reported for methyl salicylate and ethylhexyl salicylate.[67,68] Moreover, our computational studies reveal that the S_1-*keto* tautomer is lower in energy than its S_1-*enol* counterpart and it is therefore anticipated that ESIPT would remain barrierless for HMS in solution.

The elucidation of the remaining time constants extracted from our TEAS data for HMS is assisted herein by comparison with the previously studied HMS analogue, ethylhexyl salicylate (EHS), for which the ester unit connects to an alkane chain rather than the cycloalkane unit of HMS.[68,69] As presented in the SI in further detail (S2.5), equivalent TEAS studies on EHS following the same experimental methodology as for HMS have been performed. Overall, the photodynamical behaviour of EHS is virtually unaltered from that observed for HMS. As such, we assume that comparisons between the photophysical and photodynamic behaviours of HMS and EHS are valid.

In light of the aforementioned assumption (and returning to discuss τ_2 below), τ_3 and τ_4 for HMS can be assigned to radiative decay. The faster of these time constants, τ_3, is likely due to the decay of the S_1-*keto* tautomer via fluorescence, the presence of which is confirmed in the TAS of HMS in all solvents by the

appearance of the SE feature centred at 450 nm, which directly corresponds to the peak observed in the emission spectra (Fig. S8). Moreover, EHS also produces an emission peak at 450 nm, as reported by Krishan and Nordlund,[68] identical to the emission of HMS shown in Fig. S8, in terms of both central wavelength and bandwidth, further validating the comparison between these two molecules. For further confirmation, the fluorescence lifetimes of HMS in all three solvents have been determined; these were found to be within our instrument response (< 1.2 ns, see S2.4 for further experimental details). More exact fluorescence lifetimes for EHS have been quoted by Krishnan and Nordlund, and range from 150 ps in methanol to 460 ps in toluene.[68] Krishnan and Nordlund's results are in good agreement with the values of τ_3 that have been extracted for both HMS and EHS in our studies, as shown in Table 1 and Table S1, respectively. These time constants, alongside the fluorescence lifetime of the present and previous studies, thus support our assignment of τ_3 in both EHS and HMS to fluorescence.

Our assignment of $\tau_4 > 2$ ns to intersystem crossing (ISC), followed by phosphorescence, is supported by our computational results, which reveal the existence of nearby triplet states that are accessible in all solvents. The hypothesis that τ_4 in our TEAS measurements may be associated with the lifetime of a nearby triplet state is further corroborated by the previous findings of Sugiyama *et al.*,[69] who observed and measured phosphorescence for both HMS and EHS with quantum yields of $\Phi_P(\text{HMS}) = 4.9\%$ and $\Phi_P(\text{EHS}) = 5.4\%$, respectively, in ethanol at 77 K;[69] at room temperature, the equivalent Φ_P would be expected to be lower.

Although, as just discussed, both fluorescence and ISC (followed by phosphorescence), do occur in both HMS and EHS, these are unlikely to be the dominant relaxation pathways for these molecules. In EHS, the aforementioned phosphorescence quantum yield of 5.4%[69] adds to the reported fluorescence quantum yield, Φ_F, of 0.6 – 1.9% (depending on solvent),[68] while for HMS we have determined that the reported $\Phi_P(\text{HMS}) = 4.9\%$[69] is accompanied by a fluorescence quantum yield of 9.0% in cyclohexane and ethanol, and 10.1% in acetonitrile (see S2.4.1 for experimental details). Therefore, radiative decay does not solely account for excited state relaxation and, indeed, it is not the predominant relaxation pathway in either of these molecules. Hence, alternative, non-radiative mechanisms must be at play in the excited state relaxation of both HMS and EHS. We propose, therefore, that the remaining time constant extracted from our TEAS measurements for HMS (and, indeed, EHS), τ_2, may be due to excited state relaxation via a combination of internal conversion (IC) and vibrational cooling to the S_0-*keto* species. It is then energetically favourable for the S_0-*enol* species to be reformed, according to the S_0 energies calculated using TD-DFT, a full list of which can be found in the SI (S3). Given the aforementioned low yields of radiative decay, we further propose that IC would account for the remaining excited state relaxation, thus constituting the predominant relaxation pathway for HMS (and EHS).

In summary, our studies in solution on HMS reveal an initial ultrafast process which, similarly to what was discussed for the system in the gas-phase, we assign to *enol-keto* tautomerisation. Both radiative and non-radiative decay then occurs, with IC (and some component of vibrational cooling) predominantly taking place alongside lower yield components of fluorescence and phosphorescence. While it appears from our results that solvent environments have only minor effects on the observed photodynamics of HMS, it is clear that solvation seems to facilitate ISC and thus open up phosphorescence as a competing (yet non-dominant) decay pathway for HMS. This is an important consideration for sunscreen design, since triplet states are generally more reactive and their presence is therefore undesirable in sunscreen formulations.

Conclusions

In the present work we have explored the excited state dynamics of the UV filter HMS after photoexcitation in the 305 – 335 nm wavelength range. We found that these dynamics are almost unaltered in solution when compared to the gas-phase and can be broadly described by an initial ultrafast decay, which is in all cases assigned to ESIPT, followed by fast internal conversion to the ground state and lower quantum yields of fluorescence and phosphorescence (the latter of which is only directly observed in solution). In line with previous observations on analogous molecules, we also report on experimental observations in the gas-phase that point towards the presence of a second, long-lived conformer of HMS which does not undergo ESIPT.

Interestingly, the studies presented here on HMS are in stark contrast with the behaviour observed for the UVA filter menthyl anthranilate (MenA), studied by Rodrigues *et al.*.[34] In their studies, in gas-phase and in solution, Rodrigues *et al.* found that the ESIPT process is incomplete. Furthermore, while there is a nearby CI, a large energetic barrier needs to be surmounted in order for it to be accessed, which hinders fast and efficient excited state relaxation in MenA, effectively rendering its photophysical behaviour unfavourable for sunscreen use.

From our observations in the present study, it appears that by substituting the amino group of MenA with the hydroxy group in HMS, a CI becomes accessible and the excited state energy can be dissipated effectively. It is evident, therefore, that the ESIPT process plays a key role in the photodynamics of both HMS and MenA, ultimately defining their suitability for use as UV filters in sunscreen formulations. As such, a more detailed understanding of the ESIPT process (*e.g.* substituent position and functional group effects) in this type of molecule is warranted and could be crucial for sunscreen design. Overall, and within the limits of our studies, HMS appears to have mostly favourable excited-state characteristics and, on this basis alone, warrants its inclusion in sunscreen formulations. Nevertheless, the potential reactivity and toxicity of HMS triplet states warrants further investigation.

Conflicts of interest

There are no conflicts of interest to declare.

Acknowledgements

The authors would like to thank the Warwick Centre for Ultrafast Spectroscopy (WCUS) for the use of the Cary 60 and Fluorolog-3. E.L.H. and M.A.P.T. thank the Engineering and Physical Sciences Research Council (EPSRC) for a PhD studentship through the EPSRC Centre for Doctoral Training in Molecular Analytical

Science, grant number EP/L015307/1. K.M.K. also thanks the EPSRC for doctoral funding. P.M. and T.S.Z. gratefully acknowledge support from the Department of Energy Basic Energy Sciences Gas-Phase Chemical Physics program under Grant No. DE-FG02-96ER14656. N.d.N.R. thanks the University of Warwick's Institute of Advanced Study and Institute for Advanced Teaching and Learning for a joint Early Career Fellowship. Finally, V.G.S. thanks the EPSRC for an equipment grant (EP/J007153), the Leverhulme Trust for a research grant (RPG-2016-055) and the Royal Society and Leverhulme Trust for a Royal Society Leverhulme Trust Senior Research Fellowship.

References

1 D. Ekinci, M. Şentürk and Ö. İ. Küfrevioğlu, *Expert Opin. Ther. Pat.*, 2011, **21**, 1831–1841.

2 M. T. Baltazar, R. J. Dinis-Oliveira, J. A. Duarte, M. L. Bastos and F. Carvalho, *Curr. Med. Chem.*, 2011, **18**, 3252–3264.

3 N. Serpone, D. Dondi and A. Albini, *Inorg. Chim. Acta*, 2007, **360**, 794–802.

4 N. A. Shaath, *Photochem. Photobiol. Sci.*, 2010, **9**, 464–469.

5 M. F. Holick, *Anticancer Res.*, 2016, **36**, 1345–1356.

6 P. H. Hart, M. Norval, S. N. Byrne and L. E. Rhodes, *Annu. Rev. Pathol.*, 2019, **14**, 55–81.

7 Y. Matsumura and H. N. Ananthaswamy, *Toxicol. Appl. Pharm.*, 2004, **195**, 298–308.

8 F. R. De Gruijl, *Eur. J. Cancer*, 1999, **35**, 2003–2009.

9 L. A. Baker, B. Marchetti, T. N. V. Karsili, V. G. Stavros and M. N. R. Ashfold, *Chem. Soc. Rev.*, 2017, **46**, 3770–3791.

10 M. Wlaschek, I. Tantcheva-Poór, L. Naderi, W. Ma, L. A. Schneider, Z. Razi-Wolf, J. Schüller and K. Scharffetter-Kochanek, *J, Photoch. Photobio. B*, 2001, **63**, 41–51.

11 G. J. Fisher, Z. Wang, S. C. Datta, J. Varani, S. Kang and J. J. Voorhees, *New Engl. J. Med.*, 1997, **337**, 1419–1429.

12 J. D'Orazio, S. Jarrett, A. Amaro-Ortiz and T. Scott, *Int. J. Mol. Sci.*, 2013, **14**, 12222–12248.

13 C. Couteau, M. Pommier, E. Paparis and L. J. M. Coiffard, *Pharmazie*, 2007, **62**, 449–452.

14 L. E. Agrapidis-Paloympis, R. A. Nash and N. A. Shaath, *J. Soc. Cosmet. Chem.*, 1987, **38**, 209–221.

15 L. Beyere, S. Yarasi and G. R. Loppnow, *J. Raman Spectrosc.*, 2003, **34**, 743–750.

16 G. J. Mturi and B. S. Martincigh, *J. Photochem. Photobiol. A*, 2008, **200**, 410 – 420.

17 A. Benazzouz, L. Moity, C. Pierlot, V. Molinier and J.-M. Aubry, *Colloid Surface A*, 2014, **458**, 101–109.

18 M. D. Palm and M. N. O'Donoghue, *Dermatol. Ther.*, 2007, **20**, 360–376.

19 C. G. Mortz, H. Thormann, A. Goossens and K. E. Andersen, *Dermatitis*, 2010, **21**, 7–10.

20 A. R. Heurung, S. I. Raju and E. M. Warshaw, *Dermatitis*, 2014, **25**, 289–326.

21 C. L. Hexsel and H. W. Lim, in *Preventive Dermatology*, ed. R. Norman, Springer London, London, 2010, pp. 81–91.

22 N. Lowe, *Dermatol. Clin.*, 2006, **24**, 9–17.

23 D. R. Sambandan and D. Ratner, *J. Am. Acad. Dermatol*, 2011, **64**, 748 – 758.

24 C. Couteau, A. Faure, J. Fortin, E. Paparis and L. J. M. Coiffard, *J. Pharmaceut. Biomed.*, 2007, **44**, 270–273.

25 C. A. Bonda and D. Lott, in *Principles and Practice of Photoprotection*, ed. S. Q. Wang and H. W. Lim, Springer International Publishing, Cham, 2016, pp. 247–273.

26 S. Q. Wang and H. W. Lim, *J. Am. Acad. Dermatol.*, 2011, **65**, 863–869.

27 T. H. Kim, B. S. Shin, K.-B. Kim, S. W. Shin, S. H. Seok, M. K. Kim, E. J. Kim, D. Kim, M. G. Kim, E.-S. Park, J.-Y. Kim and S. D. Yoo, *J. Toxicol. Environ. Health A*, 2014, **77**, 202–213.

28 M. Erol, I. Çok, Ö. B. Gayret, P. Günes, Ö. Yigit, E. Sayman, A. Günes, D. S. Çelik, S. Hamilçikan, S. Altinay and O. Ercan, *Toxicol. Ind. Health*, 2017, **33**, 775–791.

29 J. F. Nash, *Dermatol. Clin.*, 2006, **24**, 35–51.

30 S. Yazar and S. Kara Ertekin, *J. Cosmet. Dermatol.*, 2020, **19**, 246–252.

31 L. A. Baker, S. E. Greenough and V. G. Stavros, *J. Phys. Chem. Lett.*, 2016, **7**, 4655–4665.

32 E. L. Holt and V. G. Stavros, *Int. Rev. Phys. Chem*, 2019, **38**, 243–285.

33 L. A. Baker, M. D. Horbury, S. E. Greenough, P. M. Coulter, T. N. V. Karsili, G. M. Roberts, A. J. Orr-Ewing, M. N. R. Ashfold and V. G. Stavros, *J. Phys. Chem. Lett.*, 2015, **6**, 1363–1368.

34 N. D. N. Rodrigues, N. C. Cole-Filipiak, M. D. Horbury, M. Staniforth, T. N. V. Karsili, Y. Peperstraete and V. G. Stavros, *J. Photochem. Photobiol. A*, 2018, **353**, 376 – 384.

35 N. D. N. Rodrigues and V. G. Stavros, *Sci. Prog.*, 2018, **101**, 8–31.

36 A. Iqbal, L.-J. Pegg and V. G. Stavros, *J. Phys. Chem. A*, 2008, **112**, 9531–9534.

37 U. Even, J. Jortner, D. Noy, N. Lavie and C. Cossart-Magos, *J. Chem. Phys.*, 2000, **112**, 8068–8071.

38 F. P. M. Baskin, J. Spencer and A. H. Zewail, *J. Chem. Phys*, 1987, **86**, 2483–2499.

39 S. R. Gandhi and R. B. Bernstein, *Chem. Phys.*, 1986, **105**, 423–434.

40 N. R. Pillsbury, J. A. Stearns, C. W. Müller, D. F. Plusquellic and T. S. Zwier, *J. Chem. Phys.*, 2008, **129**, 114301.

41 C. A. Arrington, C. Ramos, A. D. Robinson and T. S. Zwier, *J. Phys. Chem. A*, 1998, **102**, 3315–3322.

42 F. A. Ensminger, J. Plassard and T. S. Zwier, *J. Chem. Phys.*, 1995, **102**, 5246.

43 S. E. Greenough, G. M. Roberts, N. A. Smith, M. D. Horbury, R. G. McKinlay, J. M. Żurek, M. J. Paterson, P. J. Sadler and V. G. Stavros, *Phys. Chem. Chem. Phys.*, 2014, **16**, 19141–19155.

44 J. Snellenburg, S. Laptenok, R. Seger, K. Mullen and I. Van Stokkum, *J. Stat. Soft.*, 2012, **49**, 1–22.

45 K. M. Mullen and I. H. M. Van Stokkum, *J. Stat. Soft.*, 2007, **18**, 1–46.

46 I. H. van Stokkum, D. S. Larsen and R. van Grondelle,

Biochim. Biophys. Acta, 2004, **1657**, 82–104.
47 M. Valiev, E. J. Bylaska, N. Govind, K. Kowalski, T. P. Straatsma, H. J. Van Dam, D. Wang, J. Nieplocha, E. Apra, T. L. Windus *et al.*, *Comp. Phys. Comms*, 2010, **181**, 1477–1489.
48 J. P. Perdew, K. Burke and M. Ernzerhof, *Phys. Rev. Lett.*, 1996, **77**, 3865.
49 A. Klamt and G. Schüürmann, *J. Chem. Soc., Perkin Transactions 2*, 1993, 799–805.
50 D. M. York and M. Karplus, *J. Phys. Chem. A*, 1999, **103**, 11060–11079.
51 P. Winget, D. M. Dolney, D. J. Giesen, C. J. Cramer and D. G. Truhlar, *Dept. of Chemistry and Supercomputer Inst., University of Minnesota, Minneapolis, MN*, 1999, **55455**, year.
52 R. Charlton, R. Fogarty, S. Bogatko, T. Zuehlsdorff, N. Hine, M. Heeney, A. Horsfield and P. Haynes, *J. Chem. Phys.*, 2018, **148**, 104108.
53 C. W. Luo, Y. T. Wang, F. W. Chen, H. C. Shih and T. Kobayashi, *Opt. Express*, 2009, **17**, 11321–11327.
54 G. M. Roberts and V. G. Stavros, *Chem. Sci.*, 2014, **5**, 1698–1722.
55 J. L. Herek, S. Pedersen, L. Bañares and A. H. Zewail, *J. Chem. Phys.*, 1992, **97**, 9046–9061.
56 S. Grimme and F. Neese, *J. Chem. Phys.*, 2007, **127**, 154116.
57 D. Jacquemin, Y. Zhao, R. Valero, C. Adamo, I. Ciofini and D. G. Truhlar, *J. Chem. Theory Comput.*, 2012, **8**, 1255–1259.
58 J. C. Dean, R. Kusaka, P. S. Walsh, F. Allais and T. S. Zwier, *J. Am. Chem. Soc.*, 2014, **136**, 14780 – 14795.
59 P. B. Bisht, H. Petek and K. Yoshihara, *J. Chem. Phys.*, 1995, **103**, 5290–5307.
60 P. Zhou, M. R. Hoffmann, K. Han and G. He, *J. Phys. Chem. B*, 2014, **119**, 2125–2131.
61 R. D. Massaro, Y. Dai and E. Blaisten-Barojas, *J. Phys. Chem. A*, 2009, **113**, 10385–10390.
62 A. L. Sobolewski and W. Domcke, *Phys. Chem. Chem. Phys.*, 1999, **1**, 3065–3072.
63 A. L. Sobolewski and W. Domcke, *Chem. Phys. Lett.*, 1999, **300**, 533–539.
64 P. Zhou and K. Han, *Acc. Chem. Res.*, 2018, **51**, 1681–1690.
65 M. Rini, A. Kummrow, J. Dreyer, E. T. J. Nibbering and T. Elsaesser, *Faraday Discuss.*, 2003, **122**, 27–40.
66 S. J. Formosinho and L. G. Arnaut, *J. Photoch. Photobio. A*, 1993, **75**, 21 – 48.
67 K.-Y. Law and J. Shoham, *J. Phys. Chem*, 1994, **98**, 3114–3120.
68 R. Krishnan and T. M. Nordlund, *J. Fluoresc.*, 2008, **18**, 203–217.
69 K. Sugiyama, T. Tsuchiya, A. Kikuchi and M. Yagi, *Photochem. Photobiol. Sci.*, 2015, **14**, 1651–1659.

Chapter 5

Conclusions and Future Work

5.1 Conclusions

In this section, I will be discussing the original research that has been undertaken in this thesis as well as giving an outline of the significance of this work. I will also explain how each of the three papers individually explores the overall theme of this thesis: how solvent environment affects the photochemical properties of a molecule.

5.1.1 Determination of Secondary Species in Solution through Pump-Selective Transient Absorption Spectroscopy and Explicit-Solvent TDDFT

In this paper we sought to determine the secondary equilibria species present in an alizarin/methanol solution. This problem originally arose as, when predicting the UV-Vis spectrum and therefore the colour of alizarin in methanol, an unaccounted for excitation was observed in the experimental UV-Vis spectrum. In the literature previously there had been some suggestion of a secondary equilibrium species forming but there was some debate as to its identity.[2, 5, 3, 4] To further investigate this, temperature dependent UV-Vis spectra were taken and a clear isosbestic point was observed between the unaccounted for excitation and a neighbouring peak with respect to temperature. This led us to conclude that alizarin was in dynamic equilibrium in methanol between two forms. To ascertain the nature of this equilibrium, we used pump-selective transient absorption spectroscopy on comparable samples. We studied alizarin in methanol with different acidity to rule out a deprotonation equilibrium. Following this, we conducted explicit solvent TDDFT to test two potential tautomeric species to see which was more likely to be the unknown equilibrium product. The TDDFT results predicted the S_1 absorption energy of one these species to be close to the energy of the unaccounted for excitation. From this we were able to determine that this was the secondary species.

This paper was valuable for three main reasons. Firstly, it gave information about the properties of a widely used dye in solution. Alizarin is used as a paint and as a clothing dye. Therefore, it is useful to know how it behaves in these applications

in specific solvent environments. Furthermore, alizarin is also used in scientific fields for applications like biological staining and in the study of micelles, again, where understanding interaction with solvent environment is of vital importance.[6, 7, 8] Secondly, this paper was useful for benchmarking explicit solvent TDDFT methodology. Finally, this paper showed that knowledge of equilibrium products is important for colour prediction. Previously, it was assumed that, when considering the effect solvents have on colour, the two things to consider were electrostatic and non-electrostatic effects. This paper asserts that to accurately predict the UV-Vis spectrum, and by extension the colour, of a chromophore in solution one must also have information on the presence of ground-state tautomeric equilibria in solution. This feeds directly into the thesis' main goal of accurately assessing solvent effects on the photochemistry of solutes.

5.1.2 Examining solvent effects on the ultrafast dynamics of catechol

This paper examined the ultrafast photodynamics of catechol in acetonitrile. Catechol is a key part of the natural photoprotecting chemical eumelanin. Therefore, to know the excited state behaviour of catechol is key to understanding the photochemistry of eumelanin. This "bottom-up" approach, where one starts with a smaller building block and builds complexity into the model, is common in the study of large biological molecules. 4-*tert*-butyl catechol, a catechol analogue, has been studied previously at different concentrations in cyclohexane but its photochemistry had not been studied in depth in more interacting solvents.[9] In this paper, we study catechol in the hydrogen-bond accepting solvent acetonitrile.

Horbury *et al.* previously studied the ultrafast dynamics of catechol in cyclohexane and acetonitrile at 35 mM concentration. [1] They observed that the lifetime of catechol in the S_1 excited state was significantly longer in acetonitrile than in cyclohexane. They attributed this to the existence of two different tautomers of catechol, an "*open*" form in acetonitrile and a "*closed*" form in cyclohexane. In this paper, through comparison of explicit solvent vibrational frequency prediction with experimental FTIR data, we determined this not to be the case. We examined catechol in acetonitrile and found that, contrary to what had previously been suggested, this was in the closed form. We suggested the alternative explanation that hydrogen bonding to the solvent is what gives rise to the difference in S_1 lifetime and showed that aggregation caused a similar effect. This paper was valuable as it showed how interacting solvents can effect a key eumelanin building block, thus further elucidating the behaviour of this photo-protector in realistic environments. This fits within the broader theme of the thesis as it investigated the effects of solvent on ultrafast dynamics using explicitly modelled solvent.

5.1.3 Insights into the Photoprotection Mechanism of the UV Filter Homosalate

The role of a successful UV-filter candidate is to absorb solar radiation and harmlessly dissipate the energy. Salicylates are often used as chemical filters for UVB radiation

(280 - 320 nm).[10] Salicylates are also seen as good sunscreen candidates as they have a low solvatochromic shift and therefore the region of light they absorb is not heavily affected by different solvent environments.[11, 12, 13] Furthermore, salicylates have a favourable safety record with few reports of allergic reactions to their compounds.[14, 15] This work considers a specific salicylate: homomenthyl salicylate, which we refer to as homosalate. Homosalate is a commonly used sunscreen which can be applied in substantial quantities (up to 15% w/w). In this paper we investigated the safety and efficacy of homosalate by probing its excited state decay mechanism.

Homosalate was examined in both the gas and solution-phase in order to achieve a fundamental understanding of its reaction dynamics. In both techniques homosalate appeared to undergo ultrafast intramolecular proton transfer within the first 100 fs resulting in the *keto* tautomer being formed. This result is confirmed through density functional theory calculations. Homosalate was theoretically relaxed in the excited S_1 state, resulting in a barrierless decay to the *keto* form. To further investigate this process, a linear interpolation of internal coordinates was conducted between the S_0 Franck-Condon geometry (*enol* form) and the relaxed S_1 geometry (*keto* form). This further confirmed that there was no barrier in the S_1 to the formation of the *keto* form. Following this, the S_1 state decayed back to the S_0 through two mechanisms: internal conversion and fluorescence. In the solution phase, there is evidence of inter-system crossing (ISC) to a triplet state. This is further verified by vertical excitation and ΔSCF calculations showing the presence of nearby triple states with similar character. There is no evidence of ISC in the gas-phase but it is likely that it does still occur outside the time-window visible by the technique. Laser induced fluorescence studies were also carried out and implied that the molecule did not, in fact, undergo ultrafast intramolecular proton transfer. We suggest, however, that this could be due to a small amount of another conformer present in the tested sample. Homosalate on the whole behaves well as a sunscreen molecule however evidence of a potentially reactive triplet state forming in solution may warrant further research.

5.2 Future Work

The effect of solvation is a continually evolving field of study, both experimentally and theoretically. Experimentally, future work could look to more accurate environments rather than pure solvent. When studying dyes like alizarin, a focus could be on creating more lifelike conditions to study. For example, the study of how alizarin behaves in solvent with other solutes present or how it behaves at the interface of a solvent and a solid may prove vitally important. In the case of eumelanin, and its building block catechol, further steps can be made to experimentally observe these photo-protecting compounds in biomimetic conditions.[16] Finally, with sunscreen candidates like homosalate, further work can be done to mimic the environment experienced when on human skin. This year, a paper was published by the Stavros group that went some of the way to exploring this by studying a different sunscreen candidate, diethyl

sinapate, on synthetic skin.[17] This could be advanced further in the future by adding in more complexity to the solvent with the inclusion of sweat and sebum mimics.

As these experiments get more complex computational studies will have to evolve in turn. In the first presented paper (Turner *et al.*, *J. Phys. Chem A.* 2019) the UV-Vis spectra of different alizarin tautomers were calculated. The shape of the peaks in the prediction were generated by convolving Gaussian functions centred on predicted excitations for multiple snapshots. This could be more accurately determined, however, by also accounting for the vibronic progression of the molecule theoretically. Furthermore, spectral warping was used to mimic the effect of using a cheaper basis set on explicit-solvent models. The warping parameters for this were calculated from high-accuracy density functional theory. They could, perhaps, be more accurately assessed using quantum chemistry methods, for example CASPT2 or EOM-CCSD. When studying catechol, vibrational frequency was calculated using explicit solvent density functional theory. This was conducted on three potential snapshots of catechol in acetonitrile. In future work, one could study significantly more snapshots in order to predict a full FTIR spectrum rather than just likely positions of the primary peaks. Finally, homosalate was studied through implicit-solvent density functional theory. For the purposes of this work, implicit solvent was sufficient as solvation had little effect on the photochemical behaviour of homosalate. This was evidenced by its lack of solvatochromic shift and by the similarity of gas-phase and solution-phase ultrafast results. In future, it would be interesting to use explicit-solvent methodology to examine why this molecule feels so little influence from solvent.

Bibliography

1. Horbury, M. D., Baker, L. A., Quan, W.-D., Young, J. D., Staniforth, M., Greenough, S. E. & Stavros, V. G. Bridging the gap between the gas phase and solution phase: solvent specific photochemistry in 4-tert-butylcatechol. *The Journal of Physical Chemistry A* **119,** 11989–11996 (2015).
2. Cysewski, P., Jeliński, T., Przybyłek, M. & Shyichuk, A. Color prediction from first principle quantum chemistry computations: a case of alizarin dissolved in methanol. *New J. Chem.* **36,** 1836–1843 (2012).
3. Miliani, C, Romani, A & Favaro, G. Acidichromic effects in 1, 2-di-and 1, 2, 4-trihydroxyanthraquinones. A spectrophotometric and fluorimetric study. *J. Phys. Org. Chem.* **13,** 141–150 (2000).
4. Preat, J., Laurent, A. D., Michaux, C., Perpète, E. A. & Jacquemin, D. Impact of tautomers on the absorption spectra of neutral and anionic alizarin and quinizarin dyes. *J. Mol. Struct.: THEOCHEM* **901,** 24–30 (2009).
5. Le Person, A., Cornard, J.-P. & Say-Liang-Fat, S. Studies of the tautomeric forms of alizarin in the ground state by electronic spectroscopy combined with quantum chemical calculations. *Chem. Phys. Lett.* **517,** 41–45 (2011).
6. Springer, V. G. & David Johnson, G. Use and advantages of ethanol solution of alizarin red S dye for staining bone in fishes. *Copeia* **2000,** 300–301 (2000).
7. Ovchinnikov, D. Alcian blue/alizarin red staining of cartilage and bone in mouse. *Cold Spring Harb Protoc* **2009,** pdb–prot5170 (2009).
8. Park, J., Bauer, S., Schlegel, K. A., Neukam, F. W., von der Mark, K. & Schmuki, P. TiO2 nanotube surfaces: 15 nm - an optimal length scale of surface topography for cell adhesion and differentiation. *Small* **5,** 666–671 (2009).
9. Grieco, C., Kohl, F. R., Zhang, Y., Natarajan, S., Blancafort, L. & Kohler, B. Intermolecular Hydrogen Bonding Modulates O-H Photodissociation in Molecular Aggregates of a Catechol Derivative. *Photochemistry and photobiology* (2018).
10. Serpone, N., Dondi, D. & Albini, A. Inorganic and organic UV filters: Their role and efficacy in sunscreens and suncare products. *Inorg. Chim. Acta* **360,** 794–802. ISSN: 0020-1693. `http://www.sciencedirect.com/science/article/pii/S0020169306000259` (2007).
11. Shaath, N. A. The chemistry of sunscreens. *Cosmet. Toiletries* **101,** 55–70 (1986).

12. Agrapidis-Paloympis, L. E., Nash, R. A. & Shaath, N. A. The effect of solvents on the ultraviolet absorbance of sunscreens. *J. Soc. Cosmet. Chem.* **38,** 209–221 (1987).

13. Beyere, L, Yarasi, S & Loppnow, G. R. Solvent effects on sunscreen active ingredients using Raman spectroscopy. *J. Raman Spectrosc.* **34,** 743–750 (2003).

14. Mortz, C. G., Thormann, H., Goossens, A. & Andersen, K. E. Allergic contact dermatitis from ethylhexyl salicylate and other salicylates. *Dermatitis* **21,** 7–10 (2010).

15. Heurung, A. R., Raju, S. I. & Warshaw, E. M. Adverse reactions to sunscreen agents: epidemiology, responsible irritants and allergens, clinical characteristics, and management. *Dermatitis* **25,** 289–326 (2014).

16. Kohl, F. R., Grieco, C. & Kohler, B. Ultrafast spectral hole burning reveals the distinct chromophores in eumelanin and their common photoresponse. *Chemical Science* (2020).

17. Horbury, M. D., Holt, E. L., Mouterde, L. M., Balaguer, P., Cebrián, J., Blasco, L., Allais, F. & Stavros, V. G. Towards symmetry driven and nature inspired UV filter design. *Nature communications* **10,** 1–8 (2019).

Appendix A

Appendix

A.1 Supplementary material for "Determination of Secondary Species in Solution through Pump-Selective Transient Absorption Spectroscopy and Explicit-Solvent TDDFT"

Determination of Secondary Species in Solution Through Pump-Selective Transient Absorption Spectroscopy and Explicit-Solvent TDDFT

M. A. P. Turner,[*,†,‡,¶] M. D. Horbury,[†] V. G. Stavros,[†] and N. D. M. Hine[*,‡]

†*Department of Chemistry, University of Warwick, Coventry, CV4 7AL*

‡*Department of Physics, University of Warwick, Coventry, CV4 7AL*

¶*Current address: Top Floor Senate House, University of Warwick, Coventry, CV4 7AL*

E-mail: m.turner.1@warwick.ac.uk; n.d.m.hine@warwick.ac.uk

Supplementary information

List of files included

- Input, geometry, and output files for each of the sixty explicit solvent calculations on the alizarin tautomers
- Input, geometry, and output files for the PBE, PBE0, LC-PBE0, B3LYP and cam-B3LYP calculations on the alizarin tautomers in implicit methanol solvent
- Input, geometry, and output files for alizarin monoanion-b with fixed dihedral rotations
- Each of the six TEAS scans for alizarin in methanol at pH=3/425 nm pump; pH=7/425 nm pump; pH=7/550 nm pump; pH=9/ 550 nm pump.
- Solvent scans for alizarin at acidic and neutral pH values in methanol

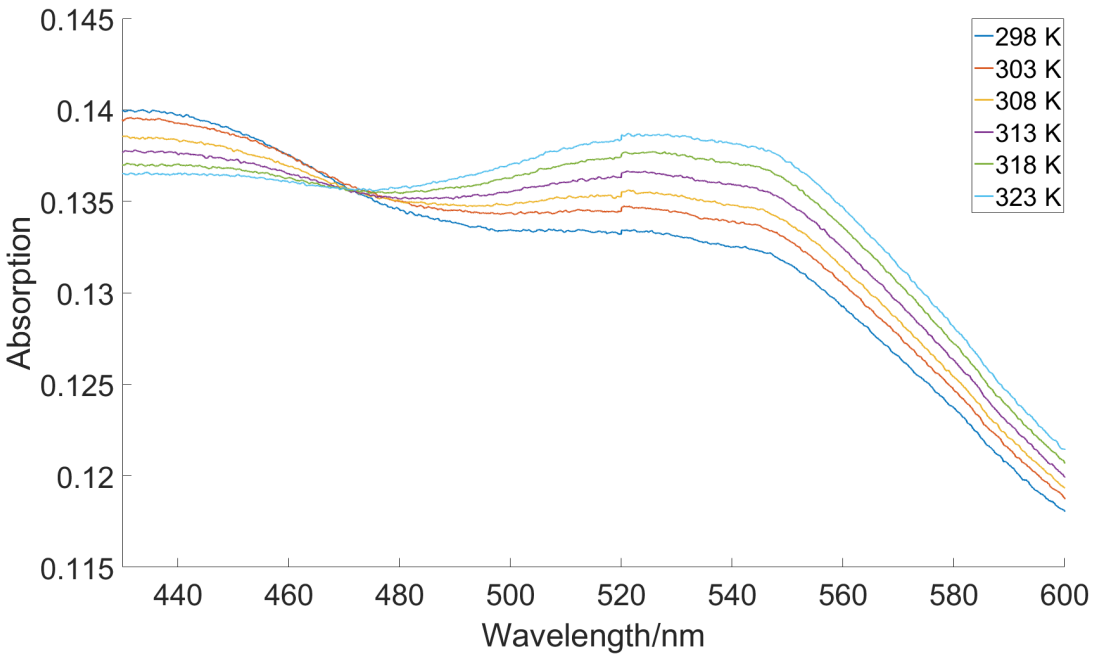

Figure 1: UV-Vis scans of alizarin in methanol at different temperatures.

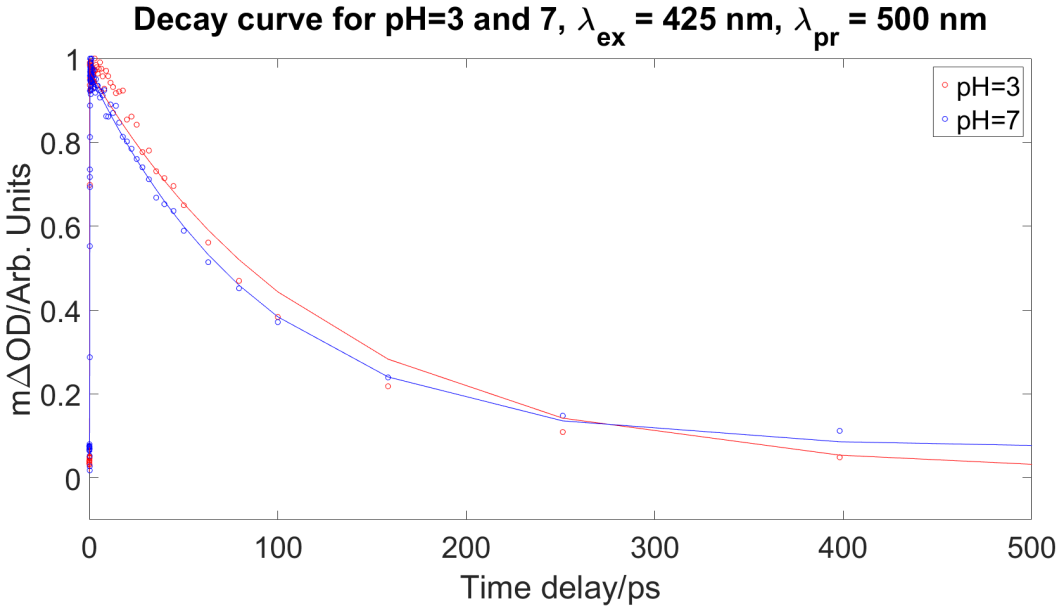

Figure 2: Fitted plots of TEAS slices of alizarin in methanol (pH=3,7), $\lambda(pu)$=425 nm , $\lambda(pr)$=500 nm.

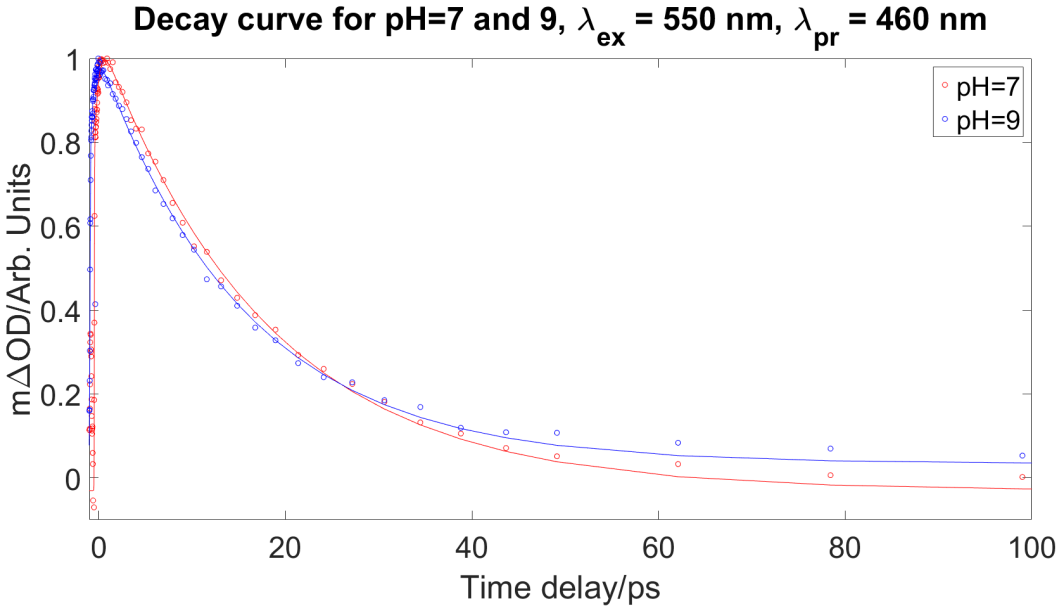

Figure 3: Fitted plots of TEAS slices of alizarin in methanol (pH=7,9), $\lambda(pu)$=550 nm , $\lambda(pr)$=460 nm.

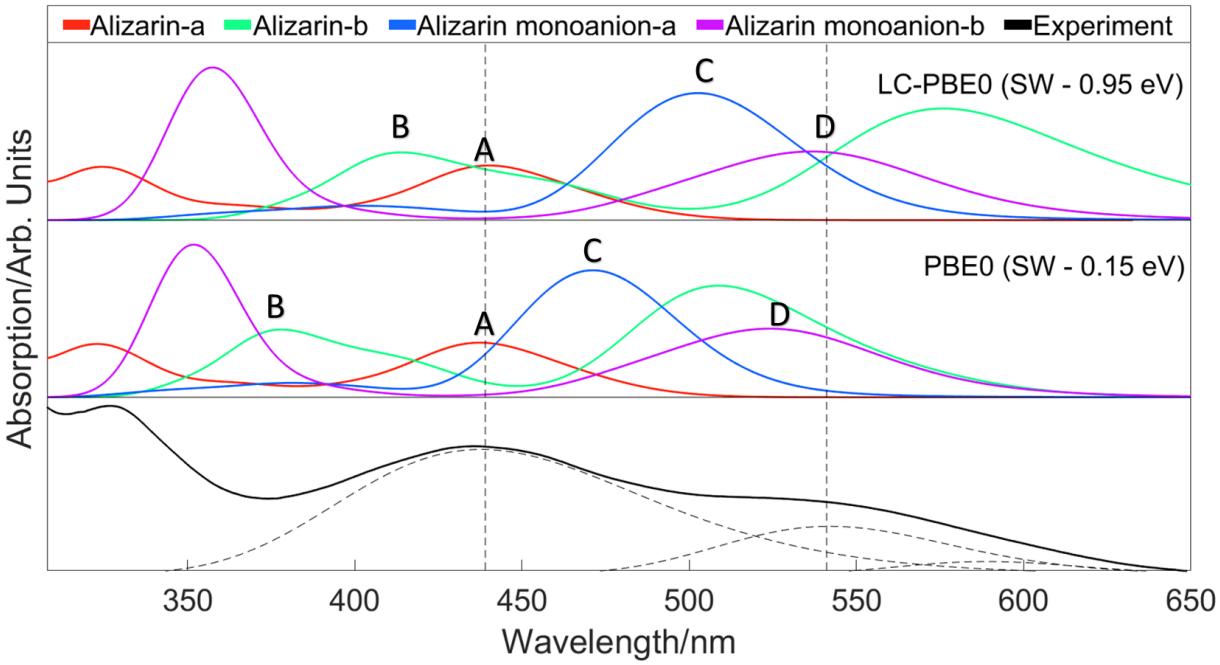

Figure 4: Predicted spectra for different forms of alizarin in methanol, A) Red is alizarin-a, B) green is alizarin-b, C) blue is alizarin monoanion-a; and D) pink is alizarin monoanion-b; the top calculations are the result of LC-PBE0 spectral warp corrections with the solid middle results being that of PBE0 corrections. The bottom black line is the experimental spectra with fitted gaussians.

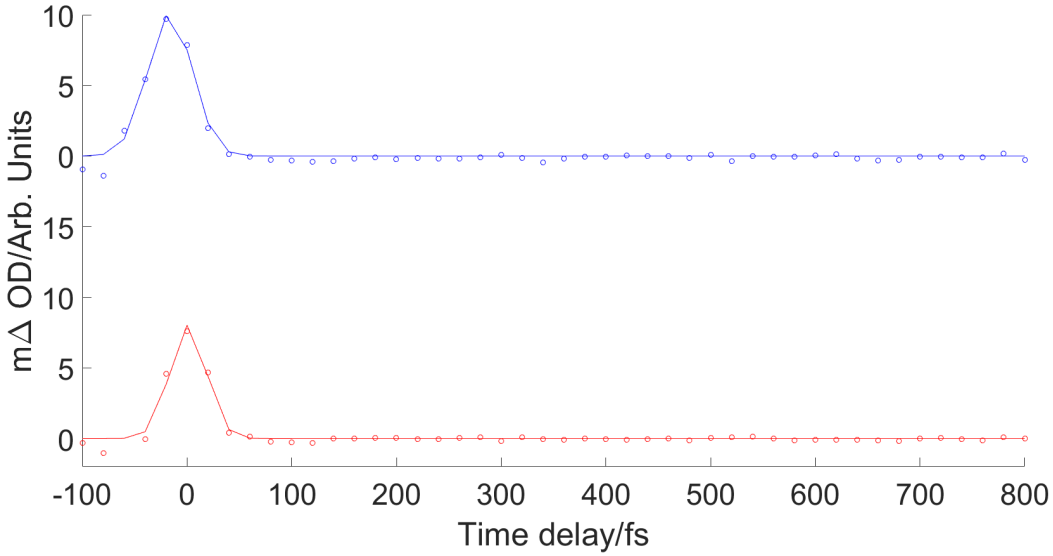

Figure 5: The instrument response of the TEAS measurements was retrieve by fitting Gaussians to the time-zero artifacts present in the solvent scans in the acidic and neutral solutions and taking the full width half maximum; this gave a value of $\approx$ 80 fs

A.2 Supplementary material for "Examining solvent effects on the ultrafast dynamics of catechol"

Examining Solvent Effects on the Ultrafast Dynamics of Catechol - Supplementary information

M. A. P. Turner,[1,2] R. J. Turner,[2] M. D. Horbury,[2] N. D. M. Hine,[1] and V. G. Stavros[2, a)]

[1)] *Department of Physics, University of Warwick, Coventry, CV47AL.*

[2)] *Department of Chemistry, University of Warwick, Coventry, CV47AL.*

(Dated: 30 July 2019)

[a)] v.stavros@warwick.ac.uk

I. LIST OF FILES INCLUDED IN ONLINE ZENODO REPOSITORY

The underlying data of this publication can be accessed via the Zenodo Archive at DOI: 10.5281/zenodo.3241438, This includes:

- Input, geometry, and output files for the geometry optimization and frequency calculations on *open* and *closed* catechol conformers with two solvent molecules included.
- Input, geometry, and output files for the geometry optimization and frequency calculations on *open* and *closed* catechol conformers in 5 Å radii explicit solvent shells.
- Input, geometry, and output files for catechol with fixed dihedral rotations.
- Averaged TEAS scans for catechol in acetonitrile at concentrations of 5 mM and 75 mM with 83 and 60 time points respectively.
- Averaged TEAS scans for catechol in acetonitrile at concentrations of 5 mM and 75 mM with 5 time points (more highly averaged).

II. A FITTED TIME-ZERO ARTEFACT FOR THE TEAS SET-UP IN ACETONITRILE SOLVENT

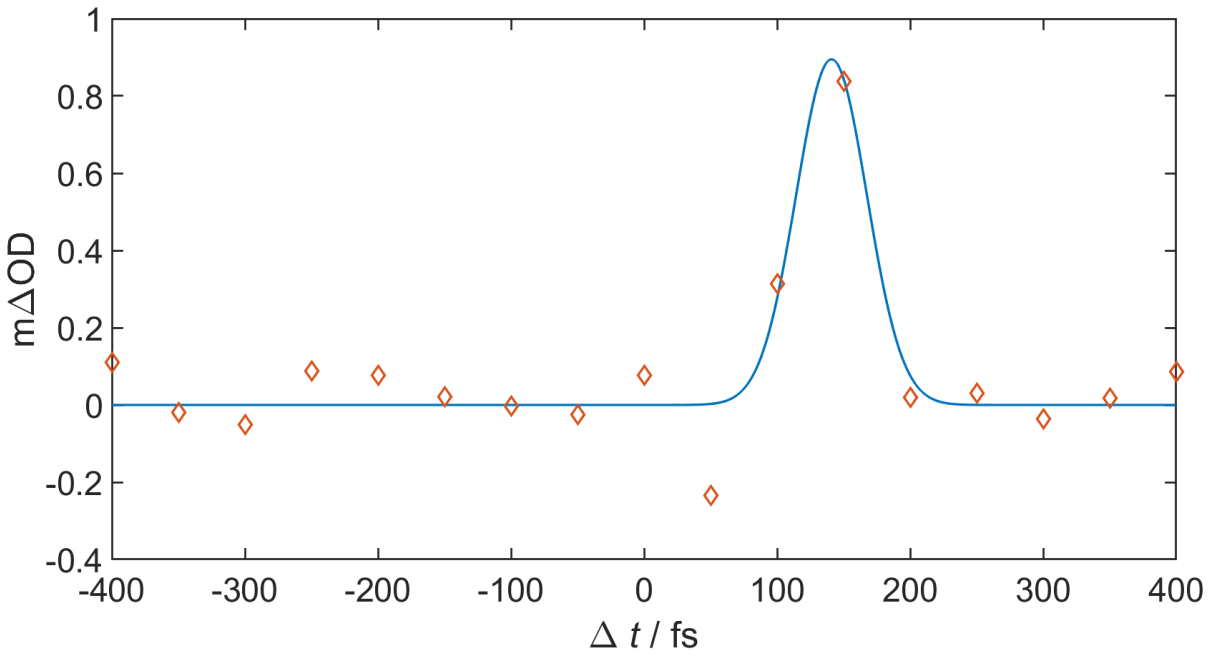

FIG. 1. The instrument response functions of the TEAS measurements were retrieved by fitting Gaussian functions to the time-zero artefacts in acetonitrile solvent scans and recording the full width half maximum (FWHM). This figure shows an exemplar data set at 540 nm probe wavelength (267 nm pump); the returned FWHM is $\approx$ 80 fs.

III. A TWO-DIMENSIONAL PLOT OF S_0 ENERGY OF CATECHOL WITH RESPECT TO THE DIHEDRAL ANGLES OF BOTH OH GROUPS

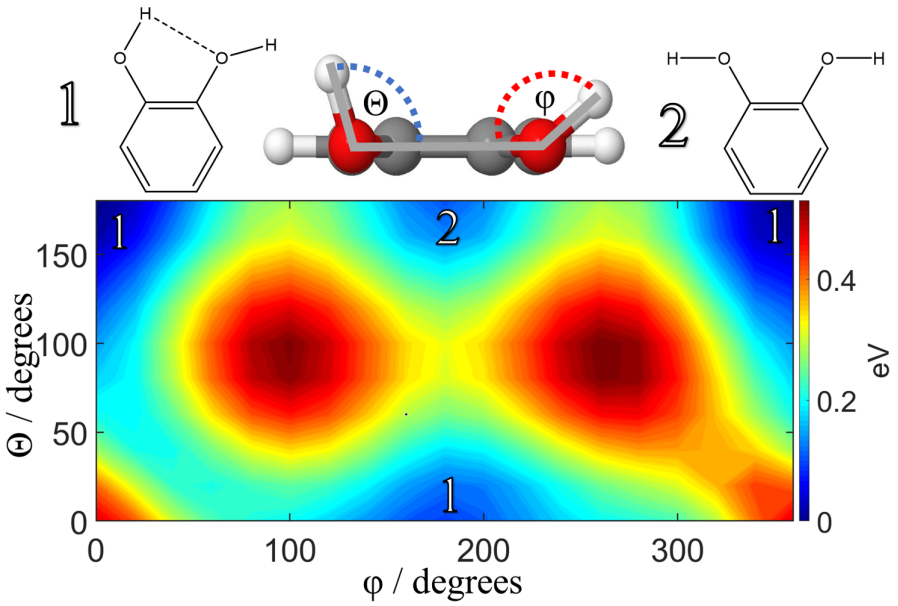

FIG. 2. 2D scan of dihedral bond angles (θ and ϕ see inset) vs. S_0 energy as calculated by density functional theory at the PBE/6-31G* level with implicit acetonitrile solvent. This was conducted by taking the optimised structure for the *closed* conformer and rotating the dihedral angle of each OH group in steps of 20 ° with all other internal coordinates fixed. For each step the single-point energy was calculated. As the only local minima observed were the *open* and *closed* structures, these were the only conformers considered in future calculations. Two important caveats should be noted: first, the absolute energies on this plot are unlikely to be reliable indicators of relative stability in solution, since we show in the main manuscript that strong solvent-solute hydrogen bonding interactions occur in acetonitrile, which will lead to a dramatic change in the relative energies of different structures; Second, the starting bond angles in the *closed* conformer of the intramolecular and intermolecular C–O–H linkages are 108.5° and 109.4°, respectively. This slight difference results in an asymmetry with respect to rotation of the two angles, and an associated error of up to 0.06 eV between the calculated energies of geometries which, if symmetry was strictly imposed, would be identical. Since this error is small compared to the overall energy scale, and this plot intended only to illustrate the landscape, we chose not to conduct the constrained geometry relaxations at each point that would be required to precisely map the potential energy surface.

IV. CALCULATED FREQUENCIES FOR CATECHOL IN THE OPEN AND CLOSED CONFORMERS AS CALCULATED USING BOTH AN IMPLICIT SOLVENT MODEL AND AN EXPLICIT SOLVENT SHELL

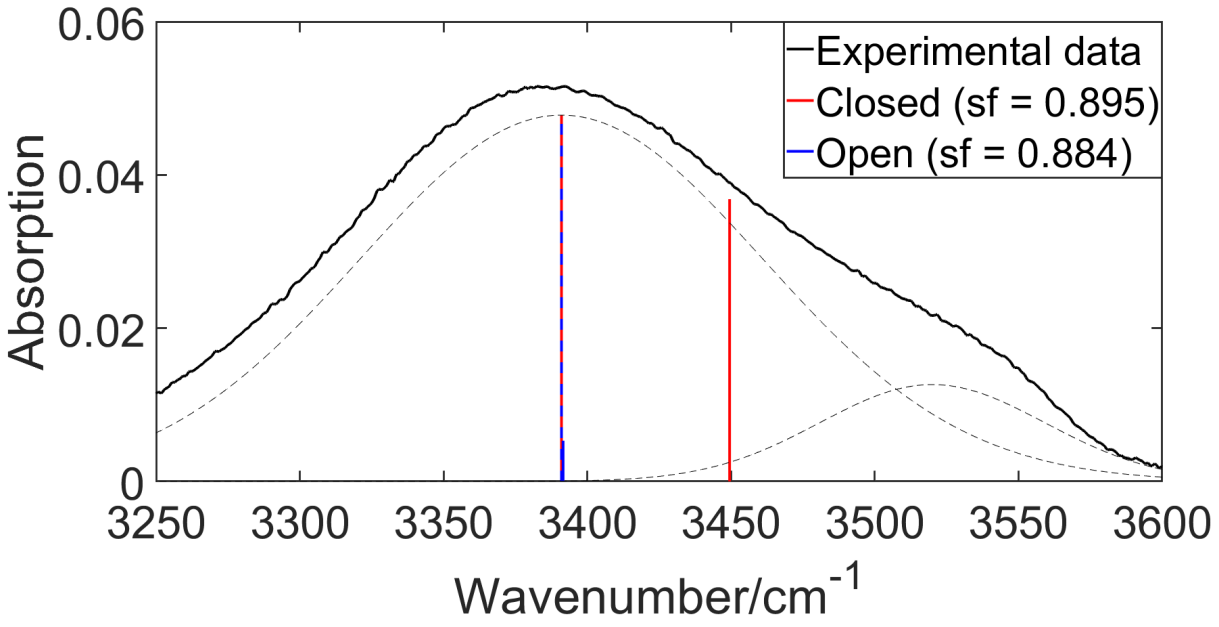

FIG. 3. Experimental FTIR spectrum for catechol in acetonitrile (solid black line) compared to theoretical predictions for vibrational frequencies of catechol in implicit acetonitrile solvent (vertical lines), calculated at the PBE0/cc-pVTZ level of theory. Red lines show predicted frequencies for the *closed* conformer and blue lines show those of the *open* conformer. Where the red and blue lines lie on top of one another, the line is dashed red and blue. The experimental spectrum has been deconvolved into two Gaussian functions (dashed black lines) after correcting for a small broad band associated with water. Predicted frequencies were scaled to align with the lower frequency peak in the experimental result. Scaling factors (denoted sf, see section 2B of the main manuscript) were applied to match the The scaling factors are quite large and even after these are applied, the results for the second peak do not match well in either model with the experimental data. It was consequently determined that calculations involving explicit representation of solvent molecules were necessary for a quantitative understanding.

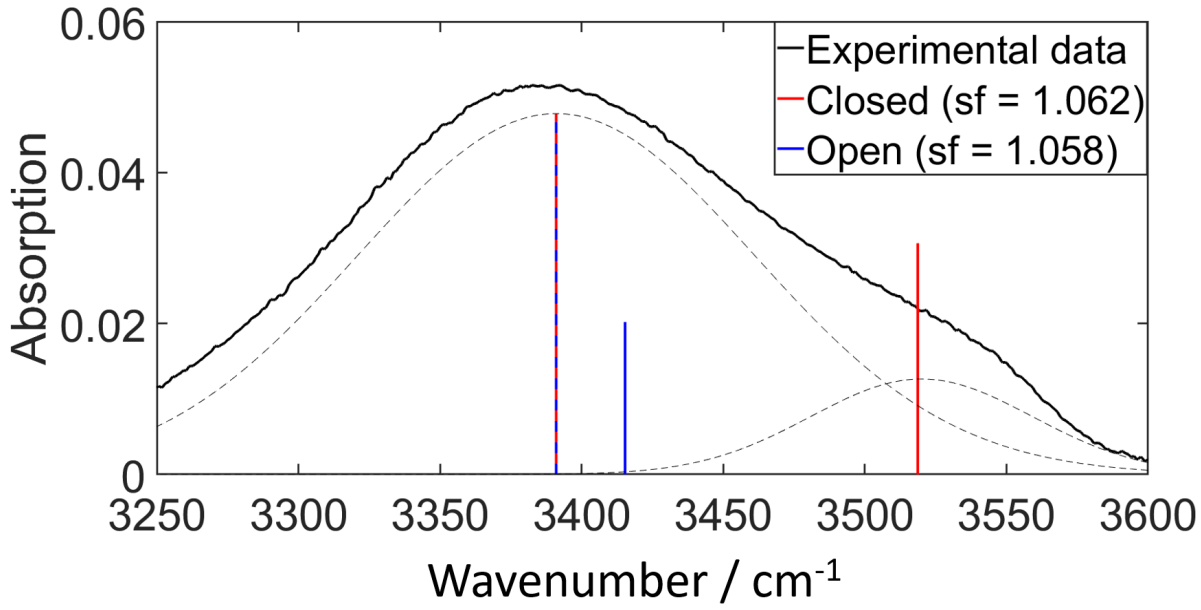

FIG. 4. Experimental FTIR spectrum for catechol in acetonitrile (solid black line) compared to theoretical predictions for vibrational frequencies of catechol complexed with explicit acetonitrile solvent shells (vertical lines), calculated at the PBE/cc-pVDZ level of theory. In this, three snapshots were analysed and the resulting predicted frequencies were averaged. Red lines show the predicted frequencies of the *closed* conformer and blue lines show those of the *open* conformer. Where the red and blue lines lie on top of one another, the line is dashed red and blue. Deconvolution has been applied to the experimental spectrum as in Fig. 3. Methodology for generating the explicit solvent shells is detailed in Sec. 2.2 of the main manuscript. Excellent agreement is seen with experimental results. It is to be noted that with only three tested snapshots, we retain a large statistical uncertainty, which is discussed further in the main manuscript. In future work, further snapshots could be analysed to fully sample the distribution of possible geometries. For our purposes, however, we confirmed that this methodology gave similar results to the method described in the main manuscript (which used only two solvent molecules).

V. THE STARTING GEOMETRIES FOR THE TWO-SOLVENT FREQUENCY CALCULATIONS

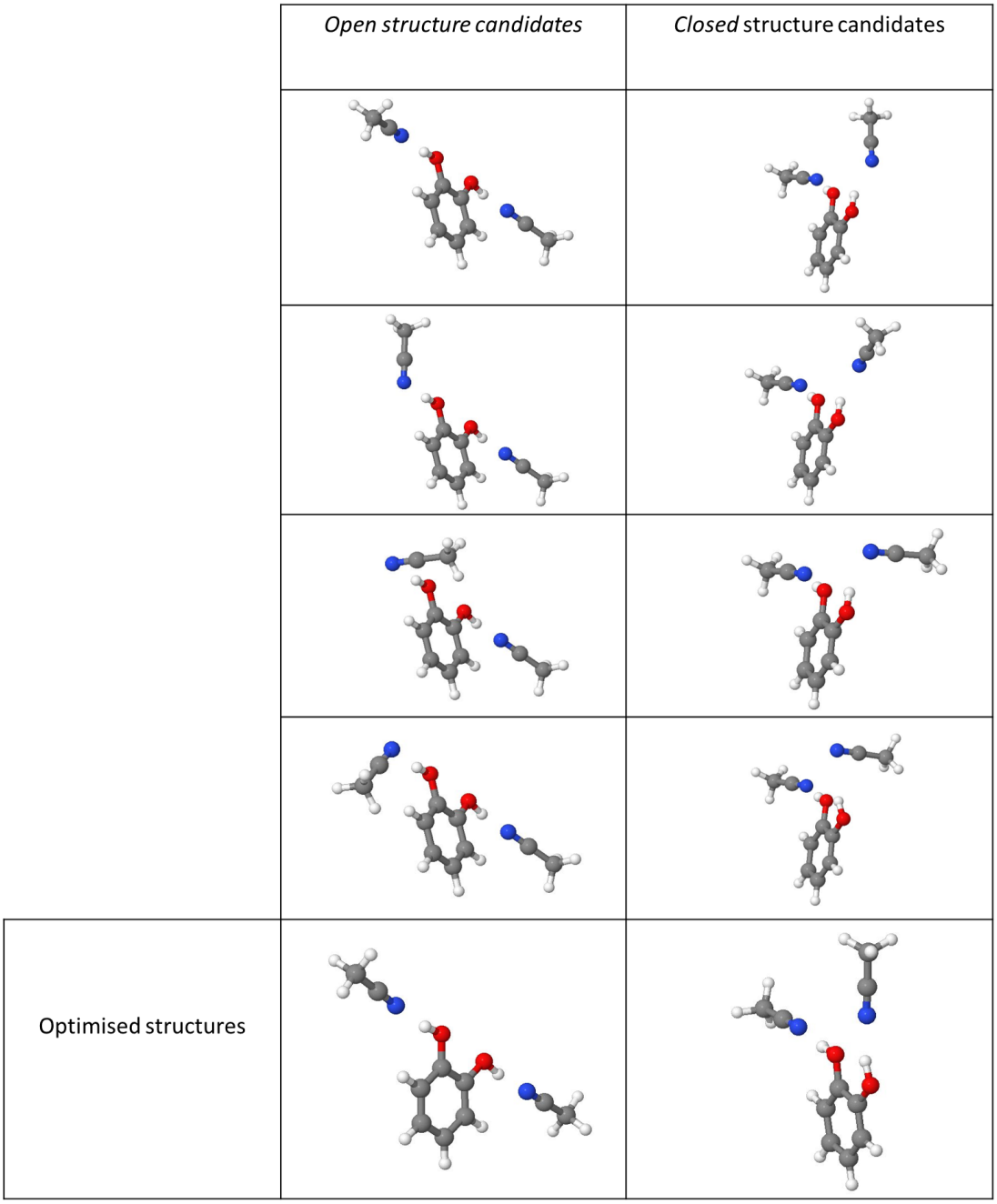

FIG. 5. Starting candidates for the *open* and *closed* structures of catechol. After geometry optimization the *open* candidates all converged to similar structures as did the *closed* candidates. Owing to this, the lowest energy optimized structure was taken forward.

VI. THE VIBRATIONAL MODES IN THE O-H STRETCH REGION ASSOCIATED WITH THE TWO-SOLVENT FREQUENCY CALCULATIONS

Form	Wavenumber (S.F.)/cm^{-1}	Relative intensity/au	Vibrational Mode
Closed	3597 (0.975)	1.24	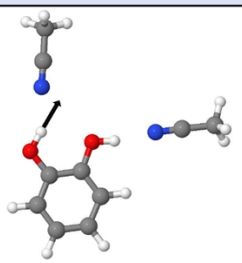
Closed	3477 (0.975)	1.97	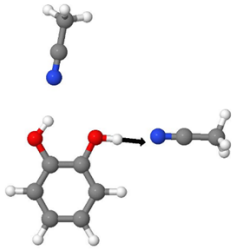
Open	3516 (0.966)	0.24	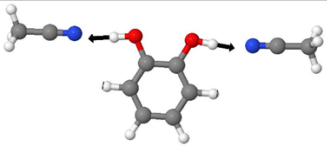
Open	3509 (0.966)	3.33	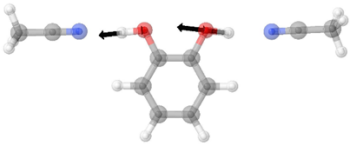

TABLE I. Calculated vibrational frequencies and normal mode plots for the *open* and *closed* conformers. The level of theory used was PBE0/cc-pVTZ. S.F. denotes the scaling factor applied to the frequencies of each structure to generate Fig. 3 in the main manuscript.

VII. A REPRESENTATION OF THE THREE DIFFERENT TYPES OF HYDROGEN BONDING POSSIBLE IN THE CLOSED CONFORMER OF CATECHOL SYSTEM IN ACETONITRILE.

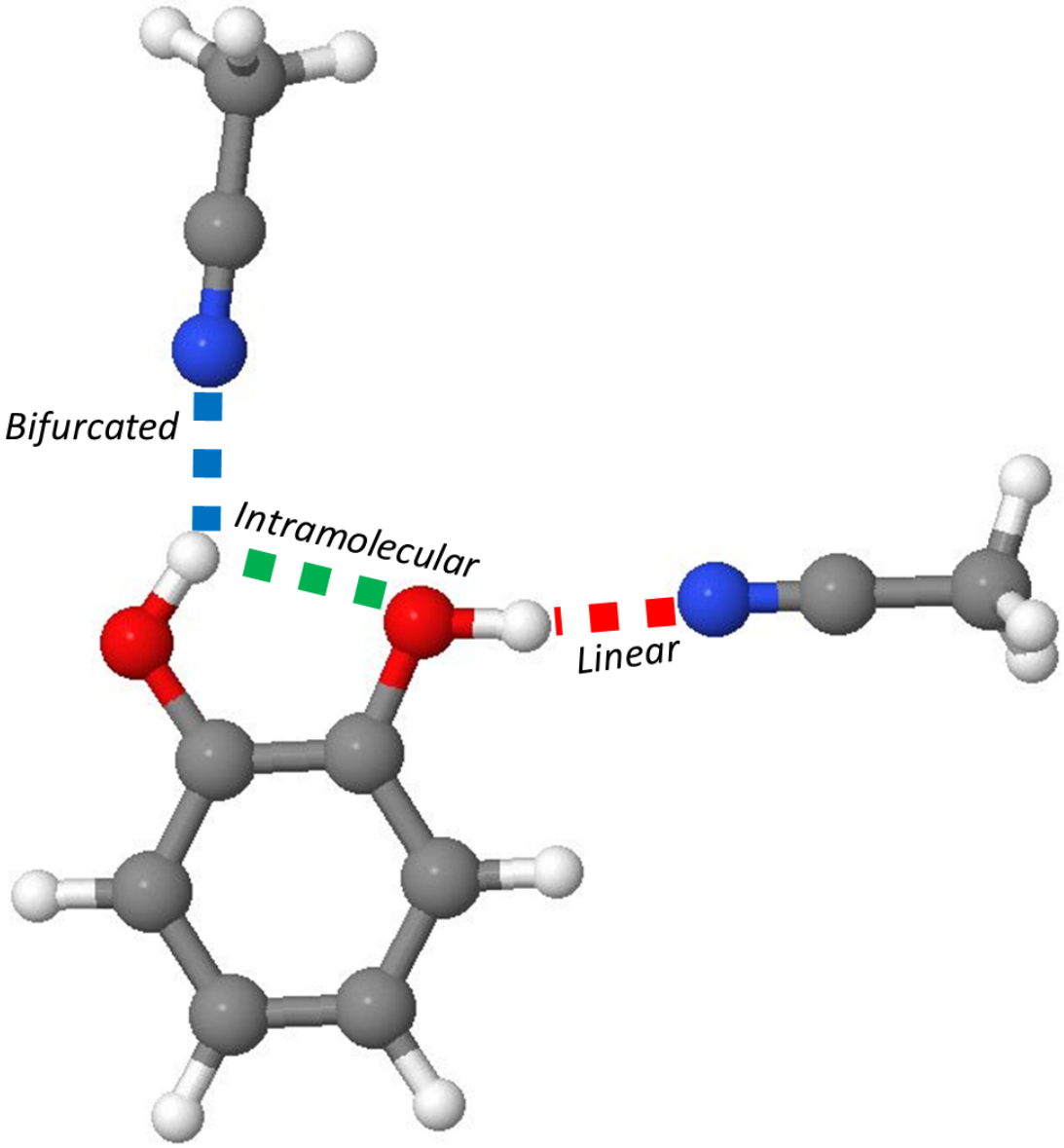

FIG. 6. Schematic of the three forms of hydrogen bonding possible with catechol in acetonitrile (at low concentrations), and the associated nomenclature we use in the main manuscript. The red bond indicates the linear intermolecular hydrogen bond; the blue bond indicates the bifurcated intermolecular hydrogen bond; and the green bond indicates the intramolecular hydrogen bond.

TABLE II. Amplitudes associated with fitted lifetimes in figure 5 of the main manuscript. The TAS data was collected for catechol in acetonitrile at different concentrations with a pump wavelength of 267 nm. This was fitted using a bi-exponential function, convolved with a Gaussian function to model the instrument response, at a probe wavelength 450 nm. Further details can be found in section 2A of the main manuscript.

Concentration/mM	Lifetime	Amplitude/ mΔOD
5	70 $\pm$ 40 fs (τ_1)	-3.4
5	730 $\pm$ 30 ps (τ_2)	2.1
75	450 $\pm$ 50 fs (τ_1)	0.2
75	1700 $\pm$ 200 ps (τ_2)	2.0

Table 2 shows the relative amplitudes of each of the fitted lifetimes in figure 5 of the main manuscript. It can be seen that the lifetime of τ_1 at 5 mM concentration represents a rise which implies the excited state absorption of the S_1 state at 450 nm was larger after vibrational energy transfer coupled with solvent rearrangement. The amplitude of τ_1 in 75 mM solution, however, is significantly smaller. One explanation for this could be that there is little change in excited state after undergoing vibrational energy transfer and solvent rearrangement. This could be due to the rigidity of the aggregate hindering structural change. This is likely a similar effect to that discussed in section 3B of the main manuscript.

A.3 Supplementary material for "Insights into the photoprotection mechanism of the UV filter homosalate"

Supplementary Information: Insights into the photoprotection mechanism of the UV filter homosalate

Matthew A. P. Turner,‡[a,b] Emily L. Holt,‡[a,b] Konstantina M. Krokidi,‡[a]
Piyush Mishra,[c] Timothy S. Zwier,[c] Natércia d. N. Rodrigues*[a] and Vasilios G. Stavros*[a]

[a] *Department of Chemistry, University of Warwick, Gibbet Hill Road, Coventry, CV4 7AL, United Kingdom*

[b] *Molecular Analytical Science Centre for Doctoral Training, Senate House, University of Warwick, Coventry, CV4 7AL, United Kingdom*

[c] *Department of Chemistry, Purdue University, West Lafayette, Indiana 47907-2084, United States*

* *To whom correspondence should be addressed. E-mail: v.stavros@warwick.ac.uk, or n.das-neves-rodrigues@warwick.ac.uk*

‡These authors contributed equally to this work.

Contents

S1 Gas-phase experiments

S1.1 Power dependence measurements

The TR-IY signal dependence on both the pump and probe laser powers was evaluated in order to ensure single-photon photodynamics take place under the current experimental conditions. The method followed in that respect can be described in three steps. Firstly, TR-IY transients are collected at three different values of laser power; the logarithm of transient signal with respect to the logarithmic value of power for each time delay (log(Signal) *vs.* log(Power)) is then plotted and finally fit using a linear function using least squares regression. The gradient of this fit provides us with the physical information regarding the signal-power dependence — a gradient of 1 (within error) is taken to be indicative of single-photon dynamics. In Fig. S1, such power study plots are indicatively shown for photoexcitation at $\lambda_{\text{pump}} = 305$ nm ($\lambda_{\text{probe}} = 200$ nm) and at selected pump-probe time delays of $\Delta t = 0$, 0.2 and 50 ps. Similar results were observed for other pump wavelengths and power dependence on probe power was also shown to be linear under our experimental conditions. Importantly, the large feature observed within our instrument response function (IRF, see below) was consistently observed to have linear dependence on both pump and probe laser powers, revealing its origin in single-photon dynamics rather than multiphoton artifacts, as is common for such IRF-limited features (see main paper for further discussion).

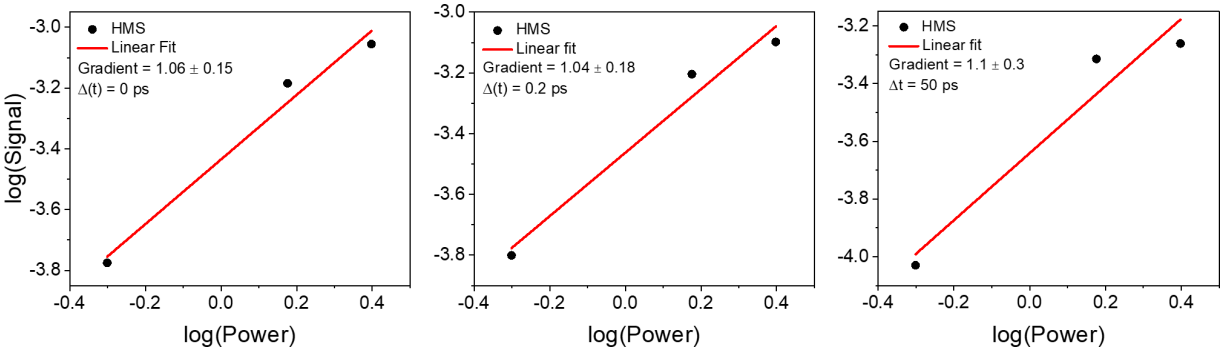

Figure S1: Power dependence study for HMS in vacuum at (a) $\Delta t = 0$ ps, (b) $\Delta t = 0.2$ ps and (c) $\Delta t = 50$ ps. The red line denotes the line of best fit attained by linear least squares regression.

S1.2 Kinetic fit

We fit our TR-IY data for the homosalate (HMS) parent ion (HMS^+) transients using a multi-parameter function that can be analytically described as follows:

$$S(t) = g(t) * \sum_{i=0}^{n} A_i e^{-\frac{t}{\tau_i}} H(t) + \text{offset} \tag{S1}$$

Equation S1 describes the convolution of a Gaussian function $g(t)$ (corresponding to the instrument response function, see below) with a sum of exponential decay functions starting at time zero ($\Delta t = 0$). A_i is then the amplitude of the i-th decay, τ_i the time constant corresponding to the i-th decay and $H(t)$ is a step function defined in Equation S2.

$$H(t) = \begin{cases} 0 & \text{if } t < 0 \\ 1 & \text{if } t \geq 0 \end{cases} \tag{S2}$$

This kinetic fit assumes parallel excited state decay pathways, *i.e.* it assumes that all dynamics begin at $\Delta t = 0$.

S1.3 Instrument response function and time zero $\Delta t = 0$

As mentioned in the main manuscript, the instrument response function (IRF) defines the time resolution of our time resolved measurements. In order to estimate the IRF, TR-IY measurements of Xenon (Xe) were performed, following $2+1$ non-resonant ionization (see Fig. S2). The resulting

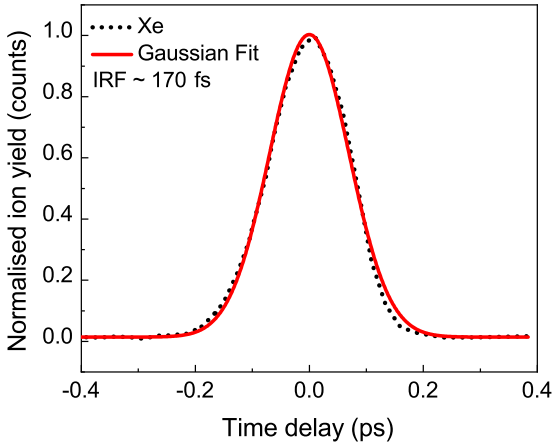

Figure S2: Gaussian fit (red line) to the Xe TR-IY transients (black dotted line). The FWHM of the fitting curve presented provides us with the pump-probe beam cross-correlation width of $\sim$ 170 fs, which we quote as our IRF.

transient, which consists of the cross-correlation between the pump and probe laser pulses, was fit with a Gaussian function; the full width at half maximum (FWHM) of this Gaussian fit, which was determined to be $\sim$ 170 fs, was taken to be our IRF.

S1.4 Dispersed fluorescence and fluorescence lifetime

Fig. S3a shows the dispersed fluorescence spectrum of HMS which was obtained following the methodology described in the main paper. Briefly, the laser wavelength was fixed to be resonant with selected transitions in the excitation spectrum and the resulting fluorescence was then dispersed with a grating and collected by an intensified CCD. Upon photoexcitation to the $S_1(v = 0)$ origin of HMS, the resulting dispersed fluorescence spectrum reveals a large Stokes shift of ~ 5800 cm^{-1} or 0.71 eV (see Fig. S3a).

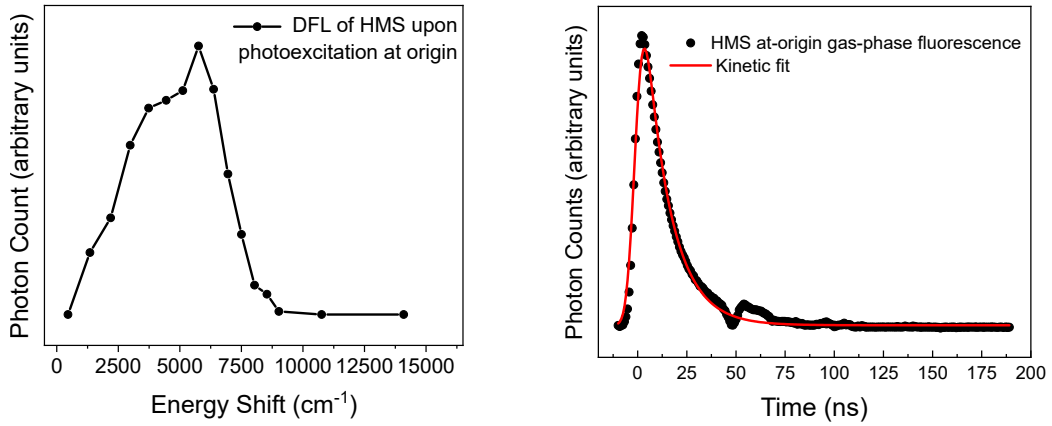

(a) (b)

Figure S3: (a) Dispersed fluorescence spectrum of HMS. (b) Fitted transient (black dotted line, with line of best fit shown in red) to extract the fluorescence lifetime of HMS at origin.

Fluorescence lifetime traces were also recorded by exciting select transitions and directly recording the time profile of the fluorescence signal from the photomultiplier tube on the digital oscilloscope. The gas-phase fluorescence lifetimes of HMS were extracted from the resulting transients following the same method described in section 1.2, using in this case an instrument response of 8 ns. Fig. S3b shows one example of such fluorescence lifetimes measurements, for which excitation was to the $S_1(v = 0)$ of HMS; a fluorescence lifetime of 12.7 $\pm$ 0.2 ns was extracted from this fit.

S1.5 LIF linewidths

The first four peaks of the LIF spectrum of HMS were fitted with Lorentzian functions as shown in Fig. S4. The linewidths of these peaks (Γ, taken here to be the FWHM of each respective Lorentzian fit) are related to the lifetimes (τ) of the species associated with each respective peak

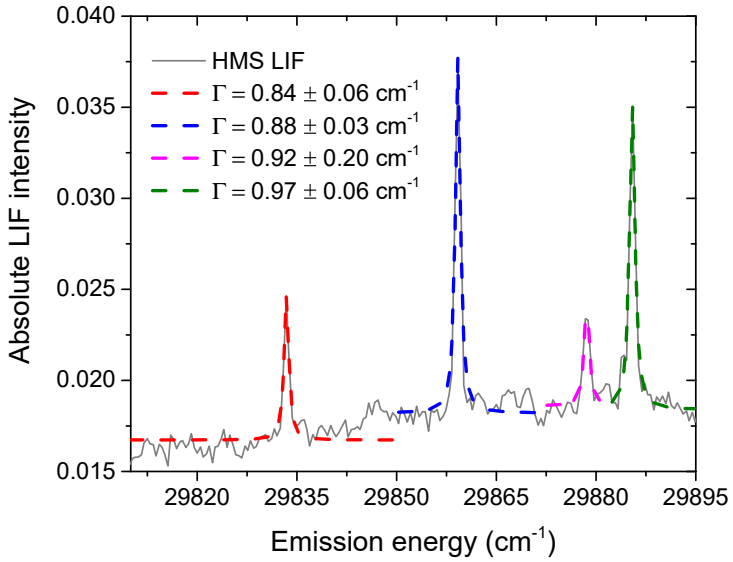

Figure S4: Lorentzian fits (dashed lines) to the first four peaks of the LIF spectrum of HMS (raw data presented as a grey solid line). These Lorentzian fits return Γ values of 0.84 cm^{-1} for the peak centred at 29833.4 cm^{-1} ($S_1(v = 0)$ origin of HMS, red dashed line), 0.88 cm^{-1} for the peak at 29859.2 cm^{-1} (blue dashed line), 0.92 cm^{-1} for the peak at 29878.6 cm^{-1} (magenta dashed line) and 0.97 cm^{-1} for the peak at 29885.5 cm^{-1} (green dashed line).

by $\tau = \hbar/\Gamma$.[1] Following this analysis, the linewidth of the origin peak of HMS is $\sim$ 0.84 cm^{-1}, which corresponds to a lifetime of the S_1-*enol* species of $\sim$ 6 ps (lower limit).

S2 Experiments in solution

S2.1 Fitting procedure

The spectra collected with our TEAS setup, further described in the main paper, are chirped, *i.e.* $\Delta t = 0$ is different for each probe wavelength, due to group velocity dispersion (GVD) artefacts.[2] To account for this chirp effect, a third order polynomial is included within the fitting algorithm within the package Glotaran.[3] This package also convolutes the Gaussian IRF (see Section S2.2) with exponential functions to extract the fitted lifetimes (τ_n) for the parallel kinetic model used for this data. This parallel model assumes that all processes begin instantaneously following photoexcitation. In the heat maps presented in the main manuscript and this SI, the chirp is corrected using the KOALA package[4].

S2.2 Instrument response functions

The IRF for our TEAS setup is determined by evaluating solvent only responses at given probe wavelengths. The resulting transients were fitted with a Gaussian function, as shown in Fig. S5,

described by:

$$f(t) = A \exp\left(-\frac{t - t_0}{2\sigma^2}\right) + \text{offset} \tag{S3}$$

where A denotes the peak amplitude of the fitted curve, t_0 is the fitted time zero, indicating the centre of the curve, and σ is the standard deviation of the curve. To convert from the fitted standard deviation to the full width half maximum (FWHM), which is the quoted IRF, a scaling factor of $2\sqrt{2\ln 2}$ was applied to the standard deviation σ. After application of this scaling factor, the extracted IRF lifetimes are $\sim$ 80 fs in acetonitrile, $\sim$ 65 fs in ethanol and $\sim$ 55 fs in cyclohexane.

S2.3 Power dependence measurements

Power dependence measurements were taken for each solution of HMS and ethylhexyl salicylate (EHS) in all three solvents: ethanol, acetonitrile and cyclohexane, to ensure a linear dependence on power across all spectral features of the TAS and exclude the possibility of multiphoton transitions, following the relation (log(Signal) *vs.* log(Power)). A gradient of 1 (within error) is suggestive of single photon mediated photodynamics. The power of the pump wavelength was varied for each set of measurements by reducing the output of the TOPAS-C.

Slices of the transients were taken in the wavelength domain where significant spectral features occur, then the slices were smoothed by using an integration window of $\pm$ 5 nm. The outcome of this power dependence study is shown in Fig. S6 for HMS in ethanol and Fig. S7 for ethylhexyl salicylate in ethanol.

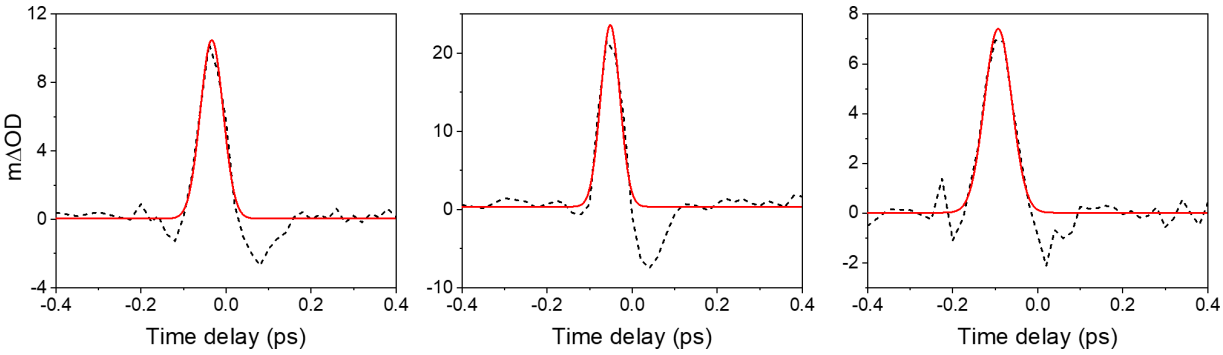

Figure S5: Selected transients for solvent only time-zero IRFs of (a) ethanol at 330 nm, IRF $\sim$ 65 fs (b) cyclohexane at 320 nm, IRF $\sim$ 55 fs and (c) acetonitrile at 330 nm, IRF $\sim$ 80 fs, plotted using black dashed line. These IRFs have been extracted from a Gaussian fit function, with the line of best fit shown in red.

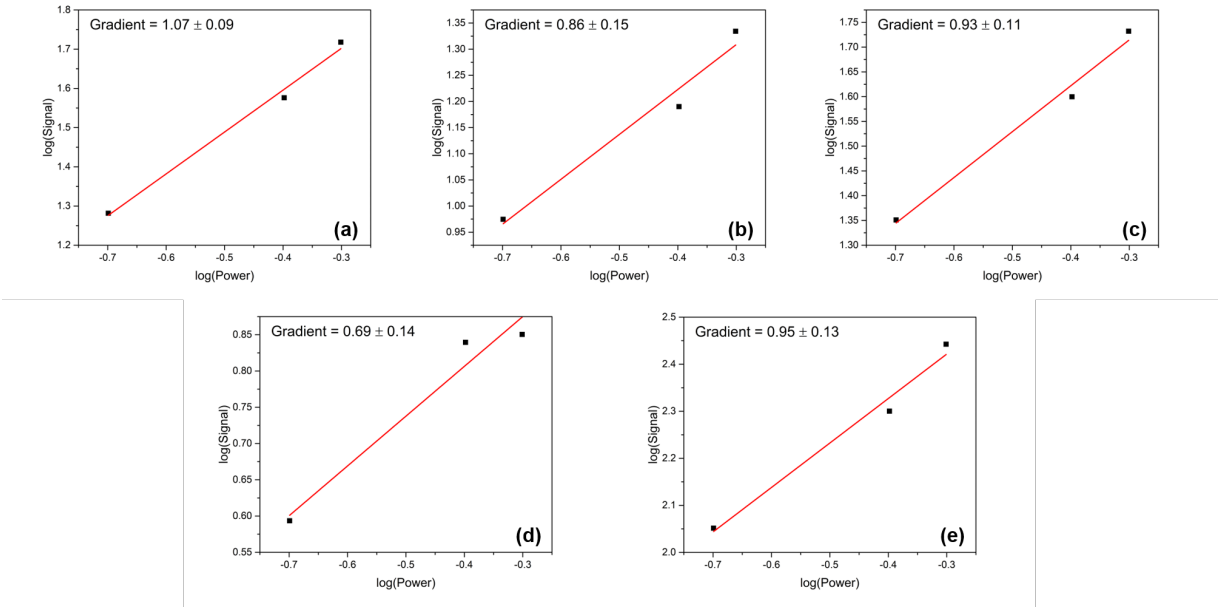

Figure S7: Power dependency study for ethylhexyl salicylate in ethanol as follows: (a) 340 nm at 1 ps, (b) 340 nm at 500 ps, (c) 450 nm at 1 ps, (d) 450 nm at 500 ps, (e) 530 ps at 1 ps.

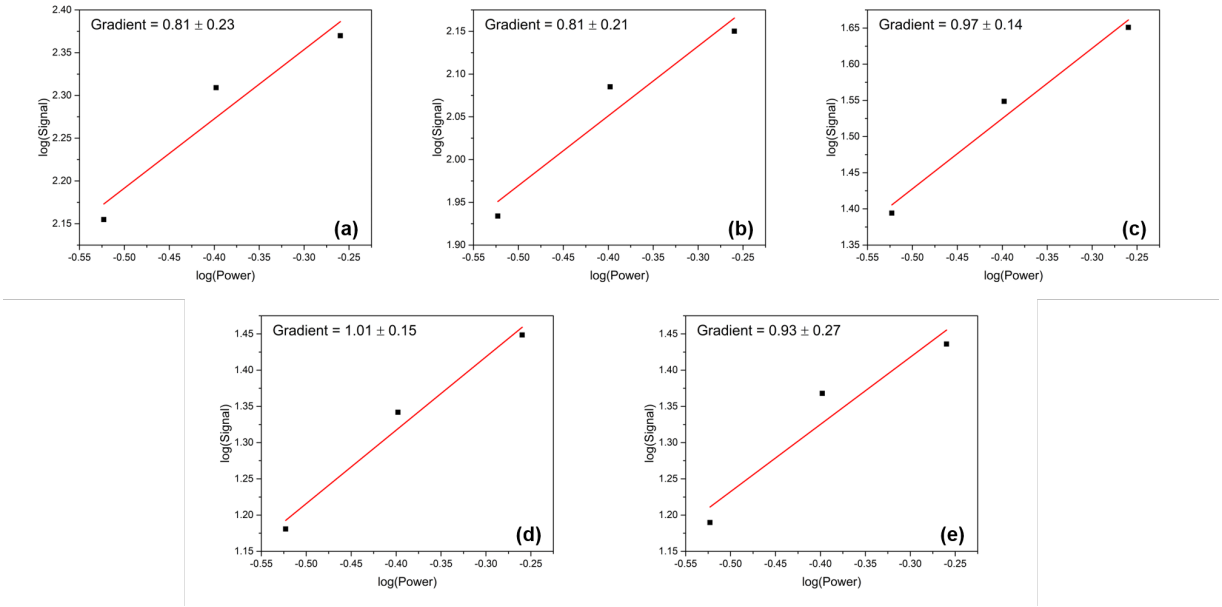

Figure S6: Power dependency study for HMS in ethanol as follows: (a) 340 nm at 1 ps, (b) 340 nm at 100 ps, (c) 450 nm at 1 ps, (d) 450 nm at 100 ps, (e) 530 ps at 1 ps.

S2.4 Fluorescence of homosalate

Emission spectra were measured for homosalate (HMS) in each of three solvents: acetonitrile, ethanol and cyclohexane. Solutions were prepared to a concentration of $\sim$ 10 μM and the path length for spectrum acquisition was 10 mm. The emission spectra were collected using a Horiba Fluorolog-3 instrument; the excitation wavelength was chosen to be the λ_{max} of each solution, 306 nm in acetonitrile, 307 nm in ethanol and 309 nm in cyclohexane, which were produced by a Xenon arc lamp with a slit width of 5 nm.

Fluorescence lifetimes for the three solutions of HMS were also determined. The same samples as the fluorescence measurements above were used to assess the lifetimes, and a 1 cm path length quartz fluorescence cuvette was used. Instead of a Xe arc lamp, the excitation source was a NanoLED with a central wavelength of 318 nm. An exponential decay function was fitted to the fluorescence signal *vs.* time transients to extract the respective fluorescence lifetimes, which were found to be within the instrument response of 1.2 ns in all instances.

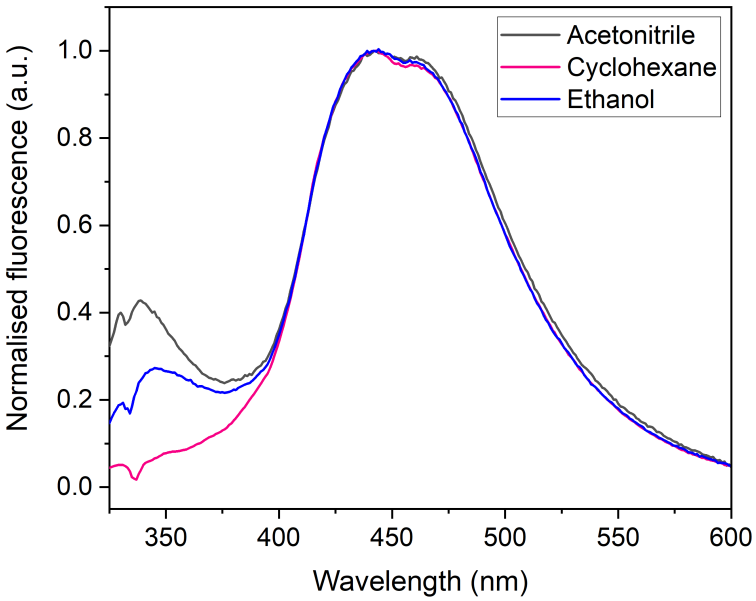

Figure S8: Normalised emission spectra with solvent baseline subtraction of HMS in cyclohexane, ethanol and acetonitrile. Excitation was carried out at the respective peak maxima of each solution: $305 \leq \lambda_{pump} \leq 310$ nm. The slit width was 2.5 nm. The slight discrepancy in the spectra at $\sim$ 330 nm is due to Stokes Raman scattering effects that could not be fully subtracted from the fluorescence spectra.[5]

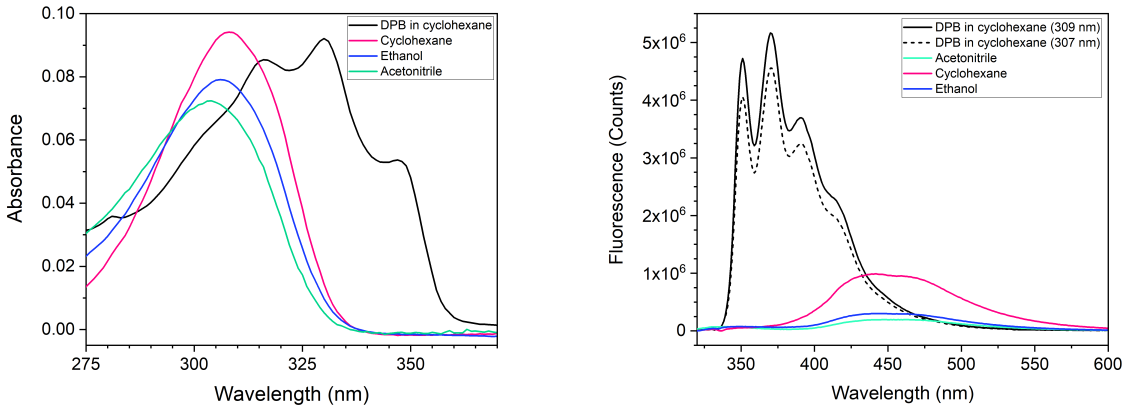

(a) (b)

Figure S9: (a) UV-visible spectra taken of three $\sim$ 20 μM solutions of homosalate in cyclohexane (pink line), ethanol (blue line) and acetonitrile (green line), with the standard solution, $\sim$ 0.5 μM 1,4-diphenyl-1,3-butadiene (DPB) in cyclohexane shown in black. (b) Averaged fluorescence spectra, attained from averaging five separate scans, which were integrated and the values substituted into Eq. S4

S2.4.1 Fluorescence quantum yield of homosalate

The fluorescence quantum yield of HMS, Φ_{F}(HMS), was determined in all three solvents following the methodology described by Würth *et al.*,[6] by comparing the fluorescence emission to that of a known standard, 1,4-diphenyl-1,3-butadiene (DPB) in cyclohexane. All three solutions were prepared such that they had an absorbance value of 0.1 or below, which corresponds to a concentration of approximately 20 μM for HMS solutions and approximately 0.5 μM for the solution of DPB in cyclohexane. The UV-visible spectra of the sample and standard solutions are shown in Fig. S9a.

Five repeats of the emission spectra were taken for each of the fluorescence samples. These five emission spectra were averaged, and this average was used for the final calculation of Φ_{F}(HMS) using Eq. S4.[6] The averaged spectra are shown in Fig. S9b.

$$\Phi_{\mathrm{F}}^{x} = \frac{F_x A_s n_x^2}{F_s A_x n_s^2} \Phi_{\mathrm{F}}^{s} \tag{S4}$$

The parameters in Eq. S4 are defined as follows: Φ_{F}^{x} is the fluorescence quantum yield of the sample solution, Φ_{F}^{s} the fluorescence quantum yield of the standard, F_x is the integrated area of the fluorescence curves of the sample (320 – 600 nm), with F_s being the equivalent integral for the reference standard (320 – 600 nm); finally n_s^2 is the refractive index of the solvent of the standard solution (cyclohexane) and n_x^2 is the refractive index of the sample solution. The value of Φ_{F}^{s} for these quantum yield calculations was 0.44.[7] However, as this value is for 330 nm excitation and

fluorescence quantum yield is a wavelength dependent quantity, some caution should be exercised with the attained homosalate quantum yields.

S2.5 TEAS measurements of ethylhexyl salicylate

TAS of ethylhexyl salicylate (EHS, also known as octisalate) were taken to compare the effects of the alkyl moiety on the action of the salicylate chromophore. The results are shown in Fig. S10 and the elucidated time constants, which were determined using the same methods as homosalate, are listed in Table S1.

As perhaps indicated by the similarities between the HMS and EHS in their UV-visible spectra (see Fig. 1 in the main paper for equivalent spectra for HMS), there are comparable spectral features in the TAS for both of these molecules. Both sets of TAS share a prominent excited state absorption feature between *ca.* 320 – 400 nm, and a stimulated emission feature centred at 450 nm. Akin to HMS, four time constants were required to adequately fit the TAS obtained for EHS; the residuals for this fit are shown in Fig. S13 (d), (e) and (f). The four time constants for EHS are comparable to those extracted for HMS, *i.e.* all four time constants are of the same orders of magnitude.

Given the similarities between HMS and EHS (and by comparison with previously published work), the extracted time constants can be confidently assigned to the same processes as were

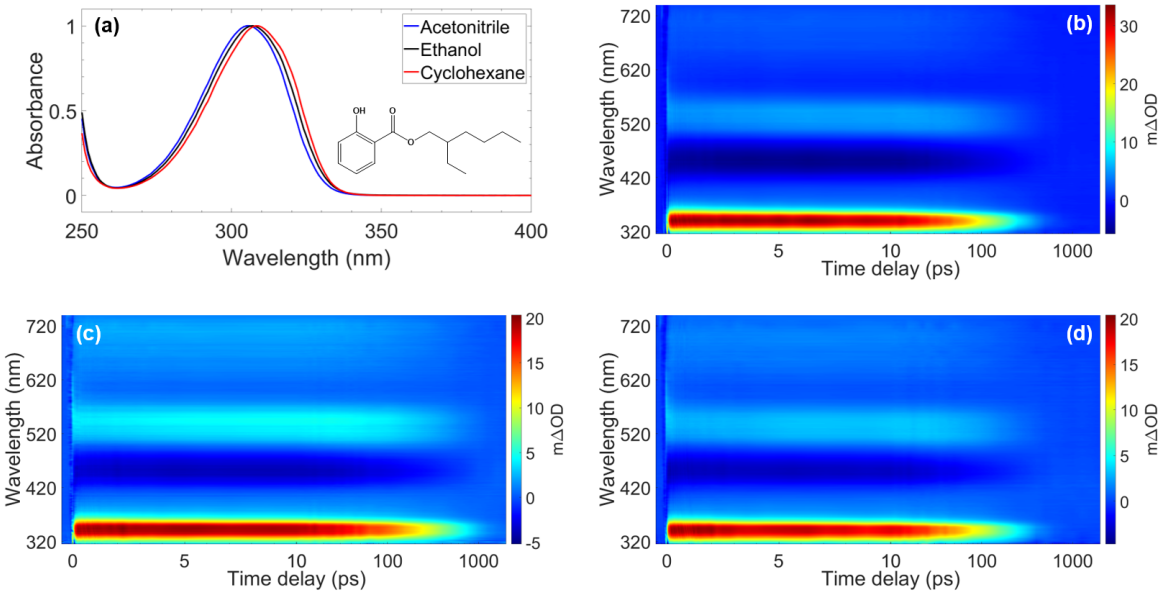

Figure S10: (a) UV-visible absorption spectra of EHS in three different solvents, with the molecular structure of EHS inset. TAS of ∼ 10 mM solutions of EHS in (b) ethanol (λ_{max} = 307 nm), (c) cyclohexane (λ_{max} = 309 nm) and (d) acetonitrile (λ_{max} = 305 nm).

elucidated for HMS in the main paper. However, according to the results presented here, relaxation of EHS has been found to be relatively faster, perhaps indicating that the suggested internal conversion relaxation pathway from the S_1 state (plus any vibrational cooling that may take place alongside it, described by τ_2) may be facilitated by a molecular motion that is hindered by the larger or more rigid structure of the ester substituent in HMS when compared to EHS. Fluorescence, described by τ_3, was also found to have a slightly shorter decay lifetime for EHS when compared to HMS. As τ_1 is defined within the constraints of the IRF, any differences in the rate of intramolecular excited-state proton transfer for EHS *vs.* HMS are inconclusive. Similarly, it cannot be determined from our TEAS measurements whether the rate of intersystem crossing is affected, as for both HMS and EHS τ_4 is beyond the temporal window of the instrument.

In summary, whilst the photophysical processes occurring within HMS and EHS following photoexcitation in the UVB region may be the same in both molecules, suggesting that these processes are predominantly dictated by the salicylate chromophore, the alkyl chains of EHS as opposed to the cycloalkane structure of HMS may facilitate slightly faster rates of decay. From these results, it follows that EHS may be a preferential sunscreen candidate to HMS, given the reduction in the value of the fitted time constants.

Table S1: Transient electronic absorption spectroscopy time constants for ethylhexyl salicylate (EHS) solutions upon excitation at λ_{max}, obtained via global parallel fitting techniques.[3]

Time constant	Ethanol	Cyclohexane	Acetonitrile
τ_1 (fs)	65 ± 35	50 ± 30	50 ± 40
τ_2 (ps)	8.8 ± 0.4	10.8 ± 0.3	9.3 ± 0.3
τ_3 (ps)	176 ± 2	412 ± 4	169 ± 2
τ_4 (ns)	$> 2^*$	$> 2^*$	$> 2^*$

* Outside the temporal window of the instrument.

S2.6 Fitting residuals

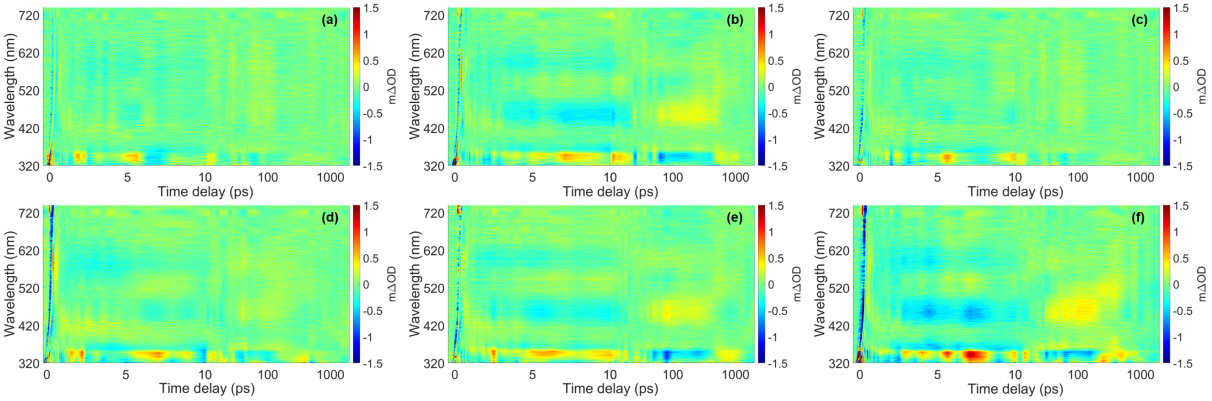

Figure S11: Residuals from the fitting of the time constants for HMS in (a) acetonitrile, (b) cyclohexane and (c) ethanol, and for EHS in (d) acetonitrile, (e) cyclohexane and (f) ethanol

The heat maps presented in Fig. S13 show the values of the residuals attained from the fitting procedure (compared to raw data), for each solute/solvent combination for both HMS and EHS.

S3 Computational studies

S3.1 Conformer structures of homosalate

Conformer	Relaxed S_0	Relaxed S_1
Conformer 1	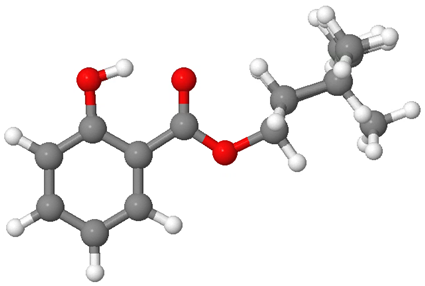 0 eV	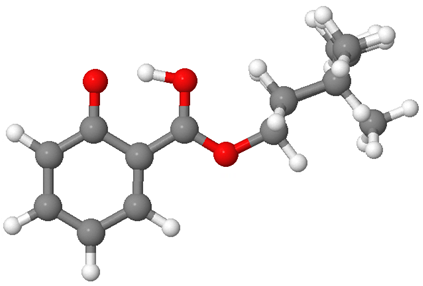 3.90 eV
Conformer 2	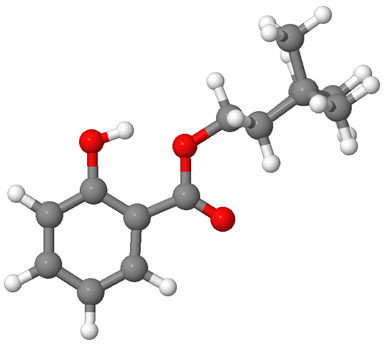 0.17 eV	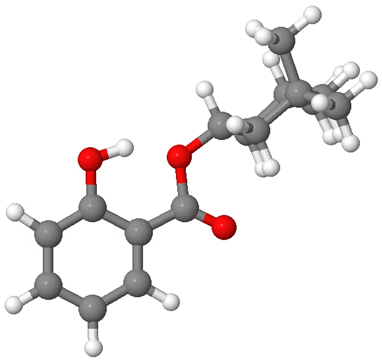 4.30 eV

Figure S12: Structure and relative energies (relative to conformer 1 in the S_0 state, the lowest energy structure/state) of both conformers of homosalate in both the S_0 and S_1 states. The ground state energies were calculated by relaxing the geometry of both conformers at the PBE/cc-pVTZ level of theory and then conducting a single point energy calculation on each at the PBE0/cc-pVTZ level of theory. The excited state energies were calculated by relaxing each conformer with respect to the S_1 state at the PBE0/cc-pVTZ level of theory.

S3.2 Potential energy cuts for homosalate

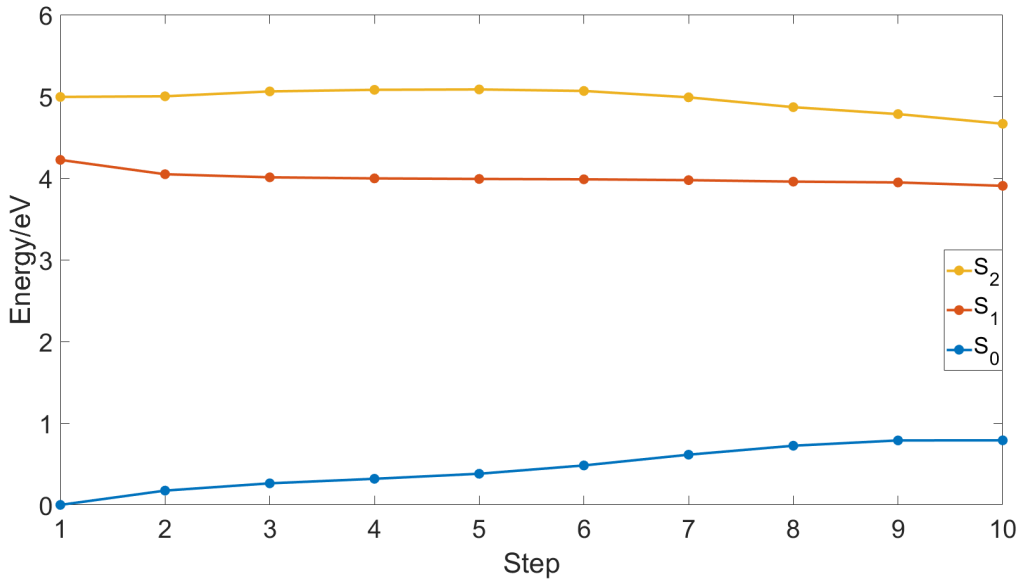

Figure S13: S_0, S_1, and S_2 energies of homosalate in specific steps between the *enol* and *keto* forms. These steps were generated through a linear interpolation of atomic coordinates. This figure is an expansion upon Fig. 2b in the main text to demonstrate the lack of intersection between the S_1 and S_2 states over the examined reaction coordinate.

A.4 Further derivations of linear-response TDDFT

This section continues on from equation 1.51 in the main text.

At this point, we note that the RG theorem states that in the limit of the exact XC functional, the Kohn-Sham and exact time-dependent densities will be equal. Therefore the exact time-dependent density can be found from Kohn-Sham response:

$$n_1(\mathbf{r},t) = \int_0^\infty dt' \int d\mathbf{r}' \chi_{\mathrm{KS}}(\mathbf{r},t;\mathbf{r}',t')\delta v_{\mathrm{KS}}(\mathbf{r}',t') \tag{A.1}$$

In this, $\delta v_{\mathrm{KS}}(\mathbf{r},t)$ calculates the change in KS potential due to the time-dependent density. This is not only the original $\delta v_{\mathrm{KS}}(\mathbf{r},t)$ term but also the Hartree and exchange correlation terms:

$$\delta v_{\mathrm{KS}}(\mathbf{r},t) = \delta v_{\mathrm{KS}}(\mathbf{r},t) + \int d\mathbf{r}' \frac{n_1(\mathbf{r}',t)}{|\mathbf{r}'-\mathbf{r}|} + \int_0^\infty dt' \int d\mathbf{r}' f_{\mathrm{XC}}[n_0](\mathbf{r},t;\mathbf{r}',t')n_1(\mathbf{r}',t). \tag{A.2}$$

Next, we consider the response function for a frequency dependent perturbation. We acquire this using perturbation theory[110]:

$$\chi_{\mathrm{KS}}(\mathbf{r},\mathbf{r}',\omega) = \lim_{\eta\to 0^+} \sum_{k,j} (f_k - f_j)\delta_{\sigma_k\sigma_j} \frac{\Phi_k^*(\mathbf{r})\Phi_j^*(\mathbf{r})\Phi_k(\mathbf{r}')\Phi_j(\mathbf{r}')}{\omega - (\epsilon_j - \epsilon_k) + i\eta}. \tag{A.3}$$

When we substitute equation A.3 into equation A.2, we get the following Dyson-like equation

$$\begin{aligned}\chi[n_0](\mathbf{r},t;\mathbf{r}',t') =& \chi_{\mathrm{KS}}[n_0](\mathbf{r},t;\mathbf{r}',t') + \int_0^\infty dt_1 \int dt_2 \int d\mathbf{r}_1 \int d\mathbf{r}_2 \chi_{\mathrm{KS}}[n_0](\mathbf{r},t;\mathbf{r}_1,t_2) \\ &\times \left[\frac{\delta(t_1-t_2)}{|\mathbf{r}_1-\mathbf{r}_2|} + f_{xc}[n_0](\mathbf{r}_1,t_1;\mathbf{r}_2,t_2)\chi[n_0](\mathbf{r}_2,t_2;\mathbf{r}',t')\right].\end{aligned} \tag{A.4}$$

The equation may look long and complicated at first sight, but it can be simplified substantially. Firstly, we move to frequency space. Secondly we note the following expression contains the Hartree kernel:

$$f_{\mathrm{Hxc}}(\mathbf{r},\mathbf{r}',\omega) = \frac{1}{|\mathbf{r}-\mathbf{r}'|} + f_{\mathrm{xc}}(\mathbf{r},\mathbf{r}',\omega). \tag{A.5}$$

Finally, we use the notation * to mean an integral with suitable coordinates in order to drop any position coordinates. That gives us

$$\chi(\omega) = \chi_{\mathrm{KS}} * f_{\mathrm{Hxc}}(\omega) * \chi(\omega). \tag{A.6}$$

We can integrate both sides *versus* $v_{\mathrm{ext}}(\mathbf{r},t)$ to get

$$[n_1(\omega) - \chi_{\mathrm{KS}}(\omega) * f_{\mathrm{Hxc}}(\omega) * n_1(\omega)] = \chi_{\mathrm{KS}}(\omega)\delta v_{\mathrm{ext}}(\omega). \tag{A.7}$$

This form is useful as it is expressed solely in terms of KS quantities, all of which we

can calculate. Further, we can write this as

$$[\hat{I} - \chi_{\mathrm{KS}}(\omega) * f_{\mathrm{Hxc}}(\omega)] * n_1(\omega) = \chi_{\mathrm{KS}}(\omega)\delta v_{\mathrm{ext}}(\omega) \tag{A.8}$$

This finally gives us the means to solve for the poles of the exact density response, which in this case are the excitations of the exact system. We achieve this using a clever, if slightly counter intuitive method. We are aware that the poles of the exact system are, by definition, not at the excitation energies of the KS system. Therefore it must be the case that if there is a pole in n_1 the operator acting on n_1, which is $[\hat{I} - \chi_{\mathrm{KS}}(\omega) * f_{\mathrm{Hxc}}(\omega)]$, must cancel it out. Therefore, one can look at the "anti-poles" of the operator. These energies, for which this operator is not invertible, are the exact excitation energies Ω_I. We can use this to turn the problem into an eigenvalue problem where $\lambda(\omega)$ are eigenvalues and $\xi(\omega)$ are eigenvectors:

$$\chi_{\mathrm{KS}}(\omega) * f_{\mathrm{Hxc}} * \xi(\omega) = \lambda(\omega)\xi(\omega). \tag{A.9}$$

We know that $\lambda(\Omega_I) = 1$ therefore we can solve for Ω_I. We must now turn this into a computational tractable equation. Firstly for a single KS transition between orbitals i and a we define a double index $q = (i, a)$ with a transition frequency of

$$\omega_q = \epsilon_a - \epsilon_i \tag{A.10}$$

Let b_q represent the ground state occupation numbers of orbitals a and i for example, if both are occupied or both are unoccupied $b_q = 0$; if just orbital i is occupied then $b_q = 2$ (this is known as a forward transition); and if orbital i is unoccupied and a is occupied $b_q = -2$ (this is known as a backwards transition). We define

$$\zeta_q(\omega) = \int d\mathbf{r}' \int d\mathbf{r}'' \Phi_q(\mathbf{r}) f_{\mathrm{Hxc}}(\mathbf{r}', \mathbf{r}'', \omega)\xi(\mathbf{r}'', \omega) \tag{A.11}$$

where $\Phi_q(\mathbf{r})$ is transition density in that

$$\Phi_q(\mathbf{r}) = \psi_i^*(\mathbf{r})\psi_a(\mathbf{r}). \tag{A.12}$$

We can now recast equation A.9 as

$$\lim_{\eta \to 0^+} \sum \frac{M_{qq'}(\omega)}{\omega - \omega_{q'} + i\eta} \zeta_{q'}(\omega) = \lambda(\omega)\xi(\omega), \tag{A.13}$$

where we have introduced the matrix elements $M_{qq'}(\omega)$, where

$$M_{qq'}(\omega) = b_{q'} \int d\mathbf{r} \int d\mathbf{r}' \Phi_q^*(\mathbf{r}) f_{\mathrm{Hxc}}(\mathbf{r}, \mathbf{r}', \omega)\Phi_q(\mathbf{r}'). \tag{A.14}$$

By defining $\beta_{q'} = \eta_q(\Omega)/(\Omega - \omega_q)$ and remembering that $\lambda(\Omega) = 1$ at the true excitations we can determine that at true excitations

$$\sum_{q'} [M_{qq'}(\Omega) + \omega_q \delta_{qq'}] B_{q'} = \Omega B_{q'}. \tag{A.15}$$

This eigenvalue problem provides, in principle, the true excitation spectrum of the interacting system. For an infinite basis set the matrix is infinite dimensional, going over all possible single excitations. To work with it, this matrix must be truncated. One method of truncation is to only consider forward transitions, this is known as the Tamm-Dancoff approximation.

A common matrix formulation to make TDDFT more practical was defined by Casida in 1995, resulting in what are commonly known as the Casida equations. By considering the poles and residues of the frequency dependent polarisability it was shown that the true frequencies Ω and oscillator strengths can be obtained from eigenvalues and eigenvectors of the following matrix equation.

$$RF_I = \Omega_I^2 F_I, \tag{A.16}$$

Where

$$R_{qq'} = \omega_q^2 \delta_{qq'} + 4\sqrt{\omega_q \omega_q'} \int d\mathbf{r} \int d\mathbf{r}' \Phi_q^*(\mathbf{r}) f_{\mathrm{Hxc}}(\mathbf{r}, \mathbf{r}', \omega) \Phi_q(\mathbf{r}') \tag{A.17}$$

and the oscillator strength of transition I in the interacting system can be defined as:

$$f_I = \frac{2\Omega_I}{3}(|\left\langle \Psi_0 \right| \hat{x} \left| \Psi_I \right\rangle|^2 + |\left\langle \Psi_0 \right| \hat{y} \left| \Psi_I \right\rangle|^2 + |\left\langle \Psi_0 \right| \hat{z} \left| \Psi_I \right\rangle|^2). \tag{A.18}$$

The KS orbitals are chosen to be real in this formulation. At this point we consider the adiabatic approximation. This holds that the system begins at the ground state when the density at time t is plugged in. This is holds when external time dependence is very slow.

A.5 Declaration of Contributions

In the first presented paper (Turner *et al.*, *J. Phys. Chem A.* 2019) all underlying research was conducted by the author. The author was the sole contributor to the writing of the paper with advisory help from M. D. Horbury, V. G. Stavros, and N. D. M. Hine.

In the second presented paper (Turner *et al.*, *J. Chem. Phys.* 2019) all underlying research was conducted by the author with aid from R. J. Turner. The writing was solely conducted by the author with advisory help from R. J. Turner, M. D. Horbury, V. G. Stavros, and N. D. M. Hine.

In the third presented paper (Turner *et al.*, in prep.) the underlying research was conducted largely collaboratively. Theoretical results were obtained by the author with help from E. L. Holt and K. M. Krokidi; solution-phase ultrafast and steady state measurements were conducted by E. L. Holt; ultrafast time-resolved gas-phase measurements were conducted by K. M. Krokidi with help from N. d. N. Rodrigues; and frequency-resolved gas-phase results were conducted by P. Mishra under the supervision of T. S. Zwier. The writing of the paper was conducted primarily by E. L. Holt, with large contributions from the author, K. M. Krokidi, and N. d. N. Rodrigues. V. G. Stavros provided advisory help. **Note:** In the first presented paper, on lines 19 and 21 of the "Computational" results section the units associated with the molecular dynamics calculation have been changed from the original paper to correct a small error in the published manuscript.